



The
University
Of
Sheffield.

**Control Techniques for Energy Management using
Energy Storage in DC Electric Railways**

By:

Hammad Alnuman

A thesis submitted in partial fulfilment of the requirements for
the degree of Doctor of Philosophy

The University of Sheffield
Faculty of Engineering
Department of Electronic and Electrical Engineering

June 2021

Abstract

This thesis is concerned with the topic of increasing energy efficiency in DC railway systems, to reduce CO₂ emissions associated with this form of transportation by minimising the energy consumption and energy loss of the system. In this work a method is proposed and implemented to model a DC railway that enables the effects of incorporating an energy storage system (ESS) to improve energy efficiency to be investigated. To date, no systematic investigation has considered the parameters by which an ESS can be controlled, the effects this has on the power flows of the electrical system and hence be able to provide an accurate energy analysis.

Electric trains are capable of regenerating energy that can be utilised by other trains operating on the same conductor rails, reducing the traction energy demand by up to 50%. However, poor synchronisation between accelerating and decelerating trains causes an excess of regenerative energy to be dissipated in braking resistors in the form of heat. ESSs have been proposed to assist in the energy efficiency improvement of electric railways by exploiting the captured excess braking energy to reduce the traction energy demand.

A simulation model for an electric railway system was developed in MATLAB software to investigate the application of a generalised ESS to the railway model. A comprehensive sensitivity analysis was carried out to explore the optimal voltage thresholds of an ESS controller that could maximise the energy savings in the electric railway system. The results show that optimising for the best energy savings will lead to a significant imbalance of the ESS import and export energy, meaning that the ESS will always trend to reach its state of charge (SOC) boundaries. As an ESS cannot have infinite capacity, and practical restrictions mean that its SOC cannot be separately managed, under normal operation the ESS would always become unavailable negating any positive effect it would have had.

A multi-objective algorithm was used to select the optimal voltage thresholds for an ESS controller, with fixed current control, and simulated under deterministic

behaviour of the railway system operation. This was then extended to investigate two adaptive control methods to dynamically change the ESS current in response to variable railway operations. The first adaptive control method used state machine control while the second method employed fuzzy logic control to adapt the ESS current to avoid ESS unavailability without compromising on the energy savings. The proposed control methods were implemented experimentally for validation.

Three case studies representing different railway operations were applied to the electric railway model and then simulated for two days to test the impact of the proposed control methods on the energy savings. The results indicate that the ESS controller applying the optimal voltage thresholds and fixed current provided energy savings of 42.34%, 41.02%, and 30.18% when simulating the first, second, and third case study, respectively. The first adaptive control method implementing state machine achieved energy savings of 38.96%, 41.55%, and 38.75%, while the second adaptive control method implementing fuzzy logic yielded 41.43%, 43.08%, and 39.21%, respectively. The proposed control methods were validated experimentally to prove their capability in real-world applications. The experimental results of the proposed controllers applied to the three case studies were compared against the simulation results, showing a percentage error ranging from 1.8 to 3.6%.

The findings reported in this thesis suggest that ESSs can effectively import and exploit the regenerative energy to improve the energy efficiency of electric railways. Moreover, the benefits of ESSs could be maximised while avoiding their unavailability through adaptive control and careful selection of the ESS operating parameters.

List of Publications

The findings yielded by this research have resulted in two journal articles and two contributions to conference proceedings, as outlined below:

- H. Alnuman, D. Gladwin and M. Foster, "Development of an electrical model for multiple trains running on a DC 4th rail track," in *IEEE International Conference on Environment and Electrical Engineering and IEEE Industrial and Commercial Power Systems Europe (EEEIC / I&CPS Europe)*, Palermo, Italy, 2018.
- H. Alnuman and D. Gladwin, "Energy storage application into a double DC electric railway," *Energy Procedia*, vol. 151, pp. 12–16, Oct 2018.
- H. Alnuman, D. Gladwin and M. Foster, "Electrical modelling of a DC railway system with multiple trains," *Energies*, vol. 11, no. 11, pp. 3211–3231, Oct 2018.
- H. Alnuman, D. Gladwin, M. Foster and T. Fantham, "Adaptive control method to manage SOC for energy storage in DC electric railways," in *IECON 2019 - 45th Annual Conference of the IEEE Industrial Electronics Society*, Lisbon, Portugal.

Acknowledgments

First and foremost, I would like to express my gratitude to Allah, who has given me the opportunity to expand my knowledge via PhD research, and gifted me with patience and vigour throughout this academic journey.

I am profoundly indebted to my supervisor Professor Daniel Gladwin for his endless support, patience, guidance, and encouragement. Whenever I was experiencing difficulties with my research, he would imbue me with confidence and encourage me to persevere with his enlightening suggestions. Professor Gladwin had a great vision for my PhD project and his unwavering support was instrumental in transforming that vision into reality. I always enjoyed our meetings, as they allowed me to learn many academic and life lessons. Professor Gladwin was always kind and supportive, and found the time to offer words of encouragement despite his busy schedule.

I would also like to thank Professor Martin Foster and Professor David Stone for their constructive feedback and advice. I wish to show my deep gratitude to Professor Martin Foster for his rigorous and critical comments that improved the clarity, presentation, and structure of this thesis. I am grateful to Dr Matthew Smith and Dr Shahab Nejad for their technical support in the experimental part of this thesis. I extend my thanks also to the staff of the Electronic and Electrical Engineering Department at the University of Sheffield, in particular Mrs Hilary Levesley, for their support in providing a healthy academic environment, thus ensuring that students could enjoy their studies.

I am immensely grateful to my mother Fadah, who inspired me through her daily calls. I wish to take this opportunity to thank my father Hamad, who is sadly no longer with us and cannot celebrate his son's achievements. I would like to thank my brother Hatem and my sisters Meaad, Lojain, Waad, and Ahad for taking care of things that could have distracted me from my PhD studies. Special appreciation also goes to my wife Milaf Ahmed for her unconditional love and support. Thanks should

also be given to my beloved daughters Yafa and Diala who fill my life with joy and happiness, and I seek their forgiveness for spending much more time on PhD research than with them.

Finally, I would like to thank the government of Saudi Arabia and Al-Jouf University for sponsoring this PhD project.

Table of Contents

Abstract.....	i
List of Publications.....	iii
Acknowledgments.....	iv
Table of Contents.....	vi
Nomenclature.....	ix
List of Figures.....	x
List of Tables.....	xviii
Chapter 1 Introduction.....	1
1.1 Background and motivation.....	1
1.2 Scope of work.....	4
1.3 Thesis contributions.....	5
1.4 Thesis structure.....	6
Chapter 2 Background and State-of-the-Art Review of Electric Railways and Related ESS Applications.....	8
2.1 Electric railways.....	8
2.1.1 History.....	8
2.1.2 Railway electrification system.....	14
2.2 DC electric railway energy efficiency.....	18
2.2.1 Electric railway modelling methods.....	18
2.2.2 Methods for improving DC electric railway energy efficiency.....	23
2.2.3 Review of ESSs.....	26
2.2.3.1 Batteries.....	27
2.2.3.2 Supercapacitors.....	29
2.2.3.3 Flywheels.....	32
2.2.3.4 Hybrid energy storage systems.....	33
2.2.4 Review of ESS applications in DC electric railways.....	37
2.2.4.1 ESS installation location.....	37
2.2.4.2 Energy efficiency improvement using ESSs.....	38
2.3 ESS control methods for SOC management in DC electric railways.....	41
2.4 Conclusion and research gaps.....	45
Chapter 3 Development of an Electrical Model for Multiple Trains Running on a DC 4th Rail Track.....	47
3.1 Introduction.....	47
3.2 Electric railway system.....	49
3.2.1 Train.....	49
3.2.2 DC railway traction power system.....	50
3.2.3 Train operation.....	54

3.3	Modelling approach.....	55
3.4	Beijing Metro and the development of a test scenario.....	60
3.4.1	Beijing Metro system.....	61
3.4.2	Test scenario.....	65
3.4.3	Train model.....	68
3.4.4	Power system model.....	75
3.4.5	Power system analysis.....	83
3.4.6	Power utilisation discussion.....	88
3.4.7	Model verification.....	91
3.5	Conclusion.....	95
Chapter 4 Voltage Control Sensitivity Analysis for a DC Electric Railway with Energy Storage.....		97
4.1	Introduction.....	97
4.2	Modes of power exchange between a DC electric railway and a stationary ESS.....	98
4.3	Energy storage system model.....	99
4.4	Voltage sensitivity analysis.....	105
4.4.1	Substation energy demand.....	106
4.4.2	Substation peak power demand.....	108
4.4.3	Transmission line losses.....	111
4.4.4	Energy dissipated in on-board braking resistors.....	114
4.4.5	Total energy saving.....	116
4.4.6	SOC drift.....	118
4.4.7	Voltage threshold selection.....	121
4.5	Location of the ESS.....	127
4.6	Conclusion.....	129
Chapter 5 Adaptive Control Methods for Managing SOC for Energy Storage in DC Electric Railways.....		131
5.1	Introduction.....	131
5.2	Proposed control techniques.....	132
5.2.1	SOC controller 1.....	133
5.2.2	SOC controller 2.....	137
5.3	Energy efficiency analysis when applying multiple traffic scenarios.....	151
5.3.1	Changing train headway scenario.....	151
5.3.2	Stochastic traffic scenario.....	155
5.3.3	Two-day simulation.....	159
5.4	Conclusion.....	163
Chapter 6 Experimental Application of Adaptive Control Methods.....		165
6.1	Introduction.....	165
6.2	Hardware configuration.....	166
6.2.1	Zenone Elettronica programmable DC power supply.....	167
6.2.2	SINAMICS DCP DC/DC power converter.....	169
6.2.3	CompactRIO controller.....	171
6.2.4	Maxwell supercapacitor.....	174
6.3	Software configuration.....	175

6.3.1	Zenone Elettronica programmable DC power supply.....	176
6.3.2	SINAMICS DCP DC/DC power converter.....	178
6.3.3	CompactRIO controller.....	183
6.3.4	Maxwell supercapacitor.....	187
6.4	Experimental results.....	190
6.4.1	Ideal traffic scenario.....	190
6.4.2	Changing train headway scenario.....	191
6.4.3	Stochastic traffic scenario.....	192
6.5	Comparison of experimental and simulation results.....	194
6.6	Conclusion.....	204
Chapter 7 Conclusions and Future Work.....		205
7.1	Summary of research objectives.....	205
7.2	Conclusions.....	205
7.3	Study limitations and recommendations for future work.....	208
References.....		209
Appendices.....		224
Appendix 1	Fuzzy controller rules.....	224
Appendix 2	SOC control test rig.....	230
Appendix 3	SINAMICS DCP electrical connection.....	231

Nomenclature

AC	Alternating current
CI	Current injection
CMI	Conductance matrix iterative
CO₂	Carbon-dioxide
CUD	Control unit direct current master
DC	Direct current
DCP	Direct current positive
DOD	Depth of discharge
ESS	Energy storage system
HESOP	Harmonic and Energy Saving Optimiser
HESS	Hybrid energy storage system
IGBT	Insulated-gate bipolar transistor
Li-ion	Lithium-ion
MCI	Modified current injection
NI	National Instruments
Ni-Cd	Nickel-cadmium
Ni-MH	Nickel-metal-hydride
PROFIBUS	Process field bus
SOC	State of charge
SOH	State of health
TCR	Traction Controlled Rectifier
USB	Universal serial bus

List of Figures

Figure 1.1: Total energy consumption in Europe by sector in (a) 1990 and (b) 2017.....	2
Figure 1.2: Illustration of power exchange process between two trains in a track section.....	3
Figure 1.3: Typical traction energy flow in metro systems.....	4
Figure 2.1: The world’s first electric tram.....	11
Figure 2.2: Train supplied by a 4 th rail traction system.....	16
Figure 2.3: Contact shoe touching a conductor rail.....	17
Figure 2.4: Photos of braking resistors mounted on the roof of trains.....	18
Figure 2.5: Snapshot of the electrical configuration of a metro system at a particular time where SC refers to supercapacitors.....	19
Figure 2.6: Schematic diagram of the INGEBER system integrated into an existing substation.....	26
Figure 2.7: Life cycle of a lead-acid battery with respect to DOD.....	27
Figure 2.8: Discharge curves of several primary (P) and secondary (S) batteries.....	29
Figure 2.9: (a) Typical charge and discharge curves of a Li-ion battery with 80 mA charge current and 400 mA discharge current; (b) charge and discharge curves of a supercapacitor at different currents.....	31
Figure 2.10: 1 MW supercapacitor system at Liyuan substation of Batong Line of the Beijing Metro, China.....	35
Figure 2.11: On-board supercapacitor at Mannheim Railway, Germany.....	36
Figure 2.12: Sitras HES installed on the roof of a train.....	36
Figure 3.1: Representation of an electromechanical system in an AC train fed by a DC traction system.....	50
Figure 3.2: Typical structure of a rail track.....	50
Figure 3.3: Configuration of a double-track DC railway power system.....	51
Figure 3.4: Schematic of a train running on a rail track and powered by a 4 th rail system.....	51
Figure 3.5: Power supply feeding schemes: (a) single-end feeding mode; (b) double-end feeding mode.....	53

Figure 3.6: Typical driving cycle of a train between two consecutive passenger stations	55
Figure 3.7: Dynamics of a single train.....	58
Figure 3.8: Electrical configuration of multiple trains running on a single-track with two substations.....	59
Figure 3.9: Electrical configuration of multiple trains running on a double-track with two substations.....	60
Figure 3.10: Topological map of Yizhuang Line in Beijing Metro.....	61
Figure 3.11: Field test in Yizhuang Line of train trajectory optimisation.....	63
Figure 3.12: Maximum tractive force and maximum braking force for vehicles in the Yizhuang Line.....	65
Figure 3.13: Double-track railway with 2 substations, 3 passenger stations, and 8 running trains.....	66
Figure 3.14: Screen capture of a single train modelled in MATLAB Simulink.....	69
Figure 3.15: Speed profile, actual tractive/braking force and limits of speed and tractive/braking force of a single train travelling between two passenger stations	70
Figure 3.16: Acceleration and jerk rate of a single train travelling between two passenger stations.....	71
Figure 3.17: Speed profiles of four trains running on a 2 km segment of a double-track railway with 90 s headway between consecutive trains.....	73
Figure 3.18: Train diagrams of eight trains running on a double-track railway serving three passenger stations.....	73
Figure 3.19: Power and speed profiles of Train 1 when travelling from Passenger Station A to B.....	75
Figure 3.20: Screen capture of the power system model created in MATLAB Simulink.....	78
Figure 3.21: Screen capture of a train equipped with a braking resistor modelled in MATLAB Simulink.....	79
Figure 3.22: Electrical resistance between Train 1 and the passenger stations in the modelled double-track railway.....	81
Figure 3.23: Calculation process illustration of the transmission line electrical resistance between two passenger stations when: (a) only train n is travelling; (b) a train is travelling behind train n; (c) a train is travelling ahead of train n.....	81

Figure 3.24: Screen capture of the MATLAB Simulink model representing electrical resistance variation: (a) ahead of Train 2; (b) behind Train 2.....	82
Figure 3.25: Number of trains running on a double-track railway during the simulation period.....	83
Figure 3.26: Voltage at two studied substations on the modelled double-track railway system.....	84
Figure 3.27: Substation currents of a double-track railway represented by the simulation model.....	85
Figure 3.28: Substation power of the modelled double-track railway.....	85
Figure 3.29: Voltages and currents of individual trains on the modelled double-track railway: (a) Train 1; (b) Train 2; (c) Train 3; (d) Train 4; (e) Train 5; (f) Train 6 (g) Train 7; (h) Train 8.....	87
Figure 3.30: Dissipated energy in the braking resistors of the eight trains as a percentage of the substations energy consumption when the headway was 90 s.....	88
Figure 3.31: The double railway line receptivity as a function of headway duration.....	90
Figure 3.32: Total energy dissipated through the on-board braking resistors of the trains running on a double-track railway as a function of headway duration.....	90
Figure 3.33: Passenger Station B, Train 1, and Train 5 voltage as a function of time.....	93
Figure 3.34: Passenger Station B, Train 2, and Train 6 voltage as a function of time.....	93
Figure 3.35: Passenger Station B, Train 3, and Train 7 voltage as a function of time.....	94
Figure 3.36: Passenger Station B, Train 4, and Train 8 voltage as a function of time.....	94
Figure 4.1: Charging and discharging process.....	100
Figure 4.2: Voltage control method.....	100
Figure 4.3: Screen capture of an ESS modelled in MATLAB Simulink	103
Figure 4.4: Sizing an ESS when located at Passenger Station A and subjected to different traffic scenarios	104
Figure 4.5: Voltage at Passenger Station A when connecting an ESS with 400 Ah capacity, 6300 A current limit, and : (a) 53 controller gain; (b) 54 controller gain; (c) 54 controller gain when the voltage is Zoomed in.....	105

Figure 4.6: Reduction of the substation energy demand under voltage limit variation when placing the ESS at Passenger Station A.....	107
Figure 4.7: Reduction of the substation energy demand under voltage limit variation when placing the ESS at Passenger Station B.....	108
Figure 4.8: Reduction of Substation 1 peak power demand under voltage limit variation when placing the ESS at Passenger Station A.....	109
Figure 4.9: Reduction of Substation 2 peak power demand under voltage limit variation when placing the ESS at Passenger Station A.....	110
Figure 4.10: Reduction of Substation 1 peak power demand under voltage limit variation when placing the ESS at Passenger Station B.....	110
Figure 4.11: Reduction of Substation 2 peak power demand under voltage limit variation when placing the ESS at Passenger Station B.....	111
Figure 4.12: Decline of transmission line losses under voltage limit variation when the ESS was located at Passenger Station A.....	112
Figure 4.13: Decline of transmission line losses with respect to voltage limit variation when the ESS was positioned at Passenger Station B.....	113
Figure 4.14: Reduction of energy losses in the on-board braking resistors with respect to voltage limit variation when the ESS was positioned at Passenger Station A.....	114
Figure 4.15: Reduction of energy losses in the on-board braking resistors with respect to voltage limit variation when the ESS was positioned at Passenger Station B.....	115
Figure 4.16: Total energy saving in percentage with respect to voltage limit variation when placing the ESS at Passenger Station A.....	117
Figure 4.17: Total energy saving in percentage with respect to voltage limit variation when placing the ESS at Passenger Station B.....	117
Figure 4.18: SOC drift with respect to voltage limit variation when placing the ESS at Passenger Station A.....	120
Figure 4.19: Absolute value of the SOC drift with respect to voltage limit variation when placing the ESS at Passenger Station A	120
Figure 4.20: Normalised total energy saving when placing the ESS at Passenger Station A.....	123
Figure 4.21: Normalised SOC drift when placing the ESS at Passenger Station A.....	123
Figure 4.22: Total score of each alternative corresponding to all criteria when placing the ESS at Passenger Station A.....	124
Figure 4.23: Terminal voltage at Passenger Station A before and after including the ESS.....	128

Figure 4.24: Terminal voltage at Passenger Station B before and after including the ESS.....	129
Figure 5.1: Flow chart of the SOC drift control.....	135
Figure 5.2: Screen capture of an ESS under the control of SOC controller 1 modelled in MATLAB Simulink.....	136
Figure 5.3: SOC and current of the ESS implementing SOC controller 1 when simulating the ideal traffic scenario	137
Figure 5.4: General structure of fuzzy control.....	138
Figure 5.5: Screen capture of an ESS under the control of SOC controller 2 modelled in MATLAB Simulink.....	140
Figure 5.6: Input and output variables of the fuzzy inference system modelled using the Fuzzy Logic Designer Toolbox in MATLAB.....	141
Figure 5.7: Fuzzy energy management system.....	142
Figure 5.8: Input variable of the running time comprising four membership functions modelled using the Fuzzy Logic Designer Toolbox in MATLAB	145
Figure 5.9: Input variable of the positive SOC drift comprising four membership functions modelled using the Fuzzy Logic Designer Toolbox in MATLAB.....	146
Figure 5.10: Input variable of the negative SOC drift comprising four membership functions modelled using the Fuzzy Logic Designer Toolbox in MATLAB.....	146
Figure 5.11: Input variable of the rate of change comprising four membership functions modelled using the Fuzzy Logic Designer Toolbox in MATLAB.....	146
Figure 5.12: Input variable of the track voltage comprising two membership functions modelled using the Fuzzy Logic Designer Toolbox in MATLAB.....	147
Figure 5.13: Output variable of the charging current limit comprising four membership functions modelled using the Fuzzy Logic Designer Toolbox in MATLAB.....	147
Figure 5.14: Output variable of the discharging current limit comprising four membership functions modelled using the Fuzzy Logic Designer Toolbox in MATLAB.....	147
Figure 5.15: SOC of the ESS when the ideal traffic scenario was simulated.....	149
Figure 5.16: Voltage at Passenger Station A under the ideal traffic scenario.....	150
Figure 5.17: The ESS current yielded by different control approaches when the ideal traffic scenario was assumed.....	150
Figure 5.18: SOC of the ESS when Train 8 headway was modified.....	152

Figure 5.19: Voltage at Passenger Station A when Train 8 headway was modified....	154
Figure 5.20: The ESS current determined by different control approaches when Train 8 headway was modified.....	154
Figure 5.21: Train diagrams for the railway system exhibiting stochastic behaviour.....	155
Figure 5.22: Train speed profiles in the railway system exhibiting stochastic behaviour	156
Figure 5.23: SOC of the ESS under a stochastic traffic scenario	157
Figure 5.24: Voltage at Passenger Station A under a stochastic traffic scenario.....	158
Figure 5.25: The ESS current determined by different control approaches under a stochastic traffic scenario.....	158
Figure 5.26: Two-day simulation based on the ideal traffic scenario.....	160
Figure 5.27: Two-day simulation based on the traffic scenario involving changes to the Train 8 headway	161
Figure 5.28: Two-day simulation based on the stochastic traffic scenario.....	163
Figure 6.1: Hardware setup.....	166
Figure 6.2: I–V characteristics of the bidirectional DC power supply with line regenerator.....	167
Figure 6.3: Bidirectional DC power supply AL 3000R.....	168
Figure 6.4: I–V characteristics of the SINAMICS DCP power converter.....	170
Figure 6.5: SINAMICS DCP DC/DC power converter efficiency measurements.....	170
Figure 6.6: SINAMICS DCP DC/DC power converter.....	171
Figure 6.7: cRIO-9063: (a) device; (b) dimensions.....	172
Figure 6.8: NI 9206: (a) device; (b) pinout.....	173
Figure 6.9: NI 9263: (a) device; (b) pinout.....	173
Figure 6.10: Maxwell supercapacitor module.....	174
Figure 6.11: Substation 1 scaled voltage under: (a) ideal traffic scenario; (b) changing train headway scenario; (c) stochastic traffic scenario.....	176
Figure 6.12: AL Manager software utilised for controlling AL3000R power supply.....	177
Figure 6.13: AL3000R power supply control interface.....	178

Figure 6.14: PROFIBUS connection: (a) USB adapter; (b) CUD.....	179
Figure 6.15: Screen capture of STARTER parameterisation tool.....	179
Figure 6.16: Real-time data monitoring using STARTER software.....	180
Figure 6.17: The terminal module cabinet.....	181
Figure 6.18: Remote initiation of the SINAMICS DCP device using STARTER.....	182
Figure 6.19: Screen capture of the static controller model built in LabVIEW.....	184
Figure 6.20: Screen capture of the SOC controller 1 model built in LabVIEW.....	185
Figure 6.21: Screen capture of the SOC controller 2 model built in LabVIEW.....	186
Figure 6.22: Voltage versus SOC profile when applying the ESS under the ideal traffic scenario: (a) without SOC control; (b) SOC controller 1; (c) SOC controller 2.....	188
Figure 6.23: Overvoltage protection control: (a) status monitoring; (b) limitation function against overcharging.....	189
Figure 6.24: Experimentally obtained supercapacitor SOC values based on different control approaches under the ideal traffic scenario.....	191
Figure 6.25: Experimentally obtained supercapacitor SOC values based on different control approaches when Train 8 headway was modified.....	192
Figure 6.26: Experimentally obtained supercapacitor SOC values based on different control approaches under a realistic traffic scenario.....	193
Figure 6.27: Screen capture of the power system model created in MATLAB Simulink.....	195
Figure 6.28: Comparison between the experimental and simulation results pertaining to the supercapacitor SOC determined by the state machine control under the ideal traffic scenario.....	196
Figure 6.29: Comparison between the experimental and simulation results pertaining to the supercapacitor current determined by the state machine control method under the ideal traffic scenario.....	197
Figure 6.30: Comparison between the experimental and simulation results pertaining to the supercapacitor SOC based on the fuzzy control approach under the ideal traffic scenario.....	197
Figure 6.31: Comparison between the experimental and simulation results pertaining to the supercapacitor current based on the fuzzy control method under the ideal traffic scenario.....	198

Figure 6.32: Comparison between the experimental and simulation results pertaining to the supercapacitor SOC yielded by the state machine control method when Train 8 headway was modified.....	199
Figure 6.33: Comparison between the experimental and simulation results pertaining to the supercapacitor current yielded by the state machine control method when Train 8 headway was modified.....	199
Figure 6.34: Comparison between the experimental and simulation results pertaining to the supercapacitor SOC imposed by the fuzzy control approach when Train 8 headway was modified.....	200
Figure 6.35: Comparison between the experimental and simulation results pertaining to the supercapacitor current imposed by the fuzzy control approach when Train 8 headway was modified.....	200
Figure 6.36: Comparison between the experimental and simulation results pertaining to the supercapacitor SOC produced by the state machine control under a realistic traffic scenario.....	201
Figure 6.37: Comparison between the experimental and simulation results pertaining to the supercapacitor current determined by the state machine control under a realistic traffic scenario.....	201
Figure 6.38: Comparison between the experimental and simulation results pertaining to the supercapacitor SOC obtained by applying the fuzzy control approach under a realistic traffic scenario.....	202
Figure 6.39: Comparison between the experimental and simulation results pertaining to the supercapacitor current obtained by applying the fuzzy control approach under a realistic traffic scenario.....	202
Figure A1: Single-line diagram for the experimental setup.....	230

List of Tables

Table 2.1: Characteristics of the most common railway traction systems	15
Table 2.2: Technical comparison between ESSs	33
Table 2.3: Examples of ESS applications	35
Table 3.1: DC traction system voltages.....	52
Table 3.2: Passenger station and substation location in Yizhuang Line.....	62
Table 3.3: Dwell time at passenger stations of the Yizhuang metro line.....	62
Table 3.4: Yizhuang Line practical data of speed limits, journey time, and energy consumption.....	64
Table 3.5: Train timetable adopted for the double-track railway (in seconds).....	67
Table 3.6: Parameters of describing the modelled electric railway system.....	76
Table 3.7: Energy consumption and losses in the modelled double-track railway.....	95
Table 4.1: Final decision calculation when charging at 755 V and varying the discharging voltage when placing the ESS at Passenger Station A.....	126
Table 4.2: Impact of varying the controller gain when placing the ESS at Passenger Station A with 6300 A current limit, and charging/ discharging at 755/740 V.....	126
Table 4.3: Impact of varying the current limit when placing the ESS at Passenger Station A with 53 controller gain, and charging/ discharging at 755/740 V.....	126
Table 4.4: Comparison between placing the ESS at Passenger Station A and charging/ discharging at 755/740 V against placing the ESS at Passenger Station B and charging/ discharging at 755/737 V.....	127
Table 5.1: The impact of applying different control approaches to the ESS on the railway's energy efficiency under the ideal traffic scenario.....	149
Table 5.2: The impact of applying different control approaches to the ESS on the railway's energy efficiency when Train 8 headway was modified.....	153
Table 5.3: The impact of applying different control approaches to the ESS on the railway's energy efficiency under the stochastic traffic scenario.....	157
Table 5.4: Energy efficiency analysis when simulating the ideal traffic scenario for two days.....	160
Table 5.5: Energy efficiency analysis when involving changes to the Train 8 headway.....	162

Table 5.6: Energy efficiency analysis when simulating the stochastic traffic scenario for two days.....	163
Table 6.1: Technical specifications of the bidirectional power supply.....	168
Table 6.2: Technical specifications of the SINAMICS DCP power converter.....	169
Table 6.3: Technical specifications of the Maxwell supercapacitor.....	175
Table A1: Rule table of the fuzzy logic controller consisting five inputs and two outputs.....	224
Table A2: Terminals on the connector board of the SINAMICS DCP power converter.....	231

Chapter 1

Introduction

1.1 Background and motivation

Global demand for fossil fuels is rapidly increasing owing to continued industrialisation and population growth. As these energy sources are non-renewable, they will eventually be depleted, necessitating the gradual adoption of alternatives such as solar and wind energy. Indeed, as climate change and many health issues have been shown to be closely linked to greenhouse gas emissions, reliance on fossil fuels must be reduced [1]. According to the Intergovernmental Panel on Climate Change, by 2050, greenhouse emissions in Europe must be reduced to 80–95% of their 1990 levels to stop these alarming trends from progressing further. However, this will require a major shift in societal attitudes as well as industry practices. As can be seen from the data on energy consumption in Europe depicted in Figure 1.1, transport is the sector that has contributed most significantly to the increase in gas emissions since 1990, as it is presently the main source of energy consumption [2].

In 2017, transportation accounted for 30.8% of the total energy consumption in Europe and was responsible for 21.1% of the total greenhouse gas emissions. Therefore, to reduce the energy consumption incurred by this sector, greater reliance on public transportation must be promoted at the policy level while ensuring that such systems run efficiently and are not solely reliant on fossil fuels [2]. Railways are the most effective public transportation systems as they can improve safety, reduce traffic congestion, and adhere to a precise timetable more closely than other public transport modes. Among railway systems, electric trains consume less energy than diesel and

steam trains due to the light weight resulting from not carrying energy sources on-board. Moreover, electric railways release fewer carbon dioxide (CO_2) emissions compared to other transportation systems. Therefore, the use of electric railways should be increased where possible. However, in recent years, increased reliance on electric railways has led to greater energy consumption; a consumption that must be managed and reduced to fully capitalise on the aforementioned benefits [3].

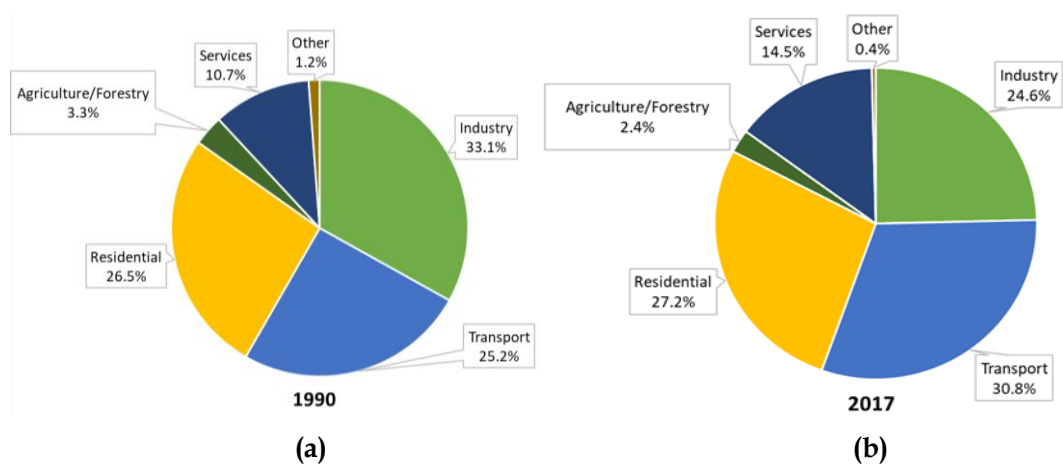


Figure 1.1: Total energy consumption in Europe by sector in (a) 1990 and (b) 2017 [2]

Most new trains include regenerative braking that is known as a process of slowing the train down by feeding its kinetic energy to braking resistors, ESSs, or the transmission line to be used by accelerating trains. [4]. In most cases of metro systems, which this study pertains to, the regenerative power cannot be utilised by the substations because, they are rectifiers where the power flow is unidirectional. As a result, the regenerative power is consumed by the available accelerating trains. However, due to the mismatch in the power requirements for acceleration and the power provided by decelerating trains, the track voltage rises and if not managed will exceed safe levels causing breakdowns. For example, the safe levels for DC traction systems of 600 V, 750 V, 1500 V, and 3000 V are 720 V, 900 V, 1800 V, and 3600 V,

respectively [5]. Therefore, trains carry braking resistors to limit the voltage rise by dissipating some of the regenerative power in the braking resistors as illustrated in Figure 1.2. Thus, rather than being utilised within the transport network to reduce the traction energy demand by up to 50%, the regenerative energy is dissipated in the form of heat and only 35% is recuperated in the best case scenario. The dumping of regeneration energy represents a wasted opportunity as shown by the energy loss explanatory diagram which includes other losses in traction and transmission, Figure 1.3 [7]–[12]. The figure shows how the traction energy supplied by substations is distributed in a typical metro system.

The wasted regenerative energy can be recuperated by energy storage systems (ESSs) to be used in improving the energy efficiency of electric railways. However, ESSs can be unavailable due to their capacity limits, which reduces their effectiveness in fulfilling their purpose. These issues have motivated the present study, the aim of which is to investigate various energy management methods and identify those that have the greatest potential to reduce ESS unavailability, reduce energy losses, and exploit the dissipated energy in braking resistors, thus maximising the energy efficiency of electric railways.

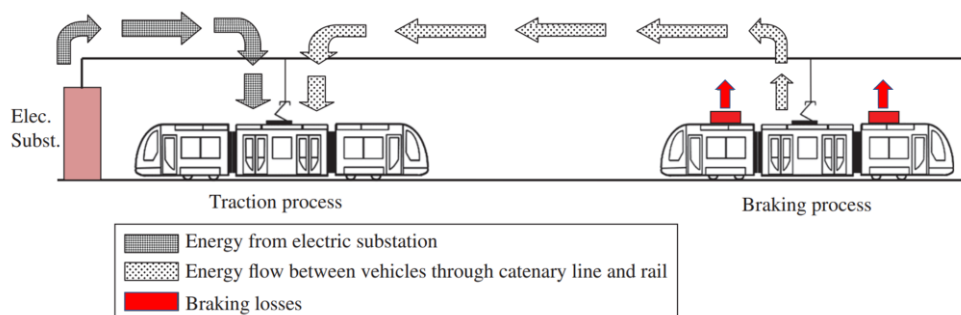


Figure 1.2: Illustration of power exchange process between two trains in a track section [6]

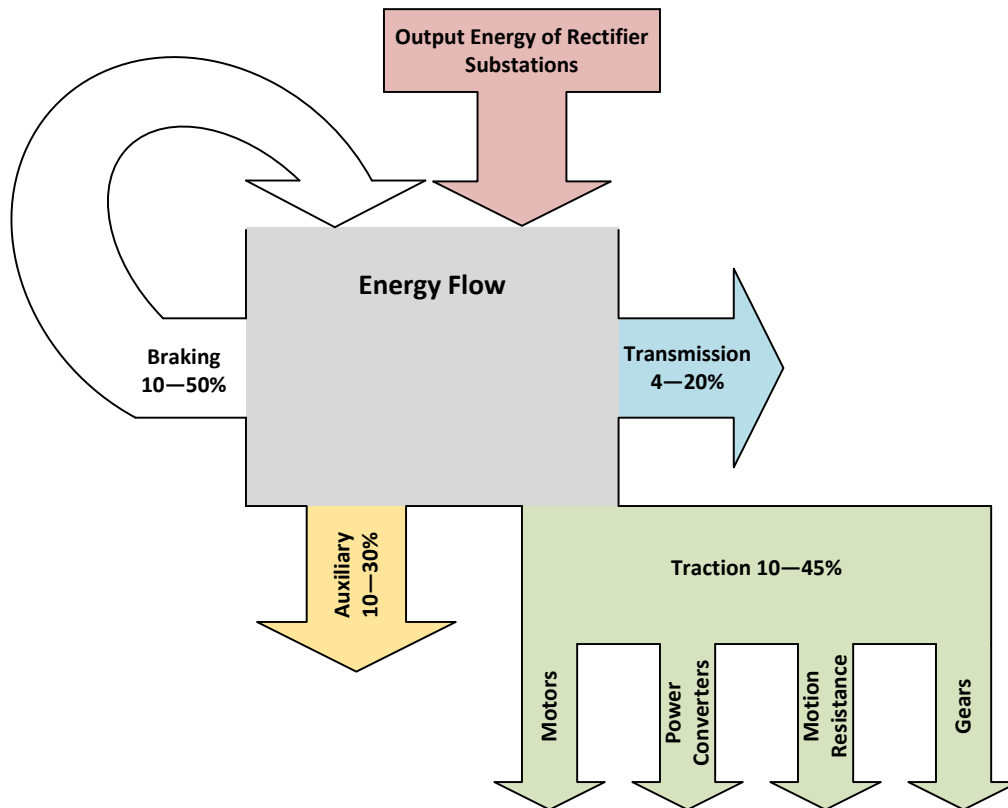


Figure 1.3: Typical traction energy flow in metro systems [7]–[12]

1.2 Scope of work

In this thesis, power system analysis is adopted to investigate the energy efficiency of direct current (DC) electric railways comprised of several passenger stations serviced by multiple trains. For this purpose, application of a stationary (wayside) ESS, as well as innovative control methods aimed at maximising the energy efficiency of electric railways, are investigated. Stationary rather than on-board ESSs are considered because of the 1–2% additional weight that on-board ESSs introduce to the vehicle, which increases its energy consumption [13], [14]. Within this thesis the term electric railway will refer to a DC electric railway only and not an alternating current (AC) electric railway. Throughout this thesis, the term energy efficiency will be used to refer to minimisation of transmission losses, braking losses and energy demands. As ESS type and chemistry are beyond the scope of the present study, only the general functionality of the ESS is considered. Evaluation of various control

approaches considered in this work are based on simulation and experimental results to test the applicability of the control methods in real-time applications. In sum, the main focus of this thesis is the ability of the investigated control techniques to improve DC electric railway energy efficiency through energy management by an ESS.

1.3 Thesis contributions

This thesis presents some novel contributions that are reported in four chapters (3–6), as outlined below:

- In Chapter 3, a novel method is proposed for modelling DC electric railways to support power flow analysis of a simulated metro train service. The model critically features regenerative braking, ESSs and supports multiple trains. The non-linear model can be employed to obtain voltages at any position along the track as well as the voltages experienced by any train. The associated publications to this contribution are:
 - H. Alnuman, D. Gladwin and M. Foster, “Development of an electrical model for multiple trains running on a DC 4th rail track,” in *IEEE International Conference on Environment and Electrical Engineering and IEEE Industrial and Commercial Power Systems Europe (EEEIC / I&CPS Europe)*, Palermo, Italy, 2018.
 - H. Alnuman, D. Gladwin and M. Foster, “Electrical modelling of a DC railway system with multiple trains,” *Energies*, vol. 11, no. 11, pp. 3211–3231, Oct 2018.
- The work presented in Chapter 4 investigates the importance of voltage control in optimal energy exploitation with metrics proposed to measure the impact of the ESS. These metrics go beyond those previously reported in literature and a sensitivity analysis of different

charge/discharge voltage limits and the effects this has is presented. The associated publication to this contribution is:

- H. Alnuman and D. Gladwin, “Energy storage application into a double DC electric railway,” *Energy Procedia*, vol. 151, pp. 12–16, Oct 2018.
- Novel adaptive control techniques are proposed in Chapter 5 aiming to protect an ESS interfaced with a DC electric railway from reaching state of charge (SOC) limits. The proposed control methods are based on state machine and fuzzy logic control strategies. It is shown that by employing the proposed control methods it is possible for the ESS to be managed despite disturbances in expected train schedules. The ESS models are validated with experimental results in Chapter 6 using a hardware setup incorporating a track emulator, DC/DC bi-directional converter and a supercapacitor module. The associated publication to this contribution is:
 - H. Alnuman, D. Gladwin, M. Foster and T. Fantham, “Adaptive control method to manage SOC for energy storage in DC electric railways,” in *IECON 2019 – 45th Annual Conference of the IEEE Industrial Electronics Society*, Lisbon, Portugal.

1.4 Thesis structure

This thesis is divided into seven chapters. Chapter 1, introduces the reader to the research objectives and Chapter 2 provides a brief overview of pertinent literature. The four main contributions outlined above are presented in the subsequent four chapters (Chapter 3–6). The thesis closes with Chapter 7, where final conclusions are reached and suggestions for further research are offered based on the knowledge gained from this study.

Chapter 1 is an introductory chapter that is designated for outlining the study aims and key contributions and presenting the thesis structure. Chapter 2 provides the background to the present study, focusing on the development of electric railways and ESS applications. It commences with a historical overview of railway systems, culminating with the suggestion that electric railways are the future of urban transport. Next, extant studies focusing on the energy efficiency issues affecting current electric railways are reviewed, followed by research in which use of ESS is considered as a solution. Finally, control techniques that can be used when ESSs are integrated with electric railways are discussed, before gaps are identified in extant research that then pave the way for the major contributions of this thesis.

A new method of modelling DC electric railways that avoids complex power flow calculations is introduced in Chapter 3. A double-track railway with single electrical section and multiple trains is analysed. Several verification methods for the system configuration are proposed and their findings are presented and discussed. The following chapter (Chapter 4) investigates the impact of voltage control of a stationary ESS and its positioning on the electric railway energy efficiency. Based on the findings yielded, recommendations for good choices of siting and voltage control are made to ensure efficient ESS integration into electric railways.

Two control methods for SOC management are proposed in Chapter 5, based respectively on state machine and fuzzy logic control. Their design and implementation is described in detail before critically examining their performance by applying each method to different traffic scenarios. The two control methods are experimentally applied and analysed in Chapter 6. The chapter commences with a detailed description of the hardware and software configuration of the equipment used in the experiments, as a part of which multiple voltage profiles are considered to practically assess the validity of the control methods. Finally, a comparison between the experimental and simulation results is carried out for validation.

Chapter 2

Background and State-of-the-Art Review of Electric Railways and Related ESS Applications

2.1 Electric railways

This chapter provides a brief overview of the history of electric railways and their importance to human development. Thereafter, a comparison between AC and DC traction systems is carried out before the main structure of common DC electrification systems is described. This is followed by an examination of different ESS types and their applications in electric railways. Finally, shortcomings in extant electric railway modelling approaches and energy management methods are identified, with a particular focus on ESS incorporation into DC electric railways.

2.1.1 History

The steam engine was invented by the Englishman Thomas Savery in 1698. Following on from this, developments in engine design during the 18th century revolutionised railway freight and later passenger transportation, which was previously limited to the use of pack animals and haulage. Not only was the use of engines more efficient, but also more cost-effective, especially in the early 19th century

when the price of horses increased rapidly as a result of their increased demand by the army during the Napoleonic Wars (1803–1815) [15]. The growing popularity of steam engines, particularly at the end of the 18th century, prompted major developments in their design in the 19th century, allowing Richard Trevithick to create the first steam locomotive in 1804, which was used to transport iron at Wylam Colliery near Newcastle. However, his engine was too heavy for the iron rails, causing them to break. To overcome this issue, John Blenkinsop cooperated with Fenton, Murray, and Wood to build a lighter engine, benefiting from Richard's experiment. This introduced other issues, most notably inadequate adhesion between the locomotive and the track, especially in sections under steep gradient. As a result, Blenkinsop invented a toothed rail and toothed locomotive wheels and used this novel design to transfer coal from Middleton Colliery to Leeds, which was commercialised in 1811. This thus represented the first commercially successful steam locomotive. In 1825, steam was used for the first time to power the Stockton and Darlington Railway as a public freight service. Initially, it took two hours to travel 15 km, but following subsequent improvements, a speed of 24 km/h was achieved. At that time, steam locomotives were only used to pull freight (mostly to transfer coal) while still relying on horses to pull passenger carriages. In 1830 the Liverpool and Manchester Railway began using steam power exclusively for passenger transportation, thus ushering in a new era in railway systems [16]–[18].

Steam railways were the major railway system during the 19th and first half of the 20th century. During that time, steam railways were limited by the heavy weight of steam engines, low speed, controllability of speed, and short distance covered before stopping for fuel and water. These drawbacks highlighted the need for diesel and electric railways that were developed for commercial use from the beginning of the 20th century. After major developments in the diesel engine during the first two decades of the 20th century it was finally deemed to be reliable for different industrial applications. This enabled the rail industry to begin to fully replacing steam trains with improved diesel versions. Relative to steam trains, the diesel trains were lighter in weight, faster in speed, could regulate their speed more easily, and could cover a longer distance before refuelling. These advantages rapidly expanded the use of

diesel-powered trains in railway transport during the 3rd and 4th decade of the 20th century. Indeed, by the second half of the same century it became the main traction system despite the rise in oil prices after 1973 [19], [20].

In terms of the main drivers of electrification of the railways early in their development, it was considered vital to avoid the high-emissions generated by steam trains, especially inside tunnels, where major collisions were likely to happen due to poor visibility. However, the cost of electric railway infrastructure in the first two decades of the 20th century could be four to six times higher than that of steam railways without improving upon the transport capacity, especially when the efficiency of power supply and transmission in electric railways was similar to that of steam railways. Over the years, electricity supply improved, while importing coal became more challenging and costly, especially during the First and Second World War, prompting some European countries to adopt electric railways. In fact, in the early years of electric railway development, only railways operating in mountainous areas were electrified due to the availability of hydroelectric power and the need for high traction power at steep inclines that could only be achieved by electric trains. Thus, gradual electrification of railways was motivated by uncertainties related to petroleum resource supply as well as a desire to reduce emissions and operating costs. And so, once electricity became more readily available, railway companies started abandoning steam engines in favour of electric traction due to higher speed and ease of operation [21].

Prior to widespread adoption though, electric railways witnessed a fairly slow evolution. The history of electric railways can be traced back to 1828 when Slovak-Hungarian Priest Anyos Jedlik used an electric motor to move a tiny model car. This prompted Strattingh and Becker to use electricity supplied by a battery to drive a two-axled vehicle in Groningen, Netherlands, in 1835. A similar experiment was accomplished in the same year by Thomas Davenport in the United States, who submitted an electric vehicle powered by a lead–acid battery for an exhibition. The first practical electric locomotive was achieved in 1842 by Robert Davidson, who used zinc–acid batteries to power a 7,000 kg electric locomotive named Galvani. The

Galvani locomotive was able to achieve a speed of 6 km/h while carrying a 6,000 kg load on the Glasgow–Edinburgh line. While this was the first locomotive to be powered by electricity, it did not attract investors due to the high cost of replacing depleted chemical batteries because rechargeable batteries had not yet been invented. Still, this prompted further developments, which led to Werner von Siemens presenting a small train powered by a 150 V electric locomotive capable of running at a speed of 12 km/h in 1879 at an exhibition in Berlin. In this pioneering design, a third rail between the running rails was used to supply current to the electric locomotive to pull the train on a 0.3-km-long electric railway. In 1881, Werner von Siemens built the world’s first electric tram in Lichterfelde, Germany (see Figure 2.1). The tram car – 5 m long and 2 m wide, weighing 4,800 kg – was able to carry 20 passengers [22]–[24].



Figure 2.1: The world’s first electric tram [25]

The advancements in the design of electromechanical generators and DC motors that took place during the 19th century motivated Gaston Plante to invent the first commercialised rechargeable lead–acid battery in 1859. However, these batteries could only be recharged by primary cells, a requirement which proved costly [24]. Still, as this was seen as the way forward, further developments ensued, resulting in

use of a lead–acid battery with 1,332 Ah capacity in 1912 to stabilise the voltage at the Maruyama and Yagasaki traction substation in Japan [26]. In 1926, the Edison battery–electric railcar was used in New Zealand to power a tram carrying 60 passengers at a speed of 48 km/h for approximately 161 km, after which it required charging for at least three hours. However, due to a fire incident in a depot in Christchurch, this project was abandoned after eight years [27]. In 1932, a rechargeable nickel–zinc battery was installed on a rail car in Ireland on the Dublin–Bray railway line. The rail car was capable of carrying 130 passengers and took only a few minutes to charge the batteries at the final station. An added bonus was that the train was able to store the regenerative energy generated while braking. However, at the time nickel–zinc batteries had very short lifetime and were costly to replace [28]. This prompted British railways to use lead–acid batteries to power a train from Aberdeen to Ballater in 1958. Unfortunately, the Ballater branch closed in 1965 [29]. Nonetheless, as this design was deemed effective, lead–acid batteries were successfully used in the Deutsche Bahn Railway in Germany between 1950 and 1995 to power trains at a speed of 100 km/h [30].

While in the past most railways operated on fossil fuels, since the end of the 20th century there has been a growing demand to replace diesel-powered with electric trains in order to reduce harmful emissions and noise, and to take advantage of lighter-weight locomotives. This transition is also being motivated by uncertainties in oil supply and the consequent rising prices due to its use in other transport modes such as cars and planes. Most importantly, electric railways produce less noise, require less maintenance, and do not rely exclusively on oil because electricity can be generated from several sources, including renewables. The operational and maintenance cost of electric trains is 50% cheaper than that in diesel trains. In addition, the trains' high power to weight ratio requires less energy for traction and allows faster acceleration, making electric railways relatively energy efficient as the overall efficiency of electric and diesel railways are 76% and 30%, respectively [31]. In contrast, diesel-powered trains expend high amounts of energy in traction mode due to their much greater weight, which is caused by the need for on-board energy sources. One of the disadvantages of electric railways is the high capital cost (four

times higher than diesel railways), especially for long-distances journeys, while upgrading existing infrastructure can also be prohibitively expensive on sections involving tunnels and bridges. Added to this is the fact that, in the last few decades, the power demand of electric railways for freight and passenger transport has increased due to the need of increasing number of services and size of trains. Accordingly, the adoption of ESS for electric railways to increase energy efficiency and limit peak demands has become a primary concern [32], [33].

In electric railways, trains are supported by regenerative braking systems that allow power to be fed back to the traction system during braking to be used for different purposes. In regenerative braking, the kinetic energy and momentum of the moving vehicle drive the motors—normally induction AC motors—acting as generators converting the kinetic energy into electrical energy, which slows the train down. This occurs when the speed of the rotor becomes higher than the synchronous speed inside the motor. If the mains frequency is controllable then regenerating power can be accomplished at a lower speed than the synchronous speed. Mechanical brakes are only acting when the regenerative braking is not sufficient to stop the train [34].

Injecting regenerative energy onto a power system can create localised over voltage if the grid is not able to accept and distribute the energy and under quite often it is easier and cheaper to dump the energy rather than reinforce grid infrastructure. Recent developments in energy storage technology have encouraged industry practitioners to develop systems capable of storing the regenerative energy coming from reversible generators in electric trains. In Japan, flywheels were installed in the Keikyu Railway in 1988 and supercapacitors were adopted in the Seibu Railway in 2007. Lithium-ion (Li-ion) batteries were first applied in West Japan Railway in 2006, prompting other railway operators across Japan (East Japan, Tobu, Osaka City, Kagoshima, and Keio) to do the same. Nickel-metal-hydride (Ni-MH) batteries were first adopted in the Osaka City railway line in 2010, followed by Tokyo Monorail in 2013, Sapporo City in 2014, and East Japan Railway in 2016. It is worth mentioning that all of the aforementioned ESS applications in Japan are wayside systems [35]. Most recently, in 2015, a Li-ion battery with a capacity of 550 Ah was installed on-

board a 185,000 kg train on Mayflower line in Essex, United Kingdom, to power the train entirely by the battery when running through non-electrified sections or in case of electric failures [36]. Another example of electrification of railways can be found in the Seville Metro in Spain, where supercapacitors that can be charged to 750 V by overhead lines at every stop have been in use since 2011. When a train stops to load and unload passengers, the energy storage charges very quickly, allowing catenary-free operation until the next passenger station [37]. A hybrid energy storage system (HESS) consisting of Ni–MH batteries and supercapacitors has been used in Portugal on the railway line between Almada and Seixal to run trains catenary-free for 2.5 km [38]. Huai’an Tram Line in China can also run catenary-free by using supercapacitors that were installed in 2015 to be charged at stops [39].

2.1.2 Railway electrification system

Electric railways can be powered by AC or DC voltage. Three phase voltage systems of 66 kV, 132 kV, 220 kV, and 400 kV are commonly used for transmitting power from the national grid before being stepped down for distribution in voltages between 11 kV and 132 kV. The distribution voltage is received by the traction substation that could be AC or DC. The most common electrification systems along with the permissible lower voltages and the economic distance between the substations are shown in Table 2.1. The choice between AC or DC traction is based on safety, efficiency, and economic benefits. Historically, DC traction was preferred, as it was easier to control the speed of trains with DC motors. However, DC traction requires short distances between feeder stations due to the supply high currents, and also necessitates the installation of thick cables capable of withstanding the high currents that are problematic as they cause high voltage drops that are limited to the levels displayed in Table 2.1. The distance between the substations also depends on the traffic density, and the vehicle type [6], [41]. Conversely, AC power traction is more economically advantageous due to its ability to step the voltage up and down, reducing conductor size. In high-voltage electric railways (above 3000 V), it is easier

to break fault currents in AC compared to DC traction. In addition, fewer feeding substations are used to span a greater distance, making it necessary to use AC traction to benefit from voltage step up and down. However, AC railways are not always more economical than their DC counterparts, since the impedance of the electric cables is higher in the former due to the skin effect and loop inductance, causing a high voltage drop across the line. In urban areas, where short distances between stations are common, rapid acceleration and deceleration is necessary. Whilst AC trains are considered faster than DC trains, the latter have the capability to accelerate and decelerate faster than the former, which makes DC traction more suited for urban transport systems [20], [42].

Table 2.1: Characteristics of the most common railway traction systems [5], [6], [40]

Electrification system	Lowest permanent voltage	Typical distance between substations
600 V [DC]	400 V	2–4 km
750 V [DC]	500 V	4–6 km
1500 V [DC]	1000 V	8–13 km
3000 V [DC]	2000 V	20–30 km
15 kV [AC]	12 kV	12–15 km
25 kV [AC]	19 kV	35–50 km

Overhead transmission lines were first introduced into electric railways in 1881 at the International Exposition of Electricity in Paris by Werner von Siemens when he powered a DC electric tram. It is important to note though that overhead transmission lines are not commonly used in urban areas because they are challenging to build in confined spaces, such as tunnels, and are not aesthetically desirable. To avoid this issue, in 1890, the 3rd rail was introduced in the City and South London Railway, making it the first underground railway in the world to use this design. Only one feeder conductor is required in this case, designed as the 3rd rail, positioned either beside the running rails or between them. The running rails are responsible for carrying the return current to the substations through the connection between the train’s wheels and the rails. However, as currents pass through the running rails, they can produce destructive arcing. Furthermore, the currents might pass through rails to

the ground and return to substations via different paths, giving rise to stray currents that cause corrosion at the locations where they leave or re-join the running rails.

In order to avoid damage to the railway track, a 4th rail is introduced as depicted in Figure 2.2. In this case, the rail track has two running rails and two power rails, whereby the live (3rd) rail is placed on the side of the running rails. The return rail, which is the 4th rail, is located in the centre, or on the other side of the track. The 4th rail acts as a return conductor to substations, eliminating the need to pass the current via running rails, and thus mitigating the aforementioned premature erosion issue. A train is connected to the 3rd and 4th rails through a contact shoe that is depicted in Figure 2.3. While in the previously used designs, the contact shoe touched the live rails at the top, it presently touches the live rails at the sides or from underneath to prevent accidents as well as to protect live rails from adverse weather conditions. While in this configuration, contact between the train shoe and the 3rd rail becomes difficult at speeds exceeding 160 km/h, but the 3rd and 4th rail lines are cost-effective to construct and maintain, and can be installed in limited spaces. Moreover, unlike overhead lines, they do not require expensive civil works for modifying existing infrastructure. However, overhead lines are safer due to a much lower risk of electrocution [20], [43].

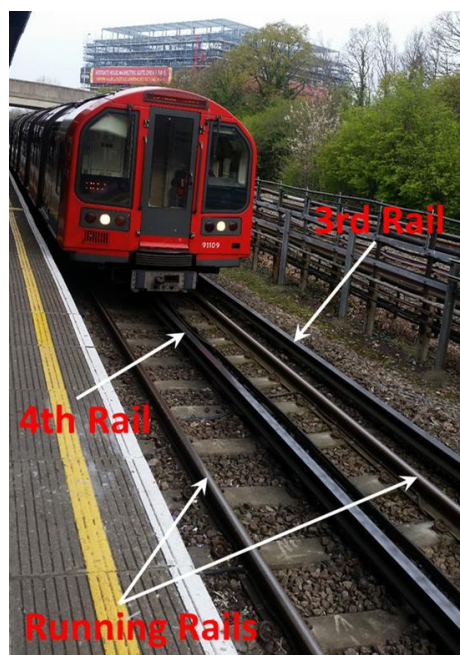


Figure 2.2: Train supplied by a 4th rail traction system



Figure 2.3: Contact shoe touching a conductor rail [44]

Metro systems implementing the 4th rail track are commonly used in densely populated urban environments, where distance between passenger stations is short (0.3–2 km). As a result of the short distances, trains need to accelerate and decelerate rapidly in order to achieve top speeds. The typical maximum speed in metro systems is 80–120 km/h and the acceleration/deceleration rate is 1–1.3 m/s² [45]. For example, in Yizhuang Line in Beijing Metro, trains take approximately 39 s to accelerate to the top speed 80 km/h and 27 s to decelerate from the top speed to zero [46]. Therefore, lightweight vehicles travelling at low speed are favoured due to their ability to accelerate and decelerate rapidly. This results in high power consumption before leaving a passenger station along with high power regeneration before reaching the next passenger station. This surge in power can cause voltage peaks and dips due to the resistance in the conductors. In braking mode, traction motors transform into generators, whereby the kinetic energy is transformed into electric energy that is then fed back through the traction system to the track. The traction inverter increases the voltage generated to a level higher than at the rail conductor. The regenerated power is first consumed by the auxiliary loads in the train before passing the excess power back to the rail track. The substations are commonly simple AC to DC rectifiers preventing any power from flowing back to the grid. Consequently, if the regenerative power cannot be consumed by other trains on the track it needs to be dissipated, this is achieved through braking resistors mounted on

the train. The braking resistors weigh up to 500 kg in a single car (see Figure 2.4). The resulting heat from the dissipated energy in the braking resistors warms up tunnels and increases the overall energy requirements for cooling underground rail systems. Thereby, to improve the energy efficiency of electric railways, bidirectional substations, on-board or stationary ESSs can be employed to store for reuse the regenerative energy of braking trains [47].

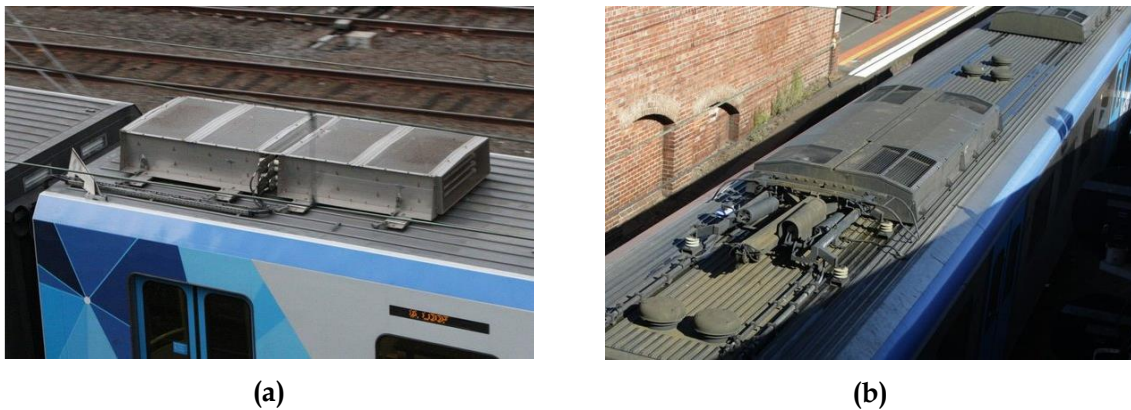


Figure 2.4: Photos of braking resistors mounted on the roof of trains [48]

2.2 DC electric railway energy efficiency

2.2.1 Electric railway modelling methods

To study the energy efficiency of electric railways and to design appropriate techniques for its maximisation, it is necessary to develop a sophisticated electrical model. The model must be capable of supporting multiple train simulations to enable realistic power flows and calculate the time-based voltages and currents at a high number of nodes in the system. The electrical configuration of the railway system is time variant based on the moving trains. Unfortunately, the network variability and

nonlinearity (mainly due to the rectifier substations) make the analysis of system power flow challenging. Figure 2.5 shows an example of an electrical network of a metro system at a particular time. In extant studies on this topic, power flow in DC railways is commonly modelled by adopting Gauss-Seidel, Newton-Raphson, and current injection (CI) methods. The Gauss-Seidel method is easy to implement but introduces convergence issues, whereas the Newton-Raphson and CI methods converge quickly but require complex formulation for the corresponding Jacobian matrix, especially when applied to large-scale networks [47], [49].

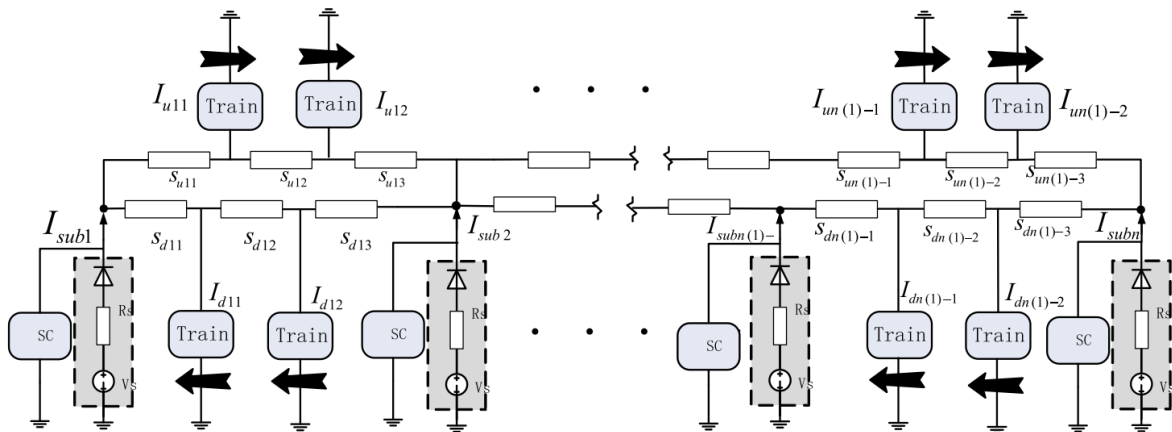


Figure 2.5: Snapshot of the electrical configuration of a metro system at a particular time where SC refers to supercapacitors [50]

In [49], the author not only solved the power flow of a multi-train model, but also avoided the complication that arises due to using derivatives within matrices. The author proposed a simplified Newton-Raphson method that is claimed to be efficient in reducing the simulation time and calculation complexity when simulating a 21.6 km railway line with 22 passenger stations serviced by multiple trains that operate with 5 min headway (time displacement between adjacent trains). In conventional iterative methods, the entire Jacobian matrix needs to be recalculated iteratively until convergence criteria have been met. However, when the simplified Newton-Raphson

method is applied, the off-diagonal elements are calculated only once while the diagonal elements are recalculated at every iteration.

Mohamed, Arboleya, and Gonzalez-Moran proposed an iterative method for solving the electric railway power flow in DC traction, which they denoted as the modified current injection (MCI) method [7]. This method is a modification of existing algorithms, aimed primarily at improving the convergence and reducing the solver time required. Moreover, MCI can be applied to solve the electric railway power flow, irrespective of whether the substations are bidirectional or unidirectional. The authors tested their method by applying it to only two trains running on a 20 km track line equipped with three substations. One of the drawbacks of this method stems from the need to provide the initial voltage profiles for the nodes in order to calculate the currents injected into the nodes. Thereafter, the voltage profiles are updated based on the iterative algorithm method that recalculates currents until convergence occurs.

The authors of [51] implemented the CI method—also known as the conductance matrix iterative (CMI) method—in a MATLAB M-file to solve the power flow of a single train running on the Sukhumvit Line in Bangkok with ten traction substations and 22 passenger stations. The study aimed to calculate the voltage at the train's location, rail voltage, traction substation power, and power losses in the system. The CI method was also used in [52] to solve the power flow of a DC railway with up to 144 running trains. This approach was modified in braking mode, thus avoiding overvoltage by adjusting the regenerative energy that is reinjected through bidirectional substations. Furthermore, when the substations are non-bidirectional (rectification only), they are switched off, and the regenerating trains are switched to voltage–current sources. The main objective of the CMI is to reduce the number of required iterations, thus reducing the time required to generate the system solution. In another related study, the authors of [53] used the CI method to solve a DC railway network incorporating modern features such as bidirectional substations, unidirectional substations, on-board ESSs, offboard ESSs, regenerative braking systems, and overcurrent and overvoltage protection circuits.

The adverse impact of the railway power network variation on the complexity of matrix formulation was avoided in [54] by adopting a new technique based on graph theory, which allowed the authors to develop a simple matrix formulation to solve the power flow of a DC power system, as well as an AC power system, which is often neglected by other researchers. The system included three trains and three substations. The proposed approach exhibited higher accuracy compared to that of the commercial software DIgSILENT. Multi-train simulation with different headways based on Yizhuang Line of the Beijing Metro case study was achieved in [55]. The simulated system had 12 substations and 14 passenger stations with 13 trains running on a 22.73 km line. The authors used the bi-factorisation iterative algorithm method to compute the formulated admittance matrix for the nonlinear system. However, the modelling method was only described in a flow chart without providing sufficient information to allow replication.

The new technique based on graph theory proposed in [54] was subsequently used in [56] to solve the power flow of a DC railway network that included four trains equipped with on-board ESSs, which increased the computation time by 18% relative to those without ESSs. The study aimed to evaluate the impact of ESSs on the substations' peak power demand and energy consumption. On the other hand, the efficiency of a light electric railway when considering on-board supercapacitors was investigated in [57], along with the impact of changes in traffic on train movements and thus overall system efficiency. The system was solved using the nodal voltage analysis method and was simulated by considering the train power requirements as a function of movement with the results being used to change the power network behaviour. The injected train speed profiles were obtained from Blackpool Tramway and the network was simulated in MATLAB Simulink. However, the train currents were not solved in the model as they were obtained from real-world measurements, which reduces the complexity of solving the system especially when simulating only one train on each of the double track system.

The authors of [58] developed a model in MATLAB Simulink to solve the power flow of an electric system with seven substations. The main aim of this work

was to improve the energy efficiency of an electric railway by 16.56% through the implementation of stationary supercapacitors. However, only the output results of the model were presented in the article without description of the modelling approach. In [59] a railway network involving a single train was implemented in MATLAB Simulink using the graphical modelling tool of energetic macroscopic representation. The model was accurate with only 2.98% error when validated against real measurements obtained on a test track involving only one train and two substations. Neural networks were implemented in [60] to develop a model that is capable of calculating energy consumption of the Valencia Metro Network. The modelling results fit real measurements with high accuracy, as the error was 0.9% based on the comparison of energy consumption and traction power, without including any voltage profiles for the metro system.

MATLAB Simscape environment was adopted in [61] to simulate a high-speed railway with a single running train. The model was used to test the impact of stationary and on-board ESSs on the energy efficiency of electric railways. However, the modelling approach and the output results of the model were presented with insufficient details. A more detailed model of regenerative braking systems on-board trains was provided in [62] to increase the accuracy of braking energy estimation before determining the most optimal ESS size. The model was validated by comparison with real measurements of Line 7 of New York City Transit system. In addition to the simulation methods developed by academic researchers, several railway simulation tools have been provided by industry practitioners, such as TrainOps, Sitras Sidytrac, eTraX, and TOM. Some simulation tools initially designed for academic research subsequently became commercially available, such as OpenPowerNet, OpenTrack, and Vehicle Simulation Program [47].

However, extant studies in the field of modelling DC electric railways have tended to focus solely on solving the power flow without comprehensive analysis of the traction system, which would involve model validation, headway impact, and ESS impact. A small number of authors have developed simulation tools that eliminated the need for complex algorithms while permitting analysis of system energy efficiency

with respect to headway and ESS factors. However, in most of these cases, simulations were limited to a small number of trains, or the authors failed to provide sufficient description of the modelling approach. Another crucial aspect that has been neglected by most of the studies, is providing the track voltage that is important for ESS control. A new multi-train modelling methodology that eliminates the need for complex algorithms is proposed in this thesis. Its design is described in detail in Chapter 3, along with the implementation and verification protocol and the results yielded. Moreover, the energy efficiency of the system is comprehensively investigated with respect to variation in traffic density, ESS location, and ESS control method.

2.2.2 Methods for improving DC electric railway energy efficiency

Up to 14% of energy saving in electric railways can be achieved by adjusting train timetables to more closely align the power demand between the decelerating and accelerating trains. Furthermore, bidirectional substations could be employed to send the regenerative power back to the grid, while on-board or stationary ESSs could be employed to store the regenerative energy to be reused by accelerating trains [47].

Train timetable optimisation and eco-driving methods can increase energy savings in a highly cost-effective manner. Timetable optimisation methods are mainly based on adjusting the train headway, dwell time, and departing time to increase the synchronisation level between accelerating and decelerating trains, while eco-driving methods provide guidance to the driver to adapt the train speed profile to improve fuel consumption. However, it is reported in [47] that these methods are more effective if applied in driverless trains to avoid conflict with human decision-making. Multi-objective algorithms were used in [63] to generate speed profiles that decreased the total energy consumption of Metro de Madrid by 3–14%. The method generated optimal speed profiles without increasing the scheduled train running time while considering uncertainties in traffic and passenger load variations. A numerical algorithm was designed in [64] to calculate the optimal train departure time in order

to synchronise the acceleration profile with the deceleration profile of braking trains for efficient use of regenerative energy. According to the authors, the method was able to reduce the total energy consumption of a metro system by 2.4% without affecting punctuality. In a case study based on the Beijing Metro, the authors of [65] applied a genetic algorithm for train timetable optimisation to reduce the energy consumption and passenger waiting time. The proposed genetic algorithm reduced the energy consumption and the passenger waiting time by 8.86% and 3.22%, respectively. Other authors have also attempted timetable optimisation for energy efficiency maximisation in electric railways [46], [66], [67].

Energy efficiency of electric railways can also be improved by using bidirectional substations, whereby regenerative energy is fed to the substation or the national grid. Bidirectional substations allow energy to be sold to the main grid on different pricing schemes to maximise profit. However, bidirectional substations do not support voltage stabilisation (keeping the voltage within certain range that reduces the trains power demands and line losses) as the regenerative energy cannot be stored to support voltage drops at the substations and can only be injected to the grid at the presence of voltage peaks. Further, the regenerative braking power injected to the grid can affect the power quality of the national grid by injecting harmonics and reactive power. As a further drawback of this technology, redirecting the DC braking power into the AC distribution network is prohibitively expensive. For example, the cost of a 3 MW unidirectional converter is 175,000 \$ while it is 600,000 \$ for a bidirectional converter. However, the energy saving caused by bidirectional converters makes them more cost effective over a life time [47], [68].

While some attempts have been made to upgrade unidirectional substations to operate in bidirectional mode, this requires complex and expensive civil works. To alleviate this issue, the INGETEAM Traction Company designed a new energy recovery system called INGEBER that connects a DC/DC converter in series with a three-phase inverter to be connected in parallel with an existing unidirectional substation as shown in Figure 2.6. In addition, to not adversely affect the system reliability, the converter was designed to be easily disconnected from the traction

system without affecting the operation. Similarly, ABB produced two commercial rectifiers—Enviline Traction Controlled Rectifier (TCR) and Enviline Energy Recuperation System (ERS)—that can work with an existing unidirectional substation to provide bidirectional power flow back to the national grid. Alstom produced the Harmonic and Energy Saving Optimiser (HESOP) converter comprising of a thyristor rectifier connected in parallel with an insulated-gate bipolar transistor (IGBT) inverter. As this converter can be installed with existing unidirectional substations, it is already used in Paris, London, Milan, Sydney, Panama City, Riyadh, Dubai, and Hamburg. The cost of these commercial bidirectional converters is 50–300 \$/kW [69]–[71]. Exporting power back to grid, however, can result in power quality issues, such as voltage fluctuations, voltage and current imbalance, and harmonics, which may require mitigation by applying transformer control techniques, reactive power compensation methods, and harmonic active/passive filters [72].

Owing to the recent advances in ESS technology, power converter design and the decline in their respective costs, ESS technology is increasingly being adopted as a means of improving energy efficiency. The main advantage of this approach is that regenerative energy can be stored in ESSs to be released when needed. It is worth mentioning that ESSs can save up to 15–30 % of the traction energy consumption while bidirectional substations can only save 7–11 % [73]. Moreover, ESSs yield benefits such as catenary-free operation, voltage stabilisation, and peak power reduction that cannot be achieved by other methods [81].

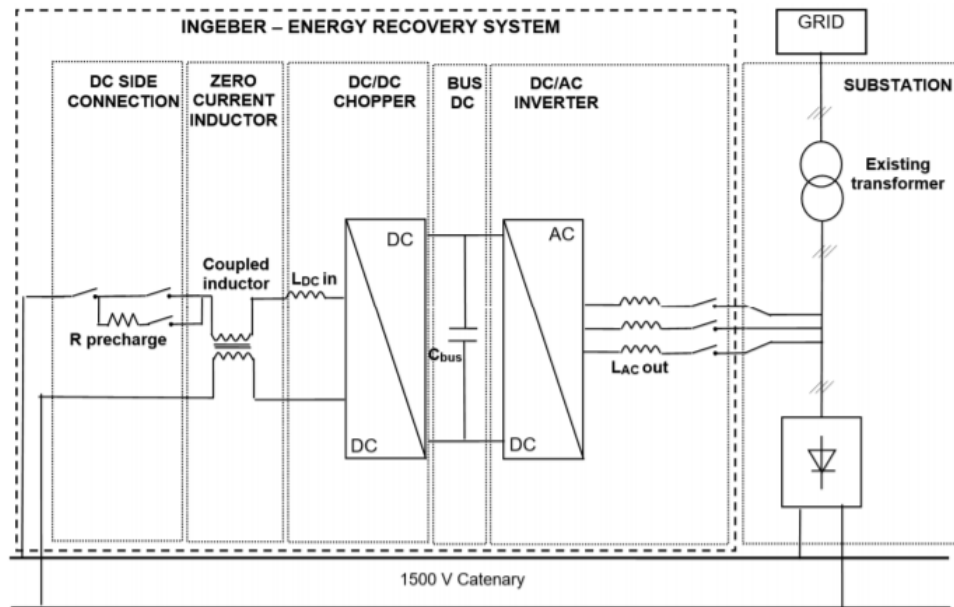


Figure 2.6: Schematic diagram of the INGEBER system integrated into an existing substation [69]

2.2.3 Review of ESSs

Since most substations in metro railway systems are unidirectional which causes the regenerative power to be dissipated as heat, ESSs have been employed in systems such as Madrid Metro, Beijing Metro, and London Underground to capture the regenerative power and release it back to trains as needed. The key requirement of using ESSs is to improve electric railway performance by reducing energy consumption and energy losses. To achieve this aim, the storing device has to satisfy the following key electric railway requirements: effective management of high power, and the ability to store high amounts of energy. The existing body of research on ESS application in electric railways suggests that batteries, supercapacitors, and flywheels are the most suitable storage technologies for recovering braking energy [7], [47], [82]. These are technically compared in Table 2.2 and explored in turn in the following subsections.

2.2.3.1 Batteries

Batteries are the oldest energy storage technology and are widely used in electric railways due to their ubiquity and developing performance. They store and deliver electricity via electrochemical reactions that occur inside multiple cells that are connected in series and in parallel. Each cell includes a cathode and an anode isolated by an electrolyte solution.

In applications with higher power demand, nickel-cadmium (Ni-Cd), Ni-MH, and Li-ion batteries are commonly used. The lead-acid is commercially the oldest and cheapest of all storage devices per kWh. Although it is characterised by high reliability and low self-discharge, it is not suitable for wayside storage applications due to its short-life cycle (denoting the number of charging/discharging cycles before the capacity declines to 80% of the original capacity), low charging currents, and low energy density (the amount of energy per unit volume). The short-life cycle is due to the changes to the positive electrode when deeply discharged. Figure 2.7 shows the life cycle of a lead-acid battery in relation to the depth of discharge (DOD)—defined as the discharged energy relative to full capacity of a storage system [37], [83].

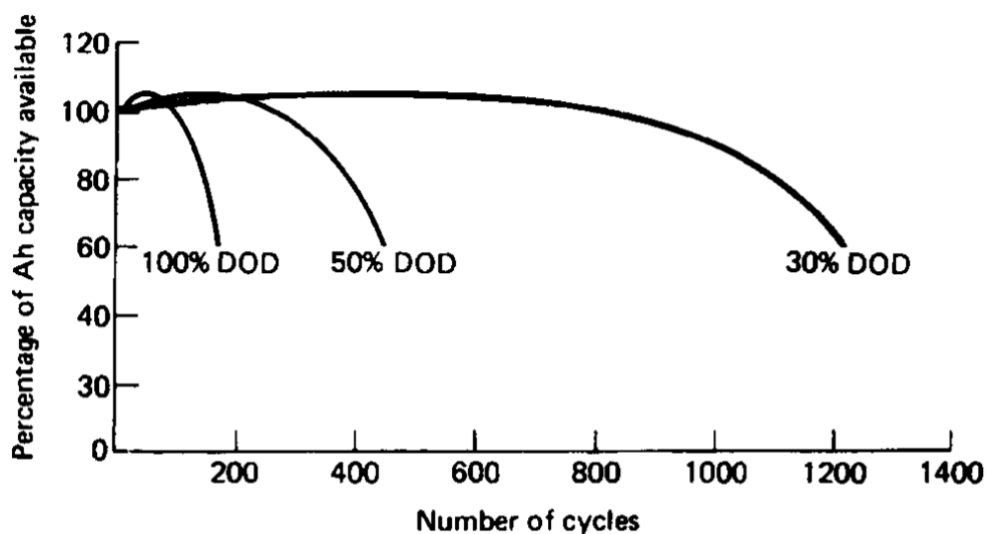


Figure 2.7: Life cycle of a lead-acid battery with respect to DOD [84]

Nickel-based batteries have high power density (the amount of power per unit volume) and high energy density. This makes them suitable for high-power applications, although they suffer from high self-discharge and low efficiency. Ni–Cd batteries are robust and durable, as well as being capable of withstanding high and low temperatures. However, Ni–Cd batteries are hazardous to the environment due to the existence of the toxic cadmium metal and suffer from memory effect – a concept which denotes the battery remembering the smallest capacity when it is repeatedly partially discharged. Mitigating this effect requires periodic deep charging and discharging cycles in order to retain capacity.

Due to the environmental concerns related to cadmium, Ni–Cd batteries have been replaced by Ni–MH batteries in which hydrogen substitutes cadmium in the cathode, while retaining the electrolyte and the anode from the Ni–Cd design. The energy storage capacity and the charge/discharge currents are higher in Ni–MH than in Ni–Cd batteries. However, Ni–MH batteries suffer from high self-discharge and short lifetime, especially when discharged at high currents. Indeed, Ni–MH has a wide temperature range, but overcharging and deep discharging produces heat that can cause leakage, fire, or explosion. Under those circumstances, a complex charge algorithm is necessary to control the charging and discharging process and maintenance is regularly required.

Li-ion batteries are currently the preferred power source in portable electrical devices due to their high energy and power density, high efficiency, low maintenance, long lifetime, long shelf-life and low self-discharge, without suffering from memory effect (see Table 2.2). The average operating cell voltage of Li-ion batteries is higher than Ni-based batteries and lead-acid batteries as described in Figure 2.8. Owing to these advantages, Li-ion batteries are considered the most promising battery technology for transportation applications [37], [83].

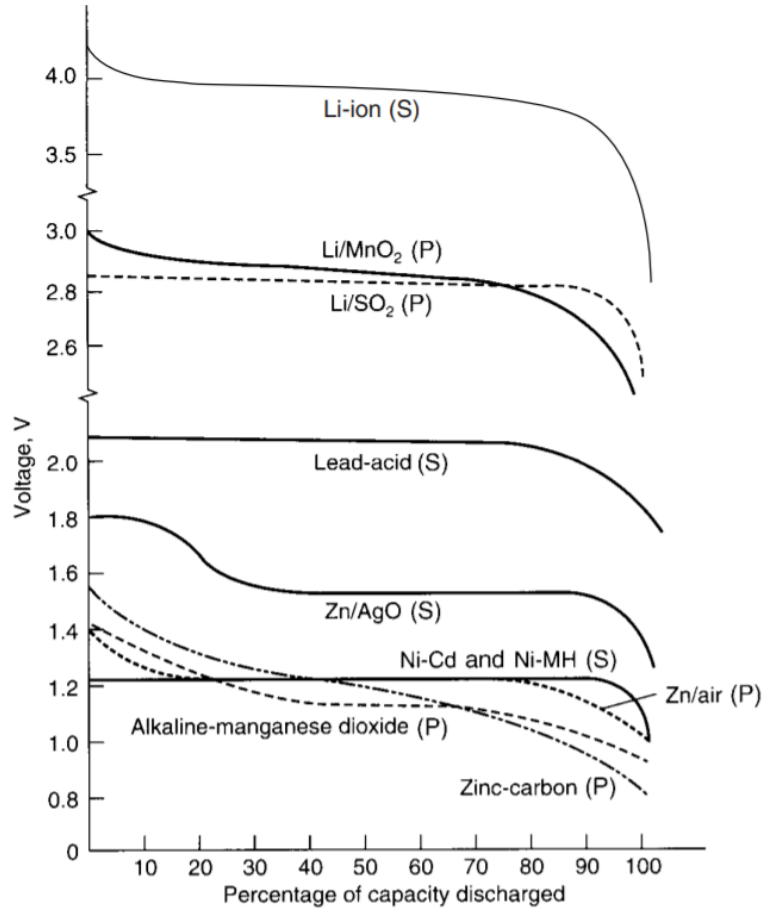


Figure 2.8: Discharge curves of several primary (P) and secondary (S) batteries [84]

2.2.3.2 Supercapacitors

Another energy storage technology with the potential for use in electric railways is the supercapacitor, also known as the ultra-capacitor. Supercapacitors exhibit high power density and have the ability to store 100 – 1000 times more energy compared to conventional capacitors. As explained in Equation 2.1, the energy stored in a supercapacitor (E_{sc}) in Joules is proportional to its voltage (V) squared and capacitance (C) in Farad. Due to the large electrode surface area, high permittivity dielectric, and small charge separation, supercapacitors have higher energy density compared with conventional devices. The E_{sc} is proportional to the area (A) in m^2 of the supercapacitor plates and dielectric permittivity (ϵ) in Farad/m as follows:

$$E_{sc} = \frac{1}{2}CV^2 = \frac{A\varepsilon}{2d_{sc}}V^2 \quad (2.1)$$

As can be seen from the expression above, it is possible to store high energy with low voltage by having high permittivity and electrode plates of large surface area. Moreover, increasing the distance (d_{sc}) in m between the electrodes decreases its capability of storing energy. The power density of supercapacitors is high as energy is stored in their electrodes, which allows them to be completely discharged. Using supercapacitors in storage applications requires consideration for the large voltage range over the SOC range where high currents will be required to be drawn by converters; compared to batteries that operate over a smaller voltage range as seen in Figure 2.9. Therefore, due to the significant decrease of the voltage, power converters need to be capable of drawing high currents from the supercapacitor to maintain the wattage level.

Ultracapacitors are frequently flexible and durable, they can be installed in different environments. Moreover, their operating temperature is wide and their efficiency is high due to the low internal resistance owing to the absence of chemical reactions in the device. Supercapacitors also have a longer lifecycle relative to batteries because their electrodes experience minimal chemical changes when working continuously in charging and discharging mode. However, the energy density in ultracapacitors is low and the self-discharge is high (see Table 2.2) [37], [83].

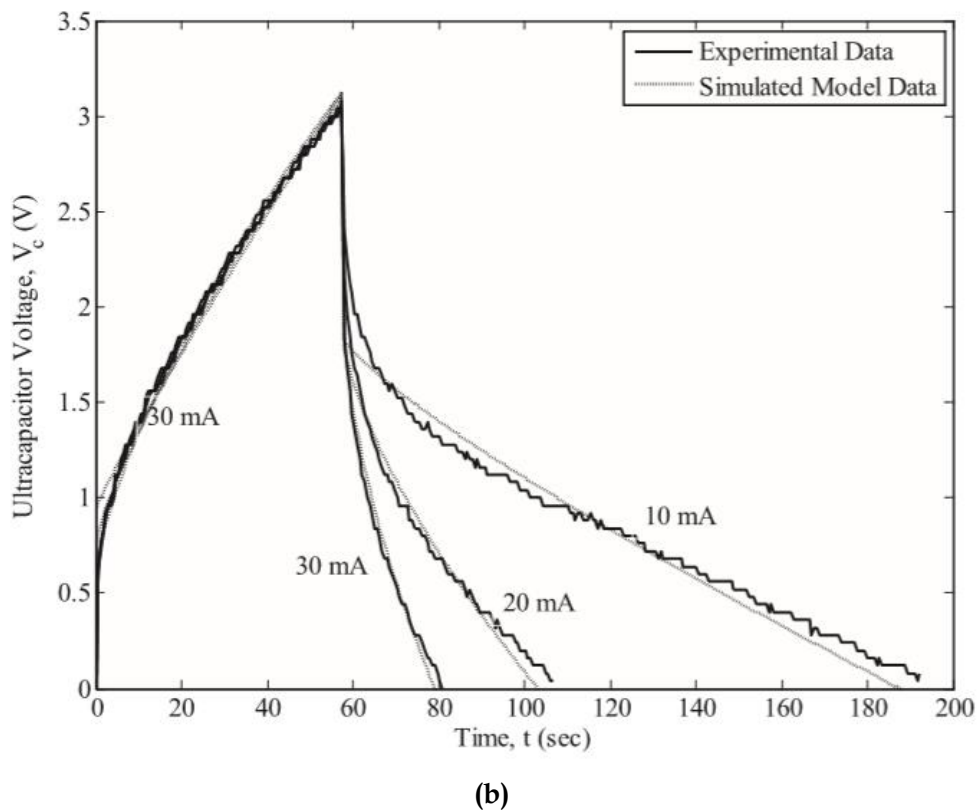
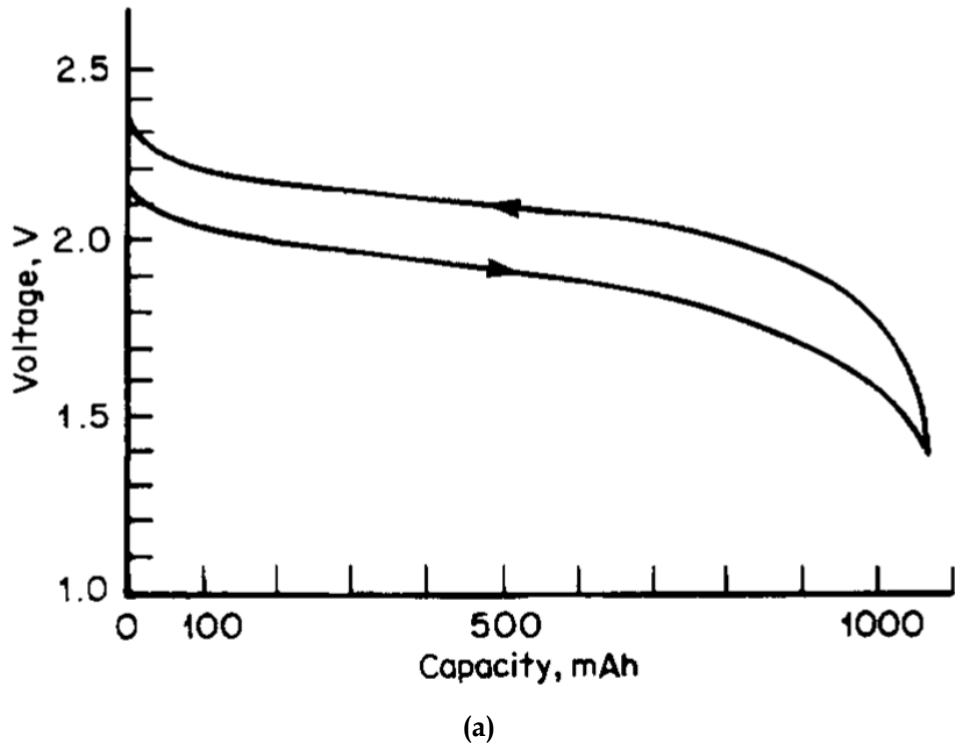


Figure 2.9: (a) Typical charge and discharge curves of a Li-ion battery with 80 mA charge current and 400 mA discharge current; (b) charge and discharge curves of a supercapacitor at different currents [84], [85]

2.2.3.3 Flywheels

Flywheels are electro-mechanical energy storage devices characterised by high response to transients, which makes them suited for electric railway applications. A rotating mass is used to store kinetic energy (E_f) in Joules, as indicated below:

$$E_f = \frac{1}{2}I\omega^2 \quad (2.2)$$

where I is the moment of inertia in $kg \cdot m^2$ and ω is the angular velocity in rad/s . A rotating machine acting as a motor or a generator is combined with a flywheel to transform the kinetic energy into electric energy. The machine acts as a motor in charge mode to increase the energy stored in the flywheel by increasing the angular velocity or the moment of inertia. In discharge mode it acts as a generator to supply the stored energy into loads. Modern flywheels are made of light material, due to which their moment of inertia is low; nonetheless, the energy stored is high due to their high angular velocity.

As described in Table 2.2, flywheels have a much longer lifetime than batteries and supercapacitors and require less maintenance. They can also operate in a wide temperature range, and have good power and energy density, as well as high efficiency. Their cost per kW is relatively low, whilst that per kWh is high. Another disadvantage is that flywheels suffer from high self-discharge and safety concerns in the event of mechanical failure to the rotor that could break apart requiring protective barriers to be installed [37], [83].

Table 2.2: Technical comparison between ESSs [37], [71], [73] – [80]

Storage type	Energy density (Wh/kg)	Power density (W/kg)	Cycle efficiency (%)	Self-discharge (daily% of rated capacity)	Operating temperature (°C)	Lifetime (cycles)	Cost (\$/kWh)	Cost (\$/kW)
Battery (lead-acid)	10–50	25–300	85–90	0.05–0.3	-5–40	200–2000	50–100	200–650
Battery (Ni-Cd)	10–80	50–300	60–90	0.2–0.6	-40–50	1500–3,000	200–1000	350–1000
Battery (Ni-MH)	30–90	200–250	50–80	1–2	-40–50	1200–1800	240–1200	420–1200
Battery (Li-ion)	100–300	125–5000	85–98	0.1–0.3	-30–60	3000–10,000	273–1000	900–1300
Supercapacitor	2.5–15	500–10,000	85–98	20–40	-40–65	10,000–1,000,000	300–2000	100–300
Flywheel	5–200	1000–5000	90–95	100	-30–45	20,000–10,000,000	1000–5000	250–350

2.2.3.4 Hybrid energy storage systems

When choosing energy storage technology for urban railway applications, it is important to satisfy the requirements of high energy density, high power density, long life cycle, and high charge and discharge rate. Examples of real-world applications are stated in Table 2.3, where supercapacitors in Seibu electric railway can supply up to 2,560 kW but with only 6.9 kWh rated energy. Similarly, flywheels were applied in Keihin electric railway to supply 3,000 kW with a low energy capacity of 25 kWh. While batteries show high energy capacity they need to be oversized as an option for overcoming the low rated power issue, this would increase the physical size and cost. Moreover, lifetime of batteries is a concern when these are employed as energy storage devices in urban electric railways where their lifetime is 5–15 years and the payback time is around 6 years [60]. The payback period of supercapacitors is twice that in batteries while their lifetime is 10–30 years [71], [76]. For the London Underground flywheel application, the payback time was estimated to be five years with a life expectancy of 20–25 years [89]. Additionally, due to the limited lineside space available in most urban railways, such as the London Underground, oversizing batteries is not the most appropriate solution. An example of a stationary ESS is shown in Figure 2.10 where large space is needed. Space restrictions also apply if ESSs are installed on-board a train, in which case the increased weight must also be considered,

as the inclusion of large-sized ESSs would increase energy demand, thus diminishing the benefit of energy recuperation. Bombardier Transportation produced on-board supercapacitor system (see Figure 2.11) that is called MITRAC Energy Saver where two supercapacitor banks are installed with each having a weight of 450 kg and dimensions of: $1900 \times 950 \times 455 \text{ mm}^3$. The system was first applied in Mannheim Railway, Germany where the added weight of the supercapacitors increased the train energy demand by 2%. Although the system has a satisfactory rated power of 600 kW, the rated energy is low with only 2 kWh [9], [46]. To alleviate the issue of low energy, Siemens produced a HESS including a Ni-MH battery and a supercapacitor bank that is called Sitras HES shown in Figure 2.12. The system has a rated power of 373 kW, a rated energy of 18.85 kWh, and a total weight of 1,646 kg increasing the train energy demand by 1.5%. The dimensions of the battery pack is $1670 \times 1025 \times 517 \text{ mm}^3$ and the dimensions of the supercapacitor bank is $2000 \times 1520 \times 630 \text{ mm}^3$ [92].

Battery energy density is high and power density is low compared to supercapacitors and flywheels (see Table 2.2). Moreover, to ensure good performance and minimise degradation, batteries must be monitored and their cell voltages, currents, and temperature must be carefully managed. In addition, their lifecycle rapidly declines if operating at high temperatures (above 20°C), while low temperatures (below -20°C) reduce their power and energy capability. Cell balancing is another concern when working with batteries, as it leads to rapid degradation and may even cause fire [83]. Given these issues, supercapacitors are the preferred storage technology in electric railways due to their high power density and long lifetime. The use of flywheels in urban railways is limited due to the high self-discharge and safety concerns resulting from overloading that may cause explosions. Regarding the capital cost, flywheels are the most expensive per kWh, whereas batteries are the most expensive and the supercapacitors are the cheapest per kW. When considering the lifecycle, batteries are the most expensive of the three technologies, which significantly increases the time required to recuperate their cost. Since no single energy storage technology can meet all aforementioned objectives, HESSs can be adopted to improve the efficiency of electric railways [37].

Table 2.3: Examples of ESS applications [9], [86] – [91]

Storage type	Application	Method	Purpose	Rated energy (kWh)	Rated power (kW)
Li-ion battery	Kagoshima City Tram, Japan	Stationary	Voltage stabilisation	18.1	250
Li-ion battery	Seishin-Yamate Line, Japan	Stationary	Energy saving	37.4	1,000
Li-ion battery	East Japan Railway, Japan	Stationary	Voltage stabilisation	76	2,000
Li-ion battery	West Japan Railway, Japan	Stationary	Energy saving and voltage stabilisation	140	1,050
Li-ion battery	Market-Frankford Line in North Philadelphia, US	Stationary	Energy saving	420	2,200
Ni-MH battery	Osaka Municipal Subway, Japan	Stationary	Energy saving	576	5,600
Supercapacitor	Madrid Metro, Spain	Stationary	Energy saving, voltage stabilisation, and peak shaving	2.3	1,000
Supercapacitor	Seibu Railway, Japan	Stationary	Energy saving	6.9	2,560
Supercapacitor	Daejeon Metro, South Korea	Stationary	Energy saving and voltage stabilisation	10.39	1,870
Flywheel	London Underground, UK	Stationary	Energy saving and voltage stabilisation	3	300
Flywheel	Los Angeles Metro, US	Stationary	Energy saving	8.33	2,000
Flywheel	Keihin Electric Express Railway, Japan	Stationary	Energy saving	25	3,000
Ni-MH battery	Nice Tramway, France	On-board	Catenary free operation	27.7	200
Li-ion battery	Sapporo Municipal Subway, Japan	On-board	Energy saving	72	600
Ni-MH battery	Sapporo Municipal Subway, Japan	On-board	Energy saving and catenary free operation	120	250
Supercapacitor	Chuo Line, Japan	On-board	Energy saving	0.28	180
Supercapacitor	Mannheim Railway, Germany	On-board	Energy saving and peak shaving	2	600
Flywheel	Rotterdam Tramway, Netherlands	On-board	Energy saving	4	325



Figure 2.10: 1 MW supercapacitor system at Liyuan substation of Batong Line of the Beijing Metro, China [92]



Figure 2.11: On-board supercapacitor at Mannheim Railway, Germany [9]



Figure 2.12: Sitrans HES installed on the roof of a train [93]

2.2.4 Review of ESS applications in DC electric railways

2.2.4.1 ESS installation location

Before addressing the impact of incorporating ESSs into electric railways, it is necessary to consider the location within the system at which they should be installed. When used in railways, ESSs can be installed on-board trains or be stationary, located alongside the track. As the ESS weight and volume significantly affect the energy efficiency, installing an ESS on-board of a train increases its traction energy consumption by approximately 2%. On-board ESSs allow peak power reduction during acceleration, as well as catenary-free operation. However, retrofitting them on existing trains is expensive due to the lack of available space. Stationary ESSs can obtain energy from multiple braking trains and they can support energy consumption reduction, voltage stabilisation, and peak shaving (charging during low power demands and discharging during high power demands). Of these, voltage stabilisation and peak shaving require complex control methods since they are dependent on the traffic on the line, whereas controlling on-board ESSs is independent of traffic. Stationary ESSs can also support voltage drop at weak points in the network, thus eliminating the need for reinforcement through additional substations. Another drawback of on-board ESSs stems from train operations disruption for maintenance and repair of ESSs, which is avoided if wayside ESSs are employed. Stationary ESSs are also preferable when the distance between adjacent substations is short due to the low losses in transmission [47], [94]. It is worth mentioning that in some countries such as the UK, Germany and Sweden investment decisions are shared between multiple organisations due to privatisation of electric railways, which adds complexity to the optimisation of railway systems. Infrastructure and train operations belong to different organisations that makes installing on-board ESSs less favoured due to the complexity of investment decisions. The infrastructure operators are normally responsible for the operation of tracks, stations, signalling, electrical supply, and the management of timetables [95]. As stationary ESSs provide broad benefits to the

power network and are cost-effective if existing trains are not equipped with on-board ESSs, they are the focus of this present study.

2.2.4.2 Energy efficiency improvement using ESSs

In stationary ESS applications, determining the optimal ESS size, location alongside the track, and control strategy for power flow management can be very challenging, as the load profile is uncertain due to unpredictable traffic density and passenger volume. Moreover, offboard ESSs might increase losses in transmission and reduce power utilisation when their location and control method are not optimal, which passively affects the energy efficiency of the railway system. Therefore, it is essential to ensure active contribution of ESSs when applied to electric railways, particularly when the initial capital investment is high.

Stationary supercapacitors were employed in [96] to increase energy savings and reduce line voltage drop in the Italian Tramway Network in the city of Naples. The case study was based on two trains operating on a single track and one unidirectional substation whereby voltage control based on the measured track voltage profile was applied to the stationary supercapacitor. The charging and discharging voltage thresholds of the controller were selected in real-time by a control algorithm that was designed to optimise the substation energy consumption, the substation peak currents, and the voltage drop along the line. The reported findings indicate that the supercapacitor working within the optimal voltage limits could meet the objectives of the study satisfactorily even when different voltages representing different traffic conditions were injected into the system. These results were validated via laboratory tests involving a scaled system with a track emulator.

A stationary supercapacitor bank was adopted by the authors of [97] to reduce the energy supplied by a substation in a railway line. A state machine was utilised to switch the voltage and current thresholds of the ESS controller to different values based on five states, i.e. charging, discharging, high charging, high discharging, and standby. In addition, a genetic algorithm was implemented to update the gain parameters of the ESS controller in real-time, with the aim of optimising its dynamic

performance and enhancing its robustness. The improvements in the electric railway energy efficiency and the ESS control robustness were verified via both simulations and laboratory tests before the system was applied at Liyuan substation of the Batong Line of the Beijing Metro. Based on the 2-week field test results, the authors reported 12% average daily savings in the energy supplied by the Liyuan substation.

A mathematical model based on the Batong Line of the Beijing Metro was used in [98] to increase the energy recovery by varying the charging and discharging voltage thresholds of a stationary supercapacitor through a designed control algorithm. The proposed energy management method was used to automatically adjust the control parameters based on the train operating conditions to achieve 1,016 kWh daily reduction in the energy consumption under normal operational conditions. The proposed control algorithm was first tested on a modelled railway system comprising of two trains operating on a double railway line with two rectifier substations separated by 2 km before it was implemented at Liyuan substation.

A numerical optimisation method was developed in [99] to select optimal voltage thresholds of a controller managing the power flow between a stationary supercapacitor and an electric railway. The objective of the optimisation method was to identify voltage limits that would minimise the line voltage drop, the substation current peaks, and the substation energy consumption, including reduction of the losses in the transmission line and in the internal resistors within the substation. The control method was applied to determine the most optimal voltage limits based on offline estimation of the traction load, which remained fixed during the entire operating cycle. The case study included one train running on a single-track of 1.4 km length with one rectifier substation and a supercapacitor on its respective terminal points. The effectiveness and robustness of the control method in terms of meeting the predetermined objectives were validated experimentally in the laboratory at the University of Naples.

Stationary supercapacitors were used in [100] to boost the voltage along the contact line. A mathematical model was generated for an electric railway serviced by nine trains and equipped with three substations. The supercapacitor storage system

performance was evaluated by increasing the ESS size and changing its location while monitoring factors that caused minimal voltage decrease along the line. When the numerical model was applied to different traffic scenario based on the railway system in the city of Naples, the ESS was shown to be capable of reducing the line voltage drop by 32%.

Line 5 of the Beijing Metro was modelled mathematically in [51], based on real traffic scenarios reflecting the network operations, including different departure times. Lineside supercapacitors with unidirectional substations were also incorporated into the model. A state machine control mechanism was employed for energy management between the ESSs and the substations, resulting in 12% energy savings, equivalent to 1,500 MWh per year. In the study provided in [58], the authors investigated the optimal size, location, and energy management method of a wayside supercapacitor storage system for economic efficiency improvement (difference between the saved electricity price and the installation cost of ESSs) and voltage compensation. The modelled railway system was based on a real case study of a 11.3 km line section in the Beijing Metro, equipped with seven unidirectional substations. Stationary supercapacitor banks were connected in parallel with each substation to reduce traction energy consumption and voltage drop along the line. A novel optimisation method based on genetic algorithm was implemented to control the ESS charging/discharging current. According to the authors, the proposed method was efficient in enhancing both economic efficiency and voltage drop. The proposed method increased the economic efficiency by 16.56% and the voltage drop compensation by 23.05%.

A battery was employed in [101] to reduce the annual energy cost of a DC railway system. A control algorithm was designed to calculate the optimal site, size, and energy management method that would maximise energy savings and improve battery lifetime. Simulation results indicated that 13% energy saving can be achieved on a route of an Italian railway system in Rome. The wayside Li-ion battery system was used in [102] for voltage stabilisation, minimisation of energy consumption, and peak power reduction at Letterly Substation located at the Market-Frankford section

of north Philadelphia Line. The authors also aimed to reduce on-board braking resistor losses and allow surplus electricity to be sold to the grid to maximise economic benefits. Field test results demonstrated that the installed batteries reduced the annual energy cost by 1 million USD.

In the work presented in [103], the authors discussed the benefits of hybridisation between batteries and supercapacitors as a means of storing the excess regenerative energy in electric railways. The case study considered in this research was based on real data pertaining to a Spanish high-speed railway, which was used to test the impact of HESSs on energy savings and economic benefits. The proposed combination of the two technologies reduced the railway energy consumption and energy cost by 3.37% and 16.37%, respectively, based on a simulation involving two trains running on a single track for full day.

In conclusion to the literature review, incorporating ESSs into electric railways is an active area of research and has the potential for substantial energy efficiency improvements. However, a comprehensive sensitivity analysis of energy efficiency to ESS voltage control has never been conducted and is not fully understood. To address this gap in extant research, the significance of voltage control is critically examined in Chapter 4 of this thesis. As a part of this investigation, the effects of modifying ESS charging and discharging voltage thresholds as well as its location are evaluated.

2.3 ESS control methods for SOC management in DC electric railways

When adopting ESSs in electric railways, it is essential to ensure that they remain within their SOC boundaries, as failure to meet the load demands could limit their utility. This critical issue was discussed in [104], where the authors proposed a SOC management method. In this work, an on-board HESS was considered, comprising batteries, supercapacitors, and fuel cells (devices that generate electricity via chemical reactions with a source of fuel). This configuration was simulated in

MATLAB Simulink and based on the actual operating conditions of a metro line in the downtown of Zaragoza, Spain. The goal of the study was to develop energy management methods to fully meet the train power demand by the HESS while reducing the energy demand, and maintaining the SOC of batteries and supercapacitors within their respective predetermined limits. The fuel cell was responsible for ensuring that the battery and supercapacitor SOC remained within the required boundaries whilst fully meeting the power demand of the train. The authors chose a 90 Ah Li-ion battery for this project and opted for a 63 Farad supercapacitor. The battery and supercapacitor SOC was actively managed to operate within the desired 50–80% and 60–95% range, respectively. The SOC of the battery was set to this range as it was claimed that the charge acceptance above 80% is poor and working below 50% degrades the battery faster. The supercapacitor was limited to a 95% SOC as this causes capacitance loss and reduces the lifetime of the device, while the minimum SOC limit was set to 60% to avoid working in the nonlinear zone (the zone where the supercapacitor simulated voltage did not match the measured voltage) when discharging at high currents. However, in this study the impact of the SOC management method on the traction power system and energy efficiency was not discussed.

An adaptive control method was designed in [105] to manage the power flow between fuel cells, batteries, and supercapacitors on-board a train that had no connection to the grid. The fuel cells were used to manage both supercapacitor and battery SOC to reduce stress imposed on these devices and prolong their useful life. The control strategy was subjected to field testing, and the findings confirmed its ability to reduce stress and minimise hydrogen consumption of the HESS. In similar research, a state machine control strategy was proposed in [106] to manage the SOC of a supercapacitor set hybridised with a fuel cell system aboard a train. The goal was to reduce the hydrogen consumption by maintaining the supercapacitor SOC within the optimal limits of 40–95% and to ensure that the final SOC (i.e. the value measured at the end of the train operating cycle) converged to the initial SOC of 80% that allowed high discharge power and satisfactory braking recovery. This target was shown experimentally to be achieved effectively and also reduced the hydrogen consumption

in the HESS by 4.18%. Although the authors of the studies reported in [105] and [106] applied different operating conditions to add uncertainty to the system, in both cases, a single-train operation was considered in the testing phase, which is inadequate to comprehensively assess the performance of the proposed control methods. Moreover, both studies focused solely on reducing the fuel cells energy consumption, while neglecting that of the traction railway system.

A feed-forward control strategy with multiple optimisation functions was implemented in [107] to control the SOC of an ESS on-board a train when imposing stringent space and size constraints. The specific objective of this study was to maximise the benefits of the ESS size by controlling its SOC. The controller generated a reference SOC profile through a simple set of rules that were formed based on train position and load profile. Its performance was tested on a multi-train model based on a case scenario from the Greater Tokyo Railway Network. The objective was to reduce the difference between the initial (at the start of the journey) and the final (at the end of the 37.8 km line) SOC value of an ESS on-board a specific train. The reference SOC was calculated based on the train position along the line, the remaining energy in the ESS, and its capacity. It was assumed that the traction load of the railway line could be predicted with high accuracy. The reported results showed that the proposed control approach reduced the energy consumption, line losses, and line voltage drop. However, the authors failed to provide sufficient evidence in support of the control method validity, as uncertainties in the load profile were neglected. Moreover, the reference SOC was generated for each train independently, which caused deviations between the reference SOC and its actual value because the impact of individual SOCs on those of other running trains was not considered. In other words, application of the proposed control method to manage the SOC of a certain ESS modified the contact voltage waveform along the line, which was not considered when managing other on-board ESSs, as their SOC profiles were established prior to executing the simulation. Finally, the controller's ability to improve the electric railway energy efficiency was only evaluated against a case in which no ESS was incorporated, which was inadequate to reach generalisable conclusions. To fully test its performance, the

proposed method should have been compared with a case in which an ESS performed under conventional control methods.

A state machine control strategy was designed in [98] to adjust the charging and discharging voltage thresholds of a stationary ESS. The ESS included supercapacitors connected to one side of a double-track railway while a rectifier substation was connected to the other side. The traction system was simulated based on parameters pertaining to the Batong Line of the Beijing Metro before real field testing was performed. The aim of the proposed control strategy was to manage the SOC of the supercapacitor set as a means of increasing its energy charge and discharge rate to reduce the imported energy from the substation. The control strategy was first validated via simulation, which confirmed its ability to enhance the energy conservation rate (the ratio between the energy discharged by the supercapacitor bank and the substation). Thereafter, it was applied in the field at substations located in Liyuan Passenger Station under seven scenarios reflecting normal operating conditions, where it was shown to increase the energy conservation rate by an average of 13.5% relative to a conventional control method pertaining to the fixed threshold condition. Although reaching the minimum SOC limit was avoided and the energy conservation was improved, these findings do not reflect the full impact of the control strategy on the traction system. Therefore, further analysis of the impact of the SOC management strategy on the line power utilisation, power losses, and power peaks is needed for accurate and comprehensive controller assessment. Furthermore, the adaptation process was not based on forecasts of future changes of the load profile, and the authors only considered a small number of voltage threshold variations and failed to incorporate adaptation of current limits.

SOC control of a stationary Li-ion supercapacitor by adjusting its current was discussed in [81]. The control strategy aimed to provide a reference SOC profile for the supercapacitor to ensure good cell balancing and to reduce the traction system energy consumption, energy losses, and voltage drops. The control strategy was tested on a scaled experimental model comprising one substation, a 30.5 F Li-ion supercapacitor, and two induction motors representing trains travelling in opposite

directions. The authors concluded that the proposed controller maintained the SOC between the allowed limits while reducing the line voltage drop, total energy losses, and total energy consumption. However, such conclusions are unsatisfactory because the authors only focused on one traffic load condition that was assumed to be known at the start of the experiment that lasted for less than a minute.

Despite the importance of ESS SOC management for maximising their benefits, there remains a paucity of systematic investigations into the sizing restrictions that diminish the ability of ESS to improve the energy efficiency of electric railways. In extant studies on ESS applications in electric railways, it is typically assumed that the traction load is predictable, which does not reflect real-world operational conditions. Surprisingly, most papers reviewed as a part of the present study that focus on ESS control methods, were aimed at improving the electric railway energy efficiency without examining the effects of SOC constraints, which is a significant shortcoming, especially since the ESS in many locations has no access to the traction substations nor external sources. Therefore, in Chapter 5 of this thesis, the impact of working at the SOC limits of a stationary ESS is examined, assuming that there is no external power source/sink available. This is followed by a systematic investigation, including global efficiency analysis of the railway system with different traffic conditions and over extended operational periods. Finally, strategies for managing the SOC of the ESS are provided, and their experimental validation is presented in Chapter 6.

2.4 Conclusion and research gaps

ESSs are considered an effective means for improving energy efficiency of electric railways while reducing gas emissions. However, practical ESSs are limited by their high cost, large physical size, and limited lifetime. Recent developments in ESS technology and a rapid decline in price have made their application in electric railways more realistic, promising improvements in the regenerative energy recovery rates, thereby improving the energy efficiency of the traction system. Moreover,

hybridising different storage technologies with appropriate energy management methods has been shown in previous research to play a vital role in reducing the ESS size and degradation, and at the same time better meeting the power and energy requirements of the system. However, considerable uncertainty in the relationship between methods of control of an ESS and the energy efficiency of an electric railway system still persist. Another issue that has not been widely studied is the potential use of ESSs operating within capacity limits, as this markedly diminishes their benefits, especially when there is no access to any external power sources/sinks. Finally, the studies reviewed in this thesis regarding modelling methods of electric railways outline the critical role of railways modelling in understanding the energy/power requirements first before applying and evaluating the ESSs. However, none of these studies developed a modelling method with sufficient details to allow replication. Therefore, a detailed multi-train simulation method that adopts ESS and allows implementation of advanced energy management methods is needed to comprehensively assess the impact on the traction power system.

Chapter 3

Development of an Electrical Model for Multiple Trains Running on a DC 4th Rail Track

3.1 Introduction

In the extant literature, employing ESSs in electric railways is increasingly recognised as desirable to enhance performance. To investigate the ESS benefits, researchers make use of simulation tools to model the electric railway to enable them to analyse the size, location, control methodology, and requirements for the storage technology type. Further, simulation tools allow changes in electrical network, timetabling, and train speed profiles, which is fundamental for the planning and development of electric railways. When simulating electric railways, it may be challenging to adequately represent their nonlinear characteristics resulting from the rectifier substations, overvoltage protection circuits, and the continuous changes of the load according to the train position. The power exchange between trains and the change of the rail resistance between them require high temporal resolution and thus results in high computational complexity. Given these goals and challenges, the main objective of this work was to develop a sufficiently simple, fast to simulate, yet accurate, simulation method based on real-world assumptions. Further, the simulation method should be extendable to ESS and control to allow designing control

methods for energy management using ESSs to maximise the energy efficiency of electric railways.

A key motivator for this research is to avoid the protracted simulation times present in the common approach of forming iterative methods for solving the nonlinear equations characterising the system. Iterative methods are complex to be formed especially when adding ESSs with advanced control methods, which is the main focus of this thesis. Alternative approaches using MATLAB Simulink for modelling electric railways which have been discussed in a few articles such as [5], [56]–[58], [61], but no sufficient details were provided to allow replication of the work. Therefore, it was decided to develop a simulation method that is able to calculate the track voltage at any point and provide the voltages to which trains are subjected during normal operation. The model should be able to support on-board or stationary ESSs into the power flow model enabling energy efficiency analysis and design optimisation.

In this work, a simulation approach was developed for modelling the mechanical and electrical characteristics of a 4th rail track in a metro system. The simulation model operation requirements and parameters were based on the publicly available data regarding the Yizhuang Line in Beijing Metro. The model included multiple vehicles, power rails and substations. The electrical performance of individual trains and their effects on the behaviour of other trains within the same railway track were studied. To simulate the actual operational conditions most accurately, all trains were assumed to be in motion unless they were stopped at passenger stations, this was then reflected in the system configuration and related equations at every time step. The primary aim of this approach was to ensure that the proposed simulation tool was capable of incorporating these features when calculating the power flow. Finally, multiple verification approaches were applied to investigate the accuracy of the proposed modelling method.

This chapter describes the development of a framework for modelling the power flow within an electric rail network referenced to case study example. Prior to describing the framework in detail the operating characteristics of an electric railway

system are introduced starting with a description of the train, then the electrical power network and finally the operation of rail network (train journeys). Then, the fundamental mathematical modelling concepts to capture the mechanical and electrical behaviour of an electric railway system is discussed.

3.2 Electric railway system

3.2.1 Train

A typical representation of a DC train is shown in Figure 3.1, where the contact shoe collects power from the DC network before being converted to AC power to operate motors. In order to move a stationary train along track—two steel rails supported by concrete (sleeper) that is placed on crushed stones (ballast) to provide a surface and guidance for the train wheels as shown in Figure 3.2—tractive force produced by motors needs to be applied to wheels through gearbox. The tractive force value depends on many factors including track gradient (rolling resistance originates due to inclination in tracks where it increases when the train moves upward while it decreases when the train moves downward), and curvature of track (rolling resistance originates due to curves in tracks). Further, while the train is moving, the drag force that consists of vehicle mass, rolling resistance and air resistance would counter its movement. The train motion is limited by the train maximum speed, maximum tractive force, and maximum power consumption. Similarly, bringing the train to a standstill requires braking force. When the train is decelerating, its kinetic energy is used to drive the motor behaving as a generator which slows the train down, a process known as regenerative braking, before applying mechanical braking to stop the train completely [108].

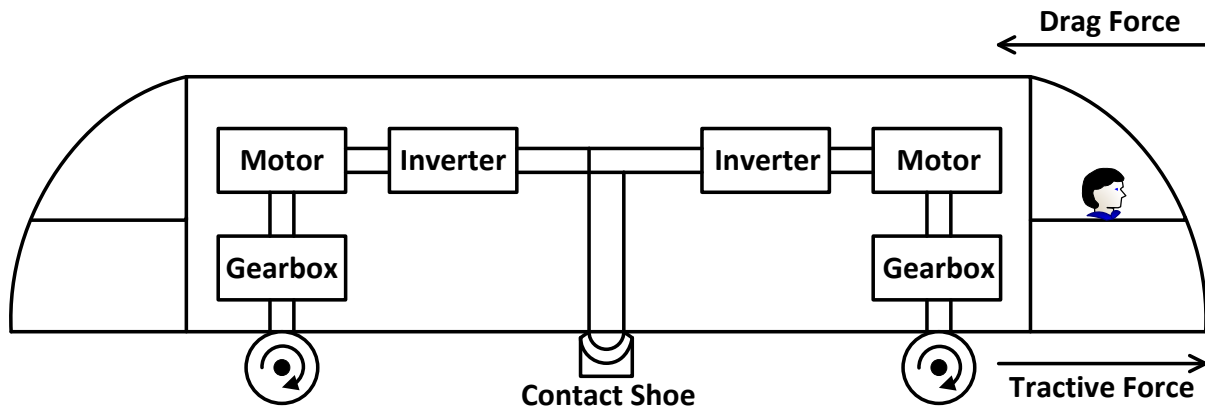


Figure 3.1: Representation of an electromechanical system in an AC train fed by a DC traction system

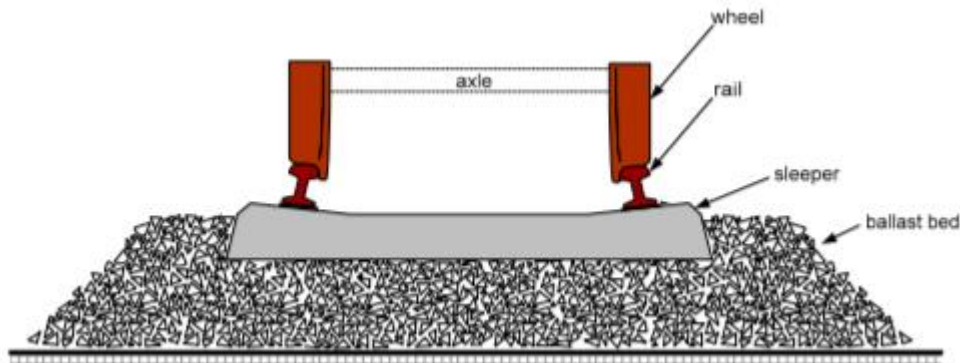


Figure 3.2: Typical structure of a rail track [109]

3.2.2 DC railway traction power system

The common configuration of a traction system—i.e. the mechanism through which electric power is converted to mechanical motion allowing the vehicle to travel along the track—in DC electric railways is shown in Figure 3.3 where the (electrical) substations include transformers and rectifiers. In such systems, transformers are responsible for stepping down the distribution network voltage and rectifiers are used to convert the distribution network AC voltage into DC voltage. The 3rd rail is responsible for conveying the electric power from the substations to the trains, whereas the power is transmitted back to the substations through the 4th rail. The train obtains power from the 3rd rail by continuous connection between its shoe and the 3rd

rail. The conductor rails are different from the rail track on which a train moves as illustrated in Figure 3.4.

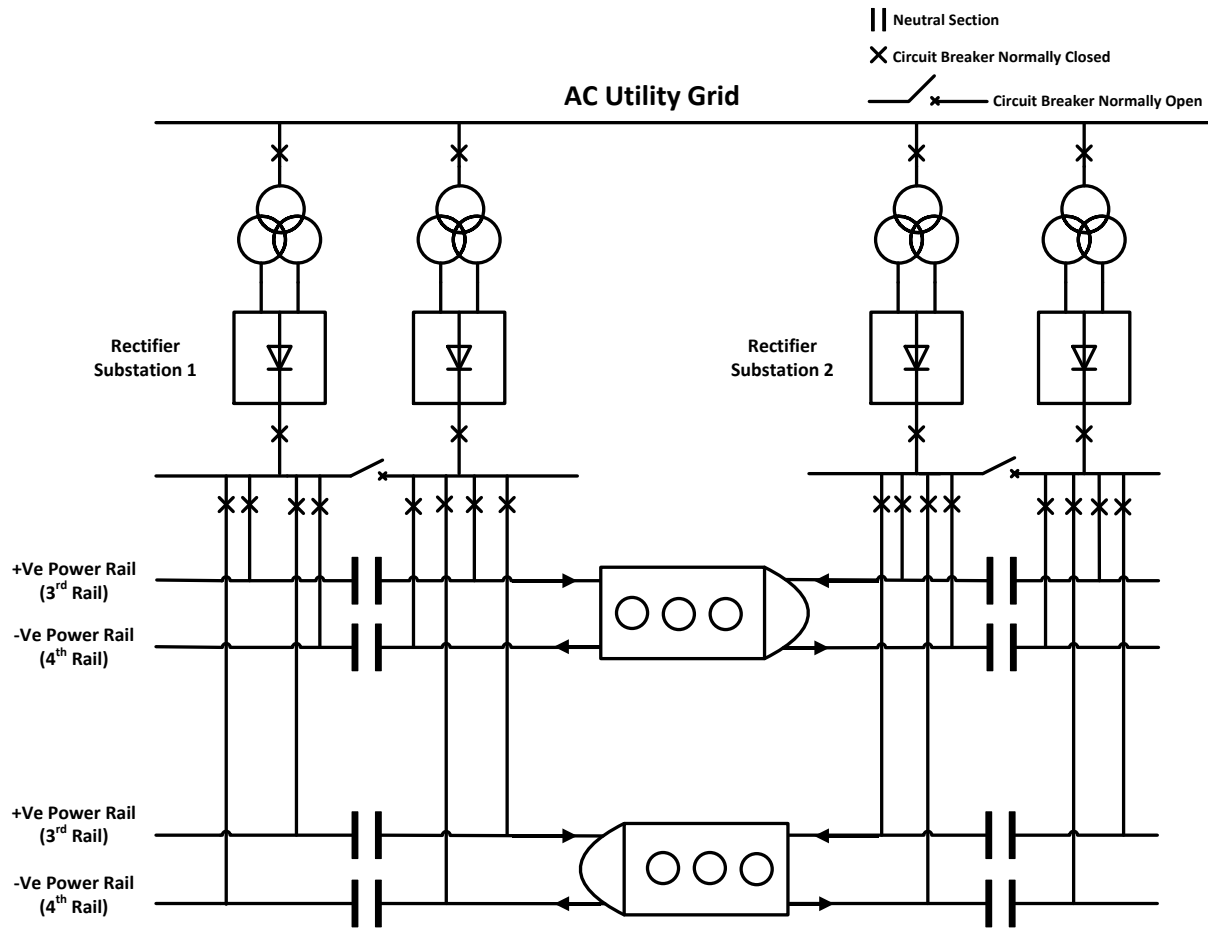


Figure 3.3: Configuration of a double-track DC railway power system

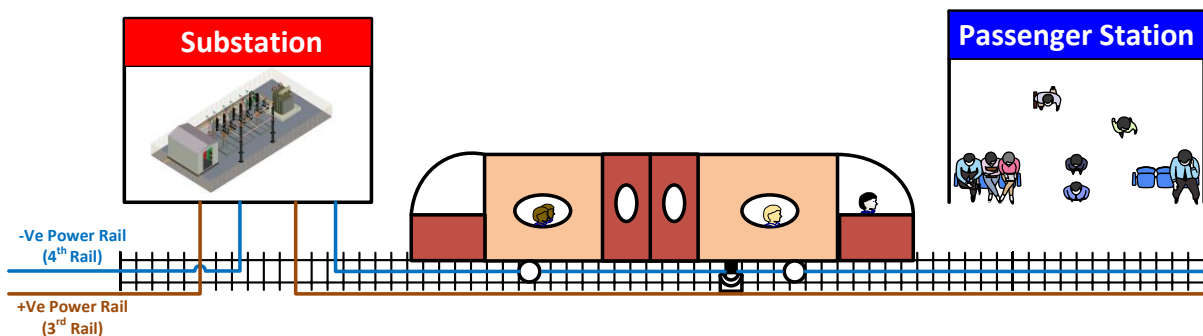


Figure 3.4: Schematic of a train running on a rail track and powered by a 4th rail system

In the Beijing Metro, the distribution network voltage is 10 kV and in each substation, two 12-pulse rectifier sets with the same capacity of 3000 kW are connected in parallel to supply the DC network with 750 V [46], [110]. The minimum voltage of a typical 750 V rectifier system is 500 V and the permanent maximum voltage is 900 V according to EN 50163 international standards for DC traction systems displayed in Table 3.1. The rated current of a typical 750 V rectifier system is 4000 A with overload capabilities of 150% (6000 A) for 1 hour, 300% (12000 A) for 1 minute, and 450% (18000 A) for 10 seconds [5].

Table 3.1: DC traction system voltages [5]

Definition of operating DC system voltages [V]	600	750	1500	3000
Lowest permanent voltage duration indefinitely [V]	400	500	1000	2000
Nominal voltage designed system value [V]	600	750	1500	3000
Highest permanent voltage duration indefinitely [V]	720	900	1800	3600
Highest non-permanent voltage duration 5 min [V]	770	950	1950	3900

At each substation location, section gaps (i.e. neutral sections) are positioned, representing a dead zone required to electrically isolate the railway sections, thus ensuring that any faults in one section are not transmitted to an adjacent section. This design allows all traction system to work normally except the faulted section. When the train reaches section gaps, the shoe (electrical contact between the train and conductor rail) is disconnected from the rail to ensure the vehicle is drawing no power in order to avoid electric arcs. Traction sectioning is also useful for maintenance, as work can be done on the traction substations without affecting the operation of the traction system, which increases the operational flexibility when the lines are subjected to frequent traffic [111].

The most common configurations for feeding substations in electric railways are single-end and double-end as shown in Figure 3.5. In single-end feeding mode, each rectifier substation is responsible for feeding the two adjacent electrical sections only. Furthermore, each train can only sink regenerative energy available within the same section. This is achieved by adding normally open circuit breakers between the

two parallel rectifier sets in each substation which allows each rectifier set to feed only one section [112]. In Beijing Metro, the substations are double-end fed where all sections are electrically connected through normally closed circuit breakers located at the substations. The length of neutral sections should be longer than the distance between collector shoes of a passing train to prevent the train from connecting adjacent electrical sections. The length of the neutral section in Beijing Metro was designed to be 14 m in order to be longer than the distance between two collector shoes in one carriage that is 12.6 m and longer than the distance between two collector shoes in different carriages that is 6.9 m [113].

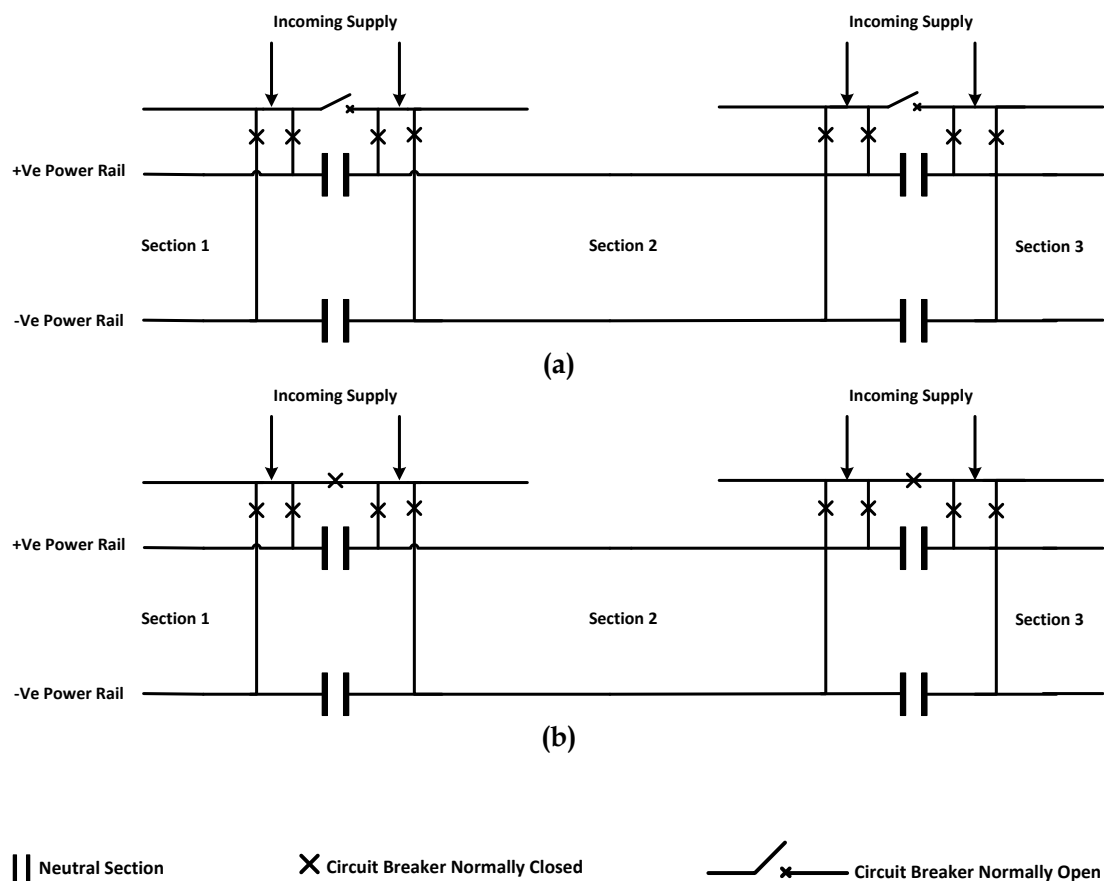


Figure 3.5: Power supply feeding schemes: (a) single-end feeding mode; (b) double-end feeding mode

3.2.3 Train operation

A passenger station is the place where the trains load and unload passengers (see Figure 3.4). The time spent at passenger stations for passengers loading and unloading is called dwell time. The departure and arrival times of trains with respect to passenger stations form a railway timetable. The timetable is cyclic when it is repeated at consistent time intervals where a train leaves a certain passenger station at the same time interval. The planned time interval between consecutive trains is known as headway. The cyclic (repeated) timetable was first used in 1931 in Netherlands for passenger convenience, making the timetables easy to memorise, before it was adopted in other countries [114].

In practice, sections between passenger stations are divided into speed segments with different speed limits. Therefore, train drivers try to achieve the target speed limits with respect to constraints such as maximum acceleration, minimum safe distance between consecutive trains, allowable travel time, and passenger comfort criterion. This driving style is known as flat-out operation [115]. A speed profile example of a train travelling between two passenger stations separated by 1000 m is shown in Figure 3.6. This speed profile represents the typical behaviour of trains in metro railway systems as stated in [116]. In acceleration mode, which is also called motoring mode, the train consumes power from the railway traction system, while in deceleration mode, the train regenerates power which is supplied to the railway traction system. In cruising mode representing the constant speed region, the drawn power is constant if the track is flat.

In principle, a train's regenerative power when decelerating can be passed to other trains in demand of power. However, in many instances a mismatch exists between a train's regenerative braking power and coincident train demand such that an excess of power is available that, unfortunately, cannot be passed to the national grid as the electrical substations are commonly unidirectional in metro systems and cannot assist in absorbing the excess power. Therefore, trains are equipped with on-board braking resistors that are switched on at a certain voltage threshold to protect

the power network from the overvoltages stated in Table 3.1. Another benefit of the on-board braking resistors is that they reduce the reliance on mechanical braking, thus extending the useful life of their disk brake pads. Typically, when braking resistors are employed, mechanical brakes are only deployed when the train speed drops below 10 km/h (2.78 m/s) to ensure correct stopping distance, whilst the electrical braking system is turned off to activate the mechanical braking system [117].

Since this thesis is concerned with capturing and recycling the energy wasted in the braking resistors a simulation model representing the typical operation of a metro will be described in the next section.

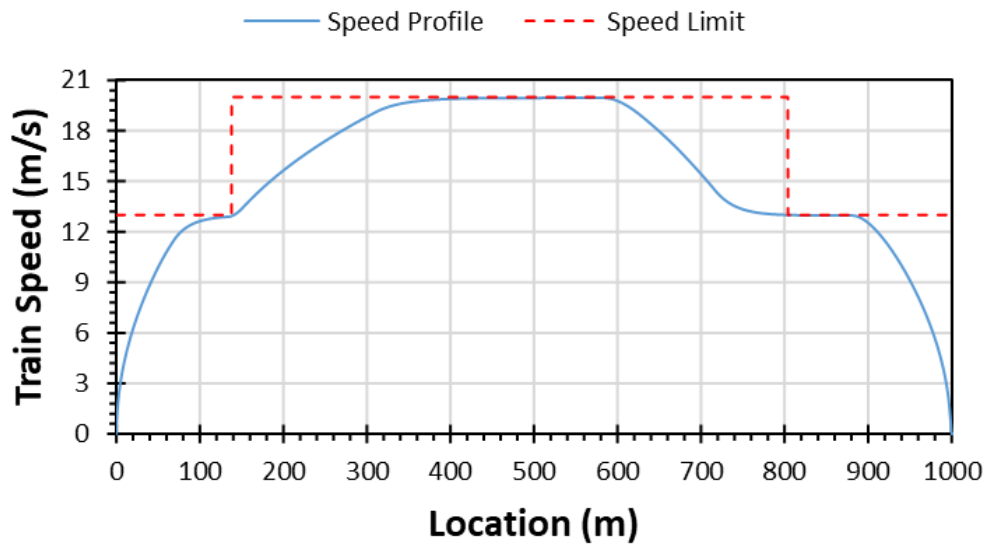


Figure 3.6: Typical driving cycle of a train between two consecutive passenger stations

3.3 Modelling approach

In train modelling, there are two main approaches called forward and backward modelling. With forward modelling, the input to the model is the train power profile and that is used to calculate the train speed. In backward modelling, also known as effect-cause modelling, the effect is the train speed that is the input to

the model and the cause is the train power demand that is calculated in the model [4]. Since metro train journeys are train/distance constrained the latter approach was adopted in this study due to the data availability in the literature regarding the typical speed profile of a train in a metro system.

To model a metro system it was decided to separate it into a train model and a DC traction power system model. This method is called decoupled modelling approach and is widely used in the literature [7], [52], [53], [55]. This modelling approach was essential, as it allowed for the impact of train behaviour on the rail track as well as the effect of the railway power network on the train, to be assessed. The premise used in this work is that the train has a specific speed/time profile to follow and the train driver, simulated here by a proportional controller, will ensure adherence to the aforementioned profile. Figure 3.7 shows the model used with the input (speed target profile such as see in Figure 3.6) on the left hand side and the outputs on the right. The outputs are the distance travelled by a particular train and the train power demand (import/export). The proportional (P) controller was added to the train model to get a realistic speed profile by simulating the driver's behaviour where in practical life the driver aims to achieve the target speed according to the reference speed limits. Therefore, the P controller aimed to achieve the target speed with respect to the maximum jerk (the change of acceleration), and the maximum tractive/braking force provided by the train manufacturer that it is measured on a test track and varies with speed.

The equations used in this work to model train dynamics were adopted from [11], [108]. Train behaviour was studied based on Newton's Second Law, given as follows:

$$Force (F) = mass (m) \cdot acceleration (a) \quad (3.1)$$

$$F(v) - B(v) = m \cdot a \quad (3.2)$$

$$F(v) - B(v) = m \cdot \frac{dv(t)}{dt} \quad (3.3)$$

where v is train velocity, $F(v)$ is tractive force in kN and $B(v)$ is braking force in kN. The drag force $Q(v)$ in kN is represented by the Davis equation:

$$Q(v) = \alpha + \beta \cdot v + \gamma \cdot v^2 \quad (3.4)$$

where, α represents bearing resistance in kN and it is dependent on the vehicle mass, where β denotes rolling resistance in kNs/m, and γ represents air resistance in kNs²/m². The coefficients of the Davis equation depend on the train type, and they are determined experimentally by the manufacturer. It should be noted that, for simplicity, gradient resistance force was neglected assuming that the track was flat in this model. Further, the curvature resistance force was ignored, i.e. a straight track was assumed. Therefore, the motion of a train is described as follows:

$$m \cdot \frac{dv(t)}{dt} = F(v) - B(v) - Q(v) \quad (3.5)$$

Power is the rate at which work is done ($P = W/t$) and work is the product of force and distance ($W = F \cdot d$). Therefore, power is ($P = \frac{F \cdot d}{t}$); since distance over time is velocity then power is ($P = F \cdot v$). The train traction power P_t and regenerative power P_r in kW are given by the following relationships:

$$\begin{cases} P_t = \frac{F(v) \cdot v}{\eta_g \cdot \eta_m \cdot \eta_i} \\ P_r = -B(v) \cdot v \cdot \eta_g \cdot \eta_m \cdot \eta_i \end{cases} \quad (3.6)$$

where η_g is the gearbox efficiency, η_m is the motor efficiency, and η_i is the inverter efficiency [4], [45], [108]. The product of η_g , η_m , and η_i represents the transmission efficiency of the train. It is worth mentioning that Equation 3.6 calculates the electrical power measured at the connection point between the contact shoe and the power rails. The mechanical traction power ($P = F \cdot v$) is calculated by multiplying the train speed by the tractive force. The mechanical traction power is divided by the transmission efficiency to obtain the electrical power collected by the contact shoe (feed in power) to meet the train speed that is assumed to be known in this modelling approach. Similarly, the mechanical braking power is calculated by multiplying the train speed by the braking force. However, the mechanical braking power is multiplied by the transmission efficiency instead of division to obtain the electrical power injected by

the train to the conductor rails through the contact shoe (feed out power) after losing power in the gearbox, motor, and inverter. The electromechanical system of a generic DC train is represented in Figure 3.1.

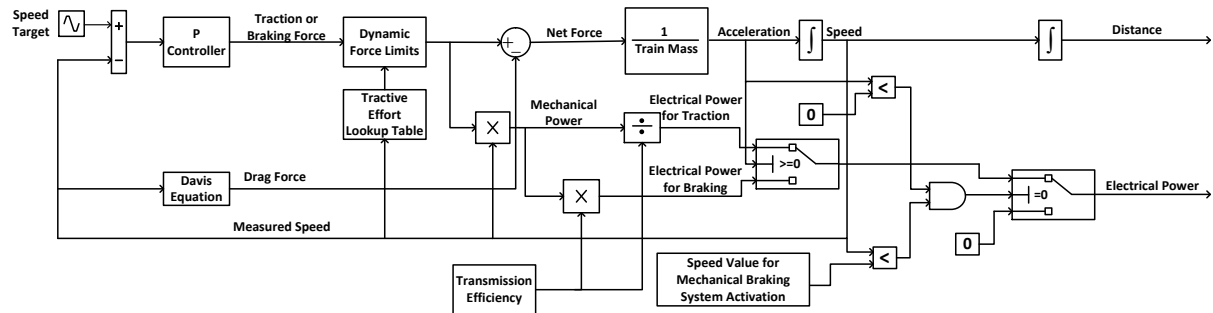


Figure 3.7: Dynamics of a single train

Figure 3.8 shows the electrical configuration of a single-track railway where the trains travel in one direction while Figure 3.9 shows the electrical configuration of a double-track railway where the trains travel in two directions. The power system includes rectifier substations, trains, and transmission lines. DC traction is the focus of the present investigation, hence, the AC side of the substation was disregarded and it was assumed to provide a fixed DC voltage. Moreover, traction substations were modelled as ideal DC voltage sources with internal resistances representing Thevenin's equivalent. The substation was grounded and positioned between the positive (the 3rd rail) and negative (the 4th rail) power lines. Ideal diodes were used to allow a unidirectional power flow by preventing braking currents from returning through the substations. The trains were represented by ideal current sources where the current demand of each train was calculated by dividing the power demand calculated in the train model by the measured voltage across the current source. A braking resistor box was connected in parallel with the train through a switch that was triggered when the voltage amplitude measured by the decelerating train exceeded the maximum allowed voltage. In Figures 3.8 and 3.9, the braking resistors of the decelerating trains are not activated due to the assumption of not reaching the

maximum voltage threshold which causes all of the regenerative power to be injected back to the transmission line to be consumed by the accelerating trains.

The transmission lines were represented by variable resistors where the resistance ahead and behind the train changed continuously according to the traffic density as will be explained later in this chapter. Since the resistance between the trains and their departure and arrival points should change instantly, each resistive line was represented by a series of variable resistances, the values of which changed based on the train positions. As shown in Figures 3.8 and 3.9, the resistance between the train and the substation changes with the distance travelled by the train, which can be obtained by multiplying the per unit rail electrical resistance and the distance between the train and substation. Since the electrical resistance between a specific train and the previous or next substation is time variant, the other trains running either behind or ahead of that particular train would change the value of the electrical resistance between that train, the next substation and the previous substation. It is worth mentioning that the electric resistance of cables will change as the ambient temperature changes. However, for simplicity in this model, it was assumed that the resistive elements and cable conductivity were unaffected by their surroundings.

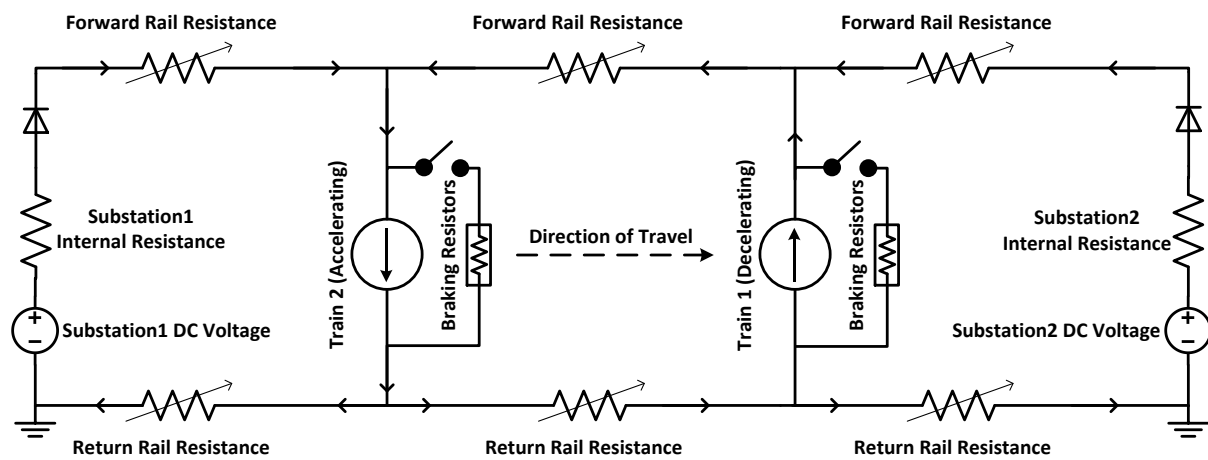


Figure 3.8: Electrical configuration of multiple trains running on a single-track with two substations

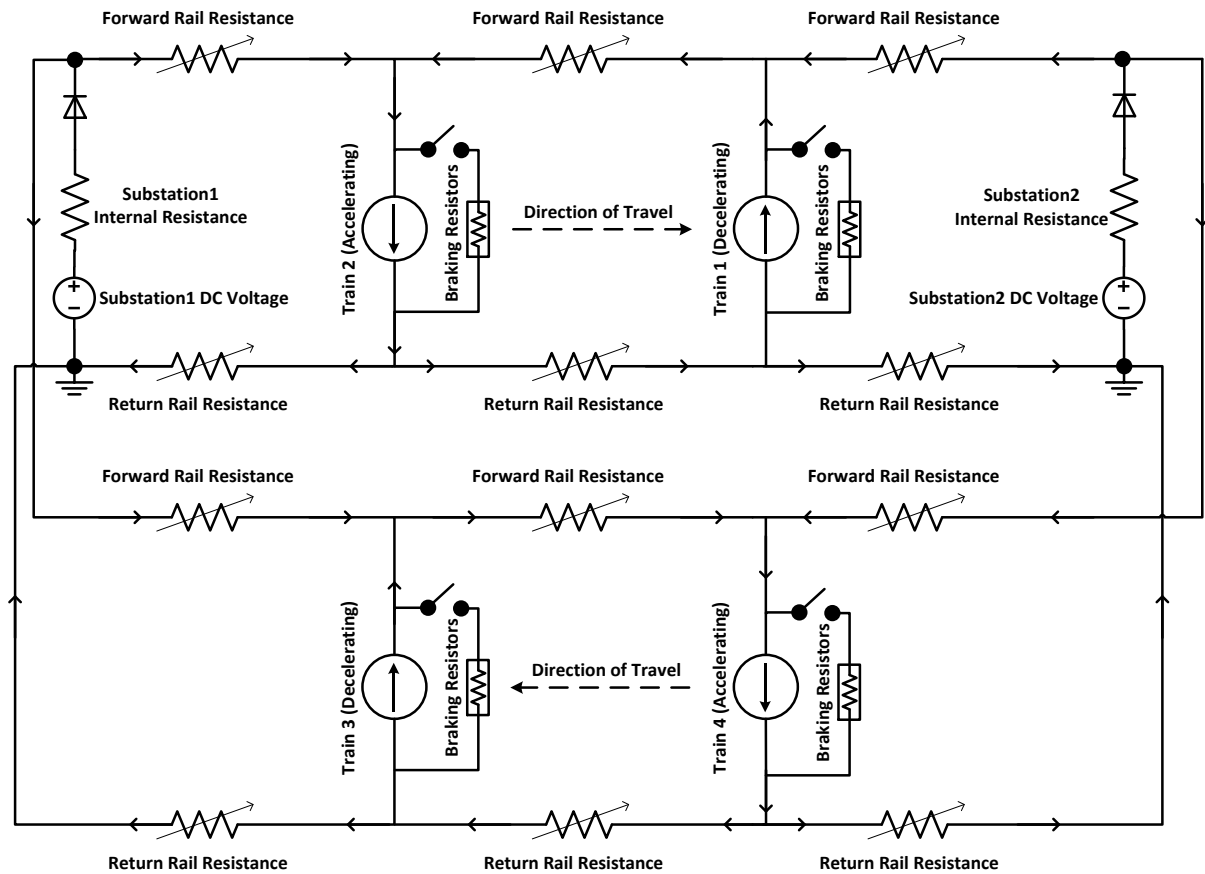


Figure 3.9: Electrical configuration of multiple trains running on a double-track with two substations

3.4 Beijing Metro and the development of a test scenario

The previous section described a mathematical model for the train traction system and set out the operating principles for the electrical simulation, the combination of which will provide a framework for obtaining the electrical demands for train and the instantaneous voltages to be used in the ESS application research presented in later chapters. This section applies the framework to a section of the Beijing Metro system with the intention of demonstrating the application of the framework. In this section, a double-track railway is described and followed by a detailed power system analysis before closing with the description of verification methods adopted for the case study.

3.4.1 Beijing Metro system

Yizhuang Line in Beijing Metro shown in Figure 3.10 was used as a case study due to the availability of published data about the system. Table 3.2 shows the locations of fourteen passenger stations and twelve substations along the line. It is noticed that the passenger stations and substations in Yizhuang Line share the same locations except for two passenger stations named Wanyuan and Ciqu that do not have any substations at their locations. The dwell time in the passenger stations is shown in Table 3.3 where it is noticed that the dwell time in most of the passenger stations is 30 s.



Figure 3.10: Topological map of Yizhuang Line in Beijing Metro [118]

Table 3.2: Passenger station and substation location in Yizhuang Line [108]

	Passenger station	Substation	Location (km)
1	Songjiazhuang	Songjiazhuang	0
2	Xiaocun	Xiaocun	2.631
3	Xiaohongmen	Xiaohongmen	3.906
4	Jiugong	Jiugong	6.272
5	Yizhuangqiao	Yizhuangqiao	8.254
6	Wenhuayuan	Wenhuayuan	9.247
7	Wanyuan		10.785
8	Rongjing	Rongjing	12.065
9	Rongchang	Rongchang	13.419
10	Tongjinan	Tongjinan	15.757
11	Jinghai	Jinghai	18.022
12	Ciqunan	Ciqunan	20.108
13	Ciqu		21.394
14	Yizhuang	Yizhuang	22.728

Table 3.3: Dwell time at passenger stations of the Yizhuang metro line [11]

Passenger station	Dwell time (s)
Songjiazhuang	30
Xiaocun	30
Xiaohongmen	30
Jiugong	30
Yizhuangqiao	35
Wenhuayuan	30
Wanyuan	30
Rongjing	30
Rongchang	30
Tongjinan	30
Jinghai	30
Ciqunan	30
Ciqu	35
Yizhuang	45

In Yizhuang Line, each section between any two passenger stations is divided into three intervals with different speed limits that cannot be exceeded under any circumstances and if this happens, emergency brakes are applied or power reduced to keep cruising. The practical speed limits across the whole line of Yizhuang are detailed in Table 3.4 [66]. For example, the section between Songjiazhuang and Xiaocun is divided into three intervals where the speed limit is 13 m/s for the distance between

0 and 133 m representing the first interval. The second interval has a speed limit of 20 m/s for the distance between 133 and 2300 m while the last interval has a speed limit of 10 m/s for the distance between 2300 and 2631 m. The table also shows the time boundaries according to the operation requirements of the Yizhuang Line, where trains travel between passenger stations with respect to the minimum and maximum journey time. The columns T and E shows the journey time and energy consumption, respectively, of a practical case of a train travelling along the whole line. The train energy consumption could increase or decrease based on the driving strategy. An example of a train travelling on Yizhuang Line with an optimised speed profile for the aim of reducing the train energy demand is shown in Figure 3.11. It is worth mentioning that not every speed profile is achievable as the train is limited to its maximum power, acceleration/deceleration, jerk, and tractive/braking force. The maximum tractive/braking force of trains on the Yizhuang Line when trains are overloaded is shown in Figure 3.12 as measured by the train manufacturer. The maximum tractive/braking force is measured experimentally and limited by the maximum adhesion, motor power, acceleration/deceleration, and jerk. In the first region, the train is limited to maximum adhesion that allows the train to move without slipping the wheels. The force is constant until reaching the base speed where the vehicle reaches the maximum power caused by the motor limitation before the force decreases as a function of speed [119].

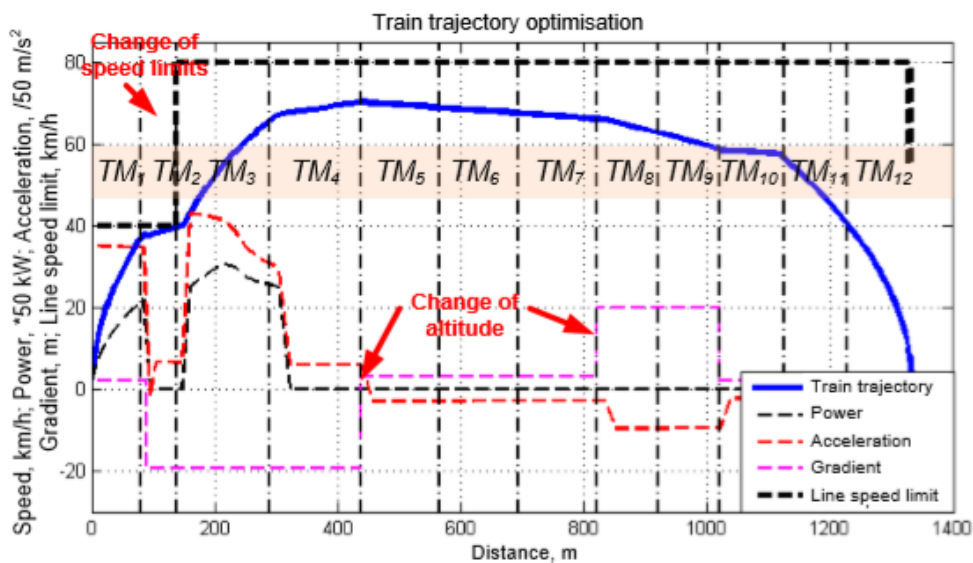


Figure 3.11: Field test in Yizhuang Line of train trajectory optimisation [120]

Table 3.4: Yizhuang Line practical data of speed limits, journey time, and energy consumption [66]

Passenger station	d (m)	$\frac{v_{max1}(\frac{m}{s})}{d1$ (m)	$\frac{v_{max2}(\frac{m}{s})}{d2$ (m)	$\frac{v_{max3}(\frac{m}{s})}{d3$ (m)	T_{min} (s)	T_{max} (s)	T (s)	E (kWh)
Xiaocun	2631	13/0–133	20/133–2300	10/2300–2631	183	234	194	29.59
Xiaohongmen	1275	14/0–130	20/130–1151	13/1151–1275	74	110	102	11.7
Jiugong	2366	14/0–128	20/128–2165	13/2165–2366	141	177	153	21.77
Yizhuangqiao	1982	14/0–123	20/123–1781	13/1781–1982	117	152	132	21.11
Wenhuayuan	993	13/0–130	20/130–796	13/796–993	49	85	84	17.5
Wanyuan	1538	14/0–130	20/130–1350	13/1350–1538	87	123	112	15.34
Rongjing	1280	14/0–130	20/130–1087	13/1087–1280	69	105	99	10.04
Rongchang	1354	14/0–130	20/130–1168	13/1168–1354	75	110	102	13.56
Tongjinan	2338	13/0–120	20/120–2143	12/2143–2338	150	185	158	12.4
Jinghai	2265	13/0–128	20/128–2073	13/2073–2265	138	171	146	22.73
Ciqunan	2086	13/0–129	20/129–1897	11/1897–2086	142	179	137	28.44
Ciqu	1286	13/0–130	20/130–1085	13/1085–1286	69	106	99	24.15
Yizhuang	1334	10/0–128	20/128–1147	14/1147–1334	70	106	102	16.57

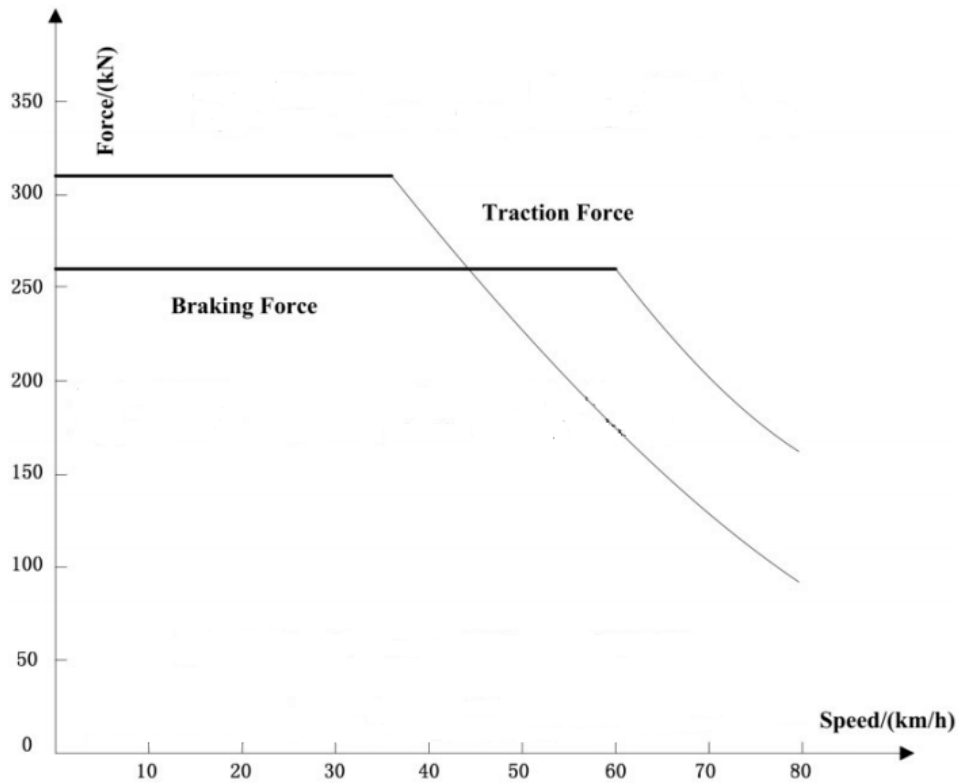


Figure 3.12: Maximum tractive force and maximum braking force for vehicles in the Yizhuang Line [121]

3.4.2 Test scenario

In the test scenario, equal distances between the adjacent passenger stations were assumed and trains were assumed to stop at three passenger stations separated by 1 km, as shown in Figure 3.13. The total track length was set to 2 km, with two substations positioned 2 km apart as this is approximately the average distance between substations in Yizhuang Line [108]. It is described in the previous subsection that it is not necessary for passenger stations to have substations at their locations. Therefore, to simulate both practical cases it was decided in the current study to place two substations at the passenger station locations except for the passenger station in the middle that did not have a substation at its location. Moreover, this assumption will allow examining the impact of ESSs when located equidistant from the two substations as will be discussed in the next chapter. Focus was given only to one

electrical section because it was assumed that the traffic is similar in different electrical sections and studying more than one section would not change the conclusions of the studies in this thesis.

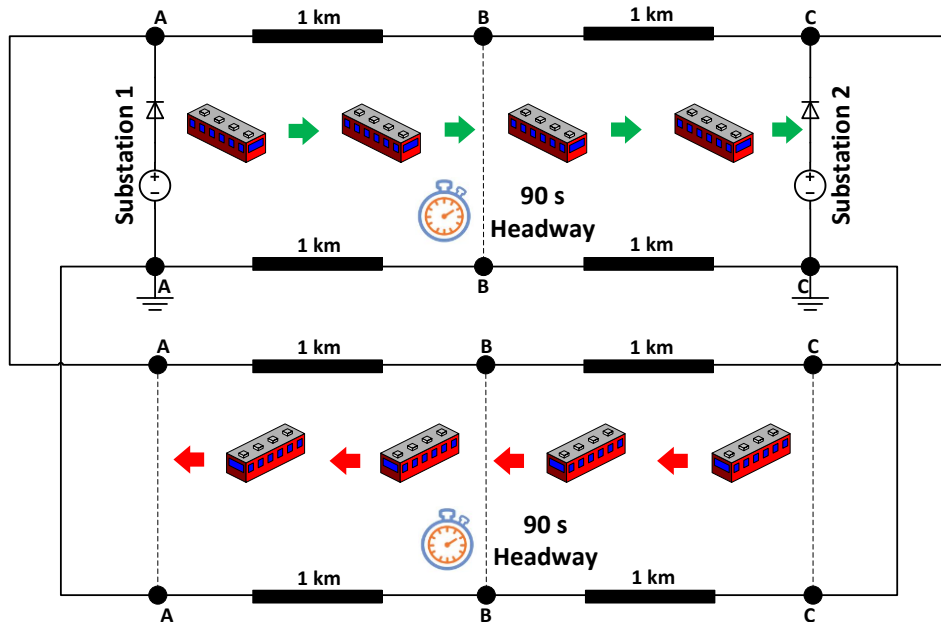


Figure 3.13: Double-track railway with 2 substations, 3 passenger stations, and 8 running trains

In the simulation, eight trains staggered by a headway of 90 s were modelled. The headway was decided to be 90 s because this is the standard headway in Yizhuang Line as stated in [122]. In the up line, each train starts its journey at Passenger Station A and finishes at C. In contrast, each train operating along the down line starts its journey at Passenger Station C and finishes at A, as illustrated in Figure 3.13. Thus, one journey – complete when the trains in the up line finish travelling from Passenger Station A to C and those in the down line finish travelling from Passenger Station C to A – was modelled as one full operating cycle, denoted here as a ‘journey’.

Since the distance between Yizhuangqiao Passenger Station and Wenhuyuan Passenger Station is 993 m, which is approximate to the distance between the passenger stations in the model considered in this thesis, it was decided to adopt its

speed limits and operation requirements. The trains in the current simulation model were set to travel between passenger stations in 84 s to match the practical case provided in Table 3.4 for a train travelling between Yizhuangqiao Passenger Station and Wenhuyuan Passenger Station. The eight modelled trains were assumed to have identical speed profiles between any two consecutive passenger stations. Whilst this may seem as a simplification, it is not too dissimilar to strictly timed automated railway systems that exist around the world.

The cyclic railway timetable shown in Table 3.5 reflects the arrival times for all passenger stations, except for the initial point in the journey, for which departure time is given instead. In the traffic scenario considered in this case study, it was further assumed that each train would dwell at the passenger stations for 30 s as this is the standard dwell time in most passenger stations of Yizhuang Line according to the actual operating schedules stated in Table 3.3. In practice, the dwell time is variable as it is governed by the number of passengers boarding and disembarking from the train carriages.

Table 3.5: Train timetable adopted for the double-track railway (in seconds)

Train number	Passenger Station A	Passenger Station B	Passenger Station C
Train 1	0 (Departure)	84 (Arrival)	198 (Arrival)
Train 2	90 (Departure)	174 (Arrival)	288 (Arrival)
Train 3	180 (Departure)	264 (Arrival)	378 (Arrival)
Train 4	270 (Departure)	354 (Arrival)	468 (Arrival)
Train 5	198 (Arrival)	84 (Arrival)	0 (Departure)
Train 6	288 (Arrival)	174 (Arrival)	90 (Departure)
Train 7	378 (Arrival)	264 (Arrival)	180 (Departure)
Train 8	468 (Arrival)	354 (Arrival)	270 (Departure)

3.4.3 Train model

The train was modelled in MATLAB Simulink as illustrated in Figure 3.14 where the model parameters are reported in Table 3.6. The speed limits between passenger stations were injected to the simulated train model as a reference speed profile that the P controller aimed to achieve with respect to the timetable, maximum tractive/braking force, and maximum jerk rate that was set to 0.75 m/s^3 as this is the recommended limit for metro systems [123], [124].

The maximum tractive force of trains is $F_{max}(v)$ in kN is given by:

$$\begin{cases} F(v) = 310, & v \leq v_1 \text{ m/s} \\ F(v) = (310 \cdot v_1)/v, & v > v_1 \text{ m/s} \end{cases} \quad (3.7)$$

The maximum electrical braking force $B_{max}(v)$ in kN is given by:

$$\begin{cases} B(v) = 260, & v \leq v_1 \text{ m/s} \\ B(v) = (260 \cdot v_1)/v, & v > v_1 \text{ m/s} \end{cases} \quad (3.8)$$

Equations 3.7 and 3.8 were derived by the author of [108] from Figure 3.12, which was provided by the train manufacturer, to approximately estimate the force limits at each speed value to be applied to the model. The first part of each equation represents the constant line while the second part represents the decreasing curve at a rate of $1/v$. The base speed in which the line starts to decrease is v_1 while v represents the measured speed. It is deduced from Figure 3.12 that the base speed in traction is 10 m/s (36 km/h) while it is 16.67 m/s (60 km/h) in braking [108].

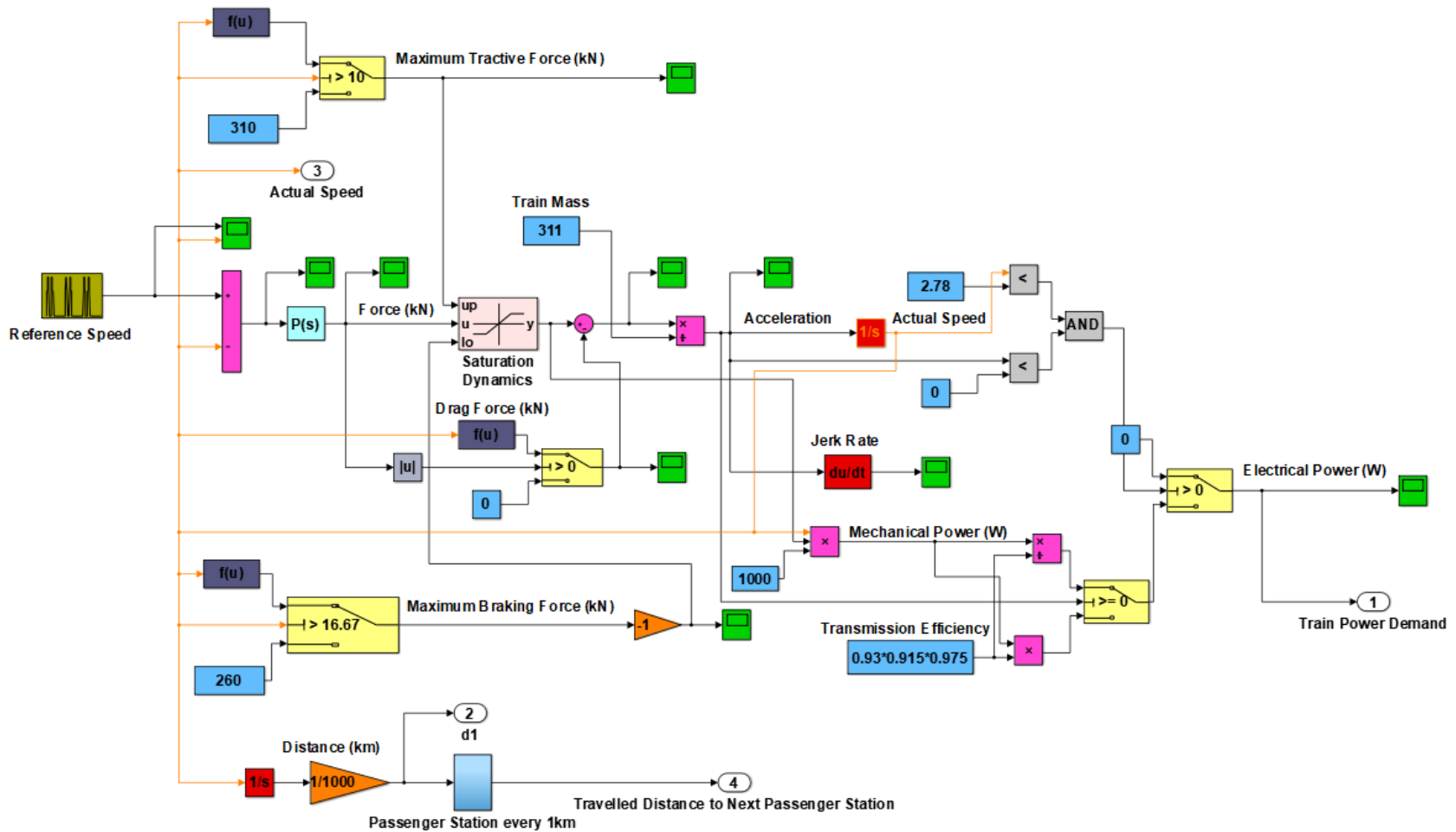


Figure 3.14: Screen capture of a single train modelled in MATLAB Simulink

Applying the above equations to Train 1 yielded the results shown in Figure 3.15. It should be noted that the same values were obtained for all trains included in the simulation. The graph shows that the train was working on the maximum tractive/braking force most of the time. The acceleration/deceleration reduced when the train approached the maximum speed or reached the maximum allowed jerk, which resulted in reduction of the applied force. The P-gain was set to 180 as this guaranteed a jerk rate below the maximum limit (0.75 m/s^3), and a journey time of 84 s matching the practical journey time. The acceleration/deceleration and jerk of Train 1 is shown in Figure 3.16.

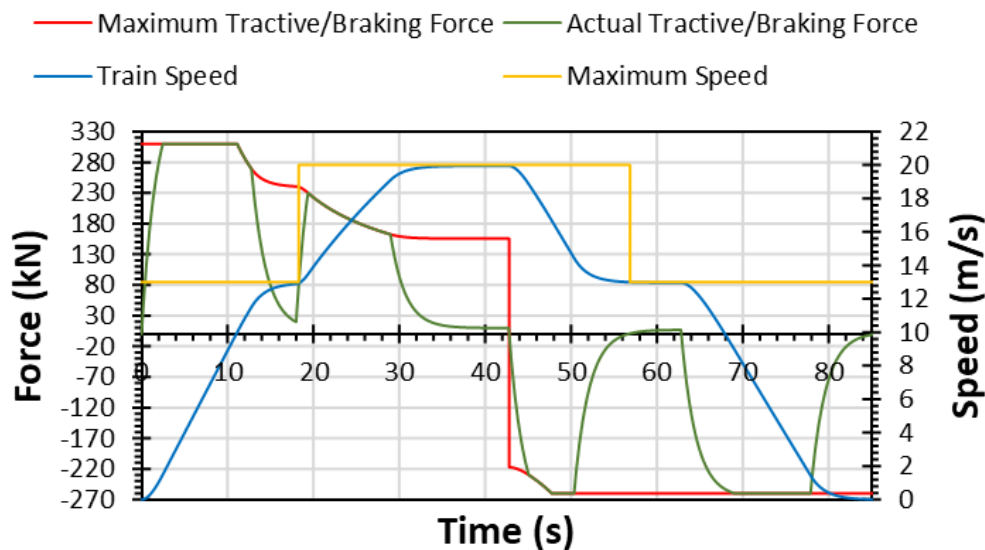


Figure 3.15: Speed profile, actual tractive/braking force and limits of speed and tractive/braking force of a single train travelling between two passenger stations

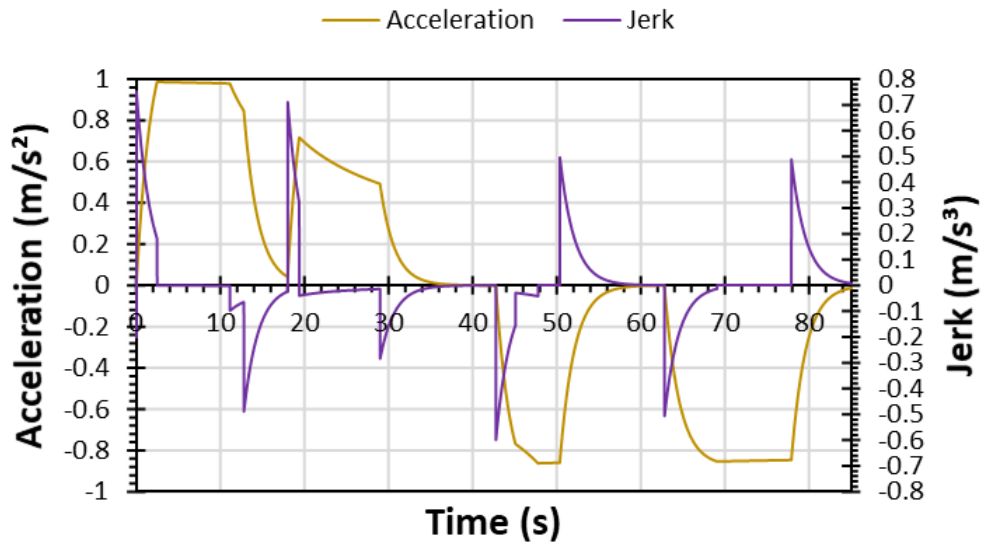


Figure 3.16: Acceleration and jerk rate of a single train travelling between two passenger stations

The speed profiles of all four trains in the up line across the complete journey are shown in Figure 3.17 where they are identical with the speed profiles of the trains in the down line. The integration of the speed profiles provided the train trajectories for the entire journey as shown in Figure 3.18. Train 1 started the journey by departing from Passenger Station A at 0 s before attempting to reach the maximum speed limit 13 m/s that was applied to the first 138 m. Afterwards, the train increased the speed to meet the new speed limit that changed to 20 m/s between 138 m and 804 m. After approximately 43 s of the train departure it started decelerating in order not to exceed the speed limit of 13 m/s that was applied to the distance from 804 m to the next passenger station located at 1000 m. When reaching 804 m the train maintained the speed at the maximum limit 13 m/s before decelerating to meet the required journey time 84 s for trains when travelling between any two passenger stations in the proposed model. The train arrived at Passenger Station B at 84 s and dwelled for 30 s before travelling to Passenger Station C with the same driving behaviour where it arrived at 198 s. This driving process was also accomplished by Train 2, Train 3, and Train 4 but after 90 s, 180 s, and 270 s, respectively, of Train 1's departure. The same operating cycle was achieved in the down line but in the reverse direction where Train 5 was synchronised with Train 1, Train 6 was synchronised with Train 2, Train 7 was

synchronised with Train 3, and Train 8 was synchronised with Train 4. This approach of synchronisation in the train departure times on each track permits electrical verification by guaranteeing that an identical load is applied to each substation, and that the trains are uniformly distributed along the railway line, as will be discussed in the verification section.

Due to the short distances between the passenger stations, trains start and stop frequently. The effect of these interruptions was modelled jointly in this simulation study. From the graphs depicted in Figures 3.17 and 3.18, an overlap between the trains is evident, whereby one train is braking while another one is accelerating. In practical railway operations, this overlap plays a vital role in the energy exchange management and voltage stability. The greater the traffic density, the greater the regenerated energy exchange between the vehicles and the lower the dissipated energy. Consequently, it is expected in this study to observe more energy dissipated at the beginning and end of the journey, as the traffic density is lower at the initial and terminal passenger stations.

When verifying the electrical aspects of the modelled scenario, several identical journeys were examined, and the same characteristics and loads were applied to all trains. This feature of the proposed simulation model permits good judgment of the validity of the results by applying logic. However, in order for the model to simulate realistic metro railways, real traffic scenarios should be considered as will be demonstrated in later chapters. Furthermore, the train mass changes dynamically due to the number of passengers travelling on the train varying between each passenger station, therefore energy demand of the traction system would also fluctuate. However, in the case considered here, the trains were considered to have fixed mass as they were assumed to be at full passenger capacity throughout each journey.

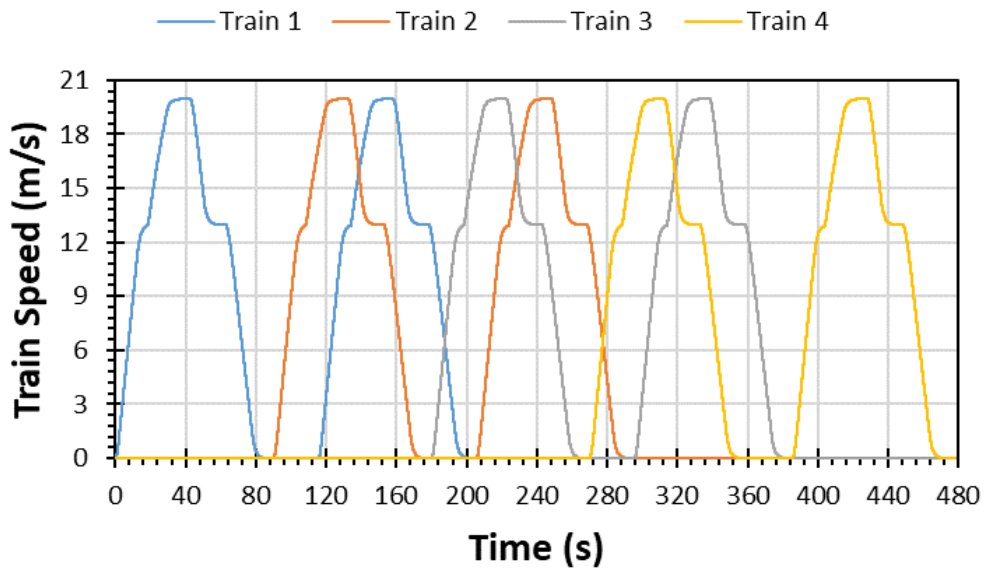


Figure 3.17: Speed profiles of four trains running on a 2 km segment of a double-track railway with 90 s headway between consecutive trains

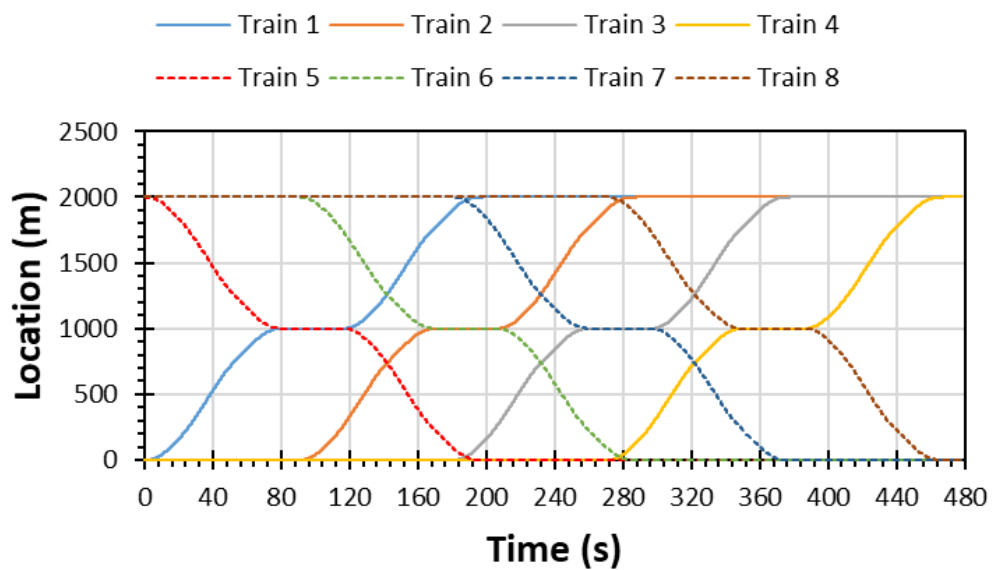


Figure 3.18: Train diagrams of eight trains running on a double-track railway serving three passenger stations

The trains were considered to import power during acceleration or in the cruising mode while decelerating trains were considered to export power. Thus as the speed profiles were variable, the train power demand would also fluctuate. The train power demand that is depicted in Figure 3.19, and the position were injected to the

power system model that will be discussed in the following subsection. The eight modelled trains had identical power profiles to enable the electrical verification of results yielded by repetitive journeys. The drop in power when approaching the speed limits is reasonable due to the decrease in the acceleration that can be seen in the practical case displayed in Figure 3.11. It is noticed in Figure 3.19 that the electrical power in traction was limited to the value of 3736.4 kW while in braking it was limited to 3596 kW. The power limits can be calculated from Figure 3.12 based on the fact that when reaching the base speed the train reaches its maximum power [108]. In other words, when calculating the mechanical power by multiplying the tractive/braking force by the train speed depicted in Figure 3.12 it is found that the power increases until reaching its maximum value at the base speed where the force starts decreasing indicating that the power never exceeds its value at the base speed. The maximum electrical power is calculated by the following equations:

$$\begin{cases} P_{t(\max)} = \frac{F_{\max} \cdot v_1}{\eta_g \cdot \eta_m \cdot \eta_i} \\ P_{r(\max)} = -B_{\max} \cdot v_1 \cdot \eta_g \cdot \eta_m \cdot \eta_i \end{cases} \quad (3.9)$$

where F_{\max} at the base speed is 310 kN and B_{\max} at the base speed is 260 kN. Therefore, the maximum electrical power is:

$$\begin{cases} P_{t(\max)} = \frac{310 \cdot 10}{0.975 \cdot 0.915 \cdot 0.93} = 3736.4 \text{ kW} \\ P_{r(\max)} = -260 \cdot 16.67 \cdot 0.975 \cdot 0.915 \cdot 0.93 = -3596 \text{ kW} \end{cases} \quad (3.10)$$

It is noteworthy that the energy consumption for each train when travelling from Passenger Station A to B was 22.41 kWh that falls within the measured energy consumption range in kWh [10.04, 29.59] of trains in Yizhuang Line when travelling between two passenger stations as described in Table 3.4.

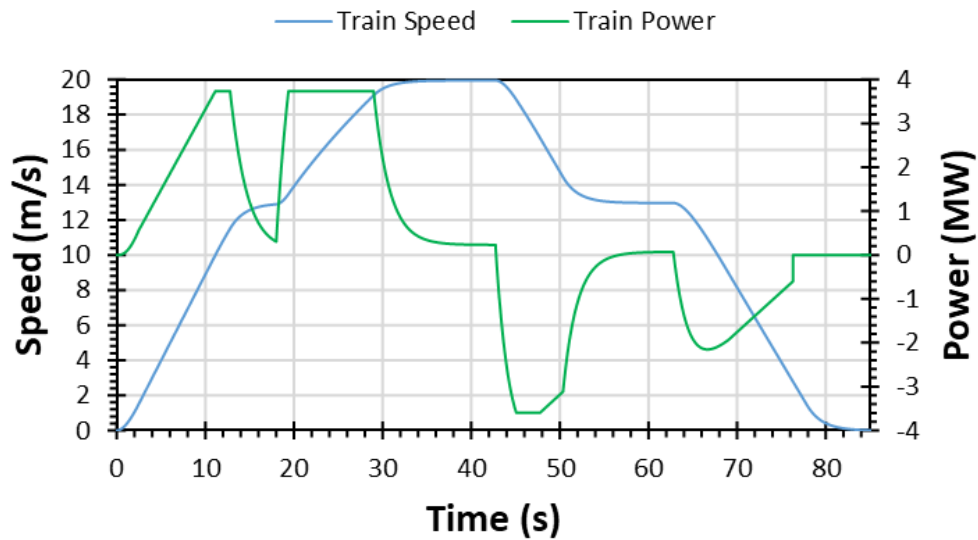


Figure 3.19: Power and speed profiles of Train 1 when travelling from Passenger Station A to B

3.4.4 Power system model

Modelling railway electrical systems is challenging because train locations are variable, and this causes instantaneous changes to the network electrical configuration. Moreover, train power demands change with location on the track, which requires a calculation of the voltages and currents at each node along the track. In other words, the network is time varying, and the circuit equations change based on the train speed and location, as well as the number of trains in operation. In order to address these challenges, as a part of the present investigation, a 4th rail track model was implemented and simulated in MATLAB Simulink using the Simscape toolbox that was integrated with the vehicle model discussed in Section 3.4.3. The Simscape toolbox allowed for changes in the network electrical configuration to be solved during the simulation. The solver type in MATLAB was set to ode14x with a time step of 10 ms. The solver type ode14x was selected as it was the only that was able to solve the model. The total simulation time was fifty minutes and it was performed using a personal computer with Intel® Core™ i5-4590 CPU @ 3.3 GHz processor and memory (RAM) with 8.00 GB. The power system parameters are summarised in Table 3.6.

Table 3.6: Parameters of describing the modelled electric railway system [11], [46]

Symbol	Quantity	Value
α	Davis equation constant coefficient	2.965 kN
β	Davis equation linear term coefficient	0.23 kNs/m
γ	Davis equation quadratic term coefficient	0.005 kNs ² /m ²
M	Train mass	311,000 kg
v_{\max}	Train maximum speed	80 km/h
$a_{c\max}$	Maximum acceleration	1.2 m/s ²
$a_{d\max}$	Maximum deceleration	-1 m/s ²
V_s	Substation DC voltage	750 V
R_s	Substation internal resistance	20 m Ω
R_d	Rail electrical resistance	9 m Ω /km
η_i	Efficiency of inverter	93%
η_m	Efficiency of motor	91.5%
η_g	Efficiency of gear	97.5%
V_{\max}	Voltage threshold for braking resistors activation	900 V

A screen capture of the DC traction power system model in MATLAB Simulink is shown in Figure 3.20 where it was combined with the train model shown in Figure 3.14 to analyse the power flow in the track. In the proposed model, the power rails were represented by two resistive lines, pertaining to the 3rd and 4th rail, denoting a feeder conductor and a return conductor. The rectifier substation was represented by a voltage source in series with an internal resistance and a diode to allow a unidirectional power flow.

The train model fed the power demand to the power system model before being divided by the contact voltage to get the train current demand that was injected to the current source representing the train. The measured track voltage affected the amount of energy exchanged between the trains and the amount of energy dissipated as heat in the braking resistors. For the purpose of simulation, the train was represented by an ideal current source to simplify the complexity of the regenerative braking model. This and other simplifications such as fixing the train weight and neglecting the track gradient and curvature resistances were made because the main objective of this work was to simulate the voltage and current profiles in the conductors in order to analyse the power flow and to develop a control system to maximise energy efficiency as will be discussed in the next chapters.

Figure 3.21 shows a closer look on the modelling approach used in this study to simulate a train equipped with a braking resistor in a housing on top of the train. In this simulation method, the trains were connected in parallel with braking resistors that were activated through switches when the trains contact voltages exceeded a predefined voltage threshold. The braking resistor represented by a diode was connected in parallel with the train to reduce the amplitude of voltage peaks when triggered. In this configuration, the contact voltage between the train and the rail track was sensed and, if the contact voltage exceeded the forward bias voltage that was 900 V, then the diode would short out the train by connecting the on-resistance that had a value of $0.1\text{ m}\Omega$ (reducing this value stopped the simulation due to failure of convergence), whereby all the regenerative power was dissipated. If the train contact voltage was below the forward bias voltage but was above the no-load voltage, then the train injected all of the braking power into the track as the diode off-resistance had a value of $1\text{ M}\Omega$ (increasing this value did not change the results). In the case considered here, the cut-off (forward bias) voltage was set to 900 V in order to correspond to high voltage constraints for a 750 V DC traction system as stated in Table 3.1. Thus, if the voltage to which a specific train was subjected was below the voltage threshold, then the train would operate normally and no intervention by the braking resistor would be required.

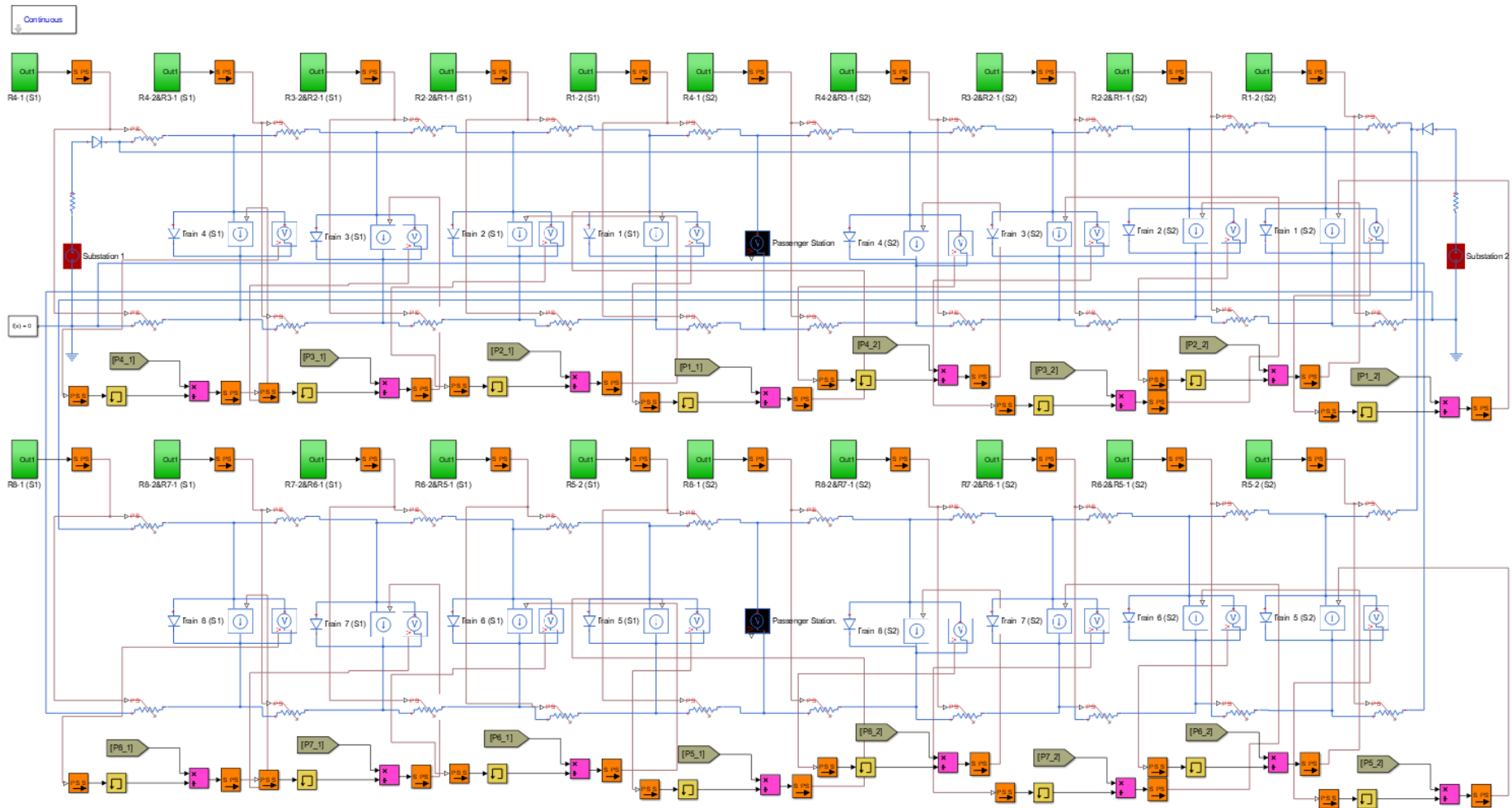


Figure 3.20: Screen capture of the power system model created in MATLAB Simulink

Where $R'_{dn}(t)$ is the electrical resistance in Ω between train n and the previous passenger station or the following train, $R''_{dn}(t)$ is the electrical resistance between train n and the next passenger station or the train ahead, R_d is the electrical resistance of the power rails, $d_n(t)$ is the distance in km travelled by train n which is time variant, and d_s is the distance between any two consecutive passenger stations, which was always 1 km. PS_2 represents the location of the passenger station ahead of train n and PS_1 represents the location of the passenger station that was most recently passed by train n . It is worth mentioning that, as $d_n(t)$ represents the travelled distance by train n between any two consecutive passenger stations, it can only vary from 0 to 1 km, and these fluctuations are replicated across all passenger station segments along the train journey. The travelled distance by a train that is running between train n and the passenger station ahead of train n is denoted by $d_a(t)$, and the travelled distance by a train that is running between train n and the last passenger station passed by train n is represented by $d_b(t)$. Figure 3.23 illustrates how Equations 3.11 and 3.12 are applied to train n when travelling between two passenger stations. In Figure 3.23 (b), $R'_{db}(t)$ represents the electrical resistance in Ω between train b and the previous passenger station PS_1 , which is calculated by the same concept provided in the first part of Equation 3.11. In Figure 3.23 (c), $R''_{da}(t)$ represents the electrical resistance in Ω between train a and the next passenger station PS_2 , which is calculated by the same concept provided in the first part of Equation 3.12.

It is worth mentioning that the resistance was varied to passenger station and not substation to allow Simscape to model a midpoint for connecting ESSs as will be investigated in the next chapter. That said, when varying the resistance with respect to Passenger Station A/C has the same meaning of varying the resistance with respect to Substation 1/2 as they share the same location. In the current study, Passenger Station B was located in the middle to allow measuring the voltage at the furthest point from the two substations. Further, in the Yizhuang Line there are 12 substations and 14 passenger stations where the substations are located at the passenger stations except for Wanyuan Passenger Station and Ciqu Passenger Station that do not share their locations with any substations, indicating that trains must accelerate at a far distance from substations causing high voltage drops [11].

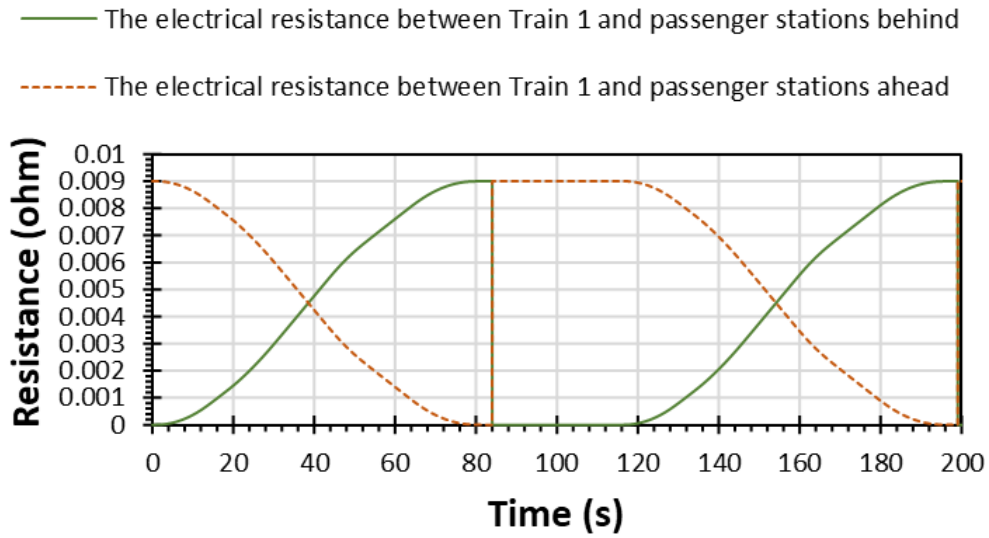


Figure 3.22: Electrical resistance between Train 1 and the passenger stations in the modelled double-track railway

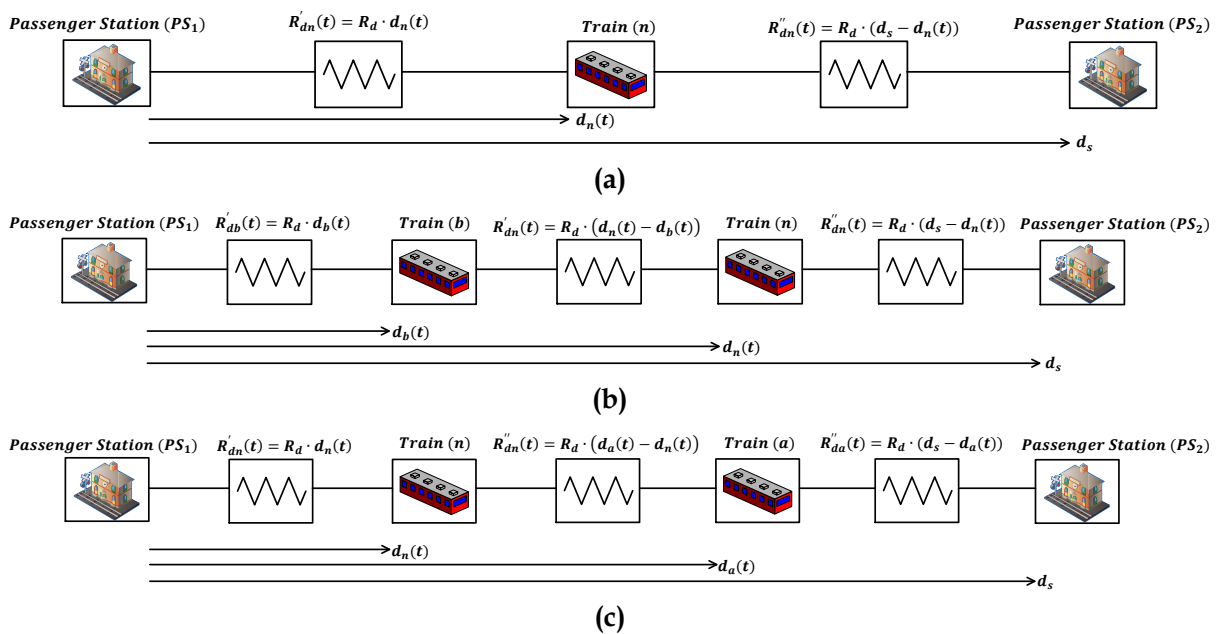
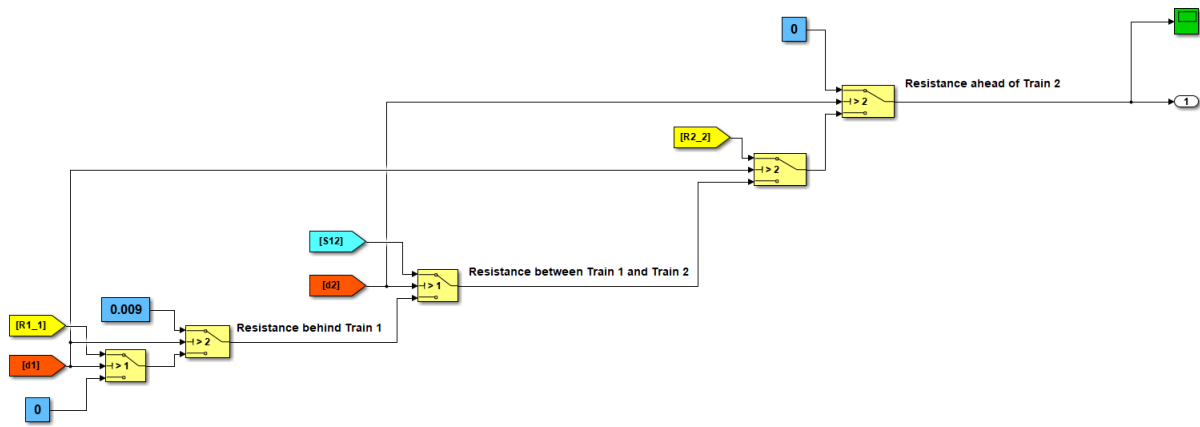
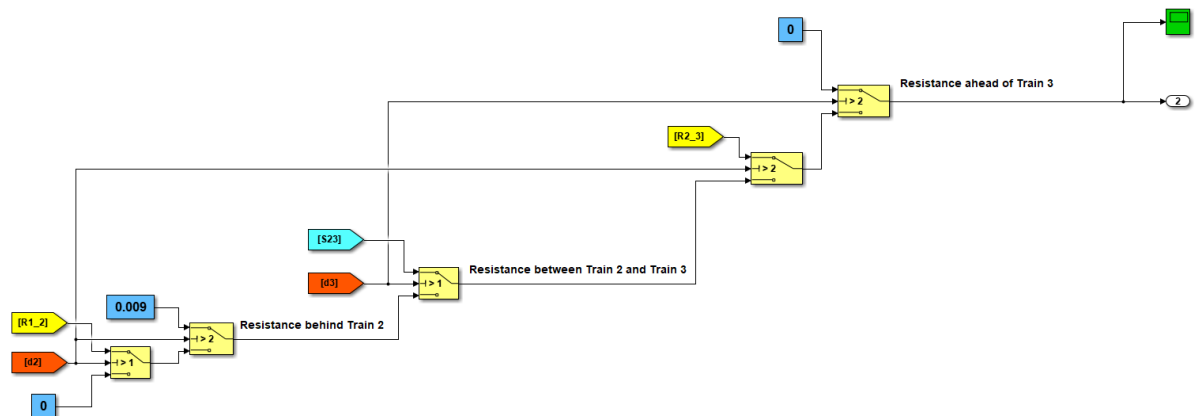


Figure 3.23: Calculation process illustration of the transmission line electrical resistance between two passenger stations when: (a) only train n is travelling; (b) a train is travelling behind train n ; (c) a train is travelling ahead of train n

In the simulations, the $R'_{dn}(t)$, and $R''_{dn}(t)$ values were injected into the variable resistors incorporated into the electrical model of the railway. The train model shown in Figure 3.14 was responsible for feeding the travelled distance by trains and meeting the power demand of the trains captured by the electrical model. Therefore, the train power demands and the electrical resistances between the trains were assumed to vary instantly. This variation with respect to time represented the train movements. However, the two substations and three passenger stations were stationary. A screen capture of how the electrical resistance was varied in the model when Train 2 travelled from Passenger Station B to C is shown in Figure 3.24.



(a)



(b)

Figure 3.24: Screen capture of the MATLAB Simulink model representing electrical resistance variation: (a) ahead of Train 2; (b) behind Train 2

3.4.5 Power system analysis

In this subsection, the power flow analysis based on the track voltage and interactions among multiple trains is presented in line with the previously described scenario. The number of trains travelling along the track from the beginning until the end of the simulation is as shown in Figure 3.25. During the on-peak periods (time periods when the track is highly congested with operating trains), four trains were operational, whereas this number declined to two during the off-peak periods (time periods when the track is less congested with operating trains). Thus, as the on-peak periods coincided with the middle portion of the simulation period, a high-power demand and good power utilisation were expected to occur due to the high traffic volume. On the other hand, as the beginning and end of the simulation period coincided with off-peak periods, high power losses in the braking resistors were expected.

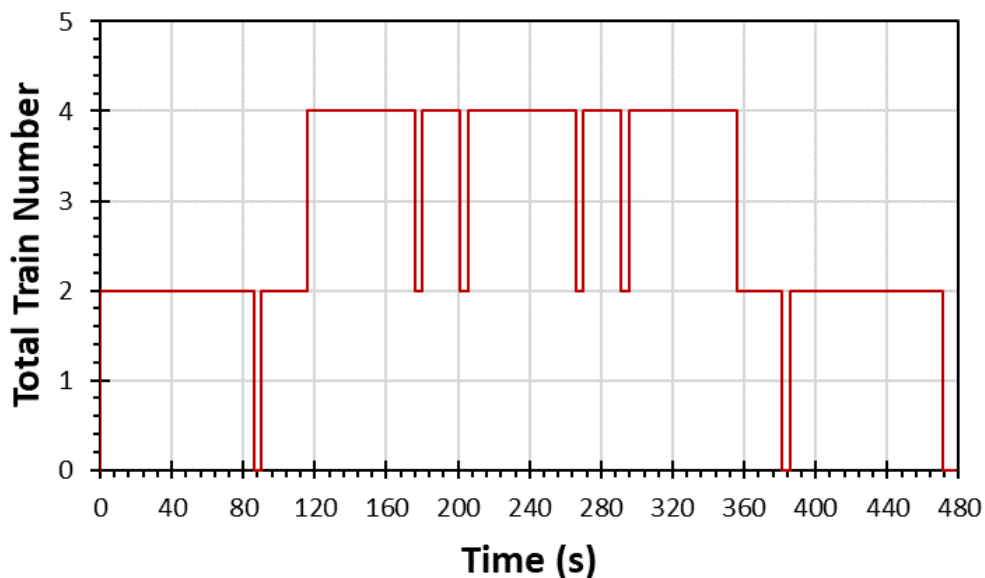


Figure 3.25: Number of trains running on a double-track railway during the simulation period

Since the load demand in the up and down line was identical, the substations behaviour should follow the same pattern. Voltage, current, and power values at the substations are depicted in Figures 3.26, 3.27, and 3.28, respectively. It is evident that voltages at the substations as well as those supplied to the operating trains were variable due to the changes in train location and power demand. It can also be observed that the substation voltages dropped below the nominal voltage when the trains accelerated in their vicinity due to supplying power. Thus, voltages below 500 V are highly problematic, as they can lead to the operational failure of the train. Moreover, to compensate for lower voltage, additional current must be supplied to meet the power requirements which results in high transmission losses. Consequently, when reaching this voltage threshold in railway systems, the train engines shut down because the power demand cannot be met by the traction substations. Voltage peaks above 900 V are undesirable as they cause the excess regenerative energy to be dissipated in braking resistors in the form of heat. This heat is particularly problematic in underground railways, as additional energy must be sourced for cooling. In practice, railway operators strive to avoid such fluctuations by varying headways to reduce the power peaks.

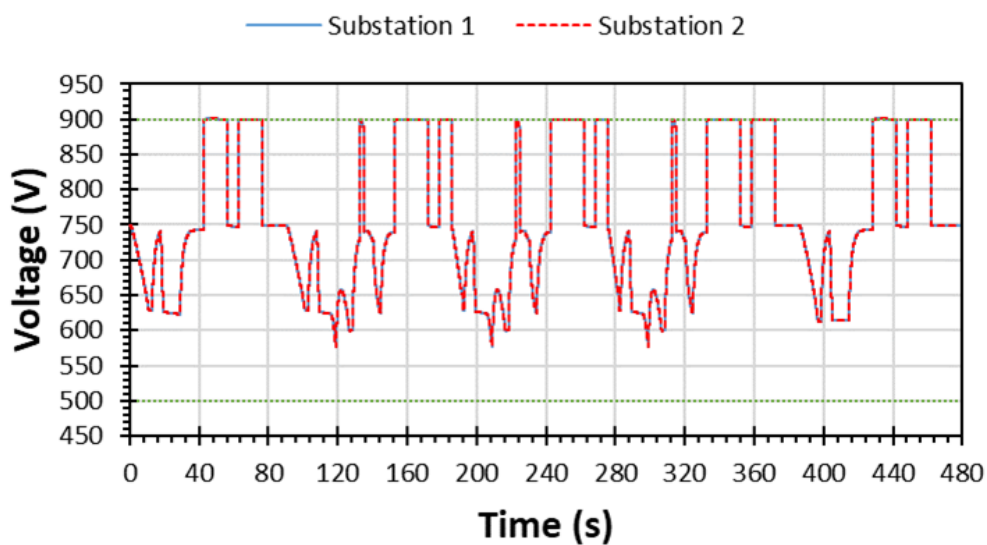


Figure 3.26: Voltage at two studied substations on the modelled double-track railway system

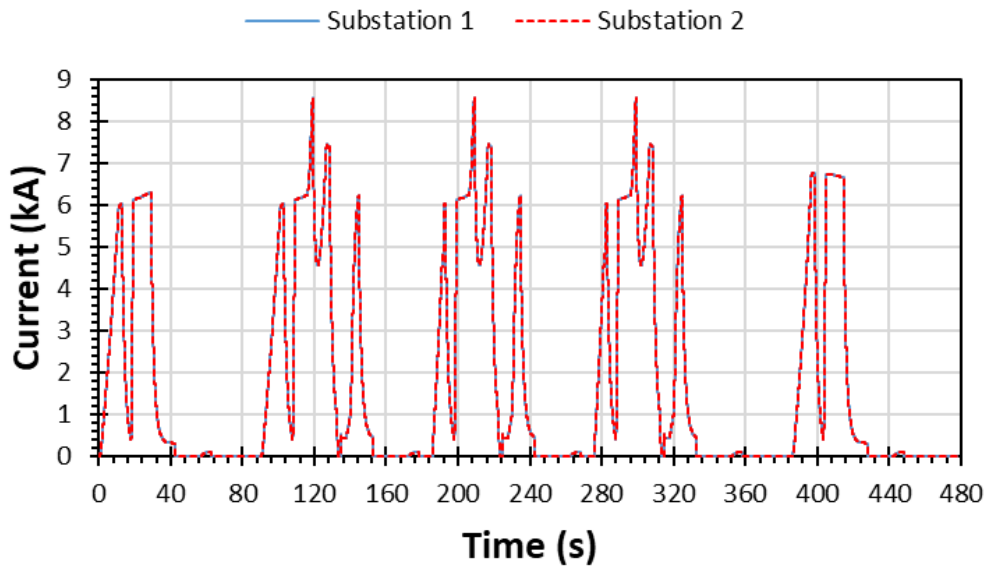


Figure 3.27: Substation currents of a double-track railway represented by the simulation model

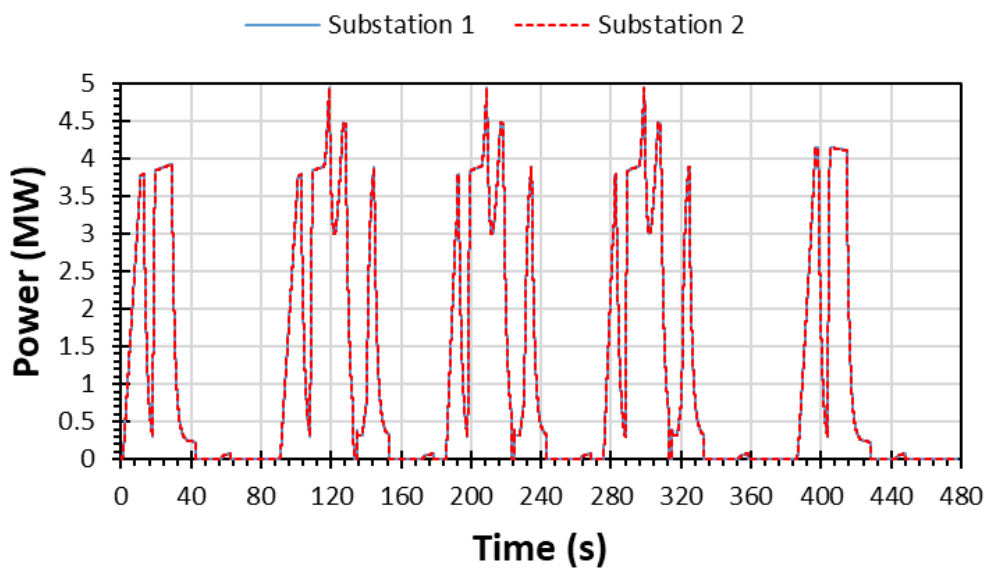


Figure 3.28: Substation power of the modelled double-track railway

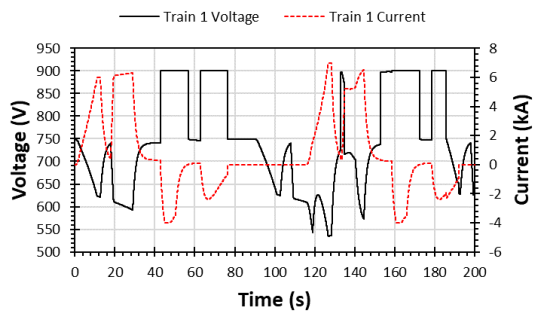
The energy consumption of a substation is calculated by integrating the power of that substation with respect to time as follows:

$$E_s = \int_0^T I_s \cdot V_s dt \quad (3.13)$$

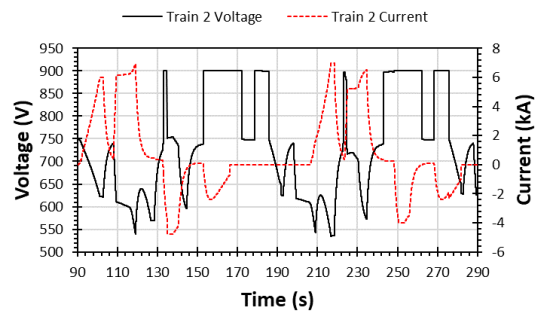
where E_s is the substation energy consumption, I_s denotes the current supplied by the substation, V_s represents the substation voltage, and T is the total simulation time. The peak power demand P_{i-peak} of the i^{th} substation is calculated by applying Equation 3.14, where P_i represents the power demand of the i^{th} substation. Based on these calculations, the two substations had the same peak power demand of 4.95 MW, which is less than the rated power of 6 MW, and they had an identical total journey energy demand of 157.9 kWh.

$$P_{i-peak} = \max \{P_i\} \quad (3.14)$$

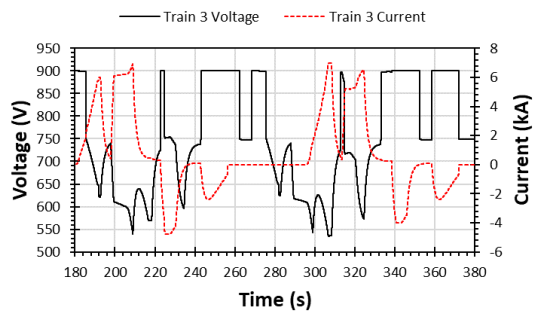
The voltages to which all eight trains were subjected during the simulation period and their current demands are displayed in Figure 3.29. Rapid changes in voltage level were induced by the fluctuations in power demand and by the location of individual trains as well as their interactions. Moreover, high transient currents caused by braking and traction further increased the voltage fluctuations. In the braking mode, the train voltages exceeded the no-load voltage at the substations before the braking resistors were activated to control for this deviation once the 900 V threshold was reached. It is worth noting that, in traction mode, the train voltages did not drop below the minimum system voltage. It is evident that, high voltage drop occurred when trains started accelerating at a track location that was equidistant to the two consecutive substations. In periods when more than one train were operational, their respective voltages were not solely governed by their individual mode of operation and position on the track, but also on that of other trains.



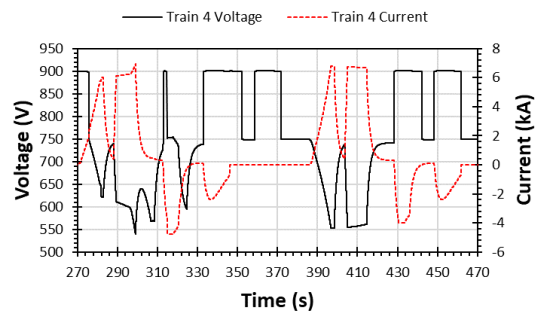
(a)



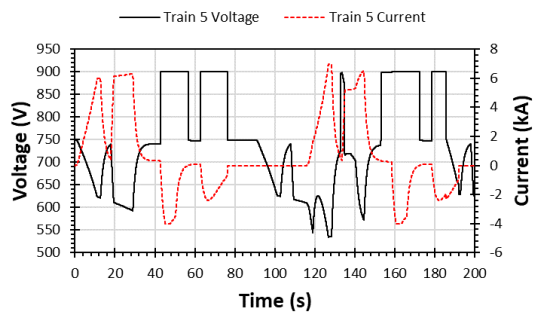
(b)



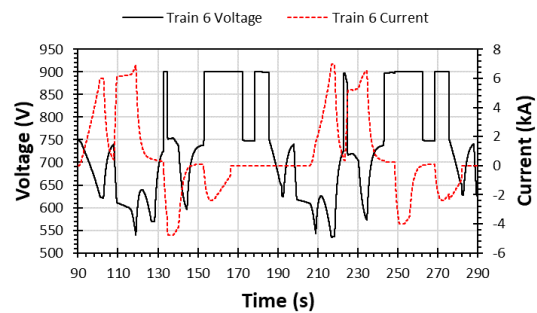
(c)



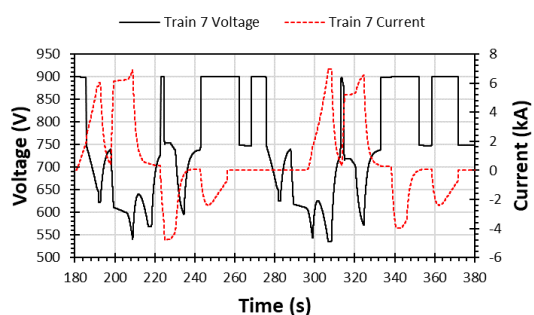
(d)



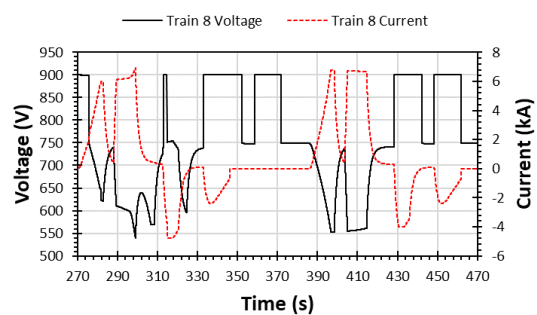
(e)



(f)



(g)



(h)

Figure 3.29: Voltages and currents of individual trains on the modelled double-track railway: (a) Train 1; (b) Train 2; (c) Train 3; (d) Train 4; (e) Train 5; (f) Train 6 (g) Train 7; (h) Train 8

The unused braking energy of each train is shown in Figure 3.30 and it is calculated via the following expression:

$$E_{br} = \int_0^T I_{br} \cdot V_{train} dt \quad (3.15)$$

where E_{br} is the dissipated energy in the braking resistor of the train, I_{br} is the current passing through the braking resistor, and V_{train} is the train voltage that is 900 V when activating braking resistors.

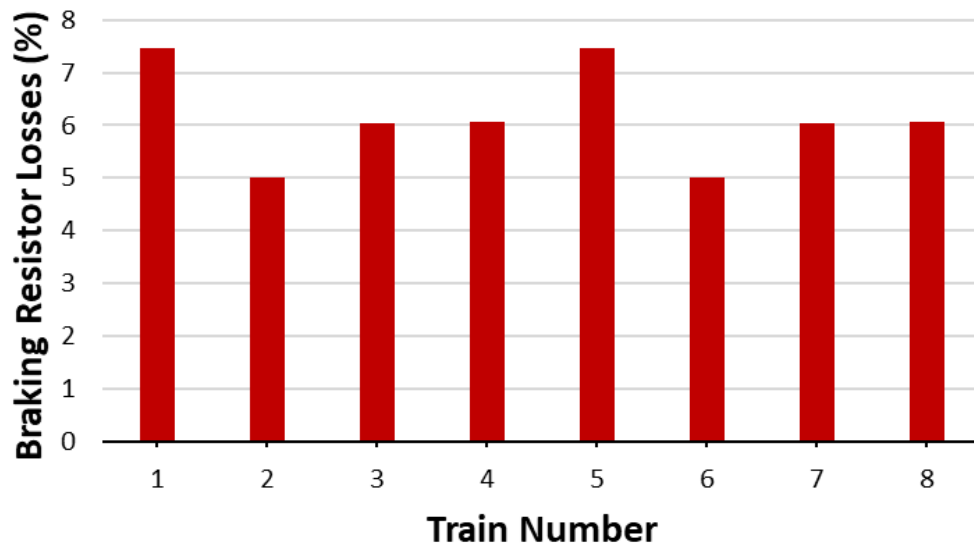


Figure 3.30: Dissipated energy in the braking resistors of the eight trains as a percentage of the substations energy consumption when the headway was 90 s

3.4.6 Power utilisation discussion

Effective power exchange between the running trains can reduce the power consumption of the rectifier substations. Based on the simulation results, it can be deduced that greater power exchange occurs when the headway between the trains is shorter. To examine this phenomenon further, different traffic scenarios were considered, whereby the headway duration varied, and its impact on energy exploitation was assessed. The quality of power exchange in the railway system was examined in terms of the utilisation factor $\eta_{utilisation}$ indicating that the ratio of utilised braking energy and the total braking energy as follows:

$$\eta_{utilisation} = \frac{\Sigma E_r - \Sigma E_{br}}{\Sigma E_r} \cdot 100\% \quad (3.16)$$

where ΣE_r is the total regenerative energy supplied by the decelerating trains and ΣE_{br} is the total dissipated braking energy in the braking resistors of all trains in operation.

The receptivity of the railway line, which is defined as the capability of trains to accept the available regenerative energy provided by decelerating trains, is shown in Figure 3.31. When simulating the 2 km railway track with a 70 s headway, a 37.6% $\eta_{utilisation}$ was obtained, suggesting that, due to the high train circulation, minimal energy was wasted. This dissipated energy was considered minimal because it was stated in [10] that in practical cases only 35% of the regenerative energy can be utilised in the best case scenario. In the second scenario considered in this investigation, the headway was increased to 90 s, due to which $\eta_{utilisation}$ declined to 27.6%. Unsurprisingly, when the headway was increased to 190 s, the $\eta_{utilisation}$ declined significantly to 0.1% as the available regenerative power could no longer be timely utilised by the accelerating trains. It can thus be concluded that increasing the headway reduces the potential for a power exchange between the trains, which increases the losses in the braking resistors as the regenerative power produced by the braking trains cannot be supplied to other trains demanding power. This assertion is confirmed by the graph shown in Figure 3.32, depicting the total wasted energy during braking in the on-board braking resistors as a function of different departure intervals for one complete cycle.

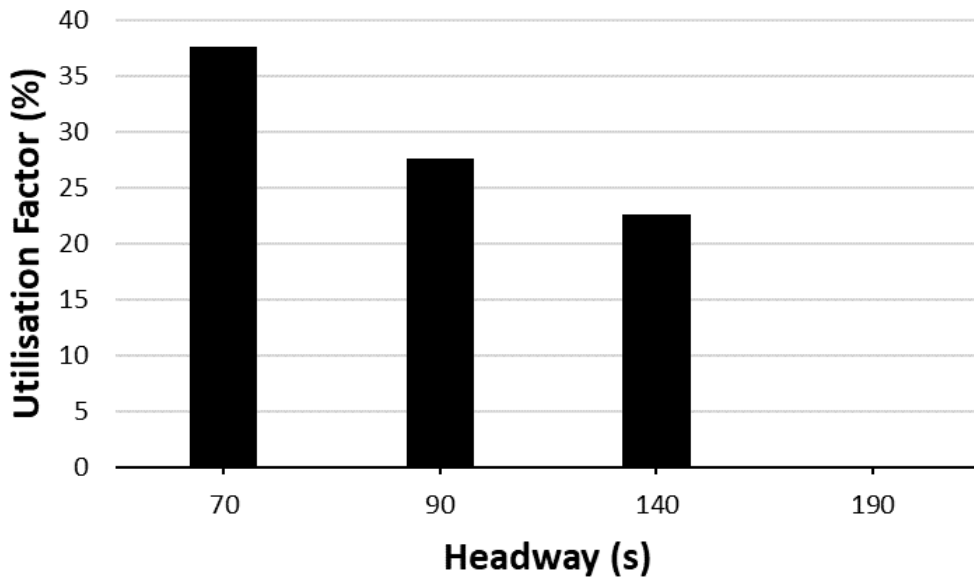


Figure 3.31: The double railway line receptivity as a function of headway duration

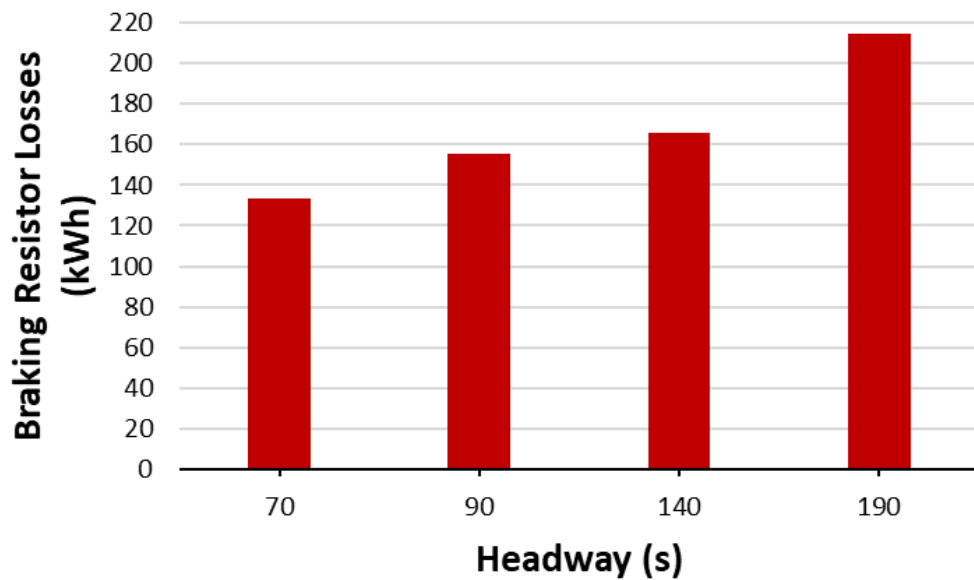


Figure 3.32: Total energy dissipated through the on-board braking resistors of the trains running on a double-track railway as a function of headway duration

These findings demonstrate that the likelihood of a power exchange between simultaneously braking and accelerating trains is higher for short headways than for long headways due to the presence of a greater number of trains on the same section of a short track. It is worth noting that, in DC electric railways, it is common to

consider short electrical sections as this would minimise the voltage drop. A strong positive relationship between headway length and energy demand observed in the present study aligns with the previously reported results [125], [126]. However, this finding cannot be generalised as, for example, if all trains start accelerating and decelerating simultaneously, then the energy dissipated in the on-board braking resistors will be high, significantly reducing the utilisation factor even if the headway is short. It is also worth noting that very short headways may cause safety issues due to the small gap between trains, whereas long headways would increase the number of passengers on-board each train causing passenger inconvenience, and increase the journey time that might not meet the operation requirement. The minimum safe distance in Beijing Metro is 100 m while it is 400 m in the London Underground. Minimising the distance between trains is one of the reasons for the Beijing Metro to be punctual in meeting the timetables. The punctuality rate in Beijing Metro is 99% where trains are counted to be punctual if they arrive within 1 minute from the scheduled time, while there are no fixed timetables in the London Underground to measure punctuality. Due to these practical considerations, changing the headway to save energy is constrained [127].

3.4.7 Model verification

Before assessing the effect of integrating ESSs into the double-track system in the next chapter, it is essential to verify the model proposed as a part of the present study. The simulation model presented in the preceding sections was verified using a number of methods. As previously noted, the track was 2 km length where the electrical resistance of the track section was calculated by multiplying the section length with the electrical rail resistance per km ($2 \text{ km} \cdot 9 \text{ m}\Omega/\text{km} = 18 \text{ m}\Omega$). To facilitate modelling, the transmission line between each two consecutive substations was represented by a series of resistors with different values depending on the locations of the individual trains. However, as the total electrical resistance of the section of the rail track should always be equal to 18 m Ω , this was the constraint imposed on the

equations adopted to determine the electrical resistance difference between the trains as well as between the trains and passenger stations. In other words, the sum of those resistances should always be $18\text{ m}\Omega$, irrespective of the individual train locations. It was confirmed during the simulation that the sum of the electrical resistances in each electrical section was maintained at $18\text{ m}\Omega$ irrespective of the network configuration variation.

Moreover, the proposed model was verified by comparing the voltage measurements at the train locations and passenger station locations with respect to time. Given that the passenger station locations are fixed, their positions along the track can be used to check the voltage measurements of the relative positions of trains as they progress on their journeys. As trains need to follow a predetermined timetable, the passenger station and train voltages should coincide when a particular train is located at a certain passenger station. This verification approach is beneficial because even though the passenger stations are stationary and the trains are in motion, when a train reaches a specific passenger station, their respective voltages should match. From the data reported in Table 3.5, it can be deduced that Train 1 and 5 reached Passenger Station B at 84 s. During their dwell period of 30 s, an identical voltage should be measured at both the passenger station and trains, which is the case as shown in Figure 3.33. Similarly, Figures 3.34, 3.35 and 3.36 confirm a match between the passenger station voltage and the train voltages when the trains were at the passenger station. As previously stated, in this scenario, the train characteristics and operational cycles were assumed to be the same. The graph shown in Figure 3.18 illustrates that Train 1 and Train 5 started and finished their journeys at the same time, but at different locations since they travelled in opposite directions. Correspondingly, Train 2 and Train 6 started and finished at the same time, and so on. As a result, each pair of trains that had the same start, stop, and dwell time should be subjected to the same voltage as illustrated in Figure 3.33–3.36. It is noteworthy that, despite the highly dynamic behaviour of the electric railway in the model, high accuracy of voltage calculation was achieved.

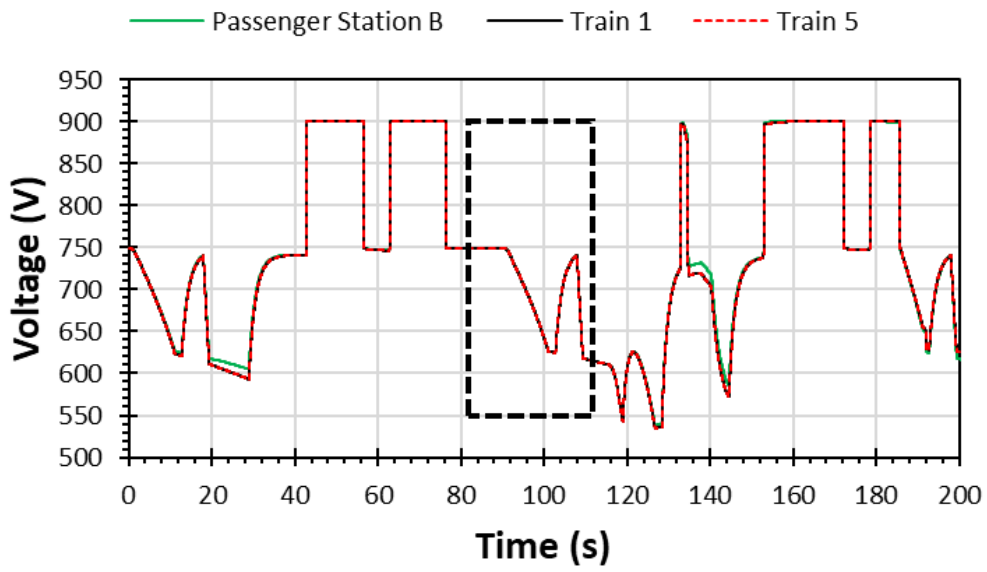


Figure 3.33: Passenger Station B, Train 1, and Train 5 voltage as a function of time

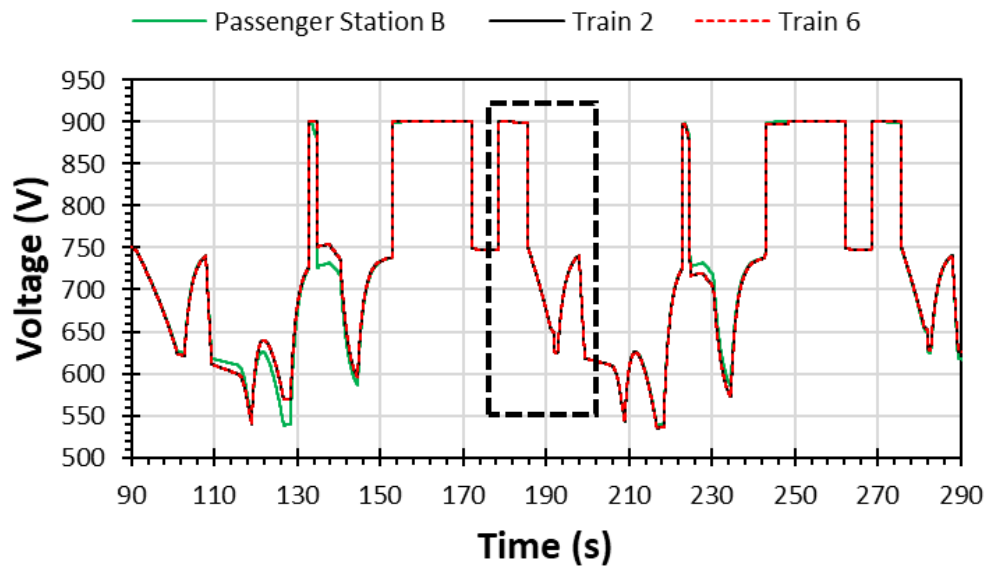


Figure 3.34: Passenger Station B, Train 2, and Train 6 voltage as a function of time

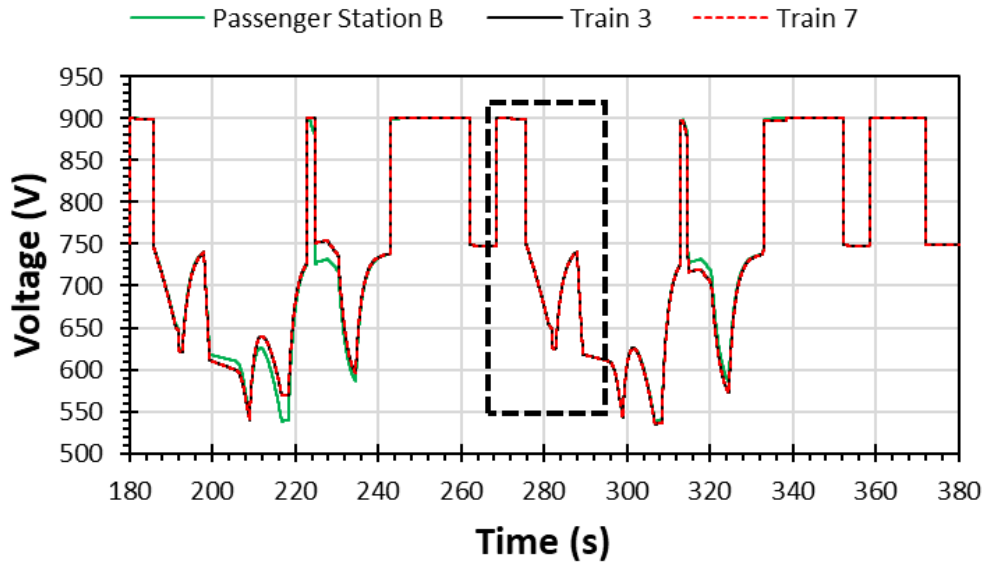


Figure 3.35: Passenger Station B, Train 3, and Train 7 voltage as a function of time

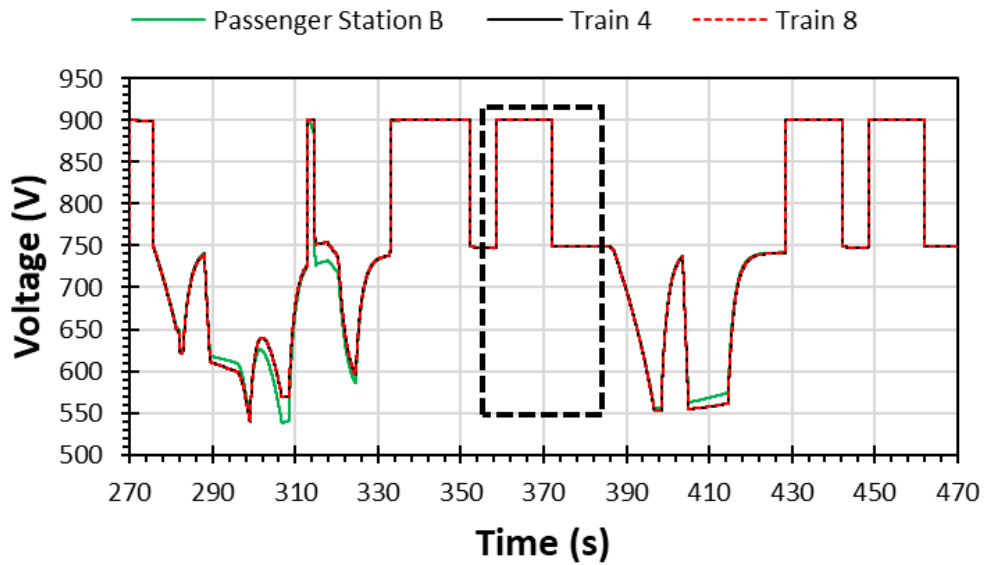


Figure 3.36: Passenger Station B, Train 4, and Train 8 voltage as a function of time

Finally, the model was also verified by comparing the total power generation and the total power demand, which should be equal in each cycle. In other words, the sum of the output energy of the two substations and the regenerative energy of all operational trains should be equal to the energy consumption by all trains on the track and the total losses in the system, as shown below:

$$\sum E_s + \sum E_r = \sum E_t + \sum E_{line\ losses} + \sum E_{br} \quad (3.17)$$

where $\sum E_s$ is the total energy supply of all substations, which is the time integral of the power profiles shown in Figure 3.28; $\sum E_t$ is the total traction energy of trains; and $\sum E_{line\ losses}$ denotes the total energy losses in the 3rd and 4th rail. The railway system energy consumption and losses per journey are reported in Table 3.7, indicating that the two sides of Equation 3.17 are equal. There is a small error of 0.11% which is attributed to the transients created by the switches incorporated in the simulation model.

Table 3.7: Energy consumption and losses in the modelled double-track railway

Energy supply		Energy consumption		
$\sum E_s(kWh)$	$\sum E_r(kWh)$	$\sum E_t(kWh)$	$\sum E_{line\ losses}(kWh)$	$\sum E_{br}(kWh)$
315.83	214.4	358.67	15.83	155.14
$\sum E_s + E_r = 530.23$		$\sum E_t + E_{line\ losses} + E_{br} = 529.64$		
$Error = \frac{530.23 - 529.64}{530.23} \times 100 = 0.11\%$				

3.5 Conclusion

The purpose of the work presented in this chapter was to develop an electrical model that describes the effect of a multi-train operation on an electric DC railway system. The train and rail track characteristics were assumed to be variable and they needed to be updated at each time step. The effect-cause modelling method was used where the data pertaining to individual trains were considered to be the inputs into an existing electric railway power system. A mechanical model was coupled with the electrical model to provide the inputs necessary for determining the power flow in the traction power system as a function of time. The proposed simulation method is sufficiently simple to be of high practical value, while being accurate and adaptable to changes in the circuit configuration. The model was simplified to provide an

understanding of the power and energy requirements of metro systems to enable the design of control techniques for energy management using ESSs.

In this chapter, a test scenario was presented comprising of eight trains running on a double rail track in order to verify the model against expected observations. The simulation model included two DC traction substations separated by 2 km and three passenger stations separated by 1 km. The model operation requirements and parameters were based on the Yizhuang Line in Beijing Metro. The proposed test scenario allowed the model to be verified for accuracy and is used in the remainder of the work in this thesis. The verification was accomplished via different methods and the obtained results confirm that the proposed modelling approach is accurate as the error between the supplied and consumed energy was only 0.11%. This model can support the integration of ESSs and therefore will be used in the subsequent chapters to investigate energy storage in railway systems and to design advanced control techniques.

Chapter 4

Voltage Control Sensitivity Analysis for a DC Electric Railway with Energy Storage

4.1 Introduction

Increasing power exchange between trains in DC electric railways is an effective method of improving their energy efficiency, as the regenerative power of a braking train is passed to other trains that require additional power. However, this regenerative braking power can only be utilised if adjacent trains are in traction mode. Moreover, a power mismatch (difference between the regenerative and traction power) or a great distance between trains reduces the energy utilisation in the railway line, as most of the regenerative power is dissipated as heat either in the braking resistors or as losses in the conductor rails. As pointed out in the literature review, incorporating ESSs into electric railways can improve their performance and reduce the dissipated energy. However, it will be shown in this thesis that employing ESSs in electric railways could also have a negative impact since they could increase transmission losses, resulting in reduced energy efficiency of the railway system. Moreover, it will be shown that the ESS control method could significantly affect the impact of the ESS on the energy efficiency maximisation. In this study, the power flow between a double railway line and a stationary ESS was accomplished via a controller that regulated charging/discharging based on track voltage. The tests conducted and presented in this chapter aim to analyse and assess the sensitivity of an electric railway to ESS voltage control for the purpose of maximising its energy efficiency. Therefore,

the aim of this chapter is to extend the electric railway model presented in Chapter 3 by including ESS to demonstrate that ESS provides operating benefits to a railway system and that these benefits can be maximised by careful selection of operating parameters.

4.2 Modes of power exchange between a DC electric railway and a stationary ESS

This section explains the modes of interaction between a DC electric railway with multiple trains and a stationary ESS:

- (a) The regenerative power is divided between the running trains, ESS, and on-board braking resistors. This scenario applies when decelerating trains regenerate more power than is needed by adjacent trains in traction power demand or they decelerate at a significant distance from accelerating trains. Simultaneously, the ESS charges at its maximum current/power or it is located far from the braking trains, which reduces the power it receives.
- (b) A portion of the regenerative power is consumed by the running of other trains on the same section; the remaining power charges the ESS. This occurs when train voltages are less than the voltage threshold that activates the braking resistors.
- (c) Running trains and braking resistors consume the braking power. Here the ESS is full or charging at a voltage threshold higher than the measured voltage. The braking resistors are activated because the braking trains regenerate power more than that required by the running trains or they brake at a significant distance from the running trains resulting in the voltage threshold being reached.

- (d) A portion of the regenerative power is passed to the ESS, and the remainder is dissipated through the braking resistors. This scenario applies when no accelerating trains are available in the section of track and the ESS is charging at its maximum current/power limit or is located far from the braking trains.
- (e) All of the regenerative power is dissipated in the braking resistor system. Here there are no trains in power demand on the track section while the ESS is full or has a charging voltage setpoint higher than the measured voltage at the terminals.
- (f) All of the regenerative power is consumed by accelerating trains. This scenario occurs when braking trains regenerate power that is less than or equal to what is needed by running trains, which should demand power from a nearby location to braking trains. Simultaneously, the ESS is fully charged or has a charging voltage setpoint higher than the measured voltage at the terminals.
- (g) All of the regenerative power is stored in the ESS, which occurs when charging the ESS requires less than the maximum current/power and is located close to decelerating trains. Simultaneously, no trains in traction power demand are available on the track.

4.3 Energy storage system model

The power flow control between the ESS and the track was achieved with a bidirectional DC/DC converter, as shown in Figure 4.1, and the ESS output and input power was controlled via a voltage controller, as depicted in Figure 4.2. The ESS was charged if the track voltage (V_a) was higher than or equal to the charging voltage threshold (V_{ch}) and discharged if the track voltage was lower than or equal to the discharging voltage threshold (V_{dis}). The ESS was in standby mode if the sensed voltage at the terminals was within the charging and discharging limits. The maximum charging and discharging current limits are denoted as I_{ch} and I_{dis} ,

respectively, with the coefficients k_c and k_d denoting controller gains. The ESS current δ represents the current before applying the ESS current limits I_{ch} and I_{dis} where it is calculated by summing the controller actions δ_c and δ_d representing the initial charging and discharging currents, respectively. The ESS current increased linearly with the voltage deviation until the maximum current of ESS was reached. The charging current was proportional to the voltage deviation between V_a and V_{ch} while the discharging current was proportional to the voltage deviation between V_a and V_{dis} .

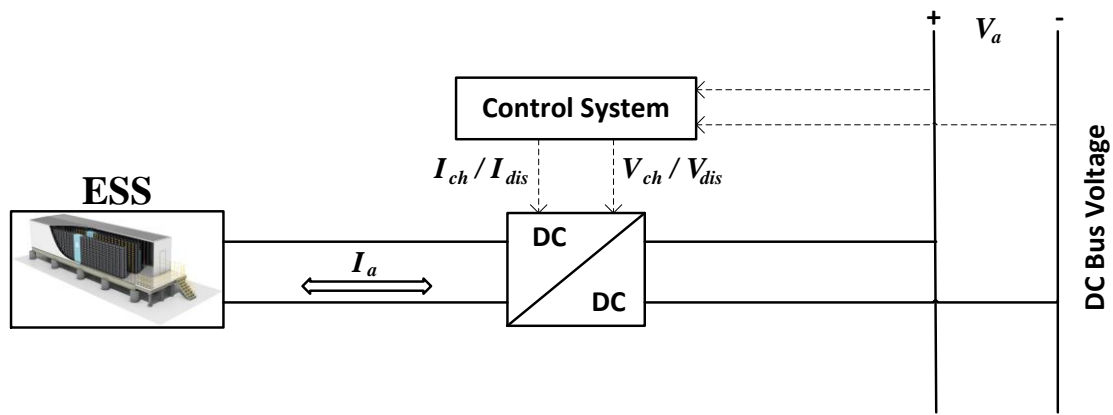


Figure 4.1: Charging and discharging process

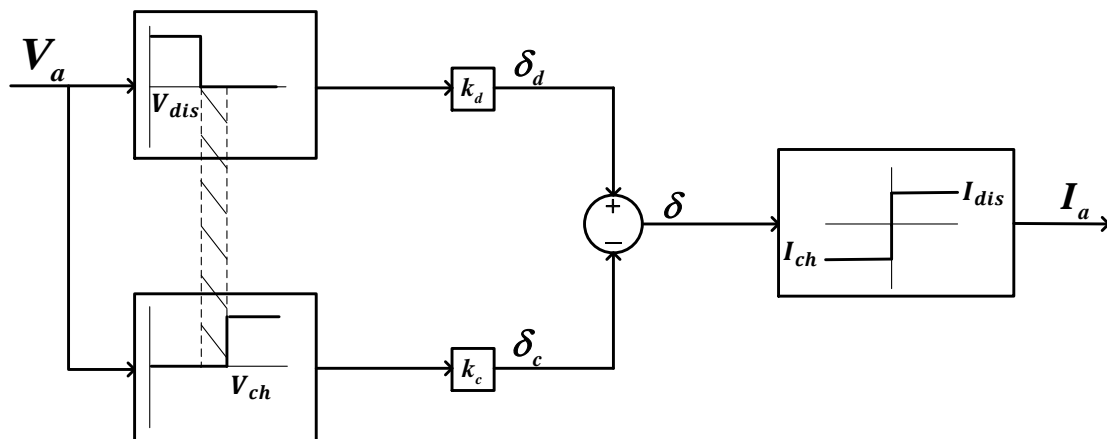


Figure 4.2: Voltage control method

Figure 4.3 shows the ESS model used in this study, which was represented by an ideal current source with no internal losses. In other words, the ESS was lossless

and did not include any internal losses. The power conversion was considered to have 95% efficiency as this is the typical efficiency of DC/DC converters as reported in [100], [128]–[131]. The representation of the ESS as an ideal current source was adopted in [100], [101], [130]–[139] to simplify solving the power flow. Since the ESS was ideal and its type was not specified, operation within 100% and 0% SOC boundaries were imposed. As recommended by the authors of [6] the initial SOC was set to 50% to allow equal capacity of the ESS to be used for storing the available braking energy and delivering the traction energy demand, which minimises the possibility of running out of capacity when experiencing uncertain load demands. The ESS size was set to 400 Ah (see Figure 4.4) to avoid running out of capacity during the journey when experiencing high traffic density (70 s headway), moderate traffic density (90 s headway), and low traffic density (190 s headway). These three traffic scenarios were discussed in Section 3.4.6. It is worth mentioning that the journey is complete when the trains in the up line finish travelling from Passenger Station A to C and those in the down line finish travelling from Passenger Station C to A, which is explained in Section 3.4.2. Figure 4.4 shows that the ESS did not reach the energy capacity limits during one operating cycle (complete journey) when experiencing the worst-case scenario of being only charged or discharged. The energy stored in Ah was calculated by accumulating the hourly current input and output of the ESS represented by a current source before being added to the initial stored energy in Ah. The ESS size was increased in steps while measuring the ESS charged/discharged energy with respect to multiple traffic scenarios. Once the increase in sizing was constant and the increase in the ESS charged/discharged energy was negligible then the ESS size was deemed acceptable, which was decided to be 400 Ah in this study as shown in Figure 4.4. The ESS sizing methodology was limited to only one journey as it was assumed that the worst-case scenario cannot remain for the rest of the day and proper selection of voltage thresholds would reduce the situation of reaching capacity limits as will be explained later in this thesis. It is worth mentioning that this sizing methodology is not cost effective and applying advanced control methods can reduce the ESS size without compromising on the ESS benefits as will be explained in Chapter 5.

To maximise the use of the ESS, the current limits I_{ch} and I_{dis} were set to 6300 A that was never reached when simulating the high, moderate, and low traffic density, meaning that increasing the current limits beyond this value did not import/export extra power. In other words, the ESS was initially applied without any current limits and simulated under multiple traffic scenarios and installation locations, before it was noticed that the current never exceeded the value of 6300 A that was then decided to be the maximum current limit in this study. The charging voltage threshold was set to 755 V and the discharging voltage threshold was set to 745 V. When the measured voltage was between 755 and 745 V it was considered to be in the dead-band zone that was set to comply with the data presented in [140] – [142]. In a real-world application, this dead-band zone is used to avoid continuous switching between charging/discharging and standby modes resulting from fluctuation in the no-load voltage. The sensitivity of the railway system to voltage thresholds is discussed in the next section. The gains of the controller k_d and k_c were set to 53 as this was the maximum value that ensured the stability of the system. Figure 4.5 shows that increasing the controller gains from 53 to 54 destabilised the system by causing voltage oscillation that was considered a perturbation to the control system. The other option for analysing the stability of the system was by providing a mathematical model for the whole system before performing eigenvalue analysis. However, the method of examining the model response when changing controller gains was adopted because the model was not represented mathematically in this study. The traction system considered in this study is a double DC electric railway representing a metro system as discussed in Chapter 3.

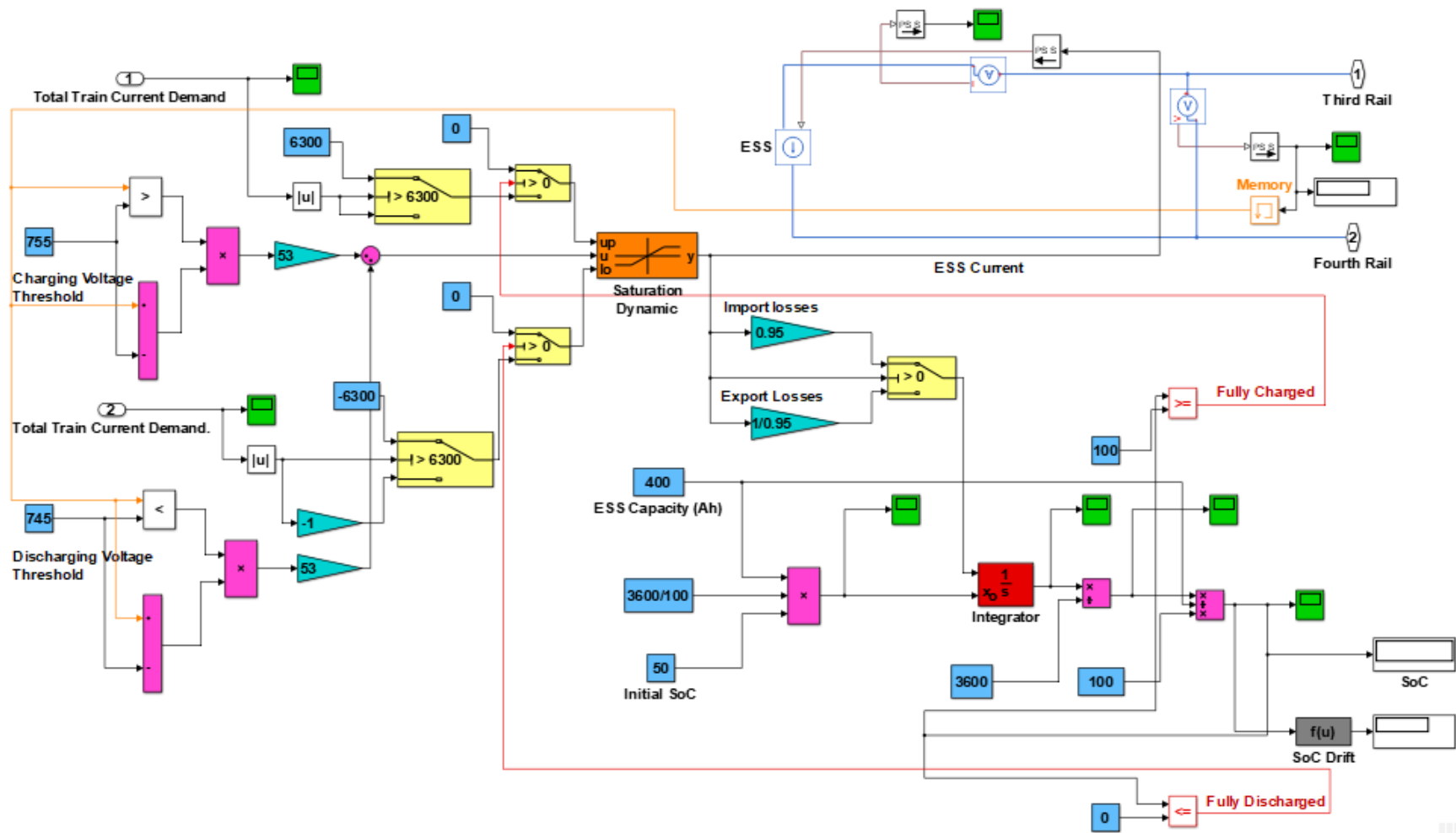


Figure 4.3: Screen capture of an ESS modelled in MATLAB Simulink

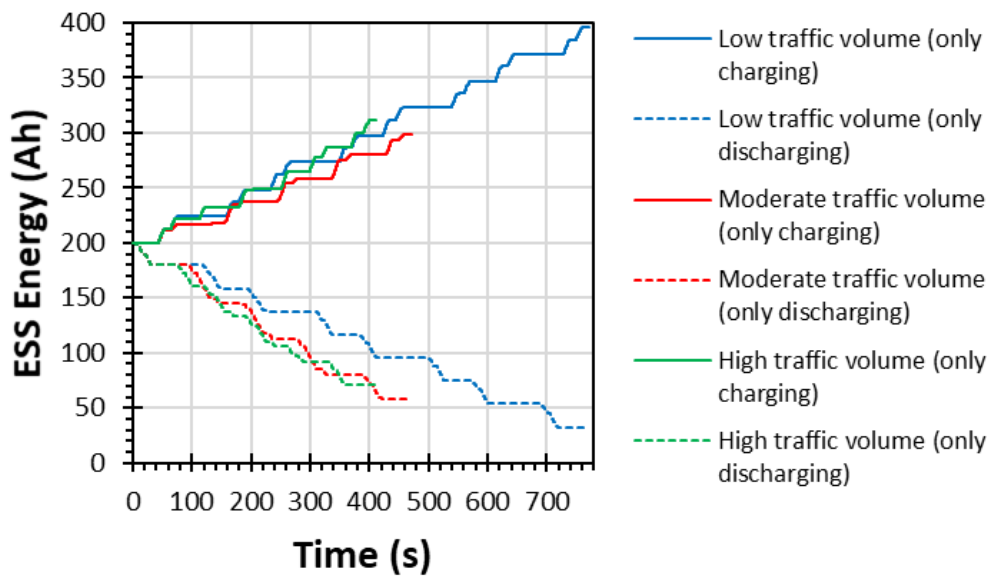
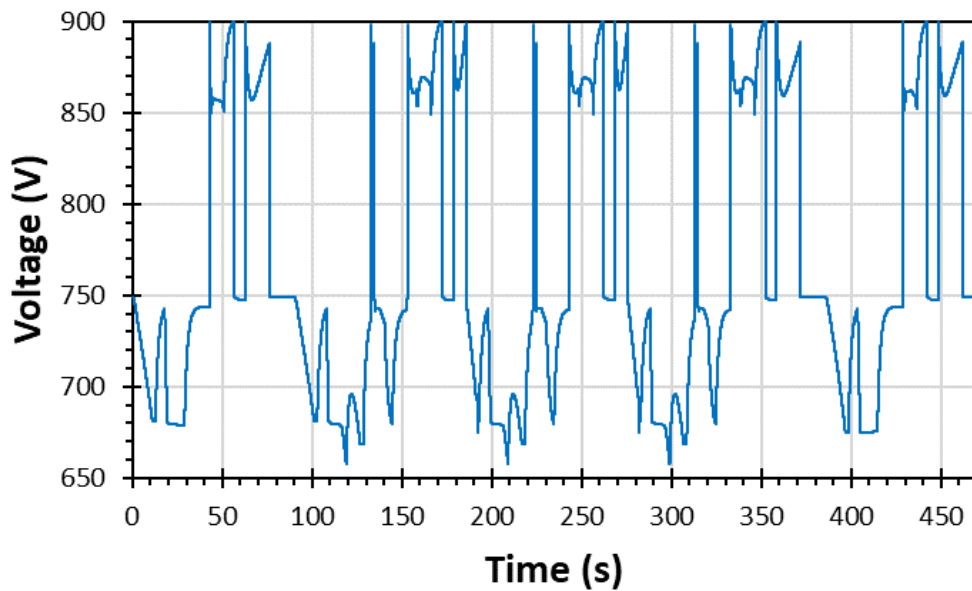
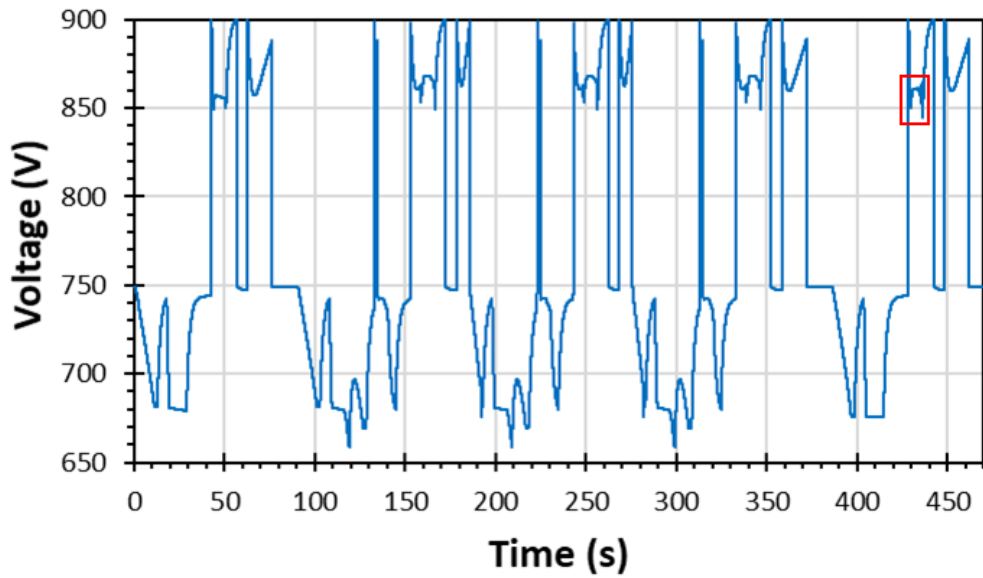


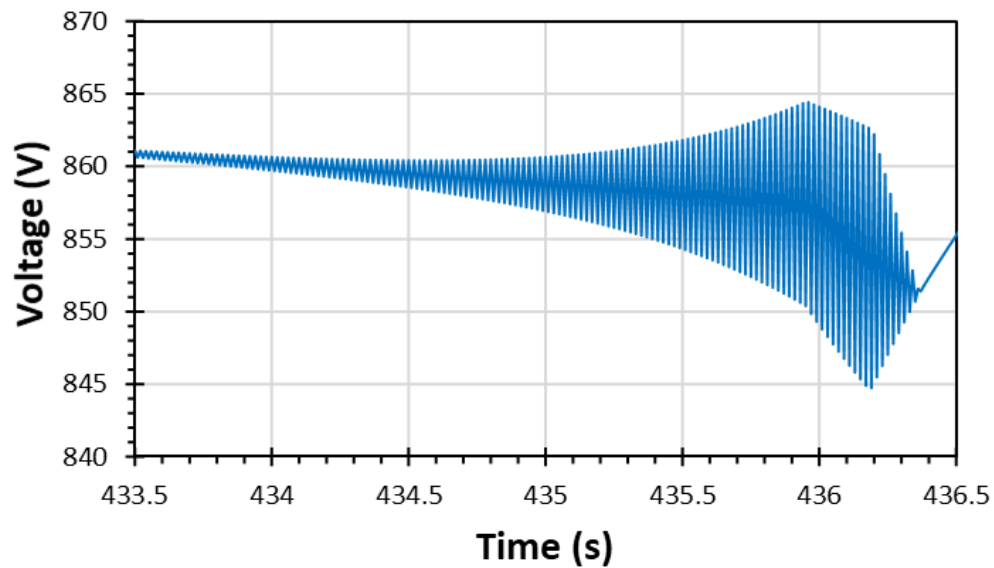
Figure 4.4: Sizing an ESS when located at Passenger Station A and subjected to different traffic scenarios



(a)



(b)



(c)

Figure 4.5: Voltage at Passenger Station A when connecting an ESS with 400 Ah capacity, 6300 A current limit, and : (a) 53 controller gain; (b) 54 controller gain; (c) 54 controller gain when the voltage is Zoomed in

4.4 Voltage sensitivity analysis

One of the aims of this study was to determine the sensitivity of railway energy efficiency to voltage control; as such, voltage control limits are investigated in this

current section. Specifically, the factors that determine the appropriate voltage limits are examined by studying the effects of modifying voltage limits in phases while testing the effect of this change on the railway energy efficiency. The results of this analysis are then compared with those of a railway system that does not incorporate an ESS. The analysis in this section is based on one journey, which is complete when trains finish travelling from Passenger Station A to C in the up line and vice versa in the down line simultaneously. All analyses presented in the following sections were carried out using MATLAB software. The solver type in MATLAB was set to ode14x with a time step of 30 ms. The time step was increased from 10 ms to 30 ms to reduce the simulation time from 50 minutes to 30 minutes approximately. The error was only 1% compared to that when using 10 ms. This action was taken due to the high number of repeated simulations to complete the sensitivity analysis in this Chapter. The simulation was repeated 540 times when varying the charging and discharging voltage thresholds with respect to two locations of the ESS installation.

4.4.1 Substation energy demand

This study calculated the reduction of Substations 1 and 2 energy demand as a percentage of the difference between the maximum traction energy of the two substations for one typical operation cycle for the system with and without an ESS. The energy demand of the two substations without the ESS was 315.83 kWh. Figure 4.6 illustrates the impact of incorporating the ESS at Passenger Station A, indicating that increasing the discharging voltage threshold reduced the energy demand in the substations while varying the charging voltage threshold had no impact. The substations were not sensitive to the charging voltage threshold modification because of their unidirectional behaviour, which inhibits their ability to absorb regenerative power. The highest impact of 29.77% was achieved at $V_{dis} = 745 V$ due to the ESS early involvement in supplying power to accelerating trains. This result is consistent with the studies provided in [47], [89], [142] that reported that stationary ESSs can save up to 30% of the substations energy demand in a metro system.

Figure 4.7 shows the impact of incorporating the ESS at Passenger Station B. Notably, when the ESS was placed equidistant from the substations, the same relationship between the substation energy consumption and the voltage threshold variation was achieved whilst saving more energy relative to Passenger Station A's location. For instance, the highest impact of 31.72% was achieved when discharging at 745 V. This improvement in reducing the substations energy demand compared to when the ESS was positioned at Passenger Station A's location was due to the ESS feeding power over a short distance from the load demand, which was a result of a lower resistance of the transmission line.

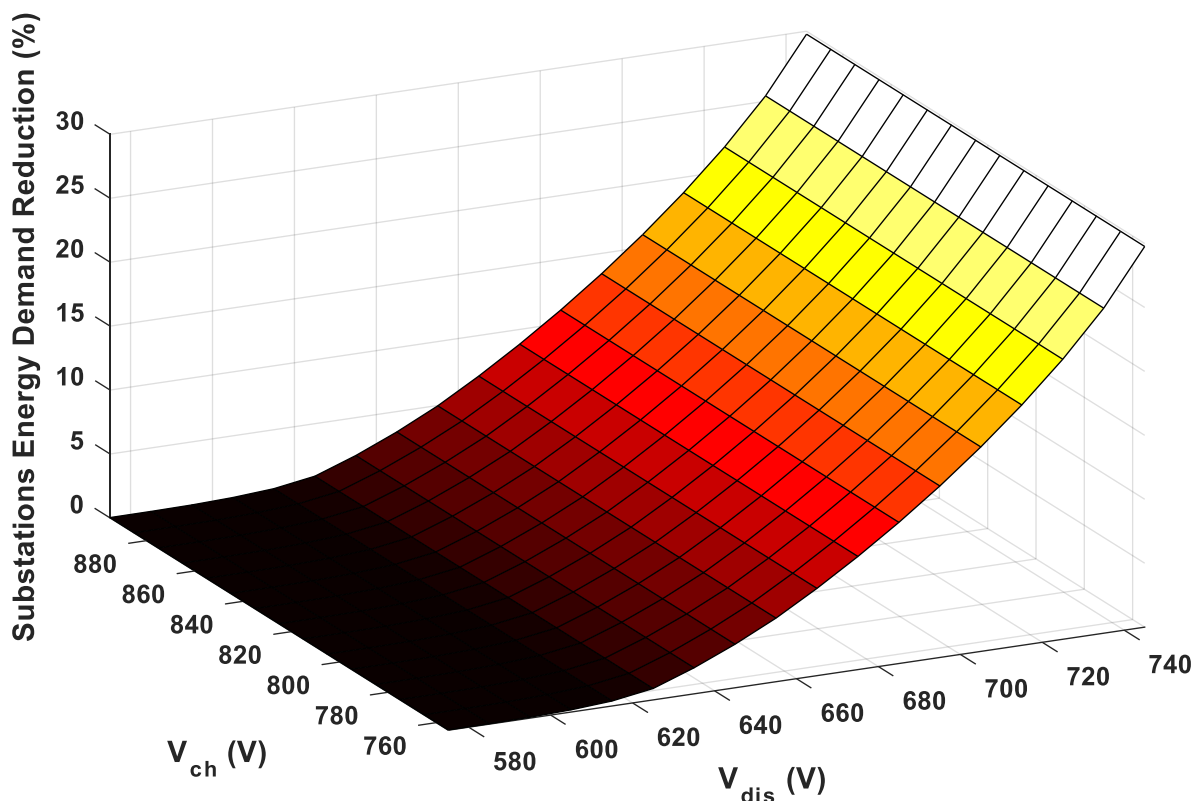


Figure 4.6: Reduction of the substation energy demand under voltage limit variation when placing the ESS at Passenger Station A

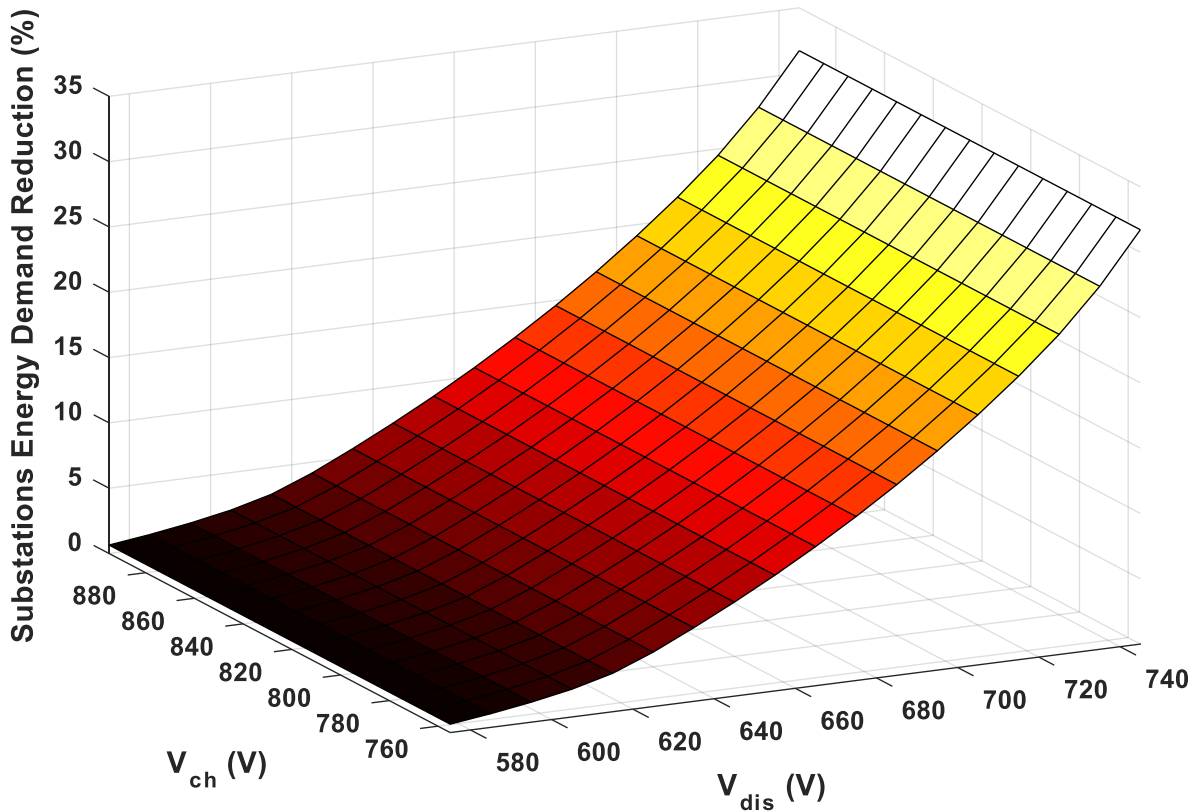


Figure 4.7: Reduction of the substation energy demand under voltage limit variation when placing the ESS at Passenger Station B

4.4.2 Substation peak power demand

Peak power is defined as the maximum power that a substation delivers. Since peak power demand is costly and places a significant burden on substations should it be close to maximum operational limit, it is desirable to choose appropriate voltage setpoints that can effectively reduce power peaks. The peak power demand for both substations before adding the ESS was 4.95 MW. Intuitively, varying the ESS charging voltage was not expected to assist in reducing peak demands since they are linked to voltage troughs rather than voltage surges. However, increasing the discharging voltage threshold was expected to decrease the substation peak power demand due to the discharge of extra energy, which provides more voltage support to the substation when experiencing voltage troughs. The results shown in Figure 4.8 and 4.9 confirm these statements. The positive contribution of the ESS to Substation 1 was

higher than that to Substation 2 because the ESS shared the same location with Substation 1. Further analysis of peak power reduction was conducted by installing the ESS at the midpoint between two substations to confirm the validity of this claim. The results confirm that the impact of the ESS on both substations was identical, as can be seen in Figure 4.10 and 4.11. This identical impact was caused by the equal distance between the ESS and each substation.

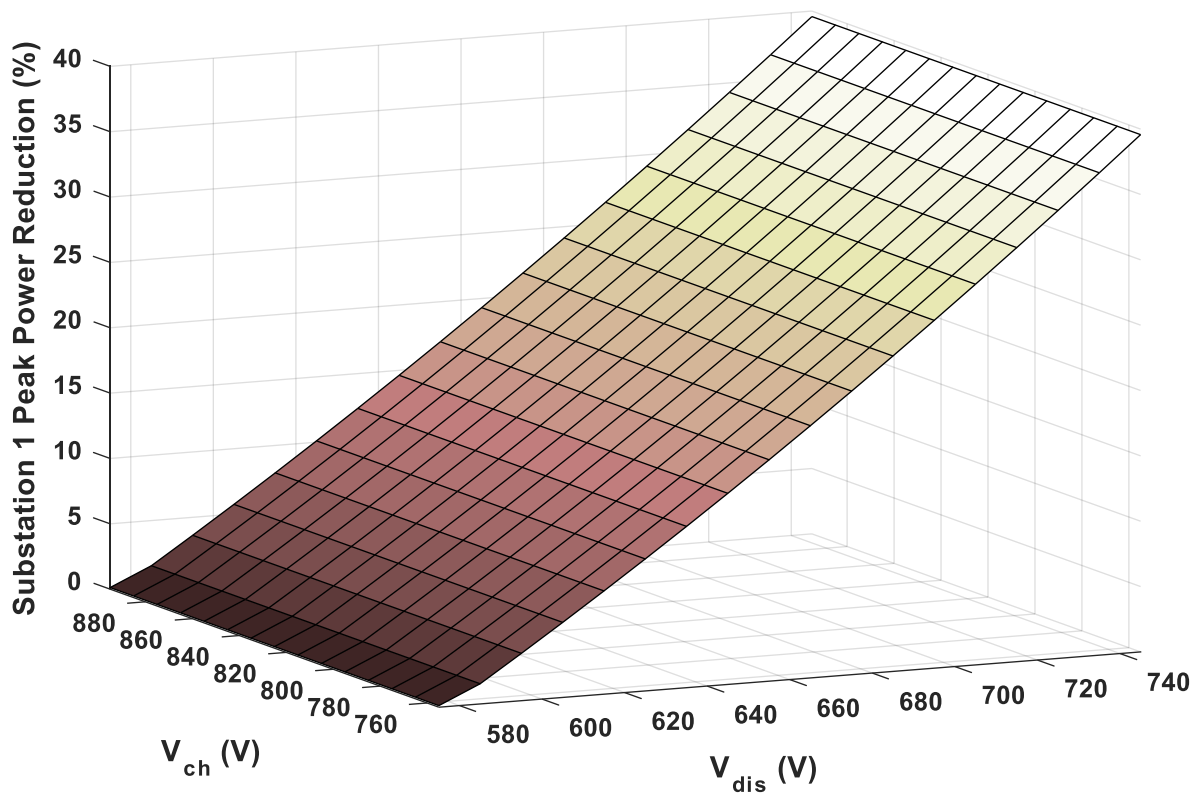


Figure 4.8: Reduction of Substation 1 peak power demand under voltage limit variation when placing the ESS at Passenger Station A

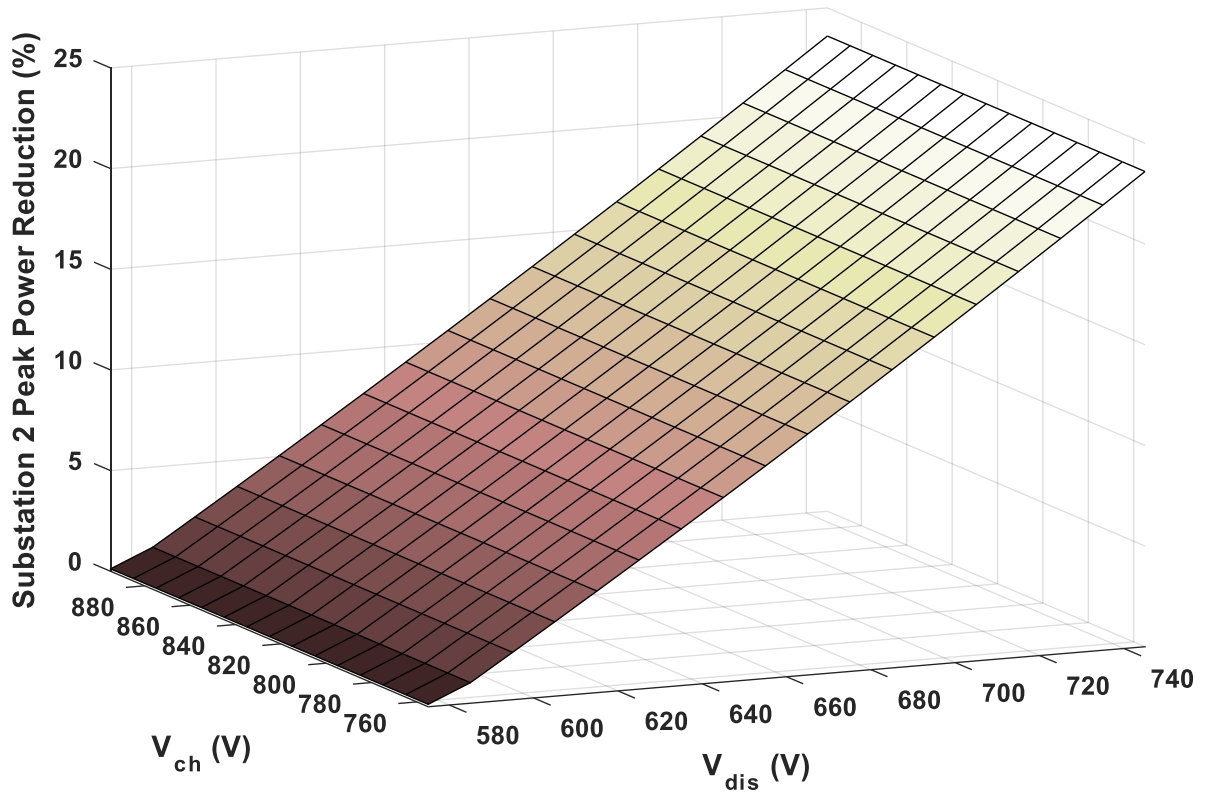


Figure 4.9: Reduction of Substation 2 peak power demand under voltage limit variation when placing the ESS at Passenger Station A

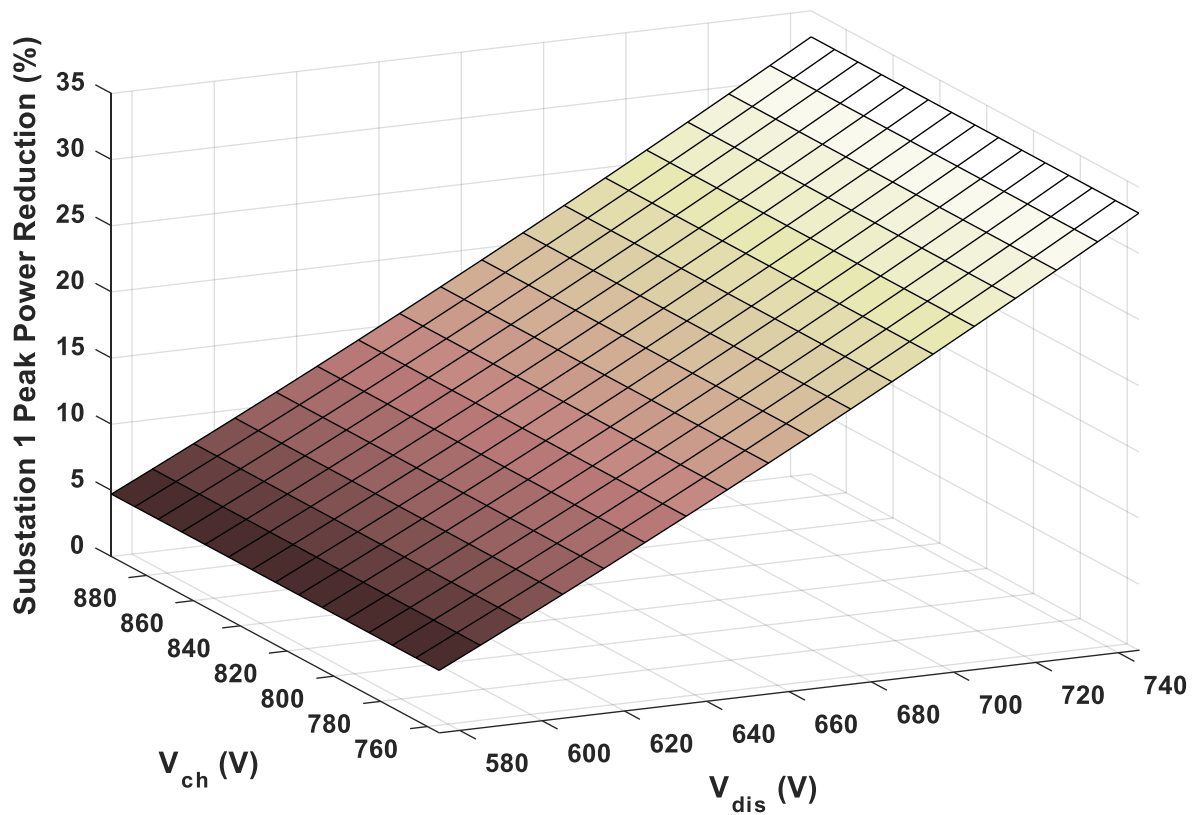


Figure 4.10: Reduction of Substation 1 peak power demand under voltage limit variation when placing the ESS at Passenger Station B

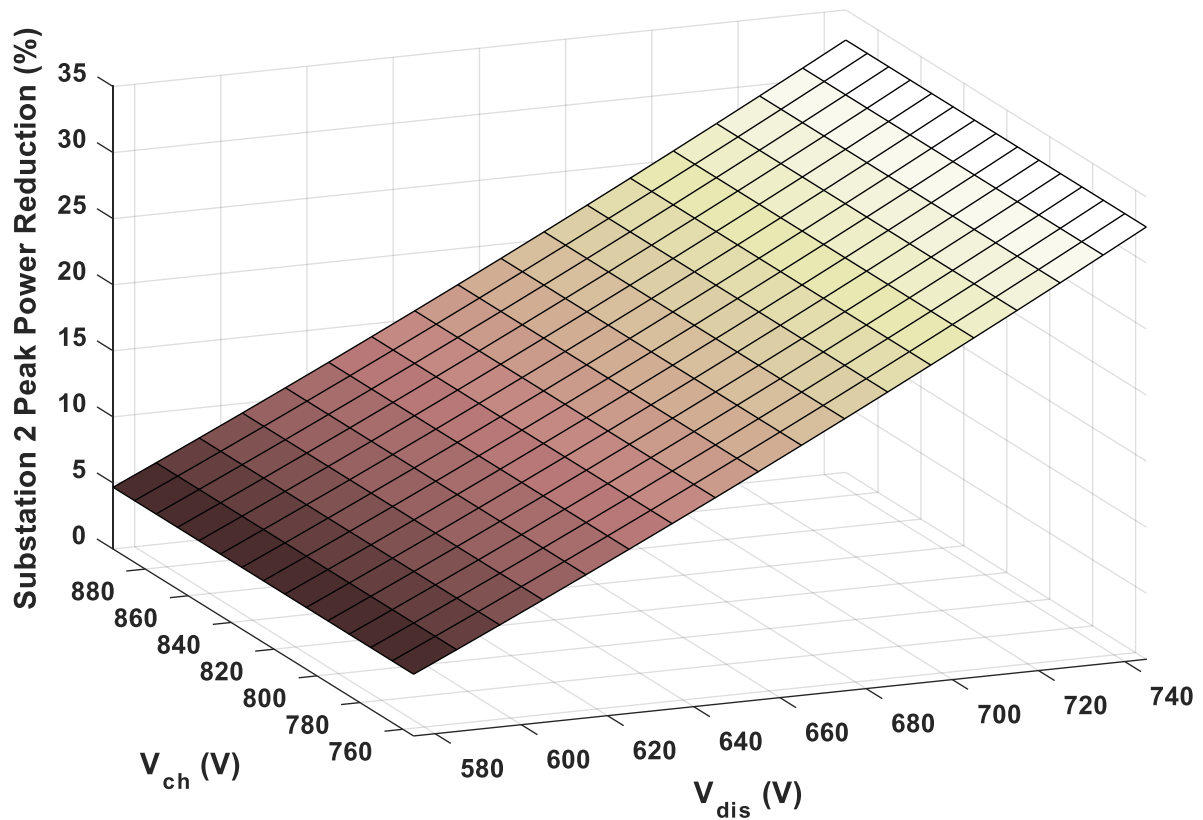


Figure 4.11: Reduction of Substation 2 peak power demand under voltage limit variation when placing the ESS at Passenger Station B

4.4.3 Transmission line losses

Transmission losses are defined in this study as resistive losses in the 3rd and 4th rails created by the power supplied by the substations and the power exchanged between the trains. The transmission losses were calculated by the product of the rail electrical resistance and the square of the passing current, before the accumulation over the simulation period. Figure 4.12 shows the reduction in transmission line losses when the ESS was located at Passenger Station A (transmission losses before introducing the ESS were 15.83 kWh). The figure shows that decreasing the charging voltage threshold increased line losses. This negative impact was caused by the extra energy utilised in the line due to early ESS engagement. In contrast to changing the charging voltage threshold, changing the discharging voltage threshold had less impact on the line losses because the ESS delivered power at the substation location.

Furthermore, discharging at higher voltages resulted in less losses than discharging at lower voltages. This decrease in losses was a result of the extra reduction in the voltage drop leading to less load current demand and less transmission losses. When charging late (large V_{ch}) and discharging early (large V_{dis}) the reduction in losses had positive values, denoting that the losses in the line reduced compared to that before including the ESS. This effect was a result of large support to the voltage drop by discharging early and small regenerative energy transmitted to the ESS because of the late action of charge.

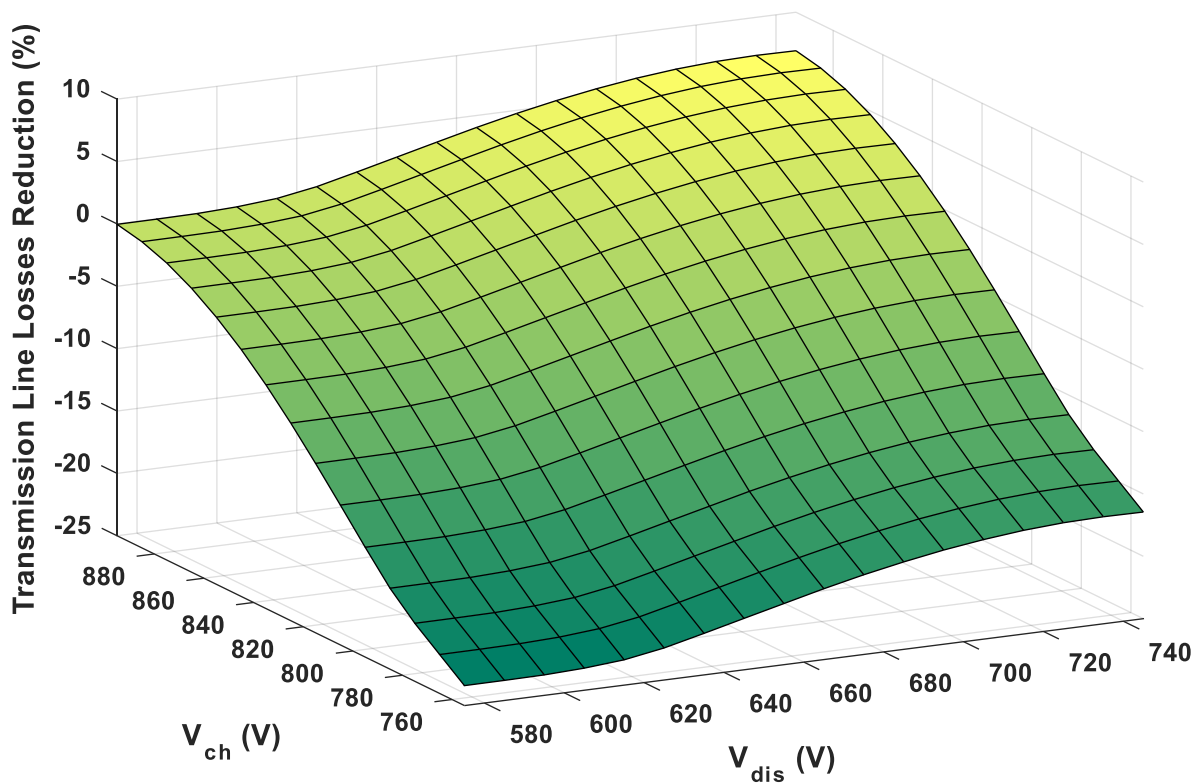


Figure 4.12: Decline of transmission line losses under voltage limit variation when the ESS was located at Passenger Station A

As shown in Figure 4.13, the ESS was placed equidistant from the two substations to confirm that the reason for the increased transmission losses was because the substation and the ESS shared the same location. The graph confirms that charging at low values of V_{ch} increased the losses. It also supports the earlier claim that the impact of varying the discharging voltage threshold on the transmission losses is highly associated with the ESS's location since increasing the discharging voltage threshold contributed significantly to reducing the transmission line losses.

For further support of the impact of location on transmission losses, consider that when the energy storage was positioned at the substation and charged at 755 V and discharged at 745 V, the ESS reduced the substation energy demand by 94.04 kWh (29.77%) and increased the line losses by 2.6 kWh (16.45%). Although the ESS reduced the energy demand of the substations, it also increased the line losses. However, using the same voltage limits but changing the ESS's location to Passenger Station B saved 100.2 kWh (31.72%) of the energy demand of the substations and reduced the line losses by 1.19 kWh (7.52%). These results suggest that if the ESS is installed at Passenger Station B, the accelerating trains in the middle consume most of their power demand from the ESS, which reduces transmission losses by reducing the distance travelled by the traction power. Moreover, when trains decelerate at a considerable distance from the ESS's location, this increases the regenerative power loss in the transmission line, which could be diminished by reducing the transmission distance of the braking energy. As a result, it is more efficient for the ESS to be located at the midpoint because that decreases the distance the power must pass.

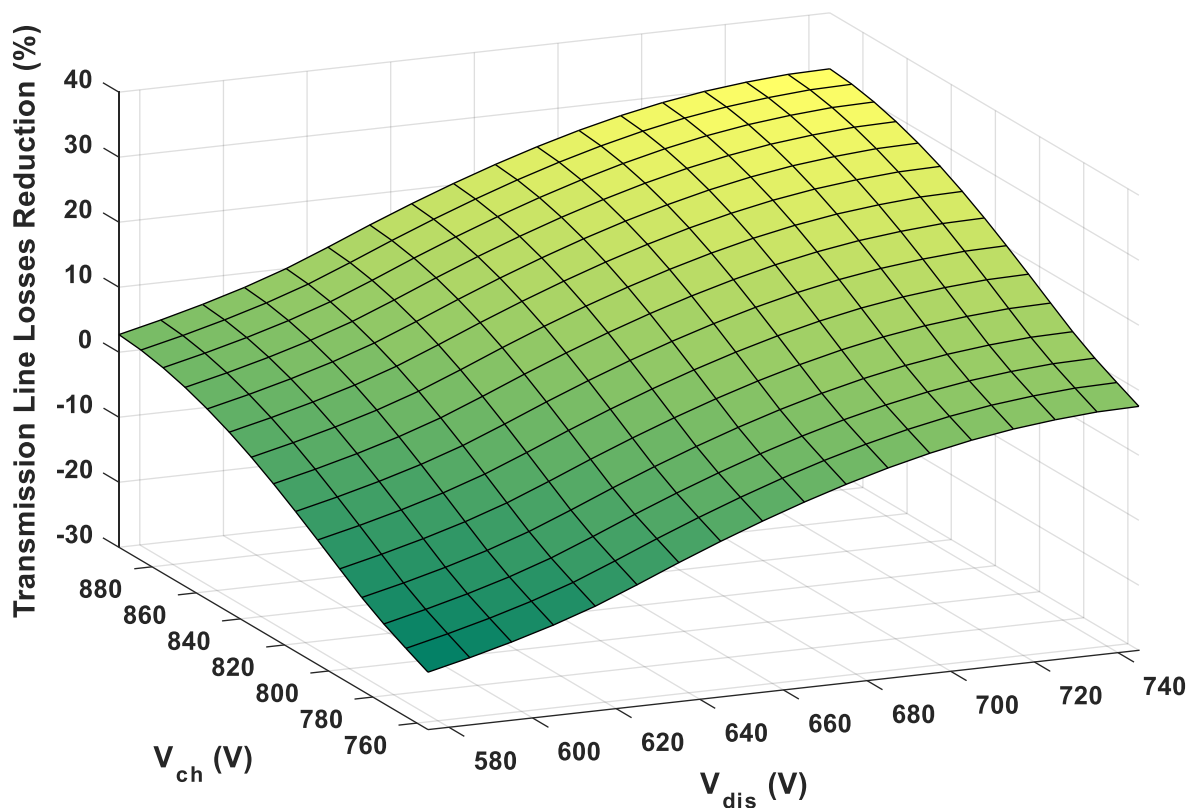


Figure 4.13: Decline of transmission line losses with respect to voltage limit variation when the ESS was positioned at Passenger Station B

4.4.4 Energy dissipated in on-board braking resistors

Braking resistors are activated at a certain voltage threshold to dissipate regenerative power as heat. In the proposed model, this threshold occurred when the trains contact voltages reached 900 V. The energy dissipated in the braking resistors before applying the ESS was 155.14 kWh. Since the braking resistors are activated on overvoltage, the dissipated energy in these resistors was not sensitive to modifications to the ESS discharge voltage threshold, as confirmed by Figure 4.14. There is however a significant positive correlation between charging at low threshold voltages and reducing energy losses in the braking resistors.

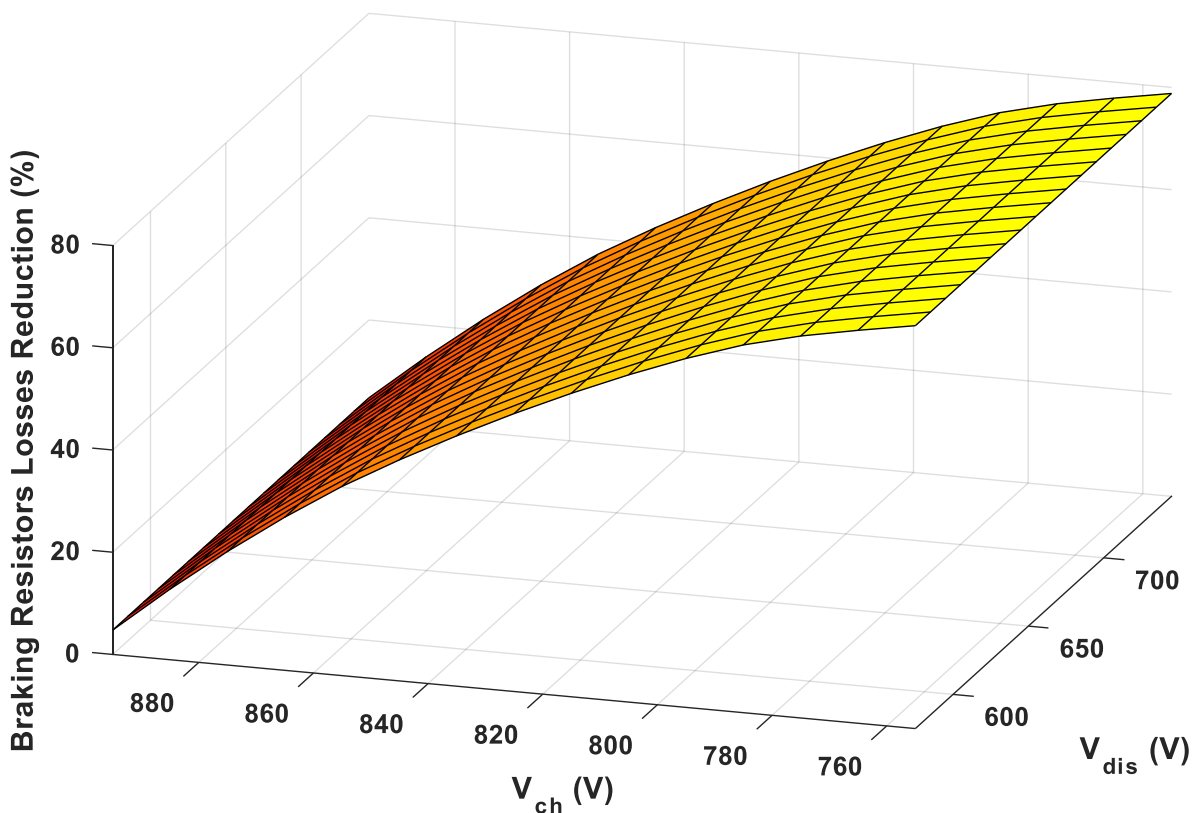


Figure 4.14: Reduction of energy losses in the on-board braking resistors with respect to voltage limit variation when the ESS was positioned at Passenger Station A

Comparing the results provided in Figure 4.14 with those in Figure 4.15, representing the case when the ESS location was changed, shows that the position of the ESS did not have a significant impact on reducing the losses in the braking resistors. This result is likely related to the appearance of almost identical voltage peaks on the line, which activated the braking resistors at different locations. Having similar voltage peaks at different locations may be explained by the fact that the discussed traffic scenario held identical power demands for the trains, and applying any changes to this ideal scenario would result in different voltage peaks at different locations. Another reason for the appearance of similar voltage peaks at different locations is that the substations were not involved in supporting the load profile in the braking mode. These results suggest that it would be more beneficial to reduce the braking losses when storing energy at the location that experiences the highest and more frequent voltage peaks.

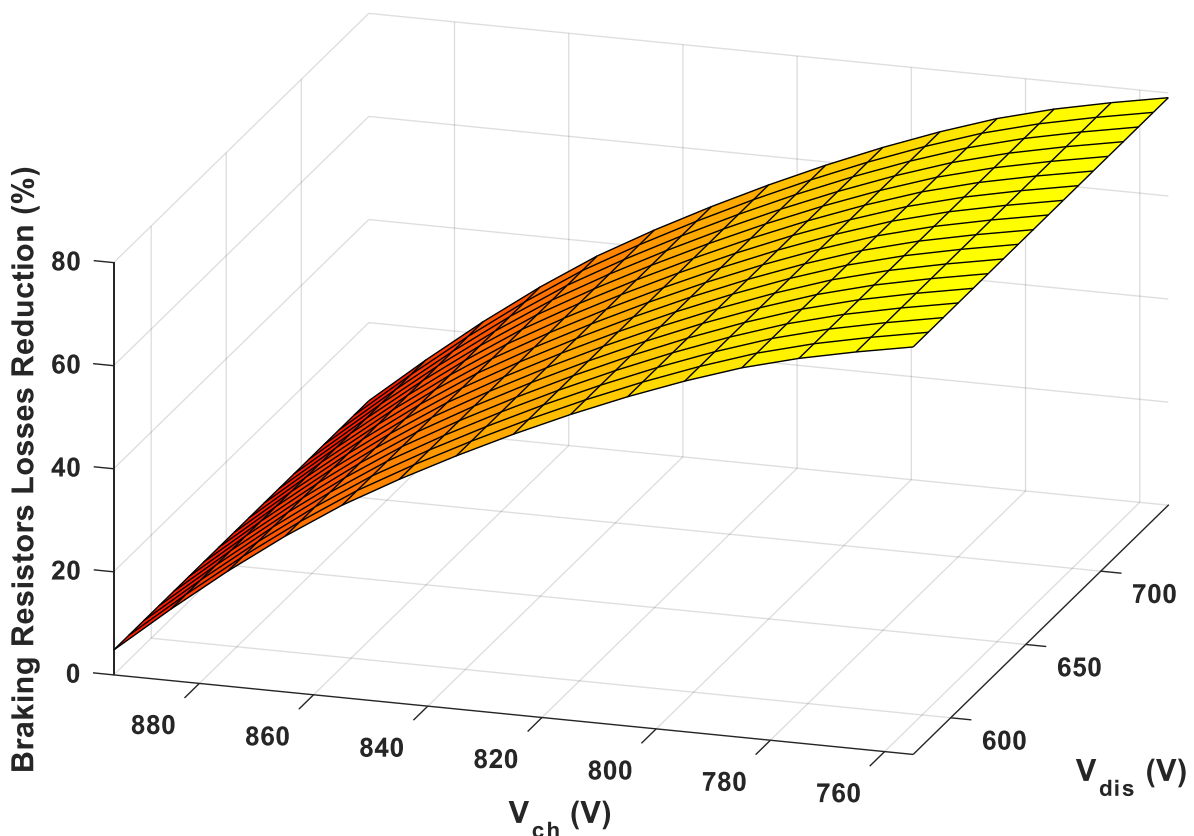


Figure 4.15: Reduction of energy losses in the on-board braking resistors with respect to voltage limit variation when the ESS was positioned at Passenger Station B

4.4.5 Total energy saving

The total energy saving is defined in this study as the reduction in the total losses in the system added to the reduction in the substation energy demand as given by the following equation:

$$E_{sv} = \sum(E_{s1} - E_{s2}) + \sum(E_{line\ losses\ 1} - E_{line\ losses\ 2}) + \sum(E_{br1} - E_{br2}) \quad (4.1)$$

where E_{sv} is the total energy saving in kWh, $\sum E_{s1}$ is the total energy demand of all substations before applying the ESS in kWh, $\sum E_{s2}$ is the total energy demand of all substations after applying the ESS in kWh, $\sum E_{line\ losses\ 1}$ is the total energy losses in the transmission lines before applying the ESS in kWh, $\sum E_{line\ losses\ 2}$ is the total energy losses in the transmission lines after applying the ESS in kWh, $\sum E_{br1}$ is the total dissipated braking energy in the braking resistors of all trains before applying the ESS in kWh, and $\sum E_{br2}$ is the total dissipated braking energy in the braking resistors of all trains after applying the ESS in kWh. It is worth mentioning that reducing the losses was considered part of the energy saving because this study pertains to metro systems where the losses contribute in extra heat in the tubes which necessitate importing energy from the grid to cool the tubes down. Further, reducing the losses in braking resistors means that the energy is stored in ESSs for later use to increase the energy saving in metro systems. The total energy saving in percentage is calculated by Equation 4.2 and displayed in Figure 4.16 and Figure 4.17. The two figures show that charging and discharging near the no-load voltage maximised the energy saving. This statement is supported by the studies provided in [134], [142], [143] where it was recommended to charge/discharge as early as possible to maximise energy saving. Figure 4.17 shows that when placing the ESS centrally between the substations, increased energy saving was achieved. For example, when charging at 755 V and discharging at 745 V the total energy saving in percentage was 46.03% for centrally located ESS while it was 43.9% when it was placed at Passenger Station A.

$$E_{sv} = \left(1 - \frac{\sum E_{s2} + \sum E_{line\ losses\ 2} + \sum E_{br2}}{\sum E_{s1} + \sum E_{line\ losses\ 1} + \sum E_{br1}}\right) \cdot 100\% \quad (4.2)$$

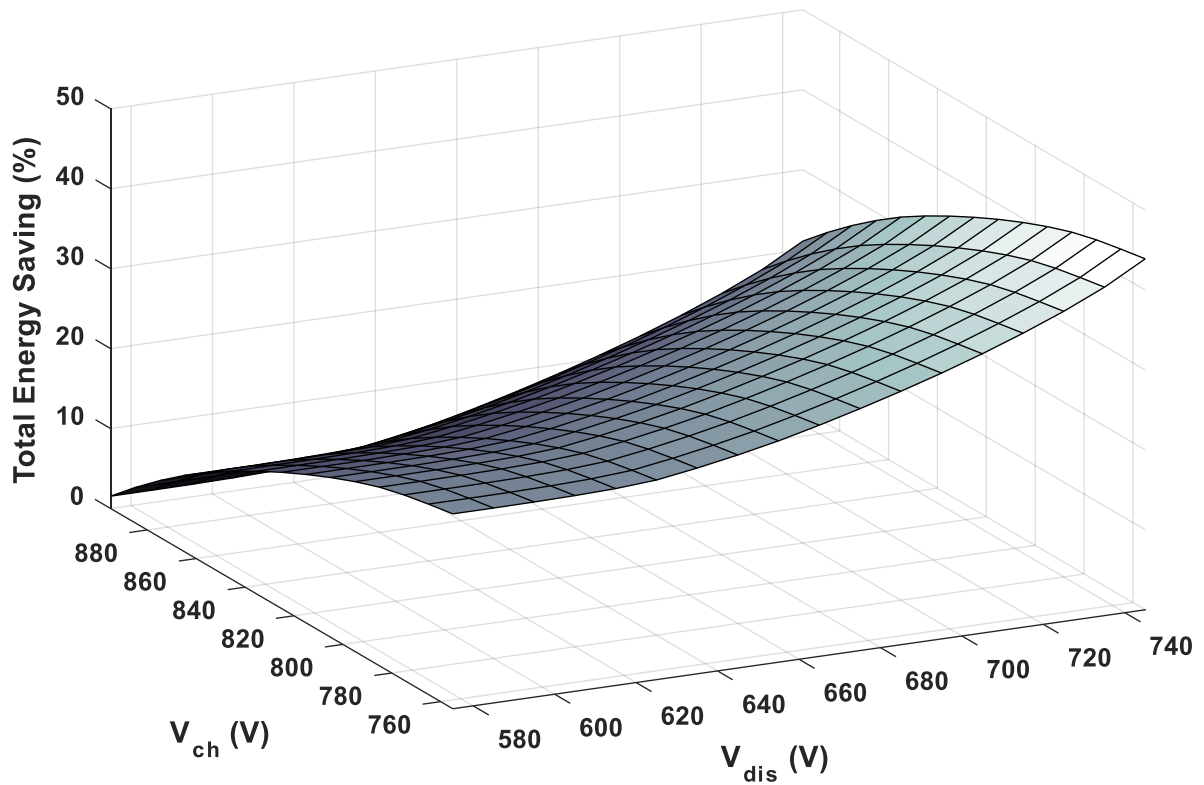


Figure 4.16: Total energy saving in percentage with respect to voltage limit variation when placing the ESS at Passenger Station A

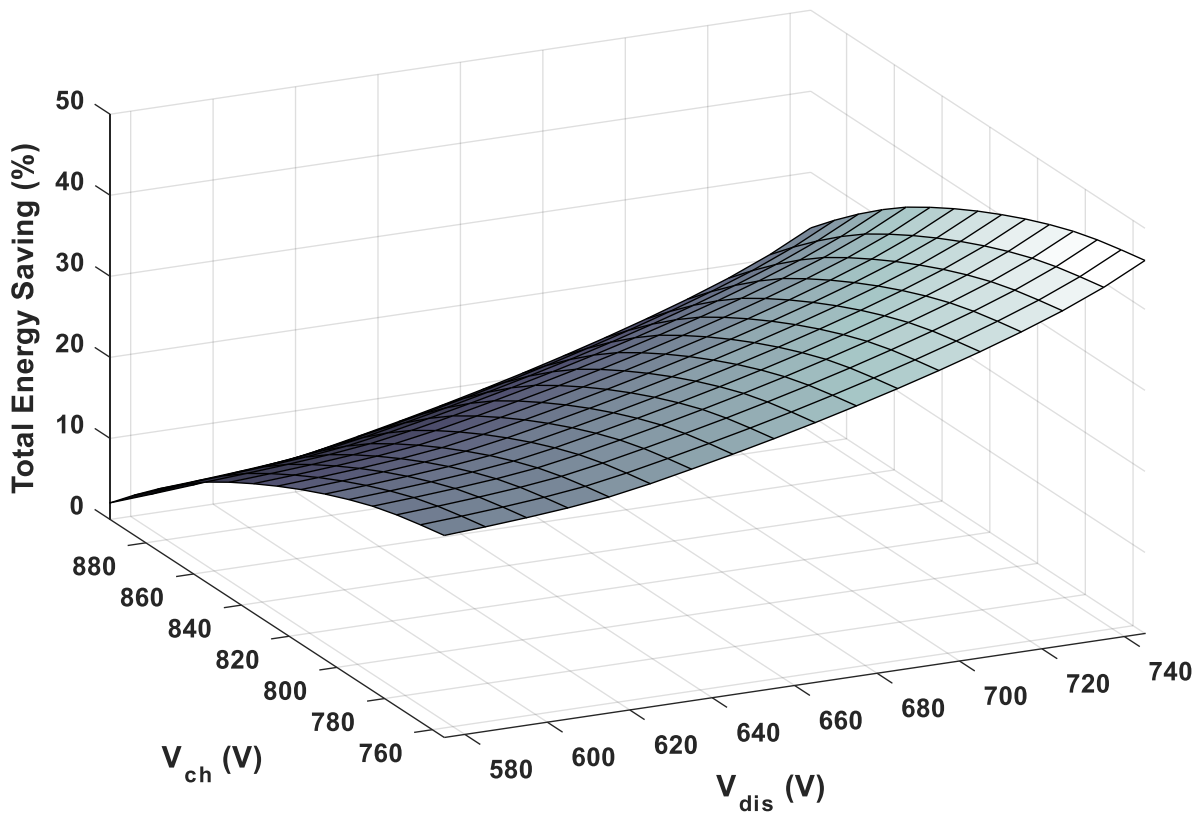


Figure 4.17: Total energy saving in percentage with respect to voltage limit variation when placing the ESS at Passenger Station B

4.4.6 SOC drift

Voltage setpoints should be selected to reduce substation energy consumption, transmission losses, braking power losses, and power peaks. These aims can be met but this results in unbalanced charging and discharging which causes the SOC at the end of the journey to deviate from the value at the beginning. It was assumed, for the purposes of this study, that the ESS could not be charged or discharged purely for the purposes of SOC management outside of train operating times. Consequently, SOC deviation would result in reaching the maximum and minimum limits of the storage capacity, potentially before the end of an operational period and certainly over a series of days, reducing the effectiveness of the ESS in maximising energy efficiency.

The SOC can be calculated by adopting Equation 4.3, whereas the SOC drift – defined as the difference between the desired SOC and the instantaneous SOC – is calculated by Equation 4.4.

$$SOC_{out}(t) = SOC(t_0) + \left(\frac{\int_{t_0}^{t_f} I_{ESS}(t) dt}{3600 \cdot Q} \cdot 100 \right) \quad (4.3)$$

$$SOC_{drift}(t) = \frac{SOC_{out}(t) - SOC_d}{SOC_d} \cdot 100 \quad (4.4)$$

Where Q is the rated ESS's capacity which is 400 Ah, $SOC_{out}(t)$ is the instantaneous SOC as a percentage (%), $SOC(t_0)$ is the initial SOC in %, $SOC_{drift}(t)$ is the instantaneous SOC drift in %, SOC_d denotes the desired SOC in %, and $I_{ESS}(t)$ represents the instantaneous ESS current in As, which has a positive/negative value during discharging/charging. The t_0 is the initial simulation time in seconds and t_f is the final simulation time in seconds. The desired SOC was set to 50% because the optimal SOC is out of the scope of this PhD study that does not relate to a specific type of ESS. Therefore, symmetrical capacity available for traction and braking modes was desired since the load profile could be unpredictable.

Figure 4.18 depicts a SOC drift sensitivity analysis on varying the charging and discharging voltage threshold for one operating period when the ESS was positioned

at Passenger Station A. In this case, positive drift represents a higher SOC at the end of the journey than the beginning, while negative drift indicates that more energy is supplied by the ESS and hence a lower SOC at the end of the journey than the beginning. Increasing the charging voltage reduced the positive drift but increased the negative drift. Similarly, increasing the discharging voltage threshold decreased the positive drift while increasing the negative drift. Figure 4.19 shows the absolute value of the SOC drift at the end of a completed journey. The graph demonstrates the nonlinear relationship between the SOC drift and the voltage limits, with the valley representing the minimum drift. In terms of maximising energy efficiency, it is important that the SOC drift remains in the vicinity of the valley, a requirement which can be achieved by choosing suitable voltage thresholds that also satisfy other energy requirements.

When the ESS was moved to Passenger Station B, the negative SOC drift was aggravated due to the appearance of high voltage drops in the measured voltage, which caused a high release of energy by the ESS. By contrast, the positive deviation was even less than when it was placed next to the substation. This result may be explained by the fact that the voltage peaks measured at the terminal were similar, while the voltage troughs were higher in the middle than at the beginning of the track. This scenario caused the ESS to release a high amount of energy, resulting in a high negative SOC drift and low positive SOC drift. For example, the SOC drift was -5.73% when placing the ESS at Passenger Station A and charging/ discharging at 755/745 V. The SOC drift increased to -7.32% when changing the ESS location to Passenger Station B.

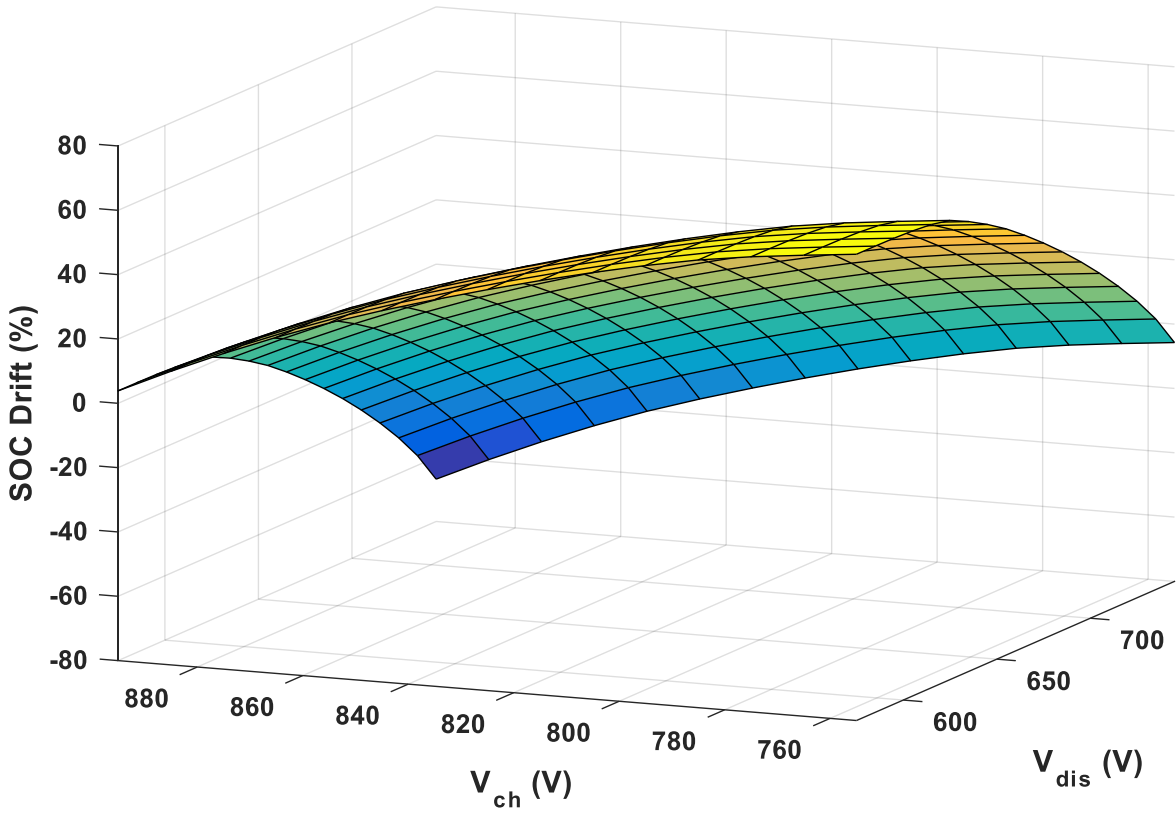


Figure 4.18: SOC drift with respect to voltage limit variation when placing the ESS at Passenger Station A

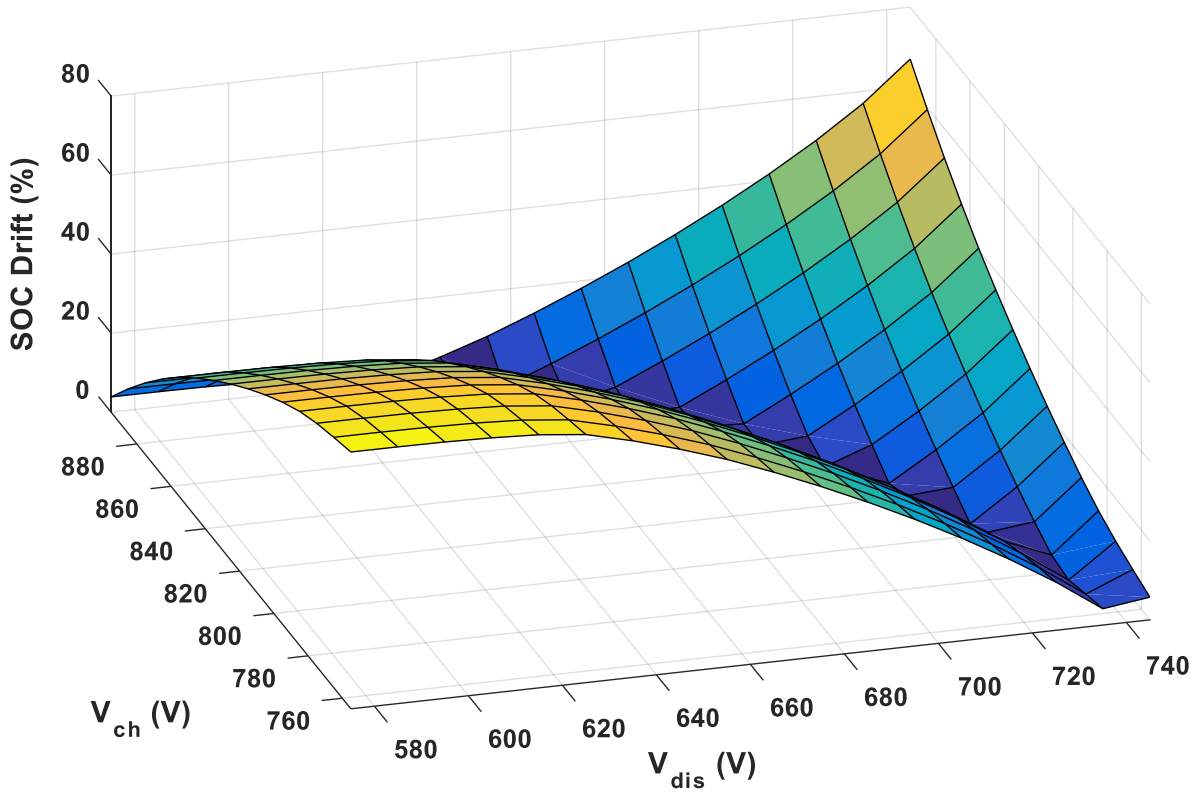


Figure 4.19: Absolute value of the SOC drift with respect to voltage limit variation when placing the ESS at Passenger Station A

4.4.7 Voltage threshold selection

The findings presented in the previous sections, where the ESS is positioned at Passenger Station A show that a high discharging voltage reduced the substation energy demand and peak power. On the other hand, a high charging voltage minimised the transmission losses, while a low charging voltage minimised the losses in the braking resistors. However, the SOC drift required a complementary choice when the drift was positive, as decreasing the charging voltage threshold necessitated increasing the discharging voltage threshold. In contrast, when the drift was negative and as the discharging voltage increased, the charging threshold had to be decreased. Thus, the results reported so far in this chapter provide insight into the challenges related to selecting the most suitable voltage thresholds to maximise the benefit of using an ESS.

It was decided in this study to use a methodology for the voltage threshold selection based on two objectives that are the total energy saving and SOC drift. Multi-Criteria Decision Making (MCDM) also called Simple Additive Weighting (SAW) method was used for decision making of the voltage thresholds. This method is widely used to select the most preferred alternative among others. In this method, a decision matrix is first identified for each criterion serving as a parameter for choosing the most preferred alternative, before normalising the matrices to a common unit. Thereafter, the importance of each criterion is represented by assigning weights and calculating the total score of each alternative, which is the pair of V_{ch} and V_{dis} . Finally, the alternative with the highest score is selected as the preferred option. The method is described mathematically in Equation 4.5.

$$S_i = \sum_{j=1}^M W_j r_{ij} \quad \text{for} \quad i = 1, 2, \dots, N \quad (4.5)$$

Where S_i is the overall score of the i^{th} alternative, r_{ij} is the normalised rating of the i^{th} alternative for the j^{th} criterion, W_j is the importance (weight) of the j^{th} criterion, N is the total number of alternatives, and M is the number of criterion [144]. The steps of finding the solution of the voltage thresholds are summarised in the following:

1. Identify criteria and measures.

The first criterion was the total energy saving that was measured by the reduction in the substation energy demand, transmission losses, and braking resistor losses. The second criterion was the SOC drift that was measured by the deviation of the final SOC from the desired value of 50%.

2. Collect data.

The data of the total energy saving and SOC drift are presented in Figure 4.16 and Figure 4.19, respectively.

3. Rescale each measure to a common unit.

To simplify the comparison, a common unit was calculated by dividing the difference between the value of each alternative and the least preferred value by the difference between the most preferred value and the least preferred value. Each alternative represented a combination between V_{ch} and V_{dis} where the alternative had two values one was for the total energy saving and the other was for the SOC drift. The most preferred value of the first criterion (total energy saving) was the highest percentage of energy saving while the least preferred value was the lowest percentage based on the data presented in Figure 4.16. The most preferred value of the second criterion (SOC drift) was the lowest percentage of SOC drift while the least preferred value was the highest percentage based on the data presented in Figure 4.19. The least and most preferred values of the total energy saving were 1.54% and 43.9%, respectively, while the least and most preferred values of the SOC drift were 66.83% and 0.16%, respectively. The new scale represented alternatives in scores between 0 and 1, where 0 represented the worst option whilst 1 represented the best option. The rescaled total energy saving is shown in Figure 4.20 and the rescaled SOC drift is shown in Figure 4.21.

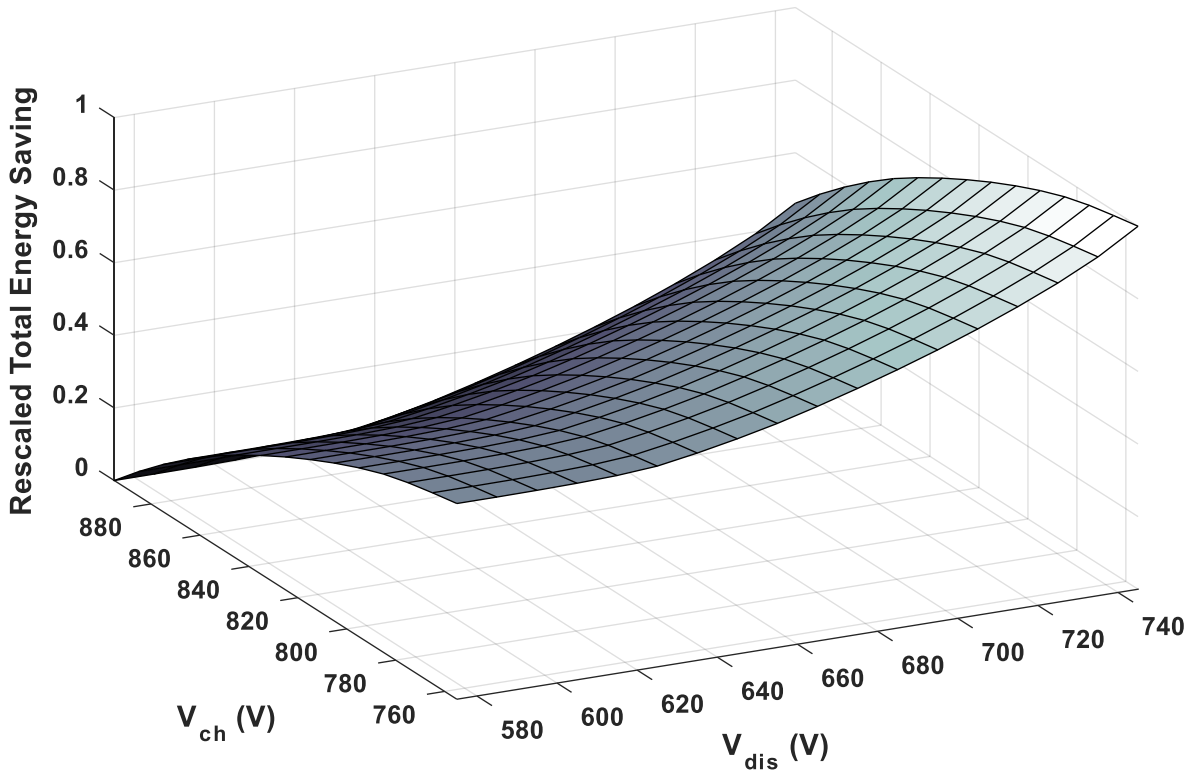


Figure 4.20: Normalised total energy saving when placing the ESS at Passenger Station A

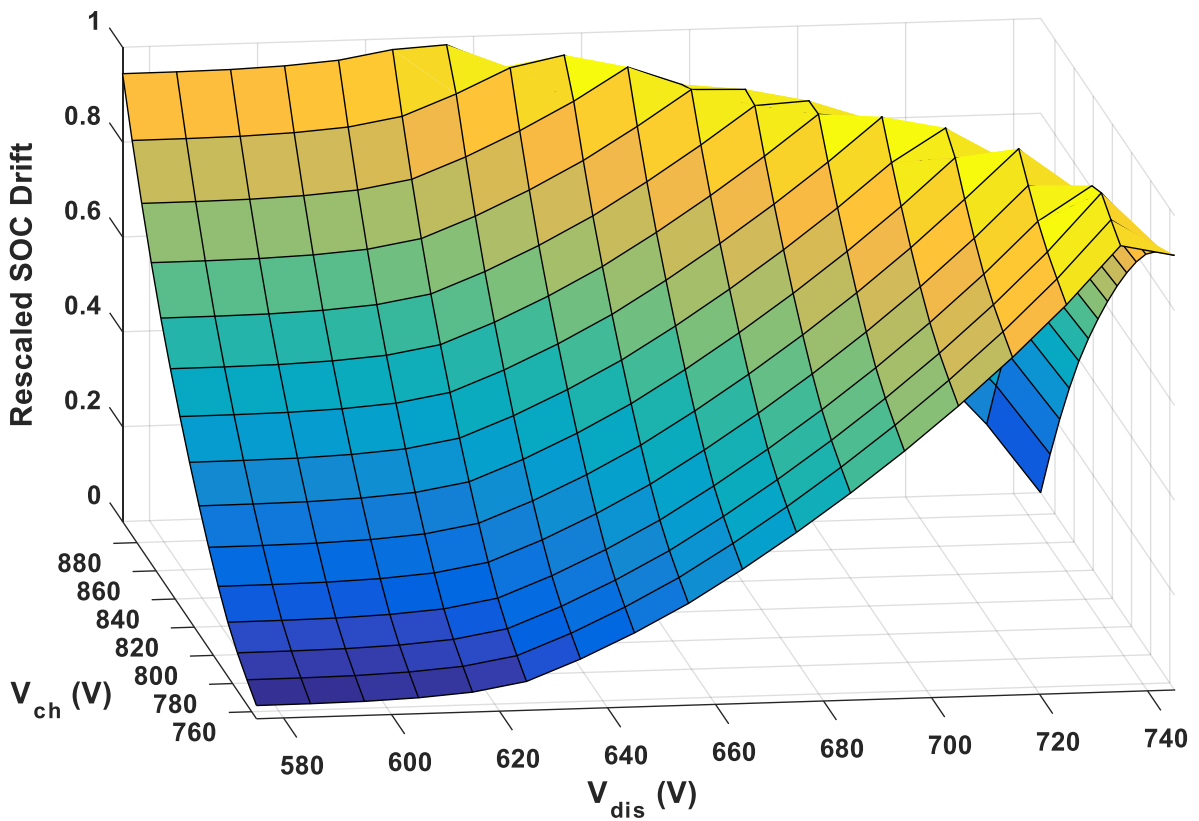


Figure 4.21: Normalised SOC drift when placing the ESS at Passenger Station A

4. Assign weights.

Weights of the measures were calculated by dividing the value of each measure by the total value. The total energy saving was given a value of 50 and the SOC drift was given a value of 50 indicating that they were equally important with 0.5 weight for each measure.

5. Calculate total scores.

The score of each alternative in each measure was calculated by multiplying the common unit calculated in step 3 and the weight assigned in step 4. Thereafter, each alternative had two scores where the sum of which represented the total score shown in Figure 4.22.

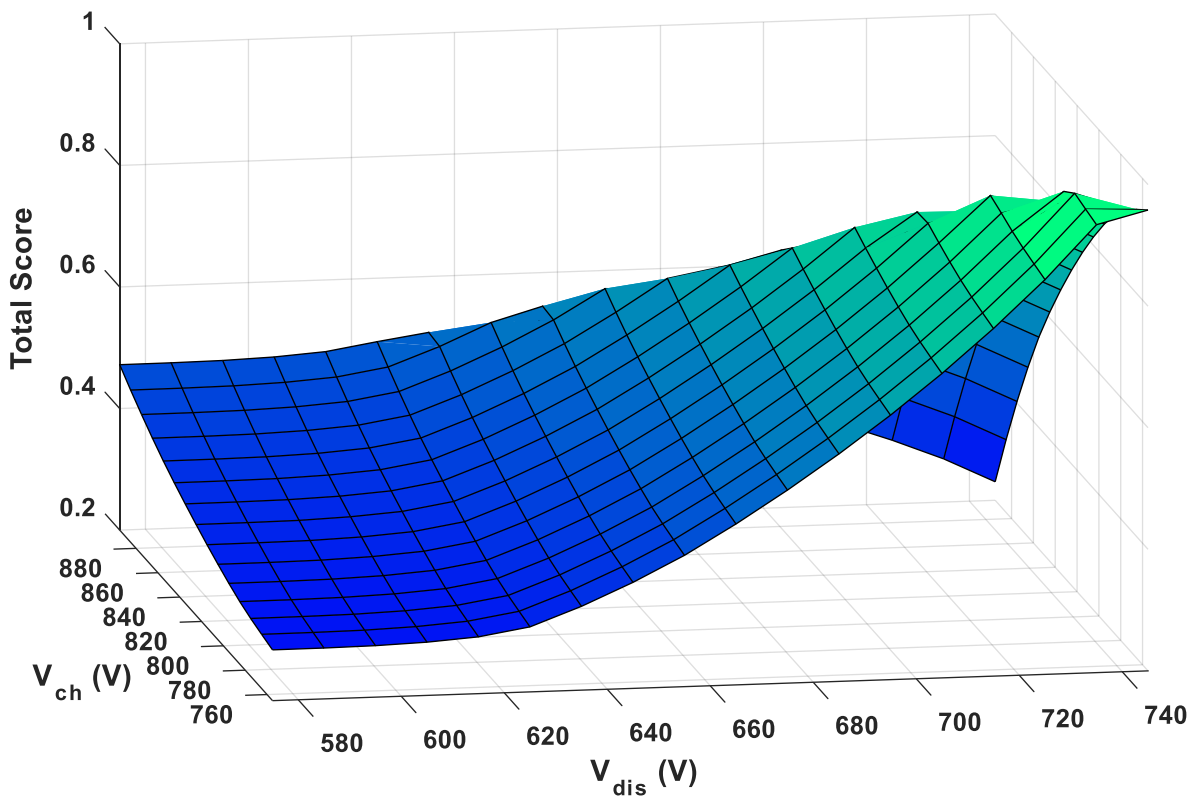


Figure 4.22: Total score of each alternative corresponding to all criteria when placing the ESS at Passenger Station A

6. Final decision.

In this step, the result with the highest score is selected as the most preferred result. Figure 4.22 shows that the highest score occurred when charging at 755 V and discharging at 745 V. However, to get a more accurate solution, the step size was decreased from 10 V to 1 V in the voltage range between 745 V and 735 V where the optimal result should locate. This speculation was based on the linear relationship between the voltage thresholds and the two measures. Further, the SOC drift transformed from a negative value to a positive value when changing the discharging voltage from 745 V to 735 V indicating that the minimum value of SOC drift was located in this range. The total energy saving only decreased from 43.9% to 41.08% when changing the discharging voltage from 745 V to 735 V, which should increase the total score when reaching the minimum SOC drift resulting from the equal weight of the two measures. The charging voltage was fixed at 755 V since increasing it reduced the energy saving and increased the SOC drift resulting in reducing the total score. Table 4.1 shows that the highest score occurred when charging at 755 V and discharging at 740 V, which was considered the most preferred solution. When the ESS was placed at Passenger Station B and using the MCDM method, the most preferred charging voltage was 755 V while the most preferred discharging voltage was 737 V. It is worth mentioning that reducing the controller gains (53) or current limit (6300 A) while setting the voltage thresholds to the values found by the MCDM method decreased the energy saving and increased the SOC drift as seen in Table 4.2 and Table 4.3. Although setting both controller gains k_c and k_d to the value of 52 and then to 51 reduced the SOC drift, they reduced the total energy saving which made them less appropriate than 53 controller gain after applying a comparison using the MCDM method. Therefore, the results presented in the tables show that it was efficient to work at the maximum value of the controller gain that guaranteed stability of the system and maximum current limit that maximised the use of the ESS.

Table 4.1: Final decision calculation when charging at 755 V and varying the discharging voltage when placing the ESS at Passenger Station A

Discharging voltage (V)	Total energy saving (%)	SOC drift (%)	Total score
745	43.9	-5.73	0.95817
744	43.58	-4.63	0.96269
743	43.27	-3.53	0.9673
742	42.96	-2.46	0.97161
741	42.66	-1.42	0.97586
740	42.38	-0.42	0.98005
739	42.1	0.53	0.97595
738	41.84	1.46	0.96592
737	41.58	2.37	0.95605
736	41.33	3.25	0.94644
735	41.08	4.13	0.93693

Table 4.2: Impact of varying the controller gain when placing the ESS at Passenger Station A with 6300 A current limit, and charging/discharging at 755/740 V

Controller gain	Total energy saving (%)	SOC drift (%)
53	42.38	-0.42
52	42.07	-0.07
51	41.75	0.29
50	41.42	0.65
40	37.67	4.18
30	32.14	5.75
20	24.62	5.84
10	14.24	3.88

Table 4.3: Impact of varying the current limit when placing the ESS at Passenger Station A with 53 controller gain, and charging/discharging at 755/740 V

Current limit (A)	Total energy saving (%)	SOC drift (%)
6300	42.38	-0.42
5300	41.62	-2.6
4300	39.69	-7.95
3300	35.84	-14.91
2300	27.81	-13.94
1300	17.3	-10.04
300	4.56	-3.31

4.5 Location of the ESS

Since the ESS in the analysed case study was positioned alongside the rail track, it is clear that selecting its location can significantly influence the electric railway energy efficiency as it may increase energy losses in the transmission line if its location is not optimal. The previous section illustrated that, in the proposed model, the location's impact on energy storage significantly affected the energy efficiency analysis. Further analysis of the location's impact on energy efficiency development is investigated in this section. When the ESS was placed at Passenger Station A the charging and discharging voltage thresholds were set to 755 V and 740 V, respectively, while the discharging voltage threshold was changed to 737 V when moving the ESS to Passenger Station B. These voltage thresholds were deemed to provide satisfactory energy saving and SOC drift based on the analysis presented in the previous section. Comparison between the two locations with respect to the new voltage threshold settings is detailed in Table 4.4. Locating the ESS at Passenger Station B compared to Passenger Station A's location increased the total energy saving from 42.38% to 43.94%.

Table 4.4: Comparison between placing the ESS at Passenger Station A and charging/discharging at 755/740 V against placing the ESS at Passenger Station B and charging/discharging at 755/737 V

	ESS located at Passenger Station A	ESS located at Passenger Station B
Substations energy demand reduction	27.42% (86.6 kWh)	28.52% (90.06 kWh)
Transmission line losses reduction	-16.42% (-2.6 kWh)	7.45% (1.18 kWh)
Braking resistors losses reduction	78.82% (122.3 kWh)	79.07% (122.7 kWh)
Total energy saving	42.38% (206.3 kWh)	43.94% (213.9 kWh)

Figures 4.23 and 4.24 show the voltage profiles before and after installing the ideal ESS at Passenger Stations A and B, respectively. Notably, the impact of the ESS on reducing the voltage drop in the second case was higher than that in the first case.

Reducing voltage peaks resulted in a reduction in the braking resistors losses, while reducing voltage troughs allowed the substation energy consumption and peak power to be lowered. Therefore, when using an ESS to import and export energy, placing it at a location where it significantly reduces system energy losses and substation energy demand achieves the most energy saving; the power analysis in this study identified that location to be Passenger Station B. However, in practical life the ESS installation at locations other than the substations has a number of serious drawbacks such as high cost and physical constraints. Locating the ESS within an existing electrical substation in most circumstances would reduce installation costs due to electrical connection availability and existing facilities for the housing of the system. Physical space at passenger stations is often limited, particularly those that are underground. Therefore, placing the ESS at the location of Passenger Station A where there is a substation will be focused on for the remainder of this thesis.

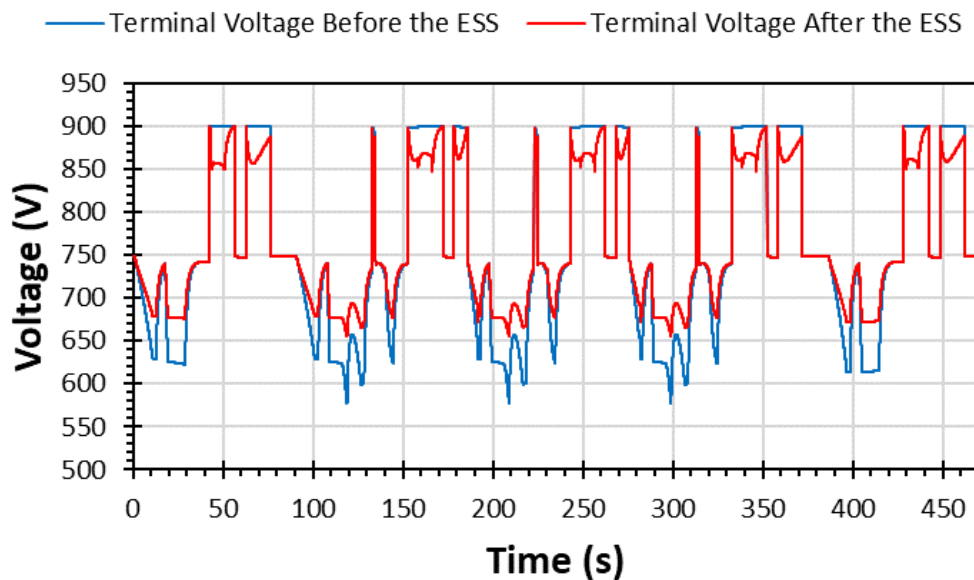


Figure 4.23: Terminal voltage at Passenger Station A before and after including the ESS

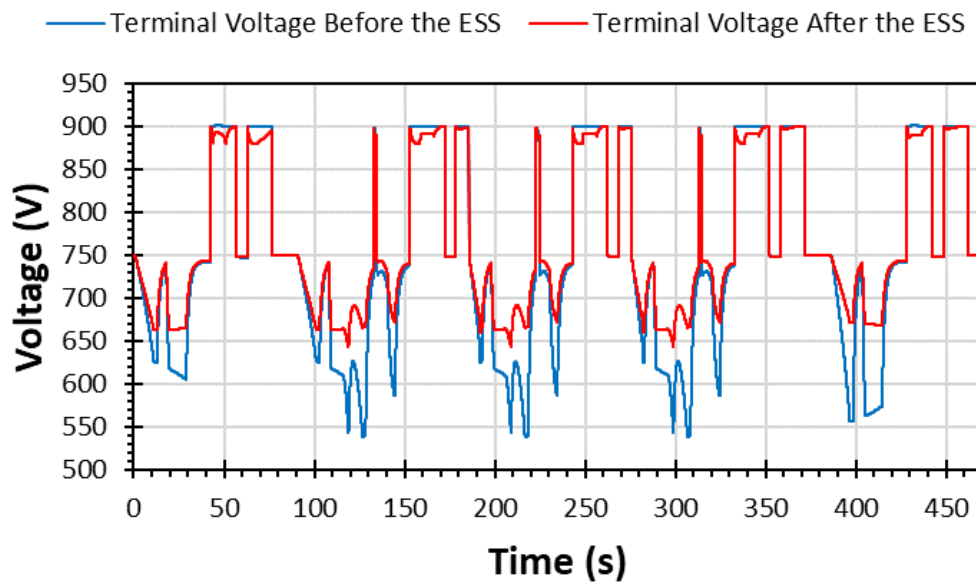


Figure 4.24: Terminal voltage at Passenger Station B before and after including the ESS

4.6 Conclusion

This chapter has presented a case study of eight trains running on a 2 km double railway with a generalised ESS. The railway system has been discussed in terms of improving energy efficiency by recovering excess energy that would have been dissipated during regenerative braking. A voltage sensitivity analysis on the control of the ESS was carried out calculating a number of metrics to explore the impact on energy efficiency.

This chapter's importance and originality stem from its exploration of the charging and discharging voltage thresholds that optimise the performance of the ESS. Optimality was demonstrated by maximising energy saving and minimising SOC drift. The results of this study indicate that a multi-objective approach to choose voltage limits is essential, as reducing the SOC deviation might result in minimising the system energy saving. However, in practice, track voltage is not deterministic and exhibits stochastic behaviour due to the presence of uncertainties in the railway system operations. These uncertainties can cause poor charging/discharging

decisions that affect the system energy efficiency improvements, especially with high SOC drift. SOC deviation is a crucial issue since the positive influence of the ESS would not extend to multiple journeys due to the ESS being full or depleted. The findings of this research suggest that designing an adaptive controller that can mitigate these system uncertainties is essential. The challenge thus facing the adaptive control method is to ensure low SOC deviation whilst maximising the energy saving in the system.

Chapter 5

Adaptive Control Methods for Managing SOC for Energy Storage in DC Electric Railways

5.1 Introduction

As shown in Chapter 4, incorporating ESSs into electric railways is advantageous for energy saving. However, for efficient use of a wayside ESS, adequate charge/discharge control must be designed. One of the key requirements in this process is avoiding reaching the minimum and maximum SOC limits while train services are running, as this could diminish the benefits of incorporating ESSs into electric railways. In certain applications, the SOC cannot be managed by charging from, and discharging to, an external source (i.e. an AC grid) as the connection is only established with the track-side DC of the power network. There are a number of reasons behind this design choice, including the need to avoid additional costs incurred by power converters and protection circuits. Moreover, as shown in Chapter 4, an ESS should ideally be located between substations, thereby preventing access to an AC grid connection. Discharging to a vacant track is not feasible since there are no trains that can absorb power and the reliance on rectifier-only substations with no bidirectional power flow capability. Similarly, charging from the track when no trains are running is not always possible as the power supplied from the substations is switched off outside the operational hours to facilitate track maintenance. Therefore,

it is important to design control methods that can be adopted to manage the power flow between the track and the ESS with respect to storage capacity. In this chapter, two control techniques are proposed to avoid the ESS from reaching the maximum and minimum SOC limits without compromising on the benefits yielded by the system.

5.2 Proposed control techniques

It is proposed here that the controller can adjust in real-time its current limits to manage the SOC. This adjustment involves changing the charging and discharging current limits in order to reduce the SOC drift. However, from the previous chapter, we know that this will affect the energy saving. In this chapter, two adaptive control methods are proposed which allow the control current limits to be adjusted in real-time depending on the operating conditions of the electric railway. The aim of the real-time control parameter tuning is to manage the SOC in scenarios characterised by unpredictable train movements and thus uncertain changes in the track voltage. It is worth mentioning that the control parameters do not require manual retuning when applying changes to the railway operating conditions. The ultimate goal of the proposed methods is to prevent the ESS from reaching the SOC limits whilst maintaining the beneficial effects of energy storage on the railway system, such as reduction in energy losses as well as substation energy usage. The analyses presented in this chapter were produced using MATLAB Simulink software with ode14x solver type and 10 ms time step. The time step was set back to 10 ms as the number of simulations in this chapter is much less than that performed in Chapter 4.

5.2.1 SOC controller 1

The flowchart for the SOC controller 1 presented in Figure 5.1 is proposed as an effective means of modifying the current limits I_{ch} and I_{dis} of the stationary ESS controller presented in Figure 4.2. The current limits in the proposed control approach were modified dynamically to address the challenges of reducing the SOC drift without sacrificing the energy saving.

The described control method based on a state machine strategy was governed mainly by the SOC deviation and the train operating times. The controller aimed to reduce the SOC drift to minimum values before the end of the journey by using the operation of the last train. It was assumed that the trains operated for 18 hours per day where the number of journeys n_t per day was defined by dividing the total train operation time per day by the duration of the journey. The journey was complete when the trains in the up line finished travelling from Passenger Station A to C and those in the down line finished travelling from Passenger Station C to A. It was assumed that the traffic scenario of each journey was identical. The V_{ch} and V_{dis} were fixed at 755 V and 745 V, respectively, as these values were the closest to the no-load voltage as recommended by the authors of [134], [142], [143]. Moreover, these voltage thresholds were found in Chapter 4 to maximise the energy saving by 43.9% but with a SOC drift of 5.73%. The initial SOC was set to 50% while the current limits I_{ch} and I_{dis} were set to the maximum value, which was 6300 A. Thereafter, the simulation of the current journey n_c representing the first journey started running. When the last train in the journey started running, the SOC drift was measured and when it was a positive drift and greater than 0.5% then the ESS discharging current limit (I_{dis}) was set to the maximum value whilst the charging current limit (I_{ch}) was set to zero. In contrast, when the drift was negative and smaller than -0.5%, then the ESS charging current limit (I_{ch}) was set to the maximum value whilst the discharging current limit I_{dis} was set to zero. This process of control continued until the end of journey to keep the SOC drift between +0.5% and -0.5%. The final SOC of the first journey was the

initial SOC of the second journey. This control process was repeated until reaching the last journey in the day.

A screen capture of the ESS model when placed at Passenger Station A and implementing the SOC controller 1 is shown in Figure 5.2. When SOC controller 1 was applied to the described railway model based on the typical traffic scenario detailed in Table 3.5, the SOC deviation was successfully controlled to the value of 0.5% as shown in Figure 5.3. The total energy saving in the system – which includes the reduction in the substation energy demand, the transmission losses, and the braking losses – was initially 213.7 kWh, decreased to 190.5 kWh after applying the SOC controller 1. Although the SOC drift was successfully kept to a small value, the total energy saving reduced significantly. This was a result of strict changes to the current limits at the end of the journey, where the discharging current that was set to zero (see Figure 5.3). Although the current limits of the SOC controller 1 can be optimised, this optimisation needs to be accomplished every time the load profile is changed. The other option is to write numerous if-then statements in order to deal with the uncertainty in the load profile which makes the design process more complex. Therefore, it is important to design a more general, simple to construct, and adaptable method for SOC control that can smoothly change the current limits to further maximise the energy saving.

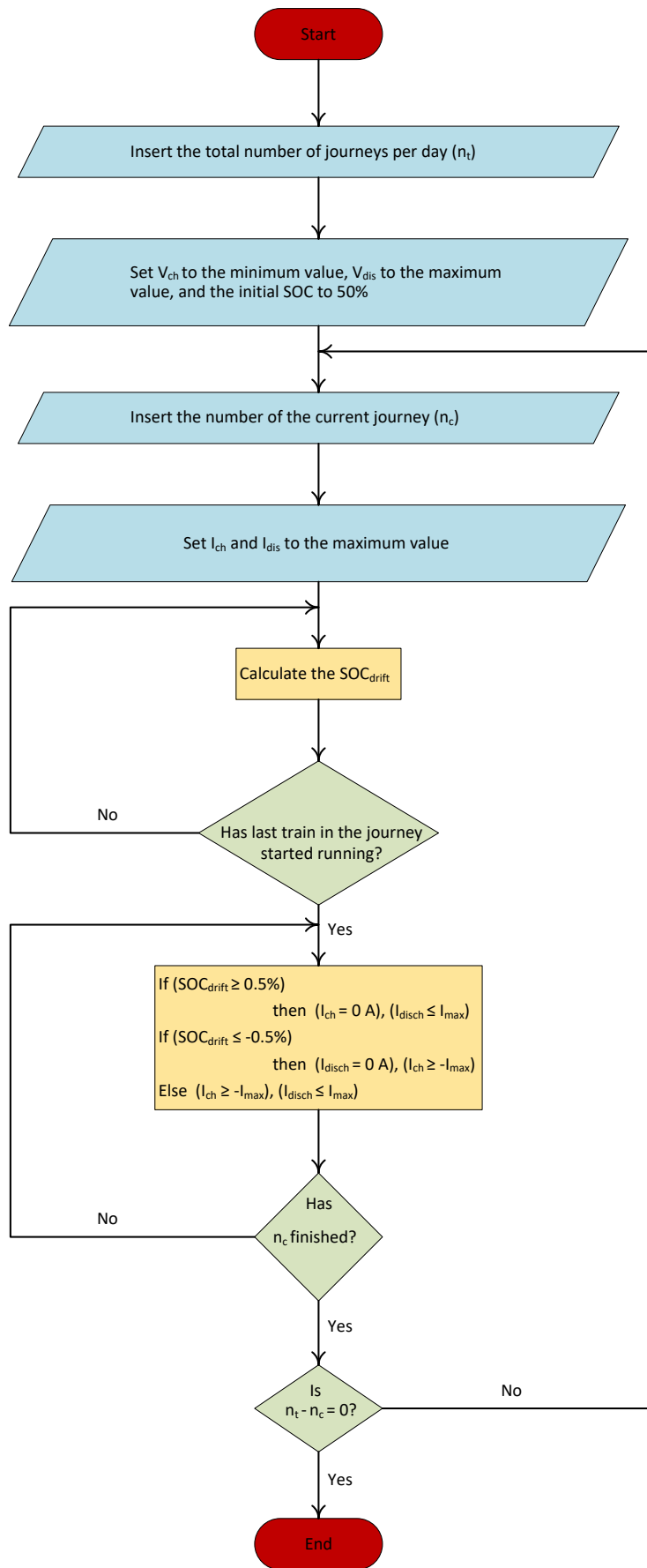


Figure 5.1: Flow chart of the SOC control

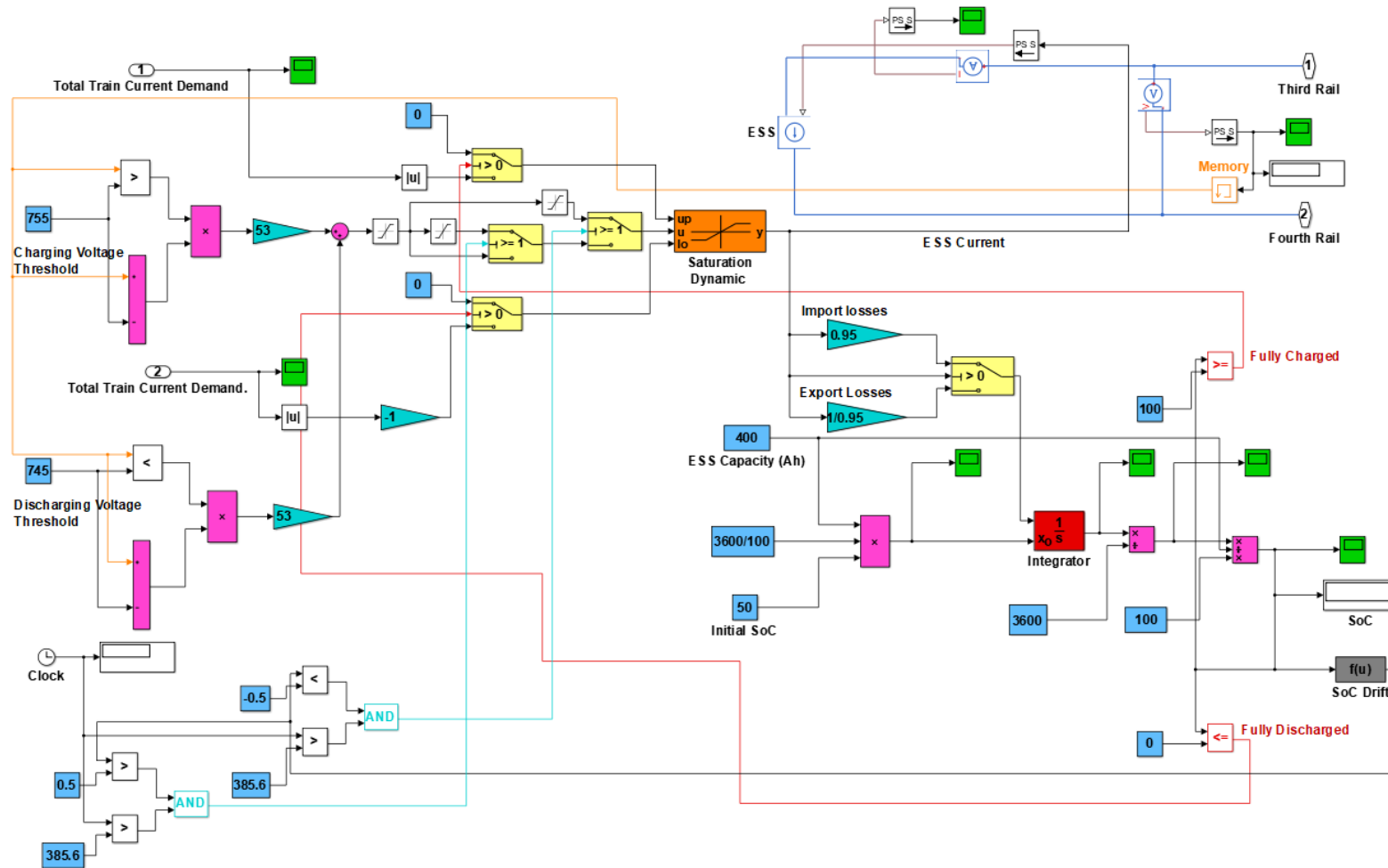


Figure 5.2: Screen capture of an ESS under the control of SOC controller 1 modelled in MATLAB Simulink

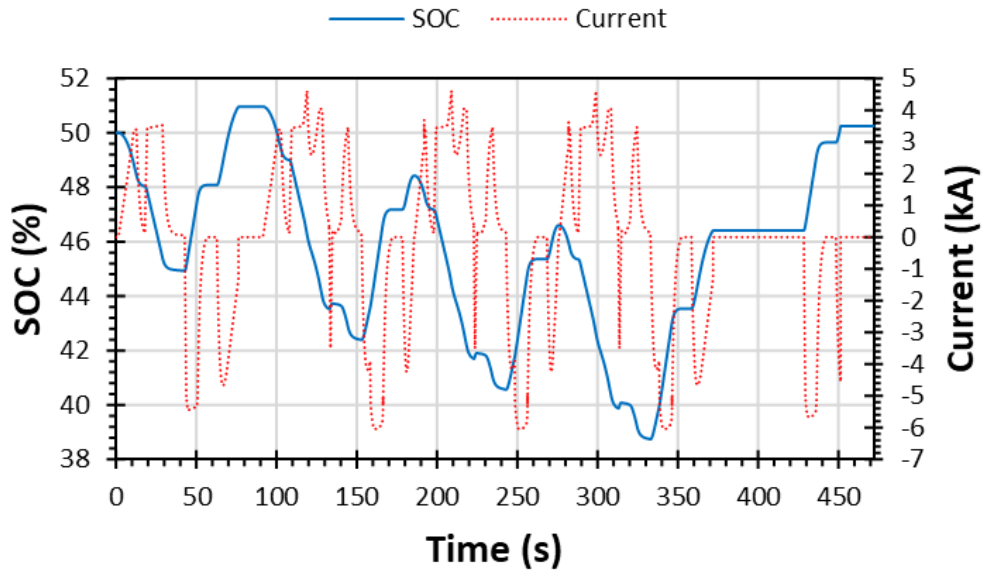


Figure 5.3: SOC and current of the ESS implementing SOC controller 1 when simulating the ideal traffic scenario

5.2.2 SOC controller 2

The SOC controller 1 discussed in the previous subsection did not gradually change the current limits until reaching the desired SOC. It simply set the input/output (as required) current of the ESS to zero when the last train started operating in order to reduce the SOC drift to minimum levels. Moreover, it did not fully capture the knowledge of future changes to SOC that could be predicted from the load profile variability. Therefore, fuzzy logic control was adopted to render the controller more flexibility in changing its control parameters by introducing additional control actions based on the variability in the load profile. Moreover, the effectiveness of the proposed state machine control can be tested by comparing its performance with that of other control methods; namely, static control and fuzzy control. The test aims to check the ability of the control methods to reduce the SOC deviation in the presence of disturbances in the traffic conditions. A fuzzy logic control technique was adopted because of its ability to adapt control decisions based on expert knowledge in the form of linguistic rules stored in the controller. Further, a fuzzy logic control method simplifies and speeds up the design process in state machine control

that requires numerous if-then statements to deal with the uncertainty in the load profile.

Fuzzy logic control is where expert knowledge with linguistic measures – known as fuzzy set theory – is used to design controllers, allowing users to represent variables in natural language. In this study, expert knowledge is referred to those who work in the field of electric railway operation and control to improve energy efficiency. This approach is illustrated in Figure 5.4, where the expert has deep knowledge about the operation of the system and classify its behaviour and response to control inputs into different regions. For example variable 1 is low, increase input 2, variable 2 is very high, decrease input 2 by a large amount. Fuzzy logic embeds this knowledge in the form of membership functions where the verbal descriptors (such as too high) as assigned a numerical range in a process called fuzzification. The set points and measurements are combined to form the outputs using an inferencing system providing ranges for the outputs. Precise output signals are then created through a defuzzification process. It is the fuzzification, inferencing system and defuzzification process embed the expert’s knowledge and it can provide remarkable results for systems that are nonlinear, subject to change or are difficult to model.

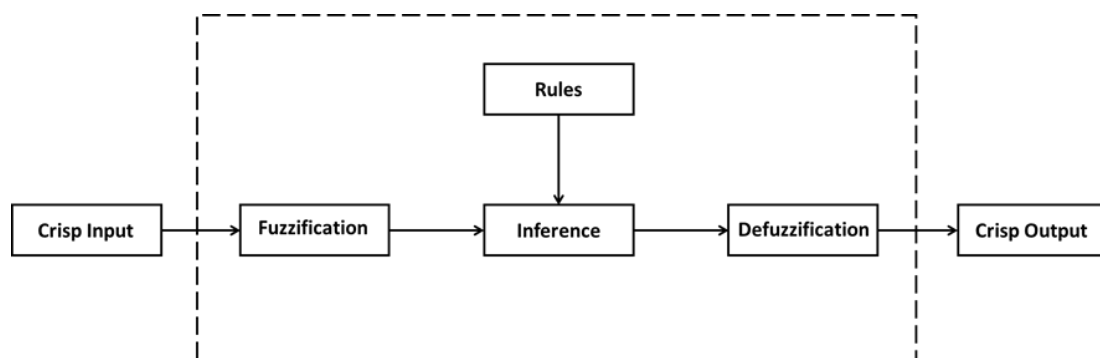


Figure 5.4: General structure of fuzzy control [145]

The inference engine produces fuzzy outputs from fuzzy inputs by applying fuzzy rules. Generally speaking, fuzzy rules are expressed in linguistic terms to describe relationships between the input and output variables. The degree of applicability is calculated for each rule and is represented in an output fuzzy set. Finally, the fuzzy outputs are synthesised and defuzzified to produce a crisp output value. As the input and output values of the fuzzy controller are crisp, the controller can be interfaced on both sides with technical devices. In the present study, the SOC controller 2 was implemented to the stationary ESS placed at Passenger Station A using the Fuzzy Logic Toolbox for MATLAB as seen in Figure 5.5. The operational block diagram of the fuzzy control system is shown in Figure 5.6.

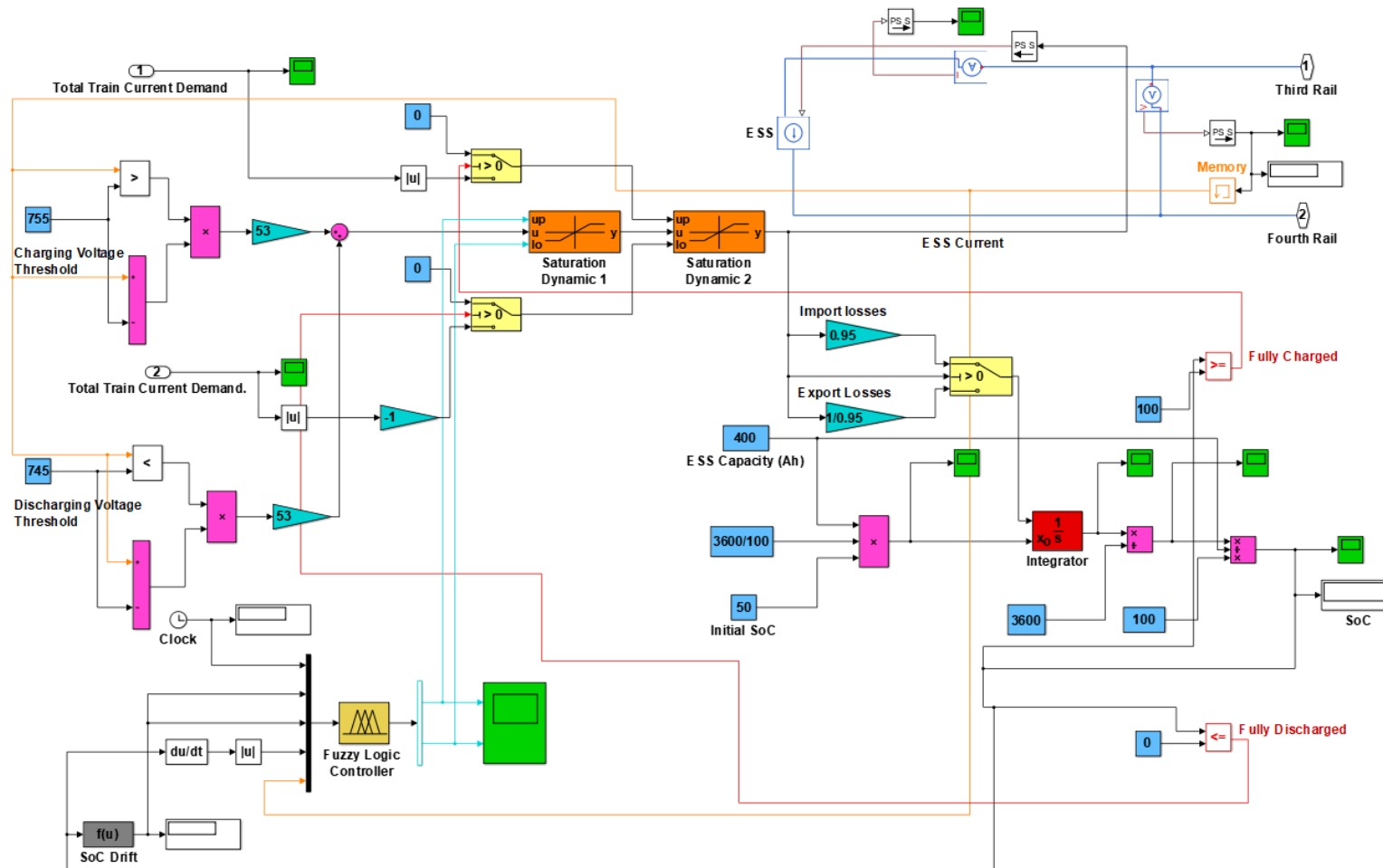


Figure 5.5: Screen capture of an ESS under the control of SOC controller 2 modelled in MATLAB Simulink

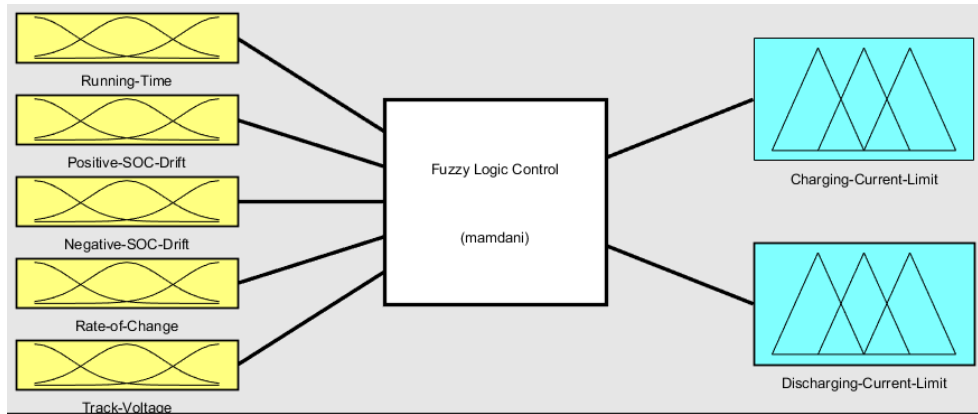


Figure 5.6: Input and output variables of the fuzzy inference system modelled using the Fuzzy Logic Designer Toolbox in MATLAB

The SOC controller 2 based on a fuzzy control strategy assessed the degree of SOC deviation with respect to time. If the SOC drift was high, the track power absorption/injection was reduced to minimum levels until it was cancelled. The remaining running time was used as an input, allowing the desired SOC value, which was 50% in this case, to be reached faster. Thus, the higher the deviation and the closer the time to the end of the predefined period (the time length of the journey) the more responsive the controller became.

The fuzzy rules were applied based on the expert knowledge regarding the railway system's operation to produce two outputs, i.e. I_{ch} and I_{dis} . These current limits were transmitted to the stationary ESS controller, as shown in Figure 5.7. The SOC controller 2 adjusted the current limits of the ESS controller based on the deviation of the actual SOC value from the desired one (SOC^*) that is 50%, SOC rate of change, and running time. Inclusion of the rate of change to the inputs was aimed to improve controller predictability by improving the forecast of the system behaviour, since both error value and its change were considered. This design should permit the controller to be more reactive to changes in the track power demand. Unfortunately, the capacity of SOC controller 1 implementing state machine to predict future changes is comparatively limited, which diminishes controller reactivity and thereby the improvements in the system performance that can be attained.

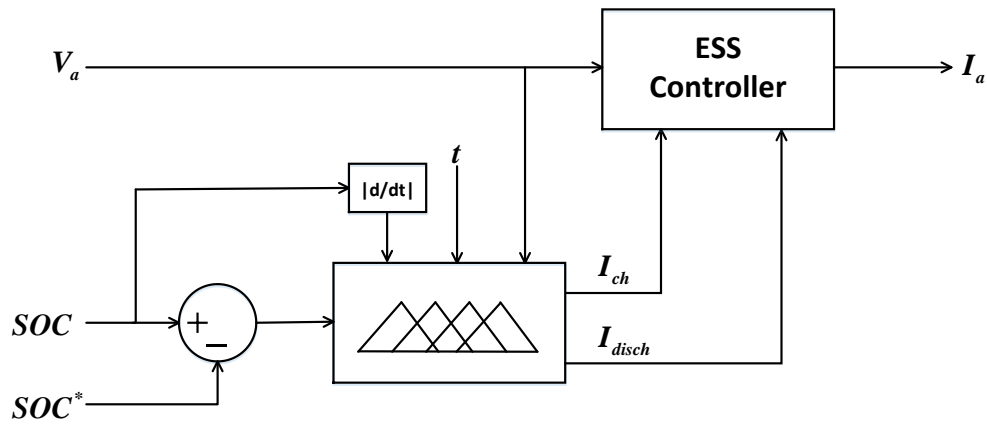


Figure 5.7: Fuzzy energy management system

As the SOC value can be both higher and lower than that desired, the corresponding SOC drift can be both positive and negative. Linguistic values of the SOC drift with a positive/negative sign indicate that the current SOC is higher/lower than the desired SOC value. Therefore, SOC drift input set was separated into positive and negative values to ensure that the controller behaved accordingly. In the negative drift stage, the controller attempted to increase the charge energy and reduce the discharge energy, while the reverse applied in the case of the positive drift stage. The “SOC rate of change” input (related to the “track voltage” input) played a vital role in reducing the SOC deviation. For example, when the SOC drift was negative, the track voltage was below the no-load voltage and the SOC rate of change was high, the fuzzy controller attempted to rapidly reduce the ESS discharge energy in order not to aggravate the situation. In contrast, when the track voltage was above the no-load voltage, the controller intervention was less intrusive because the high rate of change indicated that the energy trend would help mitigating the negative deviation causing the SOC to shift towards the required value.

The rule table that draws relationships between input and output variables to be submitted to the inference engine—as provided in Appendix 1, Table A1—comprises 256 rules that were applied to control the outputs based on if-then statements. It was mentioned in [146] that formulating the rules is the heart of the fuzzy controller design and they can be deduced from observations made by human experts. The rules have to be complete (any combination between inputs produces an

output value), consistent (no contradictions), and continuous (small change in the input value does not result in a high change in the output value). In this present study, the Mamdani fuzzy interface (a type of fuzzy inference where the input and output of each rule are linguistic variables necessitating defuzzification) was adopted for processing the input variables; namely, the SOC drift, the running time, and the rate of change in the SOC profile. The numerical input variables are transformed into linguistic format to allow the rule base to determine the output linguistic variables based on the membership degree—a real number ranging from 0 to 1. The membership degree for different elements in the universe of discourse (the set comprising of all the elements considered in the problem) forms a fuzzy set. The fuzzy sets pertaining to the input and output variables are shown in Figure 5.8–5.14, where the membership functions (fuzzy regions) denoted as VL, L, A, and H represent very low, low, average, and high, respectively, and membership function VH represents very high. It is worth mentioning that the other option for fuzzy processing was Sugeno fuzzy interface that is the same as Mamdani except for the output memberships where they are represented in mathematical functions which does not involve a defuzzification process. However, this method is less commonly used as it is more difficult to formulate [146].

In this instance, the rules governing the performance of the SOC controller 2 were formed to avoid the SOC from approaching too closely the maximum and minimum limits while satisfying energy saving. As previously noted, 50% SOC served as the reference value for the controller, the sensitivity of which was governed by the required end time. The closer the running time to the end of the chosen period, the more responsive the controller became. Consequently, the controller attempted to shift the SOC as close to the 50% reference value as was feasible before the end of the predetermined period. However, the controller was designed to be reactive to the SOC value that deviates significantly from the reference value even at the beginning of any journey under consideration. This of course will have more effect on the SOC drift as the remaining time decreases.

The design of the membership function in terms of width, shape and position in the universe of discourse of each element was determined via a trial-and-error process, which ceased once the controller performance was deemed satisfactory. There are no theoretical methods for defining membership functions and trial-and-error is the common approach as the design of fuzzy logic control mainly depends on the knowledge and experience of the designer. Therefore, the designer should make initial choices before testing and evaluating the influence on the system performance and based on the analysis results adjustments to the control parameters should be performed. The author of [146] recommended using this method for designing membership functions where Professor Lotfi Zadeh, who first introduced fuzzy logic in 1965, approved the book. It is worth mentioning that the number of membership functions describing each variable should be increased until being satisfied with the performance. However, the increase of memberships will increase the complexity of the controller because of the increase in the number of rules. Therefore, the number of membership functions is a compromise between the desired performance and control complexity. While the membership functions for all inputs and outputs were of a Gaussian shape, the outputs were subsequently defuzzified into crisp numerical values. It was stated in [146] that the performance of the system is not sensitive to the shape of the membership function and only small improvements can be achieved in particular cases. The defuzzification method implemented in this study was the middle of maximum. In this defuzzification method, the first and last from all values belong to the maximal membership degree are taken and the average of these two values is output as a crisp value. There are many defuzzification methods such as centre of area, centre of largest area, first of maximum, and last of maximum. However, no specific method has been proved to be better than the others, which allowed the middle of maximum method to be used in the current study.

The fuzzy set of the running time was set to cover the whole journey time with four subsets to give the controller the ability to behave differently in each time section. Further, the severity of the control action increased gradually until reaching the fourth subset where the controller harshly attempted to reduce the SOC drift to minimum levels. The fuzzy sets of the positive and negative SOC drift were set similarly where

the L, A, and H membership functions were uniformly distributed. The VH membership function was made wider to allow the controller to take rough actions when working in this SOC drift range to avoid the SOC drift from having high values that would make it challenging for the controller to manage before the end of the journey. The rate of change fuzzy set was set to give indications about future changes to the SOC profile to affect the control actions especially when working in the H and VH subsets of the SOC drift fuzzy set. The fuzzy set of the track voltage was only added to the controller to differentiate between positive and negative rate of change. It was noticed from the results presented in Chapter 4 that the system was more susceptible to have a positive SOC drift than that of a negative drift. Therefore, it was decided to make the VL membership function of the fuzzy set of the charging current limit I_{ch} narrower than that in the discharging current limit I_{dis} . This setting allowed the controller to charge with smaller currents than discharging currents especially at the end of the journey where there were more voltage peaks than voltage troughs. In contrast, the H membership function of the discharging current limit set was made narrower than that in the charging current limit set. This setting maximised the discharging energy while reducing the charging energy, which facilitated controlling the SOC when reaching the last time section of the journey. The A and L membership functions of the charging/ discharging current limit fuzzy set were set to allow smooth transition from very low currents to high currents.

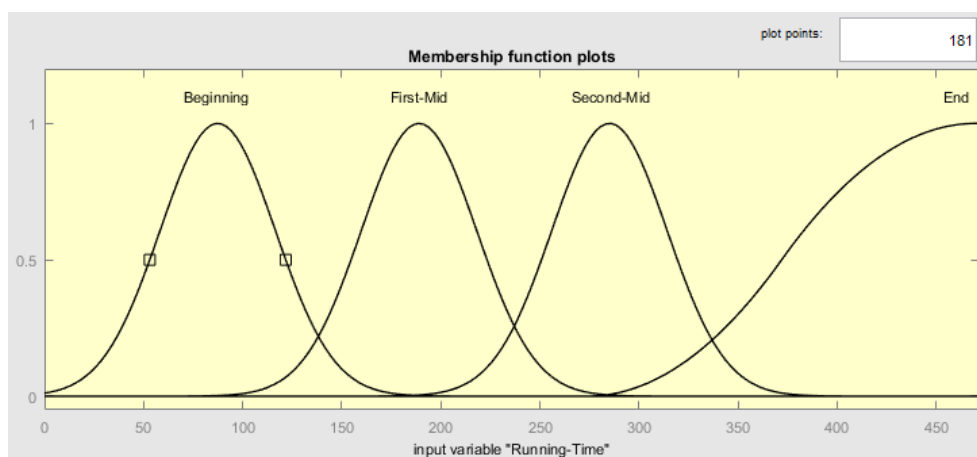


Figure 5.8: Input variable of the running time comprising four membership functions modelled using the Fuzzy Logic Designer Toolbox in MATLAB

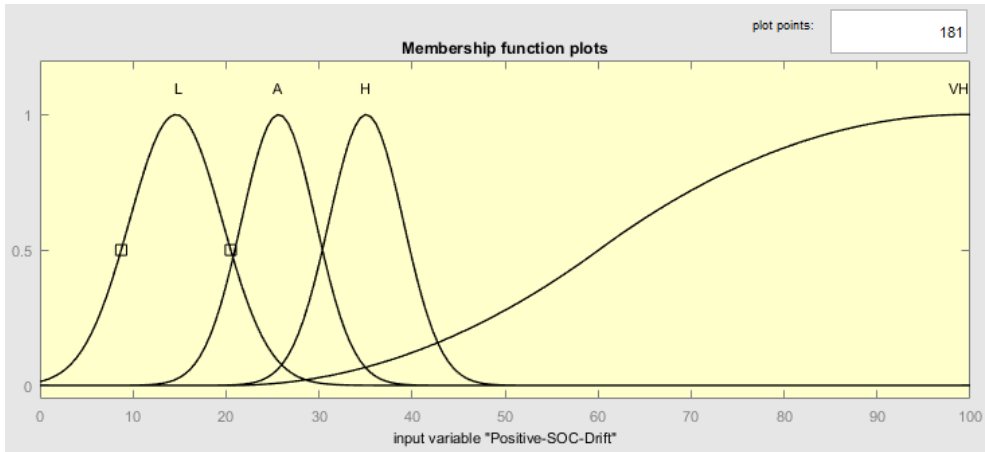


Figure 5.9: Input variable of the positive SOC drift comprising four membership functions modelled using the Fuzzy Logic Designer Toolbox in MATLAB

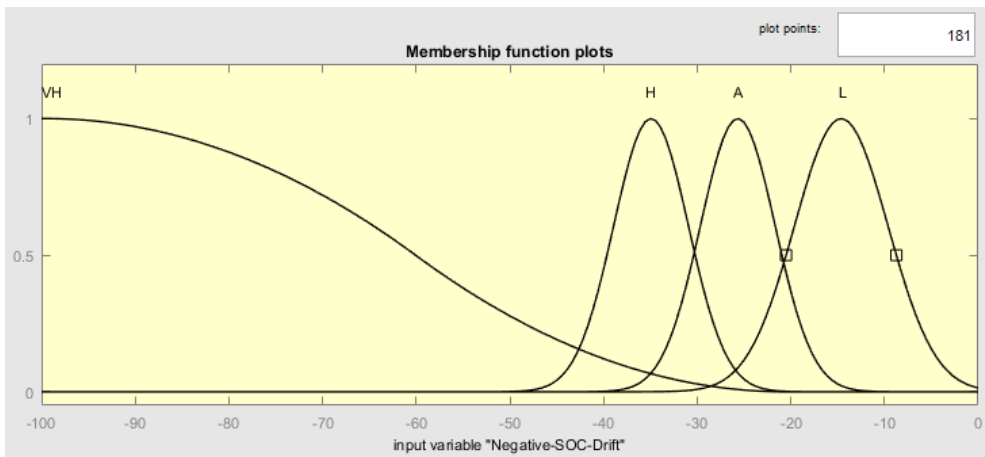


Figure 5.10: Input variable of the negative SOC drift comprising four membership functions modelled using the Fuzzy Logic Designer Toolbox in MATLAB

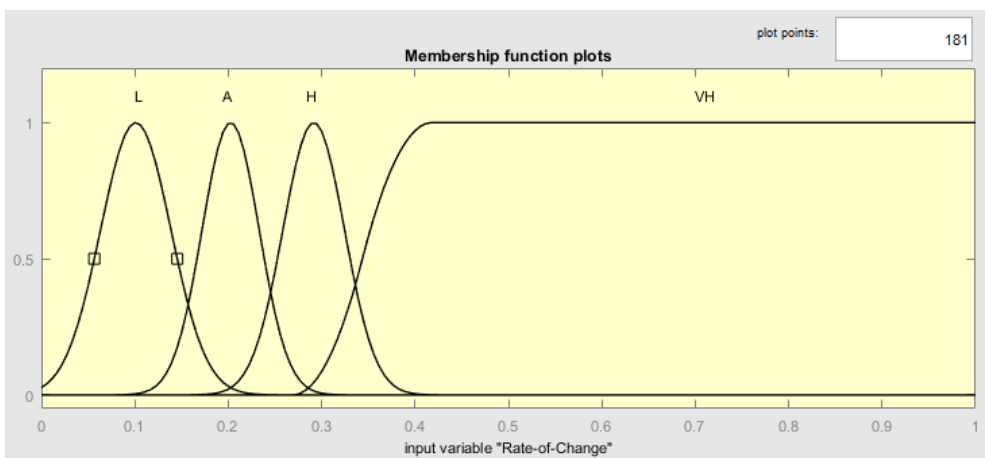


Figure 5.11: Input variable of the rate of change comprising four membership functions modelled using the Fuzzy Logic Designer Toolbox in MATLAB

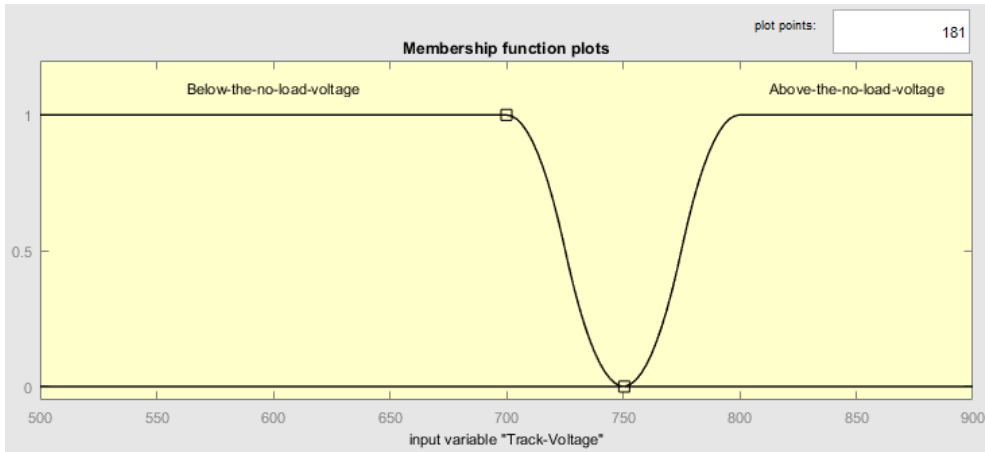


Figure 5.12: Input variable of the track voltage comprising two membership functions modelled using the Fuzzy Logic Designer Toolbox in MATLAB

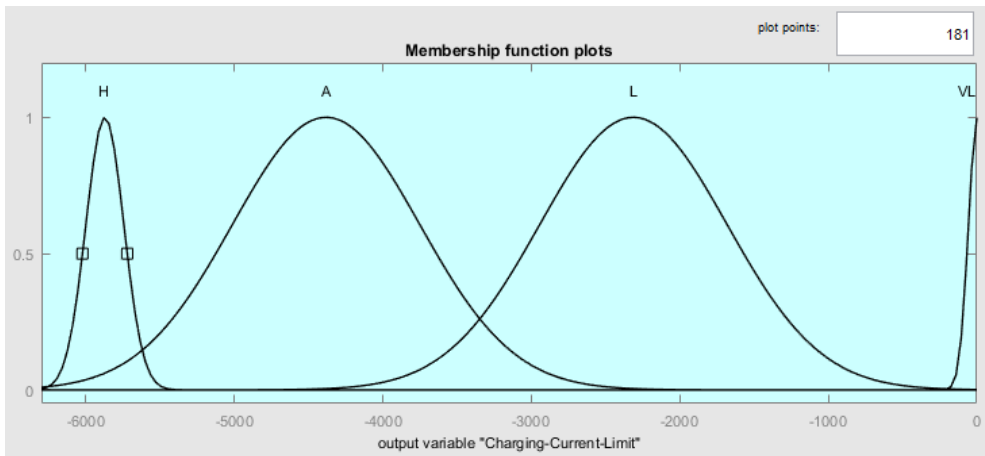


Figure 5.13: Output variable of the charging current limit comprising four membership functions modelled using the Fuzzy Logic Designer Toolbox in MATLAB

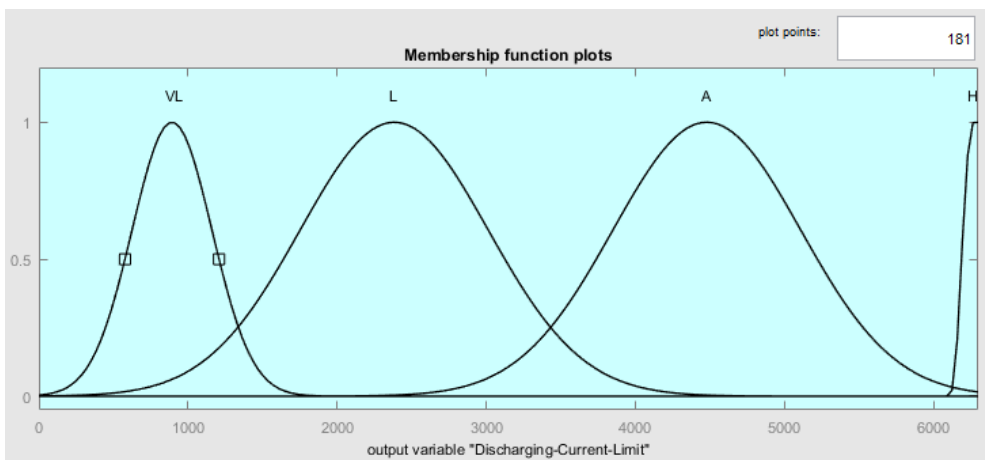


Figure 5.14: Output variable of the discharging current limit comprising four membership functions modelled using the Fuzzy Logic Designer Toolbox in MATLAB

Table 5.1 depicts a global analysis of the electric railway energy efficiency per journey when different ESS control approaches were applied under the ideal traffic scenario. The charging/discharging voltage threshold before applying the SOC control techniques was 755/740 V, whereas 6300 A was chosen as the maximum absolute current limit for charging/discharging. These limits were considered to be effective based on the energy analysis presented in Chapter 4. Although the deviation in the SOC was small before applying the SOC control methods, it declined even further to minimal levels when applying the SOC controller 2 as seen in Figure 5.15. It can be seen that the SOC drift was minimised considerably when using the fuzzy control strategy compared to the values obtained by applying the ESS without SOC control and the SOC controller 1. Moreover, the SOC controller 2 was clearly superior to the SOC controller 1 in terms of reducing the energy demand at substations. The static controller was capable of yielding the greatest reduction in the braking losses, which were least affected by the SOC controller 1. Since incorporating ESSs in electric railways increases the transmission losses, all three control techniques increased the transmission losses, especially the SOC controller 1, i.e. there was a 2.84 kWh increase in transmission losses. The impact of the static controller on the total energy saving was higher compared to those of other control methods. Even so, when interpreting these results, it should be noted that these calculations were based on a single journey. Consequently, the obtained savings cannot be extrapolated to multiple journeys when the SOC is not controlled, because the ESS is unavailable once the capacity limits are reached. The controllers were set to minimise the SOC deviation to minimum levels before the end of the journey. Therefore, the adverse impact of the controllers on the energy saving could be negated in the long term.

Table 5.1: The impact of applying different control approaches to the ESS on the railway's energy efficiency under the ideal traffic scenario

	Without SOC Control	SOC Controller 1	SOC Controller 2
Substations energy demand reduction	27.42% (86.6 kWh)	25.18% (79.53 kWh)	26.79% (84.61 kWh)
Transmission line losses reduction	-16.42% (-2.6 kWh)	-17.97% (-2.84 kWh)	-17.7% (-2.8 kWh)
Braking resistors losses reduction	78.82% (122.3 kWh)	73.35% (113.8 kWh)	77.41% (120.1 kWh)
Total energy saving	42.38% (206.3 kWh)	39.13% (190.5 kWh)	41.48% (201.9 kWh)
SOC drift	-0.4%	0.5%	0.03%

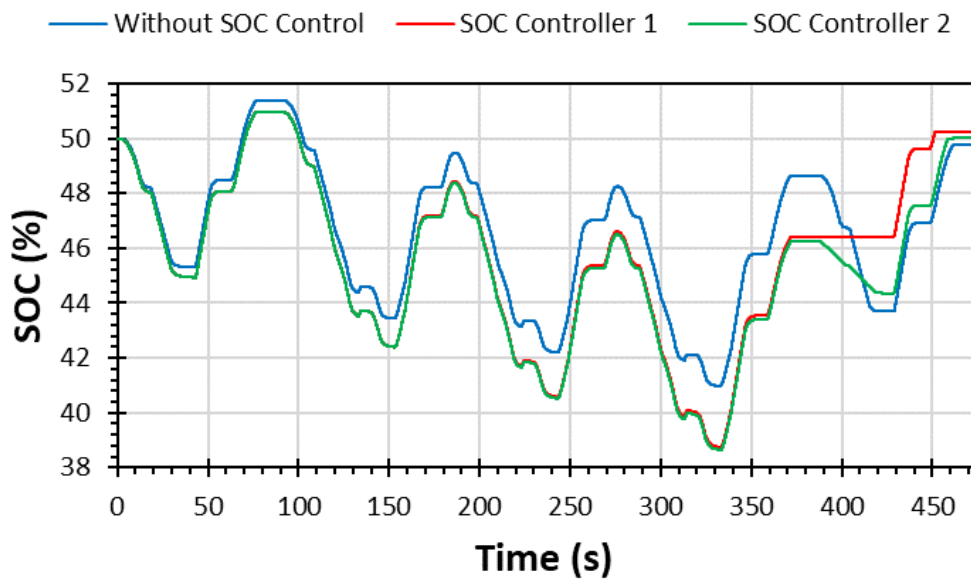


Figure 5.15: SOC of the ESS when the ideal traffic scenario was simulated

The impact of applying different control techniques to the ESS on the voltage at Passenger Station A can be seen in Figure 5.16, and the ESS current is displayed in Figure 5.17. The graphs show that, the three control techniques tended to maintain the charging and discharging current limits at high values, which reduced the voltage peaks and drops. When the SOC control was applied, at the beginning of the journey, the SOC controllers 1 and 2 maximised the charging/ discharging current, but reduced it to minimum values near the journey's end to limit the SOC deviation. The related graphs show that the fuzzy approach was more dynamic in the charging and discharging process due to the high number of subsets describing each input/output

variable. It is also noteworthy that the change in the current limit imposed by the fuzzy control near the end of the journey was more frequent than the SOC controller 1 but its amplitude was lower than the static controller. When applied, the state machine control initially maintained the current limits at maximum values, while it started vacillating between 0 and the maximum braking current near the end of the journey.

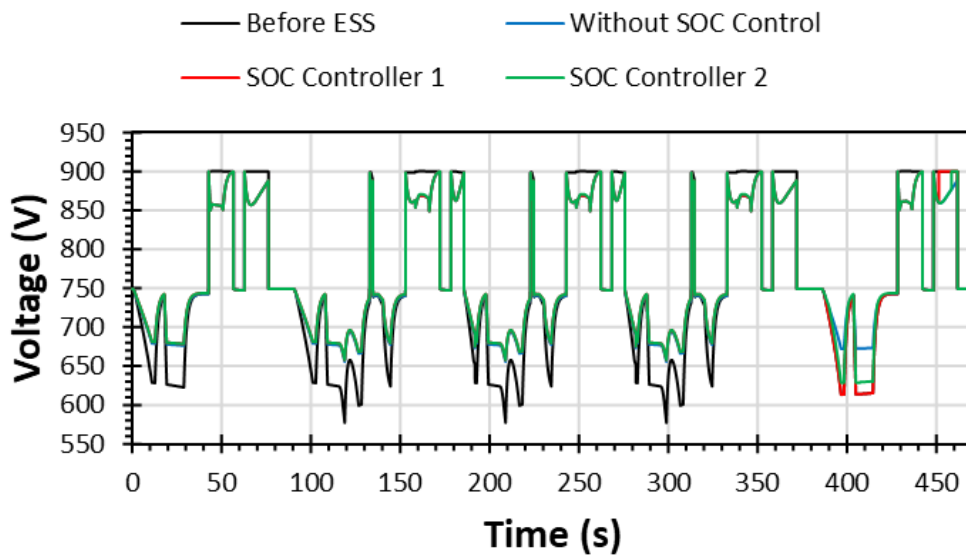


Figure 5.16: Voltage at Passenger Station A under the ideal traffic scenario

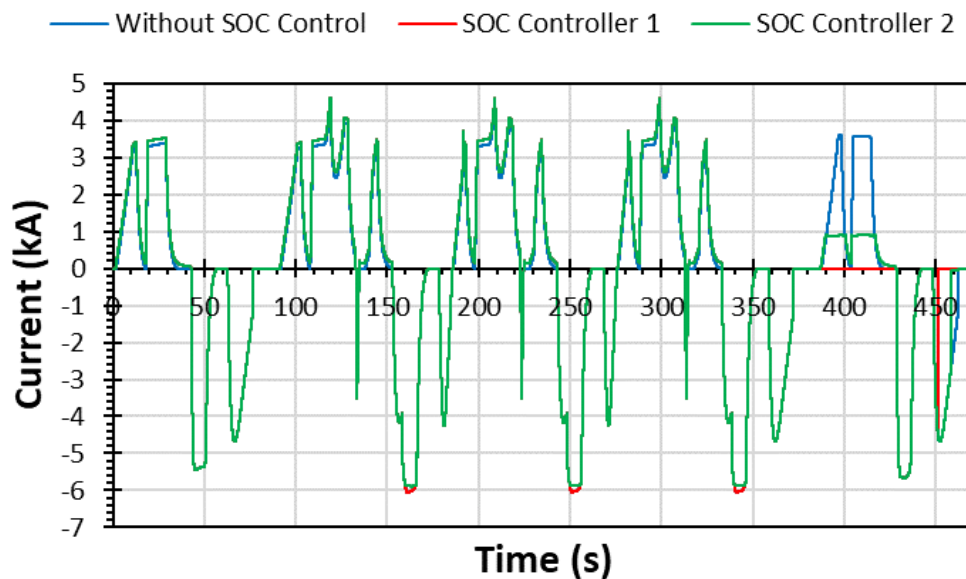


Figure 5.17: The ESS current yielded by different control approaches when the ideal traffic scenario was assumed

5.3 Energy efficiency analysis when applying multiple traffic scenarios

In this section, the performance of the proposed control methods is evaluated by observing the electric railway model response, and controller robustness to changes in operational conditions is examined. The impact of the proposed control methods on the SOC profile is evaluated by considering two scenarios, which have been specifically chosen to demonstrate the effects of variations in train timetables on the ESS SOC profile. The static controller was applied with 755/740 V charging/discharging voltage threshold and 6300 A current limit. It is worth mentioning that the SOC controller 1 and SOC controller 2 were not retuned when changing the traffic scenario. However, when using the SOC controller 2 the journey time was changed to match the new traffic scenario by adjusting the range end of the running time input variable where all membership functions were scaled automatically by MATLAB.

5.3.1 Changing train headway scenario

To assess the performance of the new proposed control methods with respect to multiple traffic scenarios, it was decided to apply a change to the headway. In practice, even a small deviation in the headway could result in significant variations in the track voltage and the ESS SOC profile. Therefore, the ability of the proposed control methods to cope with a change in train headway was examined by focusing on a scenario in which Train 8 headway was changed from 90 to 190 s. Train 8 was chosen for headway changing because this was the last train in the journey to stop at the ESS location, which was expected to lead to a significant impact on the SOC profile. The train headway was set to 190 s as this was the minimum headway to allow power utilisation as mentioned in Chapter 3, Section 3.4.6. The graph shown in Figure 5.18

indicates the capacity of the proposed control techniques to handle the impact of this sudden change in the system operation on the SOC drift. As shown in Table 5.2, the initial total energy saving in the system of 212.6 kWh declined to 207.6 kWh after applying the SOC controller 1 while the SOC controller 2 increased it to 214.3 kWh.

Although inducing changes to the Train 8 headway exacerbated the SOC deviation to a value of 5.04% (calculated using Equation 4.4), the SOC controllers 1 and 2 were successful in maintaining this deviation within the minimum limits. They were also effective at reducing the energy demand at the substations compared to the static control technique that reduced the substations energy demand by only 85.4 kWh. The SOC controller 1 had less impact than the SOC controller 2 in reducing the substations energy demand as it reduced it by 87.04 kWh where the latter one reduced it by 90.17 kWh. The dynamic controllers increased the losses in the transmission lines in slightly bigger amounts than the static controller. The SOC controllers 1 and 2 increased the transmission losses by 3.43 and 3.36 kWh, respectively, while the static controller increased them by only 3.35 kWh. The static controller outperformed others in reducing the losses in the braking resistors as it reduced the losses by 81.31%, which equates to 130.5 kWh. The SOC controller 1 was observed to be the worst in reducing the braking losses as it reduced them by only 77.27%, which equates to 124 kWh while the SOC controller 2 reduced the losses by 79.46%, which equates to 127.5 kWh.

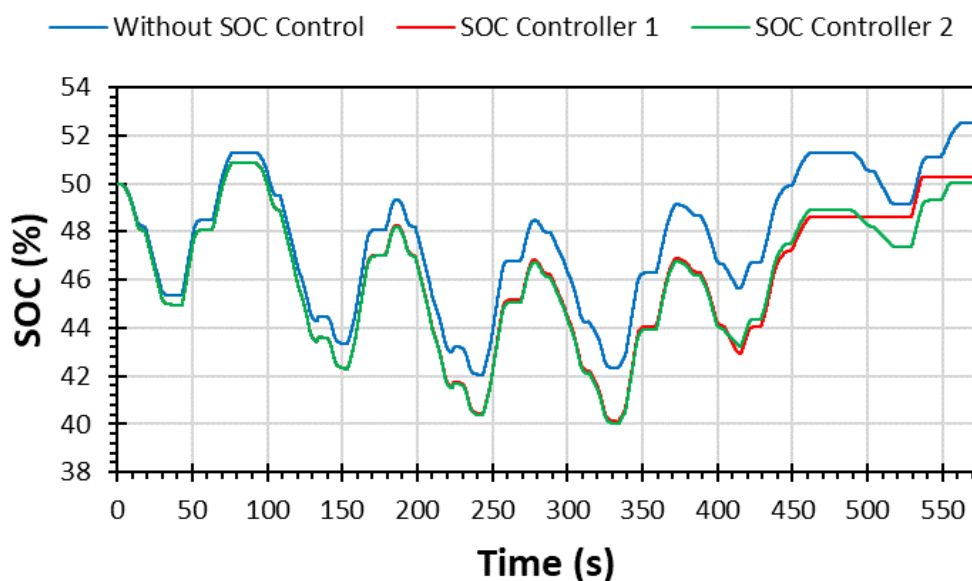


Figure 5.18: SOC of the ESS when Train 8 headway was modified

Table 5.2: The impact of applying different control approaches to the ESS on the railway's energy efficiency when Train 8 headway was modified

	Without SOC Control	SOC Controller 1	SOC Controller 2
Substations energy demand reduction	26.59% (85.4 kWh)	27.11% (87.04 kWh)	28.08% (90.17 kWh)
Transmission line losses reduction	-21.11% (-3.35 kWh)	-21.57% (-3.43 kWh)	-21.13% (-3.36 kWh)
Braking resistors losses reduction	81.31% (130.5 kWh)	77.27% (124 kWh)	79.46% (127.5 kWh)
Total energy saving	42.72% (212.6 kWh)	41.73% (207.6 kWh)	43.08% (214.3 kWh)
SOC drift	5.04%	0.5%	0.07%

The voltage at Passenger Station A shown in Figure 5.19 indicates that, there was less available traction energy for SOC management in this scenario compared to the previous case. In other words, the assumption that Train 8 headway was changed to 190 s led to a reduction in voltage drops of the ESS terminal voltage, which in turn reduced the energy released by the ESS, limiting the negative SOC deviation. Therefore, the positive SOC deviation was high which caused the SOC controller 2 to discharge more energy than the SOC controller 1 to reduce the positive SOC drift. To be more specific, at the end of the journey the charging/discharging current limit of the SOC controller 1 was maintained within a very narrow range from the maximum value as indicated in Figure 5.20. The graph shows that the ESS current in the absence of SOC control was maximised, and became dynamic after application of the two control methods, whereby the fuzzy approach can be seen to have been smoother and more flexible in adapting the limit.

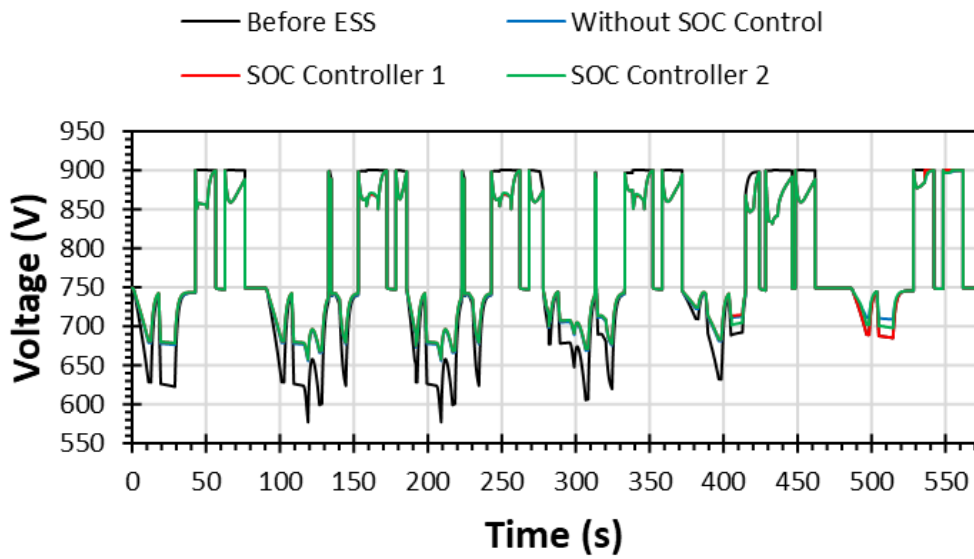


Figure 5.19: Voltage at Passenger Station A when Train 8 headway was modified

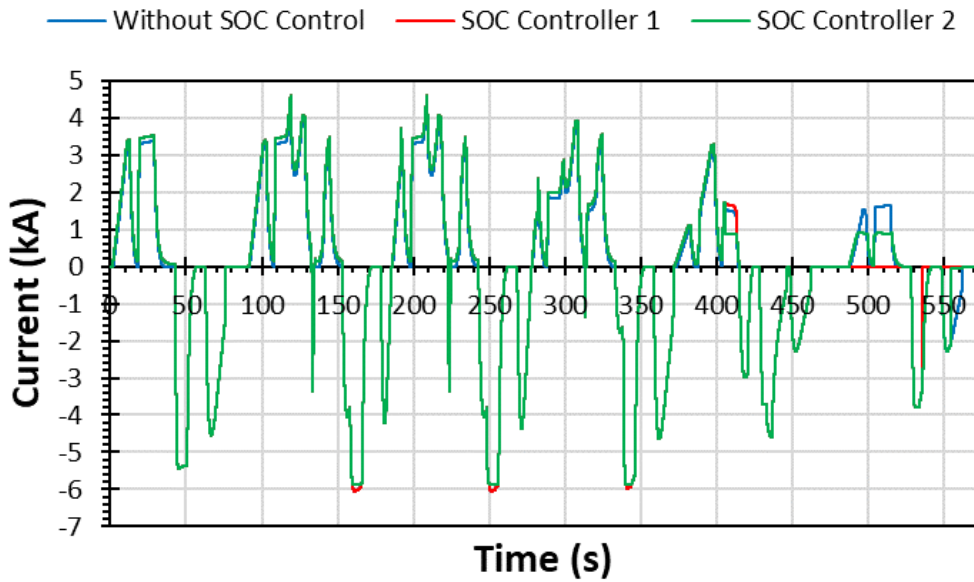


Figure 5.20: The ESS current determined by different control approaches when Train 8 headway was modified

5.3.2 Stochastic traffic scenario

The results reported in the preceding subsections were based on ideal traffic conditions, including fixed dwell time, headways, and speed profiles. Small disturbance to the ideal traffic scenario was also applied to test the performance of the controller. In this scenario, more complex traffic conditions were simulated to test the reliability of the proposed controllers. Passengers and drivers introduce random variations to the dwell time, headways, and speed profiles. Therefore, stochastic dwell time, headways, and speed profiles were adopted in this test. The new traffic scenario is illustrated in Figures 5.21 and 5.22.

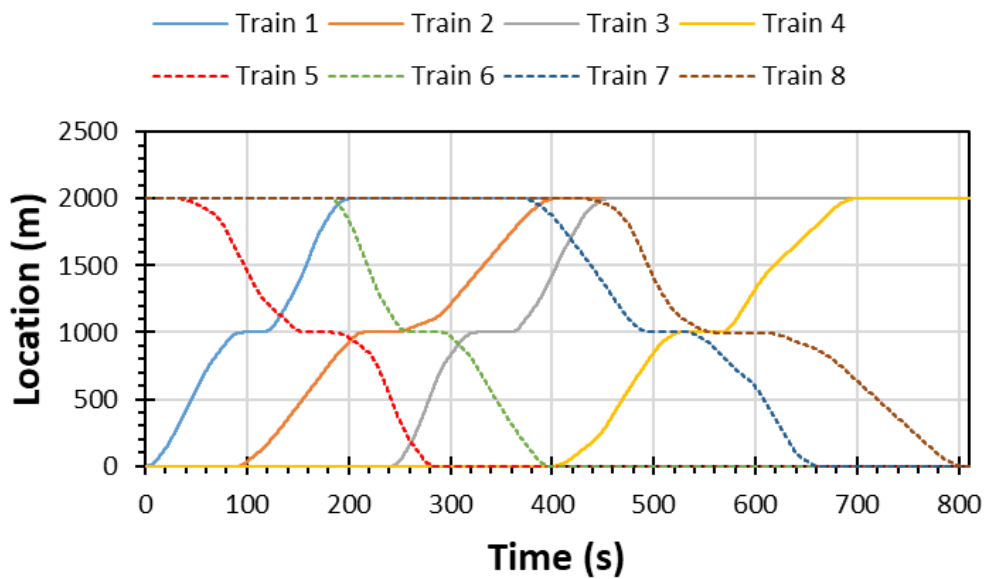


Figure 5.21: Train diagrams for the railway system exhibiting stochastic behaviour

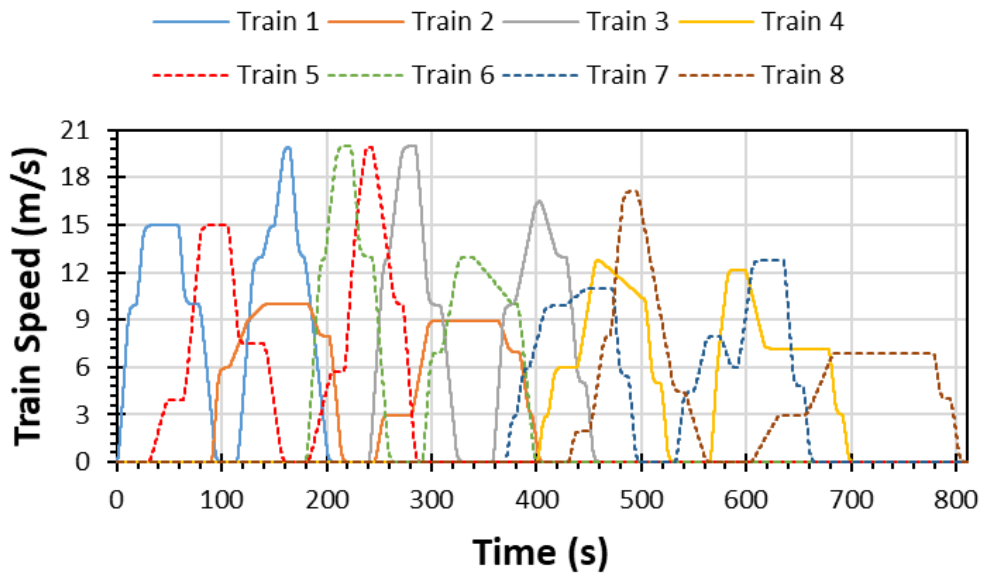


Figure 5.22: Train speed profiles in the railway system exhibiting stochastic behaviour

The simulation results demonstrate that the SOC controllers 1 and 2 were able to accommodate the more complex situation, as shown in Figure 5.23. The data presented in Table 5.3 show that the total energy saving after the first journey was increased from 80.92 kWh when implementing the static control technique to 86.21 and 86.66 kWh, after applying the SOC controllers 1 and 2, respectively. Figure 5.24 shows the voltage at Passenger Station A before and after applying the ESS, and the ESS current is shown in Figure 5.25. It can be noted that the voltage troughs were lower and the voltage peaks were more frequent than those in the previous traffic scenarios. Further, the ESS charging and discharging currents were lower in magnitude due to the traffic scenario that did not always require the trains to work on the maximum power.

According to the global energy efficiency analysis of the railway system shown in Table 5.3, the SOC controllers 1 and 2 were capable of reducing the SOC drift without having a negative impact on the energy efficiency. The only exception to this rule is the transmission line losses, as the SOC controller 1 and SOC controller 2 increased the losses by 1.3 and 1.28 kWh, respectively, while the static controller increased it by 2.11 kWh. The static controller, SOC controller 1, and SOC controller 2 reduced the braking resistors losses by 55.05, 51.00, and 51.01 kWh, respectively. In

line with the results reported in the preceding sections of this chapter, the static controller imposed a greater reduction to the losses in the braking resistors compared to the other two control techniques. The static controller was found least capable compared to the other methods in reducing the substations energy demand as it reduced the demand by 27.98 kWh while the SOC controller 1 and SOC controller 2 reduced it by 36.51 and 36.93 kWh, respectively.

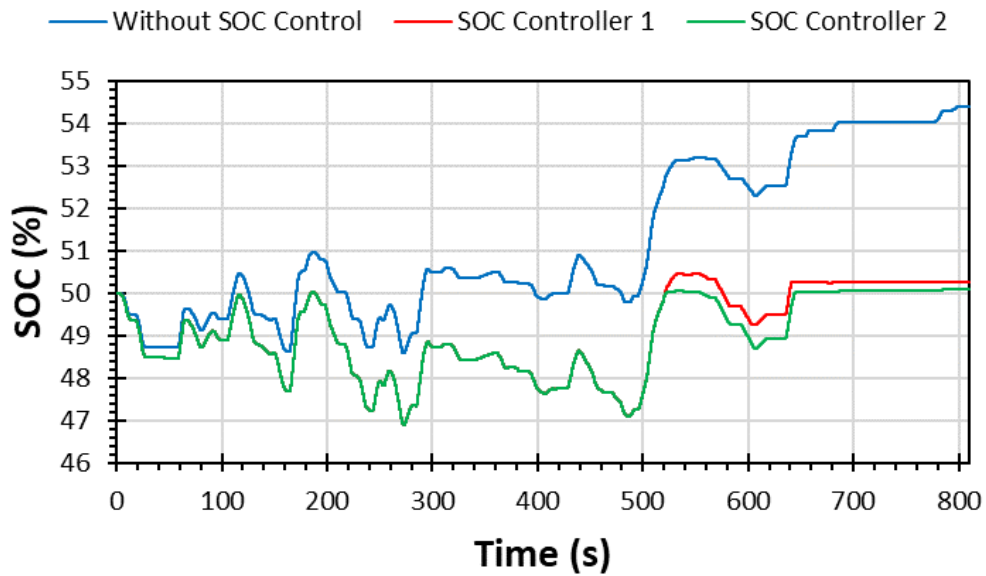


Figure 5.23: SOC of the ESS under a stochastic traffic scenario

Table 5.3: The impact of applying different control approaches to the ESS on the railway's energy efficiency under the stochastic traffic scenario

	Without SOC Control	SOC Controller 1	SOC Controller 2
Substations energy demand reduction	17.91% (27.98 kWh)	23.37% (36.51 kWh)	23.64% (36.93 kWh)
Transmission line losses reduction	-35.78% (-2.11 kWh)	-21.98% (-1.3 kWh)	-21.64% (-1.28 kWh)
Braking resistors losses reduction	95.01% (55.05 kWh)	88.02% (51 kWh)	88.04% (51.01 kWh)
Total energy saving	36.76% (80.92 kWh)	39.17% (86.21 kWh)	39.38% (86.66 kWh)
SOC drift	8.74%	0.5%	0.21%

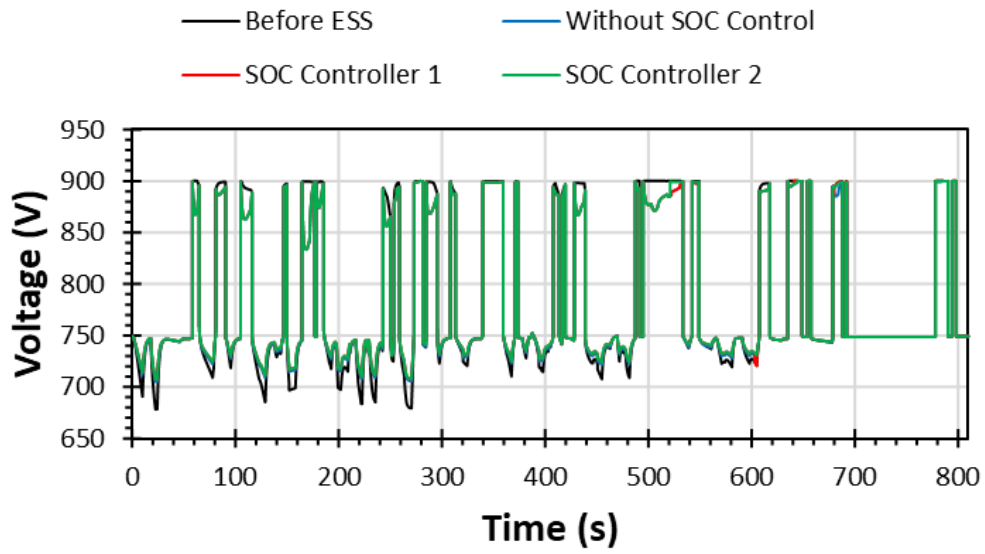


Figure 5.24: Voltage at Passenger Station A under a stochastic traffic scenario

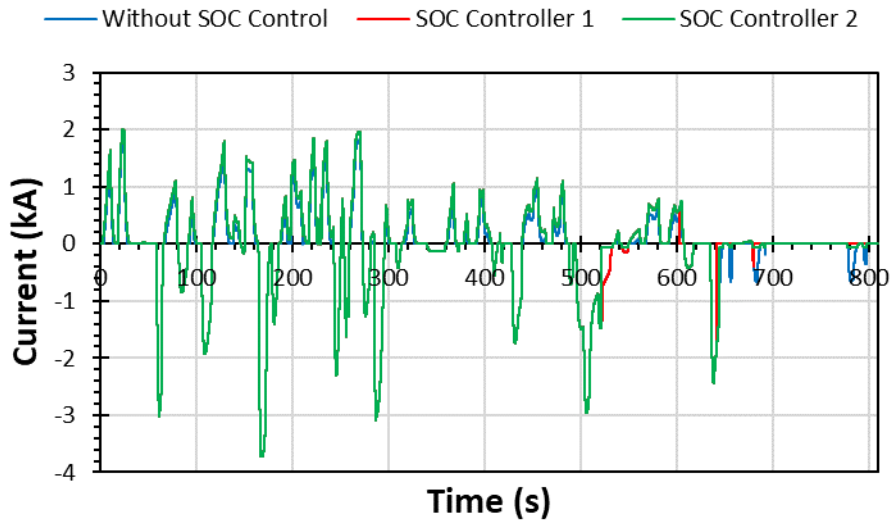


Figure 5.25: The ESS current determined by different control approaches under a stochastic traffic scenario

5.3.3 Two-day simulation

To assess the impact of the control methods considered in the present study on the railway's energy efficiency after multiple journeys, the ideal traffic scenario was simulated assuming two-day operation. It was assumed that the trains could only operate for approximately 18 hours per day which equates to 137 journeys. The two-day operation is equivalent to 36 hours and it was decided to show the impact of reaching the SOC boundaries when no SOC control was applied. The ESS was assumed to be lossless as stated previously in this thesis. It can be seen in Figure 5.26 that, in the absence of SOC control, the ESS repeatedly reached the lower SOC limit in the second day of operation, while the SOC controllers 1 and 2 were able to avoid this undesirable effect. Moreover, Table 5.4 shows that the total energy saving of 56,482 kWh for the two-day operation period without SOC management decreased to 51,971 kWh and 55,278 kWh after adopting the state machine method and the fuzzy control method, respectively. Although the SOC reached the minimum limit when applying the static controller, the ESS saved more energy than that when applying the SOC control methods that avoided reaching the minimum SOC limit. Further, the total energy saving only diminished by 0.08% compared to the case when the SOC boundaries were not reached. This was a result of the static controller applying the optimised voltage limits found by the MCDM method as explained in Chapter 4. However, the MCDM method is limited to known voltage profiles and cannot deal with online changes to the voltage profile as will be seen in the following tests. It is worth mentioning that the simulation results presented in this chapter indicate that the proposed control methods could increase the energy efficiency of a DC electric railway while minimising the ESS size and cost as they only used a small SOC range.

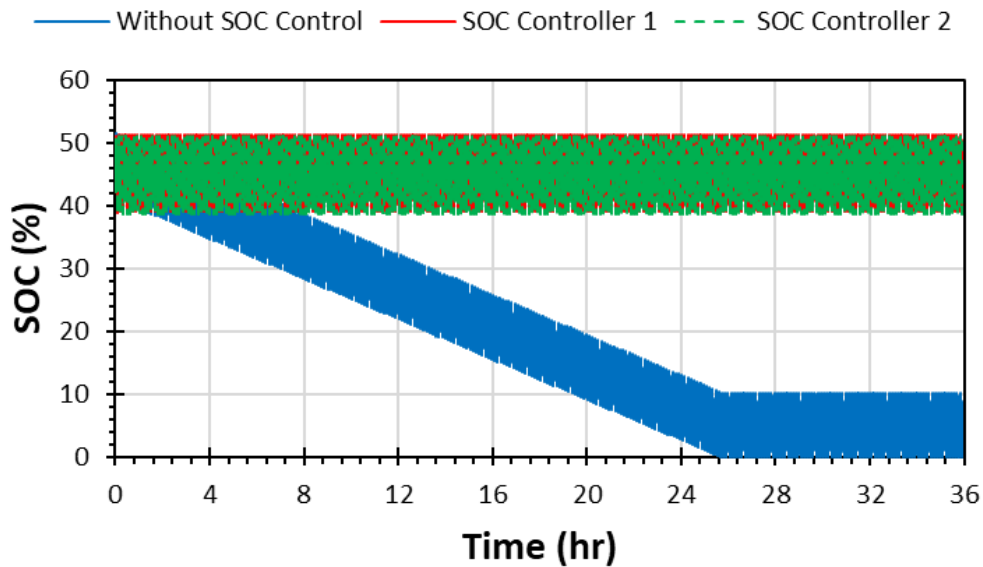


Figure 5.26: Two-day simulation based on the ideal traffic scenario

Table 5.4: Energy efficiency analysis when simulating the ideal traffic scenario for two days

	Without SOC Control	SOC Controller 1	SOC Controller 2
Substations energy demand reduction	27.37% (23,684 kWh)	25.18% (21,794 kWh)	26.77% (23,164 kWh)
Transmission line losses reduction	-16.42% (-712 kWh)	-17.82% (-773 kWh)	-17.66% (-766 kWh)
Braking resistors losses reduction	78.83% (33,510 kWh)	72.81% (30,950 kWh)	77.35% (32,880 kWh)
Total energy saving	42.34% (56,482 kWh)	38.96% (51,971 kWh)	41.43% (55,278 kWh)
SOC drift	-82.38%	0.52%	0.04%

Figure 5.27 shows the ESS SOC profile when simulating the railway system including modification to Train 8 headway. The railway system was simulated for two days (36 hours) where the number of journeys per day were 113 journeys. The static controller caused the SOC to reach the upper limit after twenty journeys, while the SOC controllers 1 and 2 avoided this undesirable effect. The SOC reached its boundaries much faster than that in the ideal traffic scenario due to releasing less energy and receiving more energy. Further, the shift in the headway caused the overlap between Train 4 and 8 to reduce, which reduced the voltage drop leading to less discharged energy. On the other hand, this shift in headway increased the number

of voltage peaks resulting in more charged energy by the ESS. The action of reaching the upper SOC limit in the absence of SOC control affected the total energy saving to diminish by 4% compared to the case when the SOC boundaries were not reached. The impact of the discussed control methods on the total energy saving in the system is presented in Table 5.5, depicting a global comparison across different cases. The total energy saving in the system after applying the ESS with static control approach was 46,112 kWh, and increased further to 46,728 kWh after applying the SOC controller 1. The SOC controller 2 increased the total energy saving to 48,416 kWh. The table shows that the static controller was the worst in reducing the dissipated energy in the braking resistors with only 27,535 kWh. Interestingly, the static controller was the best in reducing the braking resistors losses when simulating the system for only one journey as presented in Table 5.2. However, due to the frequent reach of the upper SOC limit, the ESS could not effectively store the regenerative energy which was the main reason for the static controller to cause less energy saving than the others.

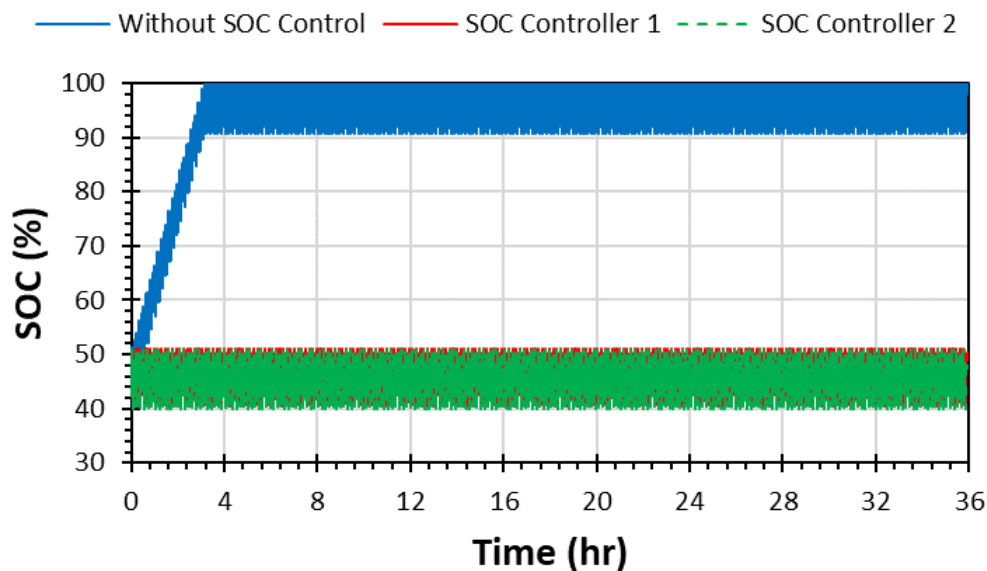


Figure 5.27: Two-day simulation based on the traffic scenario involving changes to the Train 8 headway

Table 5.5: Energy efficiency analysis when involving changes to the Train 8 headway

	Without SOC Control	SOC Controller 1	SOC Controller 2
Substations energy demand reduction	26.6% (19,303 kWh)	27.11% (19,676 kWh)	28.08% (20,381 kWh)
Transmission line losses reduction	-20.24% (-726 kWh)	-21.46% (-770 kWh)	-21.11% (-758 kWh)
Braking resistors losses reduction	75.94% (27,535 kWh)	76.73% (27,822 kWh)	79.41% (28,793 kWh)
Total energy saving	41.02% (46,112 kWh)	41.55% (46,728 kWh)	43.08% (48,416 kWh)
SOC drift	100%	0.5%	0.06%

Finally, the system was simulated under the stochastic traffic scenario for two days with 80 journeys per day. Figure 5.28 shows the ESS SOC profile where it shows that the static controller could not avoid the SOC from reaching the upper boundary while the SOC controllers maintained the SOC near the desired value. The SOC boundary was reached only after 12 journeys, which was faster than that in the previous tests. This adverse impact was a result of the low voltage drops and frequent voltage peaks. The low voltage drops were induced by the low train power demand and the frequent voltage peaks were induced by the low synchronisation between the trains when they were in the decelerating mode. Table 5.6 shows the global energy efficiency analysis where it can be seen that the SOC controller 2 successfully surpassed the other controllers in all aspects except for the transmission line losses reduction where it was better than the SOC controller 1 but worse than the static controller. The total energy saving when simulating the railway system for two days with the static controller reduced by 17.9% compared to the case when the SOC boundaries were not reached. The main reason for this significant effect was the inability of the ESS to receive sufficient regenerative energy, causing the dissipated energy in the braking resistors to increase. This can be explained by noting the reduction in the braking resistors losses after only one journey (see Table 5.3) where the static controller was superior before it became the worst among others after two-day operation.

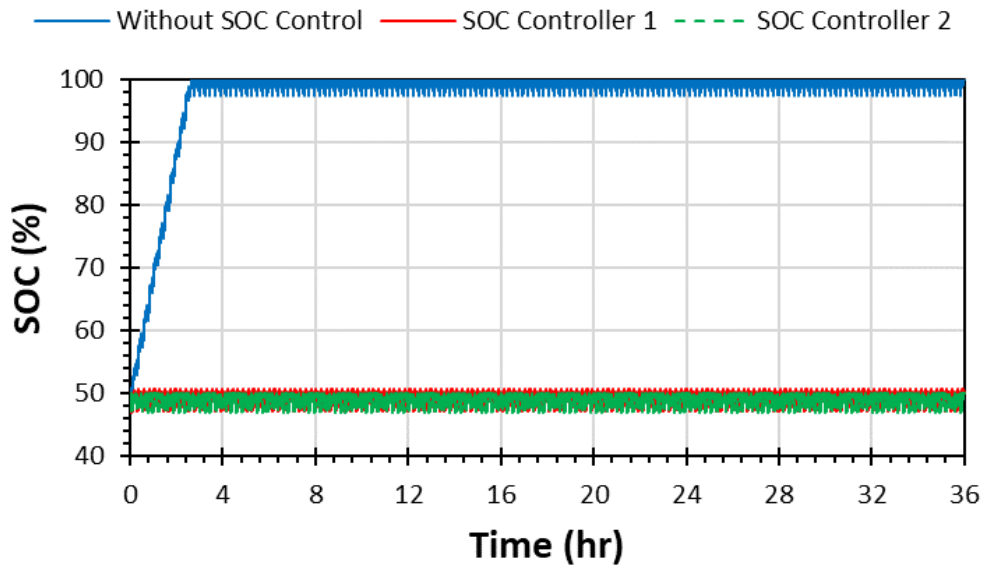


Figure 5.28: Two-day simulation based on the stochastic traffic scenario

Table 5.6: Energy efficiency analysis when simulating the stochastic traffic scenario for two days

	Without SOC Control	SOC Controller 1	SOC Controller 2
Substations energy demand reduction	17.88% (4,471 kWh)	23.37% (5,842 kWh)	23.64% (5,909 kWh)
Transmission line losses reduction	-19.76% (-187 kWh)	-21.91% (-207 kWh)	-21.54% (-204 kWh)
Braking resistors losses reduction	68.44% (6,345 kWh)	86.41% (8,011 kWh)	87.39% (8,101 kWh)
Total energy saving	30.18% (10,629 kWh)	38.75% (13,646 kWh)	39.21% (13,806 kWh)
SOC drift	100%	0.5%	0.2%

5.4 Conclusion

In this chapter, simulation results pertaining to a number of operating conditions were presented and compared to test the validity of the proposed control methodology. In addition, multiple traffic scenarios, involving changes to the headway, dwell time, and train speed profiles, were applied to introduce a degree of uncertainty to the system. The proposed controllers were demonstrated to be effective

under different traffic conditions, as they were successful in controlling the SOC by inducing dynamic variation to the current limits. The proposed SOC control methods eliminated the unavailability of the ESS due to the ESS being fully charged or discharged. The modifications in the ESS control characteristics resulting from adapting the configurations governed by the disturbance in the operating conditions were shown to improve the system energy efficiency. The applicability of the two discussed control methods to real application systems will be tested experimentally in the next chapter.

Chapter 6

Experimental Application of Adaptive Control Methods

6.1 Introduction

In Chapter 5, implementation in MATLAB software of two control methods for SOC management was explained in detail. The reported findings have demonstrated that the SOC levels can be adequately managed by applying appropriate dynamic charge/discharge control, without the need for an external load or power source. In this chapter, the experimental work is reported; the manner in which the previously discussed methods were applied to a lab-based supercapacitor ESS using a NI CompactRIO controller and a track voltage emulator. The main purpose of these experiments was to assess the applicability of the proposed control methods to practical hardware-based systems. Thus, this chapter also presents an evaluation of various track voltage profiles in order to determine their impact on the obtained SOC results. This series of evaluations is subsequently compared with the simulation results for validation.

6.2 Hardware configuration

During the experiments, the power flow between two DC sources was managed by a SINAMICS DCP bidirectional DC/DC converter (Siemens, Germany). For this purpose, an AL3000R programmable power supply (Zenone Elettronica, Italy) was connected to one side of the SINAMICS DCP converter to emulate the track voltage and a supercapacitor (Maxwell Technologies, United States) was connected to the other side to represent the ESS. A CompactRIO 9063 controller (National Instruments, United States) was used for data acquisition, transmission, and control. The hardware setup is depicted in Figure 6.1; a single-line diagram can be viewed in Appendix 2, Figure A1.

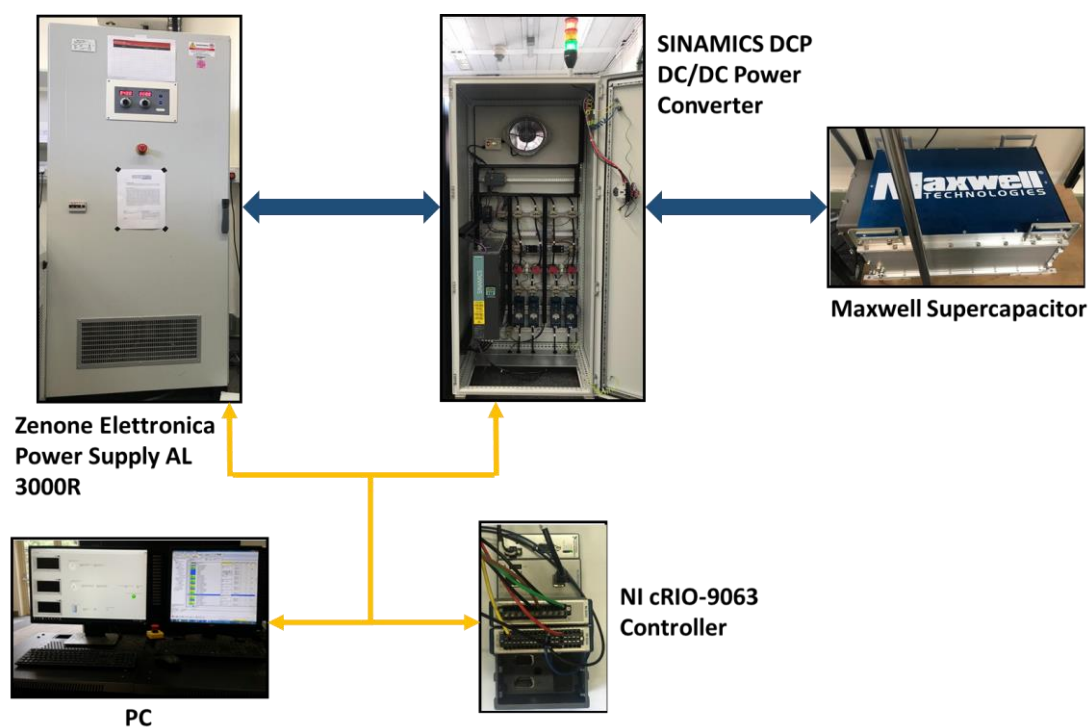


Figure 6.1: Hardware setup

6.2.1 Zenone Elettronica programmable DC power supply

A Zenone Elettronica power supply AL 3000R series with 600 V maximum voltage and 100 A maximum current was used according to the I–V characteristics shown in Figure 6.2. This type of power supply contains a series of fast AC/DC static converters that feature IGBT devices contained within two power conversion units, allowing it to supply/absorb power to/from the load. Due to the high conversion speed, this equipment can be used in applications characterised by highly dynamic requirements [147]. Therefore, this bidirectional power supply was used to emulate the track voltage that was previously simulated in MATLAB. The power supply is shown in Figure 6.3 and the relevant technical data are reported in Table 6.1. The front panel of this equipment contains a voltage adjustment potentiometer, current adjustment potentiometer, digital voltage display, digital current display, emergency stop, and line main circuit breaker.

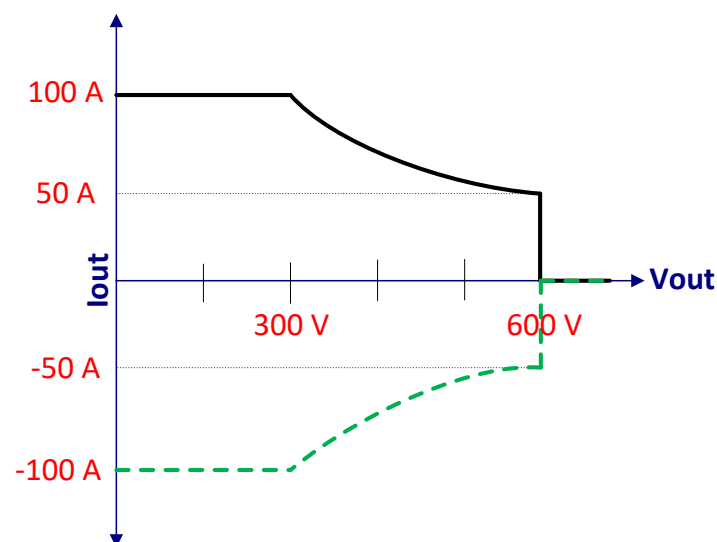


Figure 6.2: I–V characteristics of the bidirectional DC power supply with line regenerator [148]



Figure 6.3: Bidirectional DC power supply AL 3000R

Table 6.1: Technical specifications of the bidirectional power supply [148]

Quantity	Value
Voltage input	400 V, $\pm 10\%$
Frequency	45–65 Hz
Maximum line current	52 A
Maximum output power	30 kW
Maximum regenerated power	30 kW
Voltage output	0–600 V
Current output at V_{\max}	-50 to 50 A
Current output from 0 V to 300 V	-100 to 100 A
Dimensions (depth \times width \times height)	1000 \times 800 \times 1900 mm
Weight	500 kg
Operating temperature	5–40 °C

6.2.2 SINAMICS DCP DC/DC power converter

The SINAMICS DCP power converter is capable of controlling the power flow between two DC systems by performing voltage and current control. In the present study, this device was used due to its ability to charge/discharge ESSs with dynamic setpoints, which was required for the practical assessment of the control methods described in Chapter 5. During the experiments, the input side of the power converter was connected to the track emulator; the output side was connected to the supercapacitor. The technical specifications of the device are provided in Table 6.2, and the device voltage and current limitations are depicted in Figure 6.4. High power transfer efficiency of the SINAMICS DCP converter was established through measurements, as is shown in Figure 6.5.

Table 6.2: Technical specifications of the SINAMICS DCP power converter [149]

Quantity	Value
Rated voltage	600 V
Rated current	50 A
Rated power	30 kW
Switching frequency	20 kHz
Maximum power loss	800 W
Minimum operating voltage	30 V
Maximum operating voltage	800 V
Electronic power supply	24 V
Dimensions (depth × width × height)	545 × 150 × 600 mm
Weight	38 kg

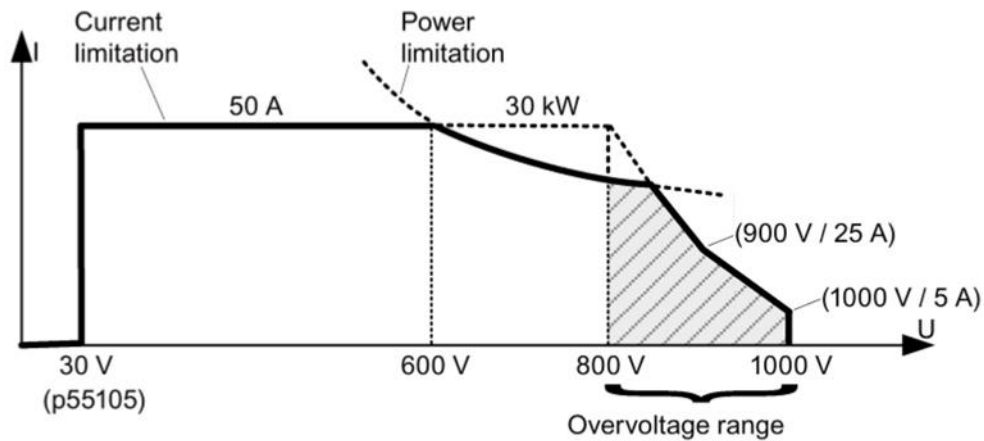


Figure 6.4: I–V characteristics of the SINAMICS DCP power converter [149]

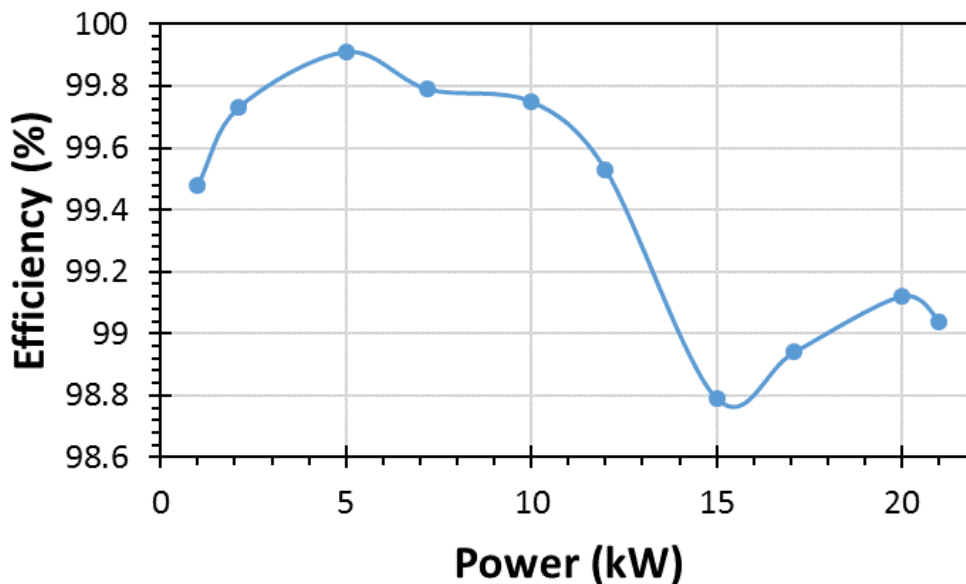


Figure 6.5: SINAMICS DCP DC/DC power converter efficiency measurements

The device was designed for cabinet mounting, as shown in Figure 6.6. In the present study, it was mounted vertically to allow the air to flow in the upward direction. Fuses, and line contactors were connected to the input and output side of the SINAMICS DCP converter. Four precharging resistors were also added to the cabinet to protect the capacitors on both sides of the drive unit from high current peaks. There were capacitors on the input and output of the SINAMICS DCP converter that were charged to the voltages of the connected devices on both sides. Therefore, the precharging resistors were used to slowly charge the capacitors to

protect the SINAMICS DCP converter from damages. Direct connection of the capacitors without the precharging resistors could result in high current peaks causing arcing that could permanently weld the contactors. Finally, an emergency stop, AC isolator, and on/off switch were attached to the cabinet's front door. Switching the device on switch enables the precharging resistors on both sides and the controllers.



Figure 6.6: SINAMICS DCP DC/DC power converter

6.2.3 CompactRIO controller

The CompactRIO controller is a real-time embedded controller equipped with a microprocessor and input (I)/output (O) modules. It was employed in the experiments to allow the SINAMICS DCP converter charging/discharging setpoints to be modified in real-time, according to the application requirements. In the work presented here, an NI cRIO-9063 controller with a microprocessor speed of 667 MHz was employed. The device can operate at temperatures ranging from -20 to 55 °C, and

since its voltage input ranges from 9 to 30 V, it was powered by an external power supply of 24 V capacity [150]. The device and its dimensions are shown in Figure 6.7.

The data exchange between the SINAMICS DCP converter and the microcontroller was accomplished by connecting two series I/O modules (the NI 9263 – 4 x analogue output and NI 9206 – 32 x analogue input) to the CompactRIO which imported voltage measurements from the SINAMICS DCP and exported voltage and current setpoints to the device. The NI 9263 and NI 9206 modules were used for analogue signal export and import, respectively. The track emulator voltage and the supercapacitor voltage measurements were measured using the analogue input ports of the NI 9206 module at 100 ms intervals. The sampling time was set to 100 ms as recommended by the manufacturer of the Zenone Elettronica power supply that cannot process data faster than 100 ms. The SINAMICS DCP DC/DC converter was configured to accept a ± 10 V analogue reference for both voltage and current setpoints. For each ESS controller update, the calculated voltage and current setpoints were scaled appropriately to provide the reference signal through the output ports of the NI 9263 module.

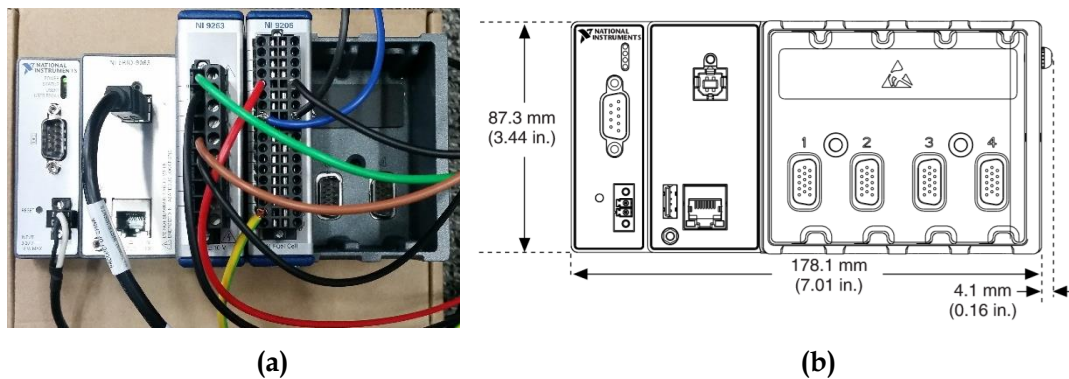


Figure 6.7: cRIO-9063: (a) device; (b) dimensions [151]

The NI 9206 module has 32 analogue inputs with ± 10 V signal range, as shown in Figure 6.8. The NI 9263 module has four analogue outputs with ± 10 V signal range, as indicated in Figure 6.9. During the experiments, pin 49 and 56 of the SINAMICS DCP were connected to pin 5 and 23 of the NI 9206, respectively, to import voltage

measurements of the track emulator. Moreover, pin 51 and 33 of the SINAMICS DCP were connected to pin 8 and 26 of the NI 9206, respectively, to import the supercapacitor voltage measurements. Finally, pin 0 and 1 of the NI 9263 were connected to pin 7 and 8 of the SINAMICS DCP converter, respectively, to export the voltage setpoints, while pin 4 and 5 of the NI 9263 were connected to pin 5 and 6 of the power converter, respectively, to export the current setpoints.

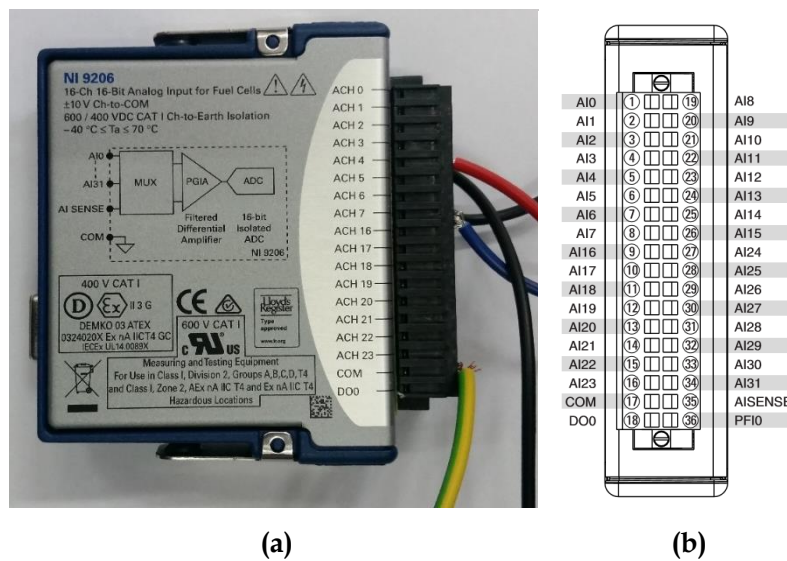


Figure 6.8: NI 9206: (a) device; (b) pinout [152]

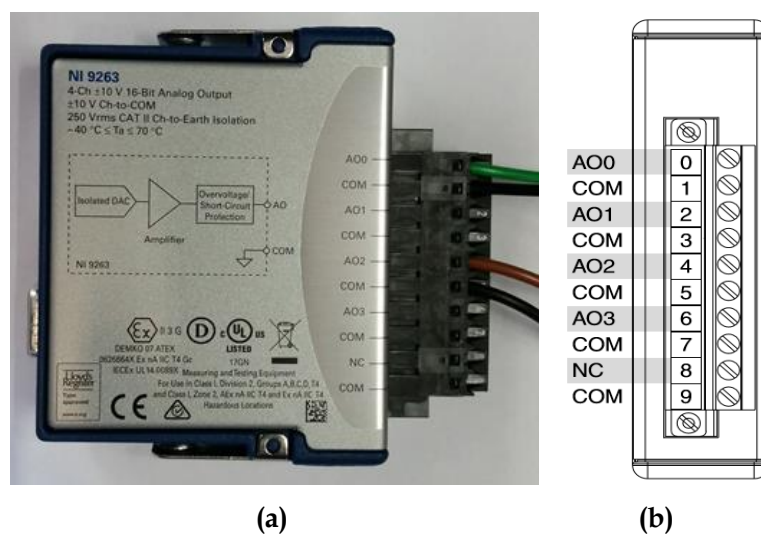


Figure 6.9: NI 9263: (a) device; (b) pinout [153]

6.2.4 Maxwell supercapacitor

For experimentation a Maxwell BMOD0063P125B08 supercapacitor module, that is pictured in Figure 6.10, was connected to the output side of the SINAMICS DCP converter. This electrochemical double-layer capacitor has a wide voltage and temperature range, and is designed to sustain 1,000,000 cycles when cycling between the rated voltage and half voltage at 25 °C. The technical specifications of the supercapacitor are provided in Table 6.3 [154].



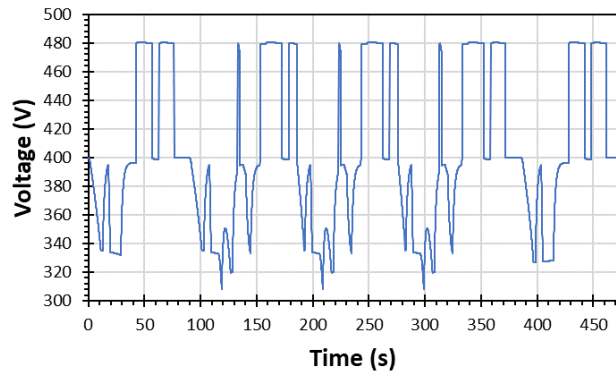
Figure 6.10: Maxwell supercapacitor module

Table 6.3: Technical specifications of the Maxwell supercapacitor [154]

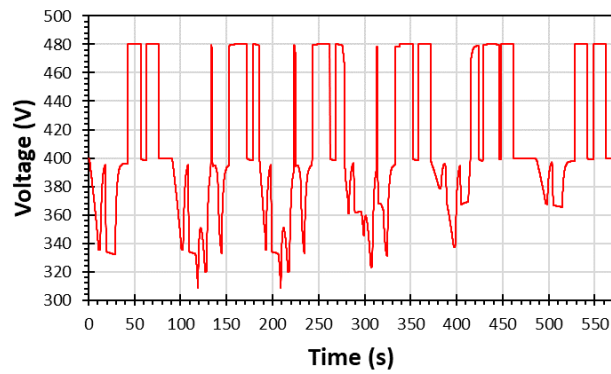
Quantity	Value
Rated capacitance	63 F
Rated voltage	125 V
Absolute maximum voltage	136 V
Absolute maximum current	1,900 A
Equivalent series resistance	18 mΩ
Specific power	1,700 W/kg
Specific energy	2.3 Wh/kg
Stored energy	140 Wh
Dimensions (depth × width × height)	619 × 349.8 × 313 mm
Weight	61 kg
Operating temperature	-40–65 °C

6.3 Software configuration

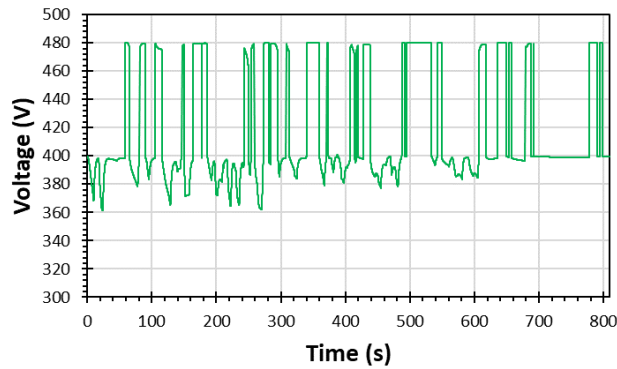
In the present study, the SINAMICS DCP was monitored and controlled using STARTER software provided by Siemens. This software exported voltage measurements on both sides of the SINAMICS DCP converter to the microcontroller. Under different traffic conditions the voltage profile was injected into the power supply after scaling the simulated no-load voltage down to 400 V to match the Zenone Elettronica capability. Therefore, the simulated track voltage profiles were multiplied by a scaling factor of (400/750). LabVIEW software was used to inject the simulated voltage profiles at the terminals of Substation 1 shown in Figure 6.11 into the programmable power supply as well as to build the control methods in the CompactRIO controller. The data exchange between the drive unit and the CompactRIO controller was accomplished using STARTER and LabVIEW software.



(a)



(b)



(c)

Figure 6.11: Substation 1 scaled voltage under: (a) ideal traffic scenario; (b) changing train headway scenario; (c) stochastic traffic scenario

6.3.1 Zenone Elettronica programmable DC power supply

During the experiments, the power supply output voltage followed the track voltage profile generated by MATLAB. The track voltage profile was supplied to the

microprocessor inside the programmable power supply by external analogue signals via serial interface communication. In terms of its principle of operation, the microprocessor is responsible for the energy management as well as for monitoring the system parameters. It controls the output voltage by receiving an analogue input in the 0–10 V range and providing an output voltage ranging from 0 and 600 V. The voltage/current setting and monitoring is allowed via AL Manager software, as shown in Figure 6.12. The voltage and current levels in this device could be modified by sending commands through the communication port or directly by adjusting the potentiometers on the front panel, as shown in Figure 6.13. Since the track voltage has been shown to exhibit high and frequent variations due to the fluctuations in train power demand, in this work, voltage was injected into the power supply using the serial port. AL Manager was replaced by LabVIEW because it did not allow importing the simulated voltages to be injected into the power supply.

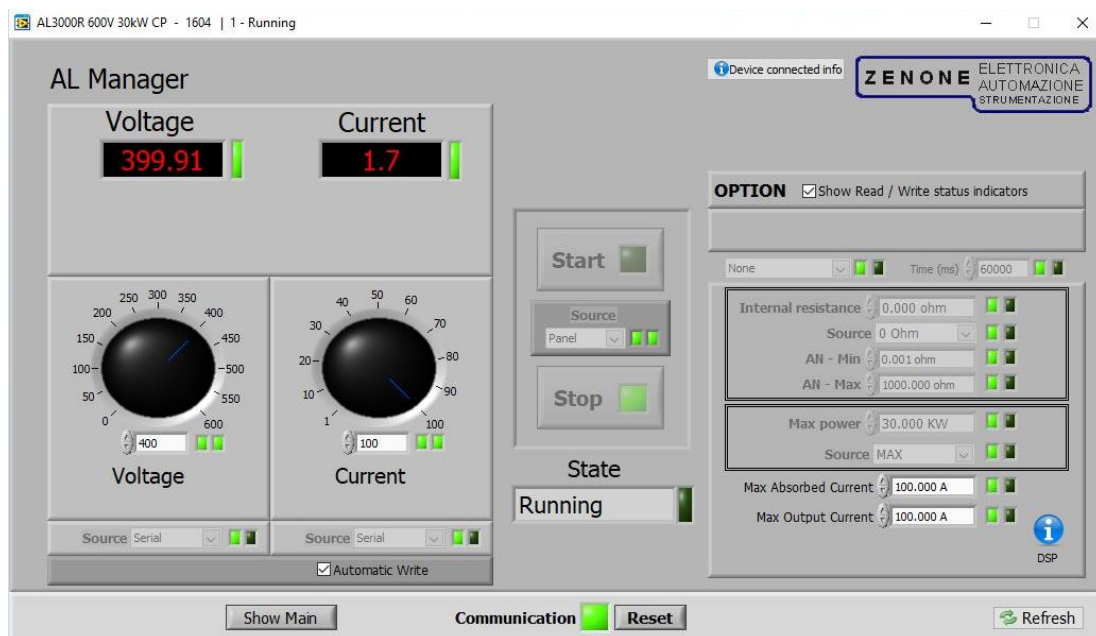


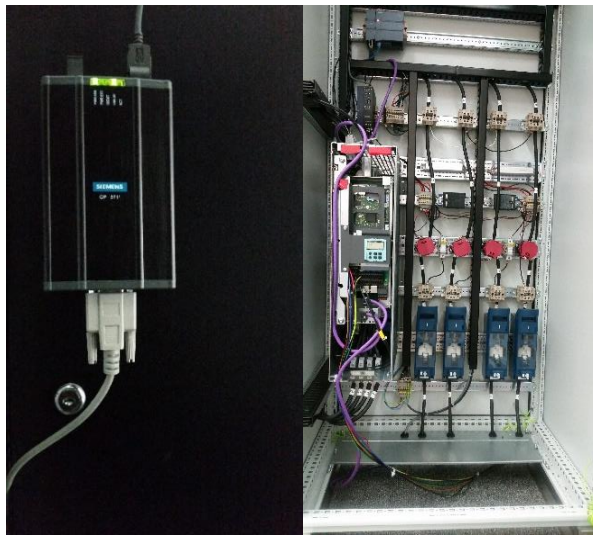
Figure 6.12: AL Manager software utilised for controlling AL3000R power supply



Figure 6.13: AL3000R power supply control interface

6.3.2 SINAMICS DCP DC/DC power converter

In this work, the SINAMICS DCP was programmed using STARTER software version 4.4.1 to manage the power flow between the track emulator and the supercapacitor. Communication with the device was accomplished via a process field bus (PROFIBUS) connection; specifically, the connection was achieved via the Siemens universal serial bus (USB) PROFIBUS adapter CP5711 shown in Figure 6.14. The USB adapter was connected to the control unit DC master (CUD) via an X126 socket to allow parameters to be monitored and adjusted via STARTER software. The desired functionality of the drive unit was established by setting the adjustable parameters in the parameterisation tool shown in Figure 6.15. It is worth noting that the adjustable parameters displayed on the STARTER user interface can be both read and written, and that some of the parameters can also be adjusted in real-time. Moreover, these parameters can be interconnected to modify the device functionality according to the application requirements. An example of real-time data monitoring by the device when changing its functionality is shown in Figure 6.16.



(a)

(b)

Figure 6.14: PROFIBUS connection: (a) USB adapter; (b) CUD

Param...	Data	Parameter text	Online value DC_CTRL_02	Unit	Modifiable to	Access level	Minimum	Maximum
621 p54007	All	MPP tracker current reduction factor	90.00	%	Operation	2	0.1	100
622 p54009	All	MPP tracker energy flow direction	[-1] Negative (side 2 to side 1)		Ready to run	2		
623 p54010	All	CI MPP tracker actual power signal source	DC_CTRL_02 : r55540[0]		Ready to run	2		
624 p54011	All	MPP tracker actual power smoothing time constant	0.05	s	Operation	3	0	100
625 p54013	All	BI MPP tracker lower voltage threshold reached signal source	DC_CTRL_02 : r55125.11		Ready to run	2		
626 p54014[0]	All	BI MPP tracker enable signal source	DC_CTRL_02 : r899.11		Ready to run	2		
627 r54015	All	CO: MPP tracker actual power smoothed	0.00	%		2		
628 r54020	All	CO: MPP tracker output	-0.00	%		2		
629 r54021	All	CO: MPP tracker output total	-0.00	%		2		
630 p54030	All	MPP tracker operating mode	1H		Operation	3		
631 p54035	All	MPP tracker characteristic plot interval	300	s	Operation	2	80	3600
632 p54036	All	MPP tracker characteristic plot duration	10	s	Operation	2	1	60
633 p54037	All	MPP tracker current search range	10.00	%	Operation	2	1	100
634 r54040[0]	All	MPP tracker characteristic current	0.00	A		2		
635 r54041[0]	All	MPP tracker characteristic power	0.01	kW		2		
636 p54100	All	CI: Voltage controller setpoint signal source	DC_CTRL_02 : r52025		Ready to run	2		
637 p54101	All	Voltage controller ramp-up time/ramp-down time	0.050	s	Operation	2	0	10
638 p54102	All	Voltage controller actual value selection	[2] Actual value voltage side 2		Ready to run	2		
639 r54103	All	CO: Voltage controller setpoint after the ramp-function generator	1.16	%		2		
640 p54105	All	BI: Voltage controller activation signal source	1		Ready to run	2		
641 p54121	All	Voltage controller actual value rate time	10.00	ms	Operation	2	0	100
642 p54122	All	Voltage controller actual value smoothing time constant	2.00	ms	Operation	2	0	100
643 p54124	All	Voltage controller DC link buffering dead range	0.00	%	Operation	2	0	100
644 p54125	All	Voltage controller proportional gain	2.000		Operation	2	0.001	30
645 p54126	All	Voltage controller integral time	0.30	ms	Operation	2	0.01	1000
646 p54127	All	Voltage controller droop	0.00	%	Operation	2	0	20
647 r54130	All	CO: Voltage controller actual value	1.30	%		2		
648 r54131	All	CO: Voltage controller P component display	0.00	%		2		
649 r54132	All	CO: Voltage controller I component display	0.00	%		2		
650 r54135	All	CO/BO: Voltage controller state	0H			2		
651 p54141	All	CI: Voltage controller positive current limit signal source	DC_CTRL_02 : r20129		Ready to run	2		
652 p54142	All	CI: Voltage controller negative current limit signal source	DC_CTRL_02 : r20111		Ready to run	2		
653 p54145	All	BI: Voltage controller enable signal source	1		Ready to run	2		
654 p54146	All	Voltage controller DC link buffering minimum time	0.00	ms	Operation	2	0	100000
655 p54200	All	CI: Battery charging char. manual current setpoint signal source	DC_CTRL_02 : r2050[1]		Ready to run	2		
656 r54201	All	BI: Battery charging characteristic manual fault signal source	1		Ready to run	2		

Figure 6.15: Screen capture of STARTER parameterisation tool

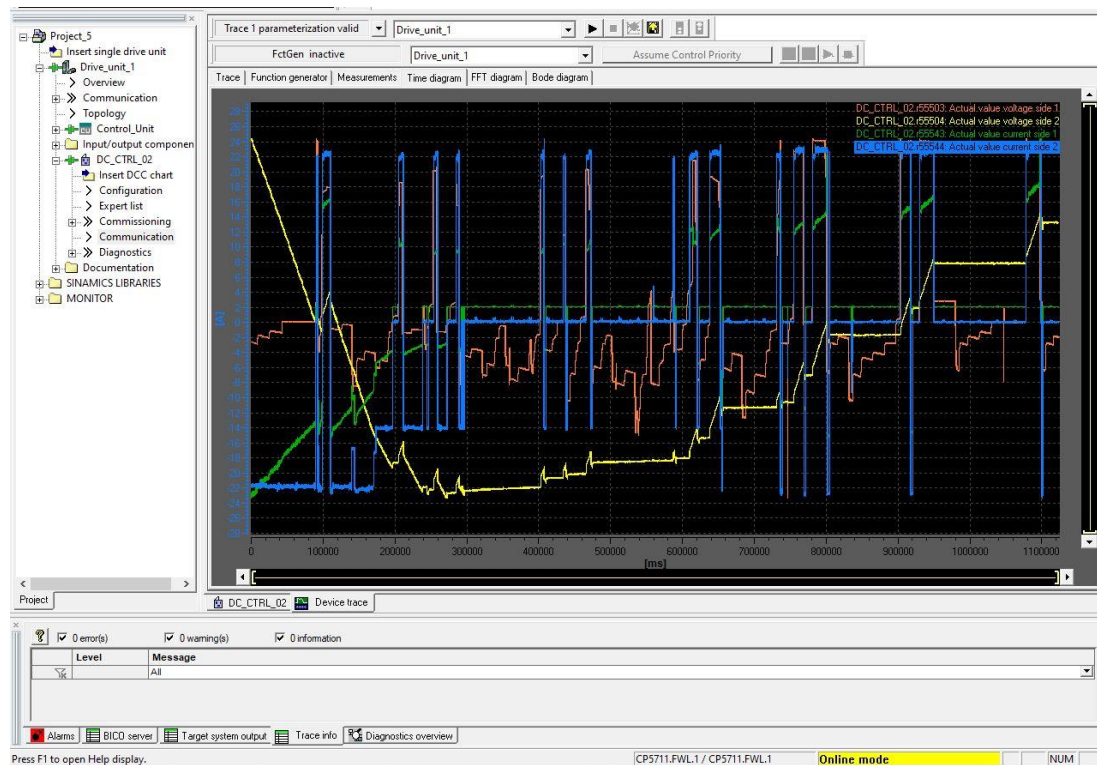


Figure 6.16: Real-time data monitoring using STARTER software

Prior to conducting the experiments, the CompactRIO external microcontroller was connected to the test rig to adjust the SINAMICS DCP DC/DC converter voltage and current setpoints. For correct and efficient operation, all data to be sent to and received by the external controller had to be connected to certain parameters in the software. Owing to this link between software parameters and the exchange data, the SINAMICS drive unit could be managed by the CompactRIO controller, which was used as an external controller. In addition, the I/O terminals fixed on the CUD (see Figure 6.17) were used to import/export measurements. Voltage measurements on both sides of the SINAMICS DCP converter were transmitted to the CompactRIO via the CUD outputs; voltage and current setpoint supplied by the CompactRIO were captured by the CUD input terminals. An overview of the input and output terminals of the CUD module can be seen in Appendix 3, Table A2. Analogue output 0 (terminal 49) was programmed to export the voltage measurement on the track side of the SINAMICS DCP converter to the CompactRIO controller. Similarly, analogue output 1 (terminal 51) was programmed to export the voltage measurement on the ESS side

of the SINAMICS DCP converter to the CompactRIO controller. Moreover, dynamic current and voltage setpoints were imported from the CompactRIO controller using analogue input 5 (terminal 5) and analogue input 6 (terminal 7), respectively. Although STARTER software allowed controlling the SINAMICS DCP converter, it did not permit dynamic variation of the voltage and current setpoints within the parameterisation tool. Therefore, the CompactRIO controller was integrated with the SINAMICS DCP converter to adapt the voltage and current settings according to changes in the track voltage and supercapacitor SOC.



Figure 6.17: The terminal module cabinet [149]

The manufacturer settings of the parameters appear in the parameterisation tool shown in Figure 6.15 were kept the same except for the following parameters. The voltage controller setpoint signal source (p54100) was set to CUD analogue input 6 result (r52025). The positive current limit (p54141) and negative current limit (p54142) were set to the CUD analogue input 5 result (r52023) measuring the current setpoint. The first analogue output signal source (p50750) was set to the measured voltage on the track side of the SINAMICS DCP converter (r55501). The second analogue output signal source (p50755) was set to the measured voltage on the ESS side of the SINAMICS DCP converter (r55502). Finally, the minimum voltage on both sides (p55105) was set to 0% to allow the device to work below 30 V that was originally set

by the manufacturer to mandate its use at voltages above 30 V, thus preventing the supercapacitor from reaching low voltages.

The device could be switched on and off by pressing the push button on the front door or by sending commands to the parameter p0840. However, as the adaptive controller behaviour changed according to the operating time when managing the SOC, the operation of the Zenone power supply and the SINAMICS DCP had to be synchronised. Consequently, in this work, both devices were operated remotely from the same computer to ensure that the measurements sent by the SINAMICS DCP converter to the microcontroller matched the time count of the operation cycle that was initiated when the power supply started emulating the track voltage. While LabVIEW software was used to operate the programmable power supply, STARTER was adopted to send the digital signal required for operating the SINAMICS DCP converter, as shown in Figure 6.18.

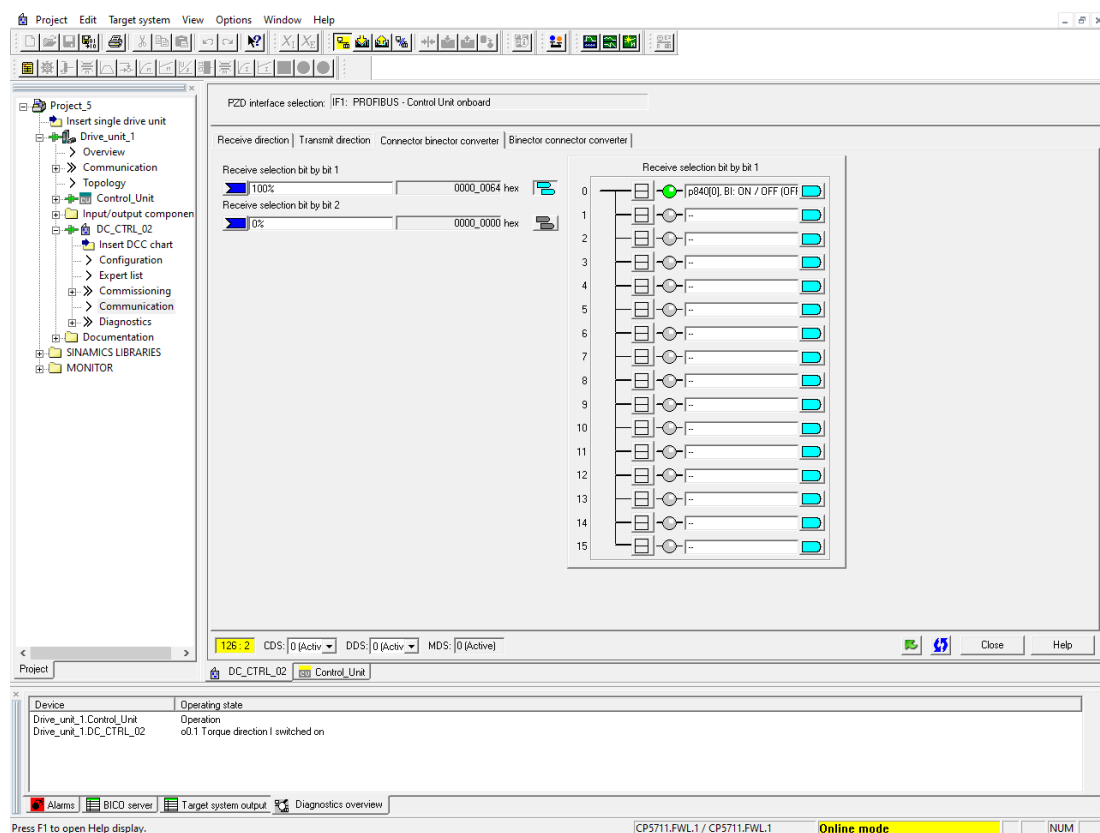


Figure 6.18: Remote initiation of the SINAMICS DCP device using STARTER

6.3.3 CompactRIO controller

Static and dynamic control, including the state machine control and fuzzy control technique, were implemented in LabVIEW to supply the information of the voltage/current setpoints to the SINAMICS DCP DC/DC converter. The CompactRIO controller transmitted the setpoints to the SINAMICS and received actual measurements from it. The ESS controller was built in LabVIEW Real-Time Module, which was added to LabVIEW for direct access to the I/O modules. The Real-Time Module allows complex algorithms to be downloaded to hardware applications. Screenshots of the static controller (Chapter 4, Section 4.3), SOC controller 1 (Chapter 5, Section 5.2.1), and SOC controller 2 (Chapter 5, Section 5.2.2) that were built in LabVIEW Real-Time Module are shown in Figure 6.19, Figure 6.20, and Figure 6.21, respectively. The SOC controller 2 implementing fuzzy logic was designed using the Fuzzy System Designer tool that is available in LabVIEW. The same fuzzy rules and sets discussed in Section 5.2.2 were implemented in LabVIEW but with multiplying the track voltage fuzzy set by the scaling factor (400/750) and scaling down the charging/discharging current limit to 0–20 A range. After building the SOC controller 2 in the Fuzzy System Designer tool in LabVIEW it was saved in a file in an accessible location. The file path was entered to a block named FL Load Fuzzy System VI to load the SOC controller 2 into the FL Fuzzy Controller VI block for implementation of the fuzzy system in the control structure shown in Figure 6.21. In this work, after graphical programming of the control methods in LabVIEW Real-Time Module, they were downloaded to the NI cRIO-9063 for execution and selection of I/O. The communication between the NI cRIO-9063 and the host computer was accomplished via ethernet network.

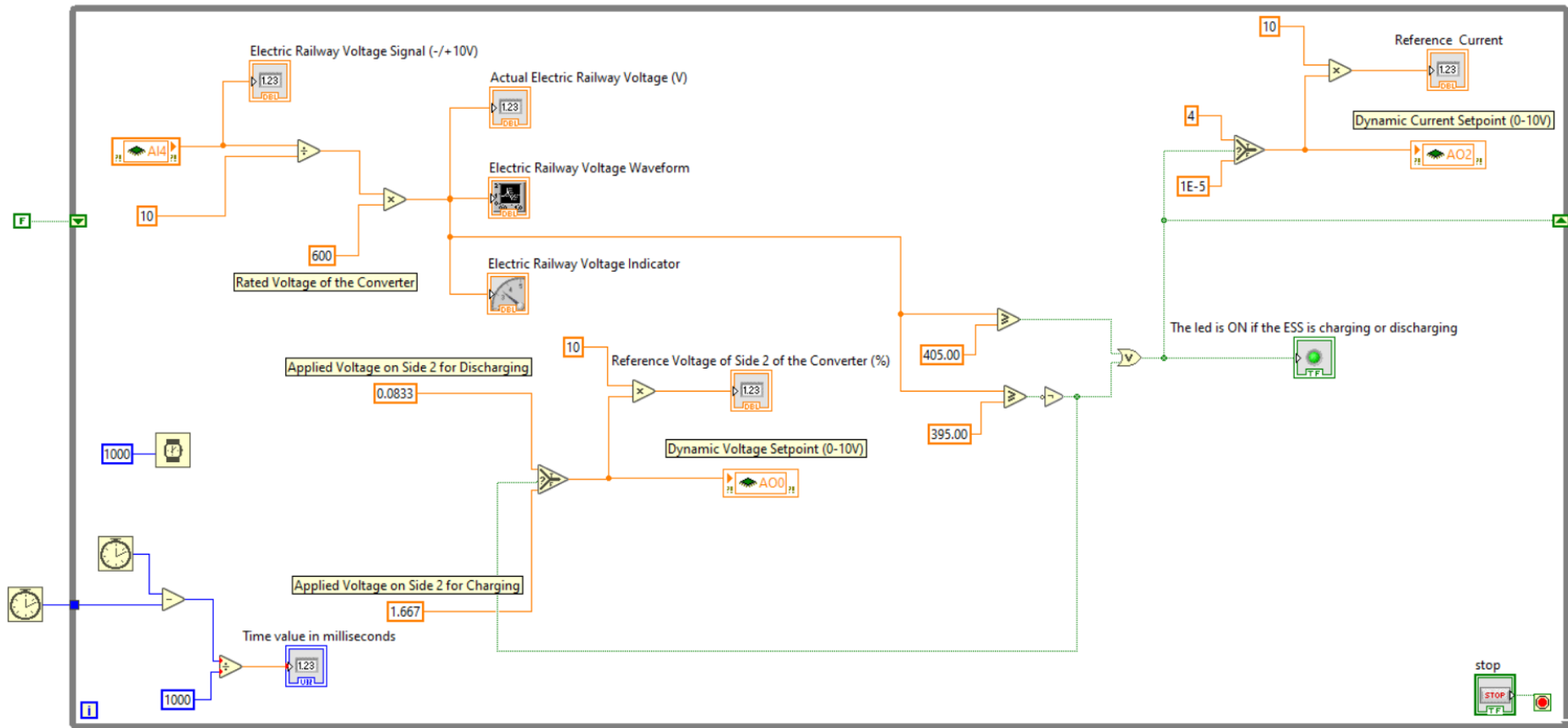


Figure 6.19: Screen capture of the static controller model built in LabVIEW

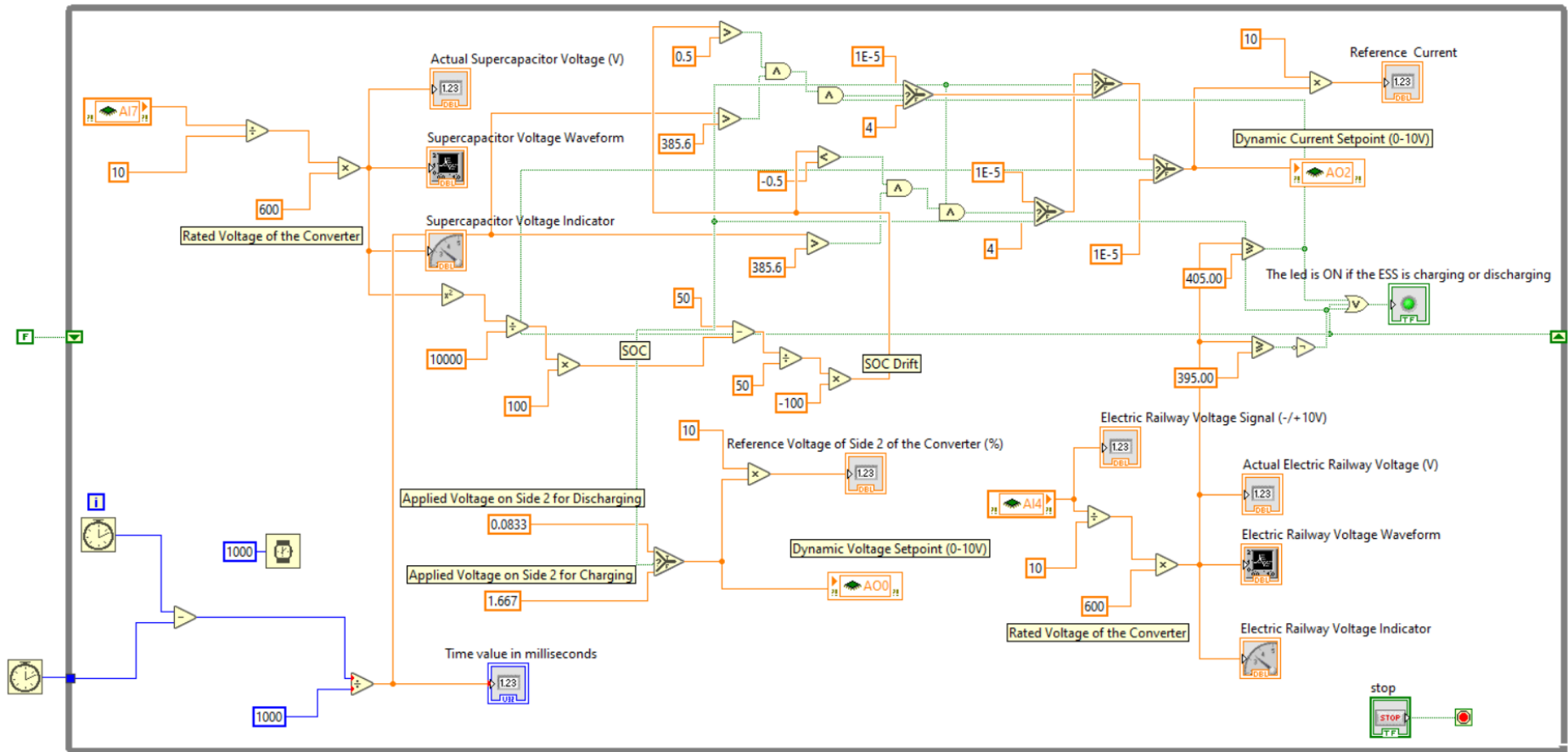


Figure 6.20: Screen capture of the SOC controller 1 model built in LabVIEW

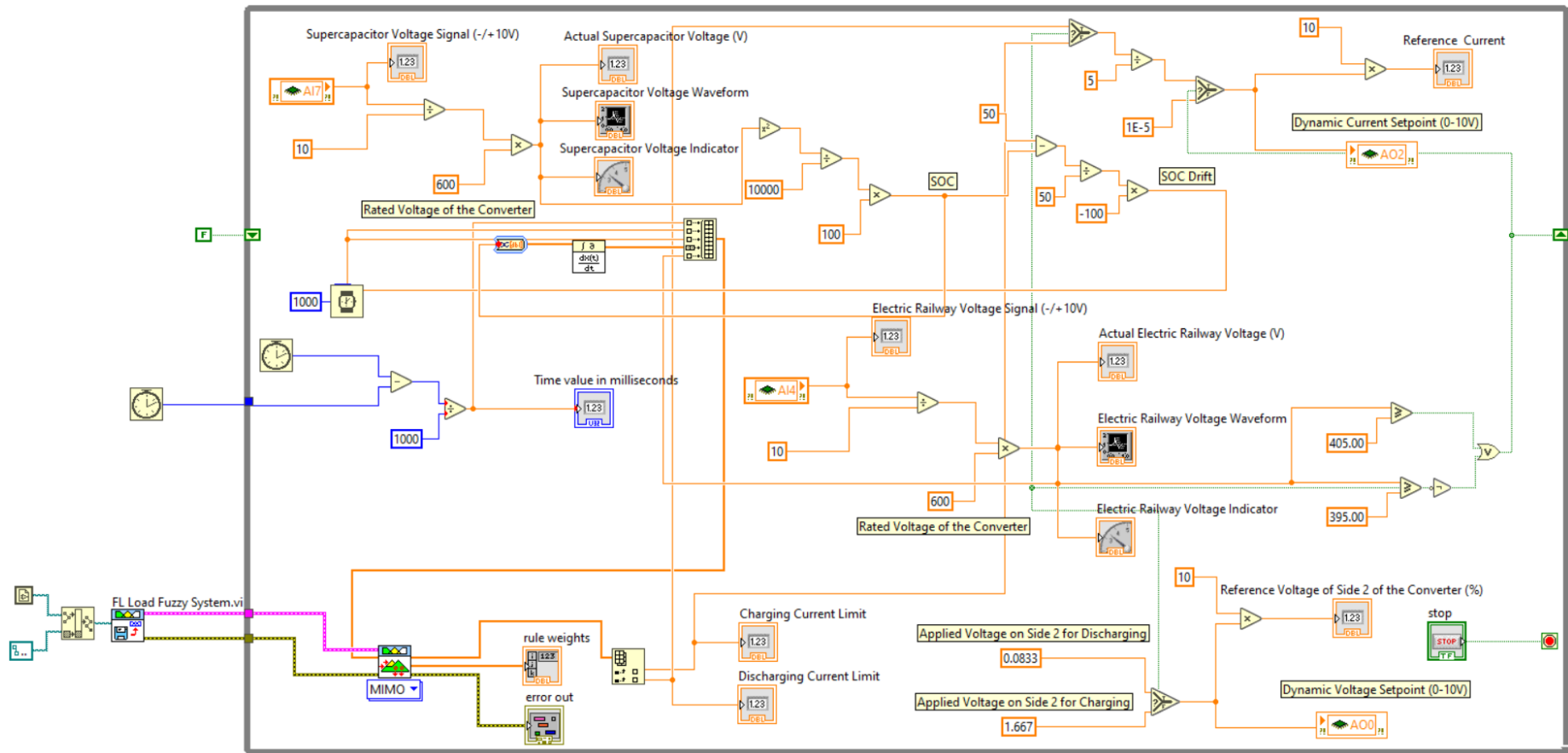


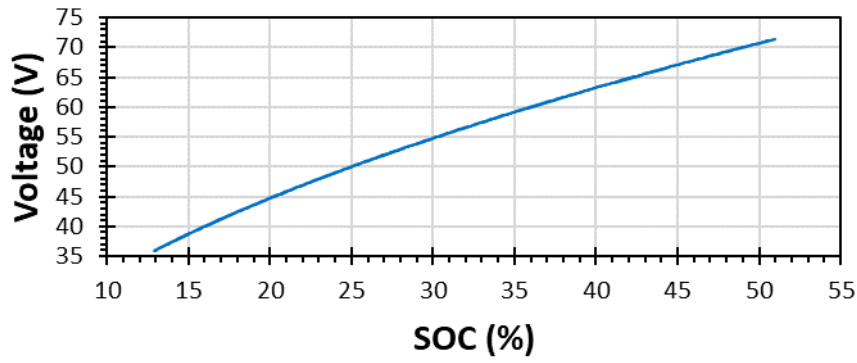
Figure 6.21: Screen capture of the SOC controller 2 model built in LabVIEW

6.3.4 Maxwell supercapacitor

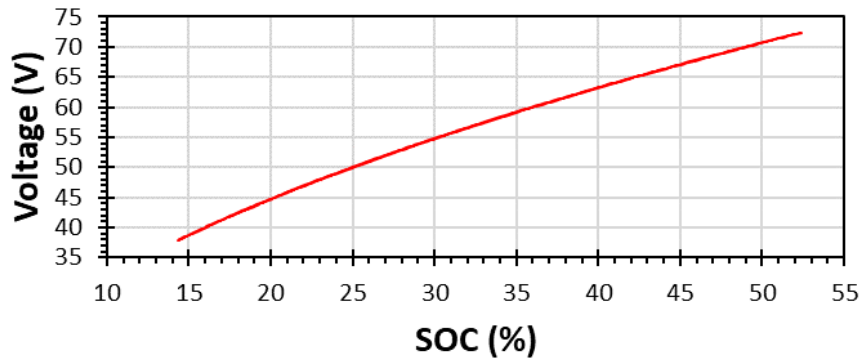
In the present study, the supercapacitor is discussed only in terms of the SOC, neglecting any other considerations, such as state of health (SOH), cell balancing, and life cycle. The energy stored in the supercapacitor is proportional to its voltage squared and capacitance. Since the capacitance is stable, for the purposes of analysis, it was assumed that the SOC is calculated as the square of the measured voltage divided by the square of the design voltage as follows:

$$SOC_{SC}(t) = \frac{V_{SC}(t)^2}{V_{SC(\text{design})}^2} \cdot 100 \quad (6.1)$$

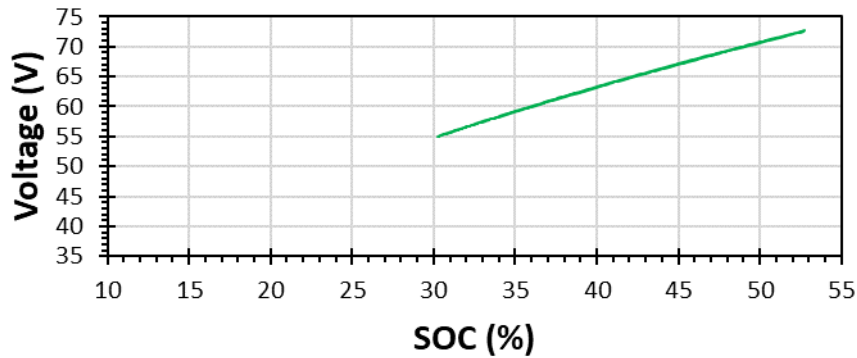
Where $SOC_{SC}(t)$ is the instantaneous SOC of the supercapacitor in %, $V_{SC}(t)$ is the measured voltage of the supercapacitor in V, and $V_{SC}(\text{design})$ is the maximum allowed voltage of the supercapacitor that is a 100 V in this study. When the relative voltage reaches the maximum allowed voltage, the SOC is considered to be 100%, and when the voltage reaches the minimum allowed voltage, the SOC is 0%. The supercapacitor voltage against SOC when applying the ESS controllers under the ideal traffic scenario is shown in Figure 6.22. The measured voltage at the output terminals of the supercapacitor to be communicated to the microcontroller could be obtained via STARTER. As a result, in this work, no communication modules were added to the supercapacitor, and STARTER was used for remote voltage diagnostics.



(a)



(b)



(c)

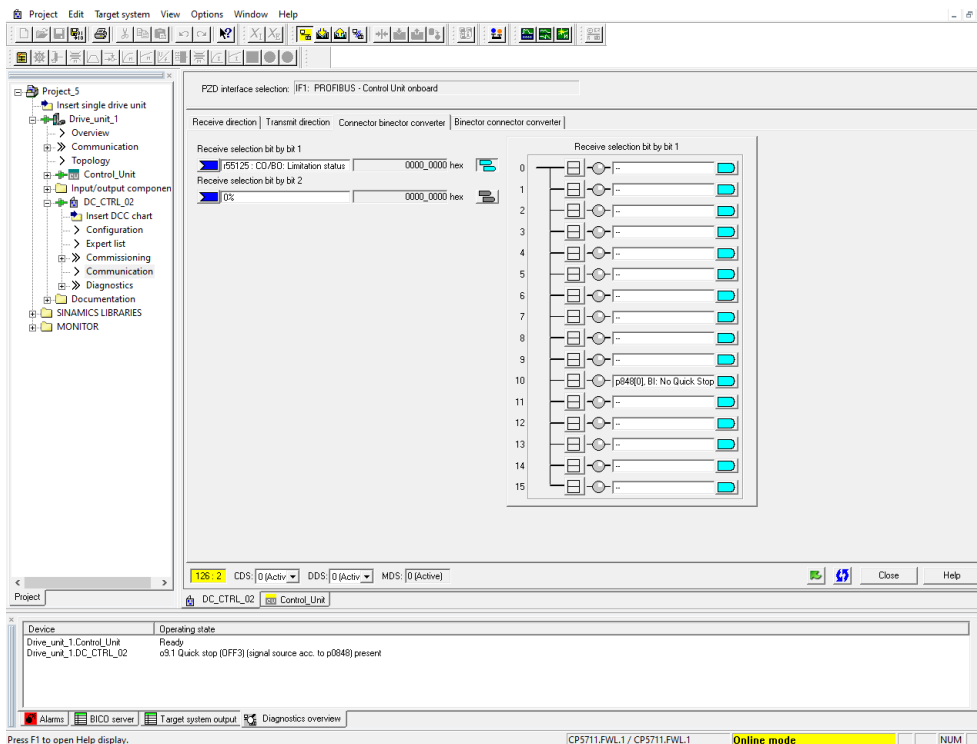
Figure 6.22: Voltage versus SOC profile when applying the ESS under the ideal traffic scenario: (a) without SOC control; (b) SOC controller 1; (c) SOC controller 2

Exceeding the rated voltage of the device is a serious issue because it can lead to capacitance loss, equivalent series resistance increase, and heat accumulation that reduces the device lifetime. Such issues can occur when the device operates at high ambient temperatures, even if the operating voltage is below the rated voltage [155]. Moreover, high voltage ripples at the SINAMICS DCP DC/DC converter terminals that manifest as large amplitudes, due to increasing the voltage ratio between the two

sides of the converter, could result in reaching the rated voltage of the supercapacitor when working in the vicinity of the rated voltage. Hence, to avoid these issues, the operating voltage was limited to a maximum value of 100 V. Moreover, the supercapacitor was protected against overcharging by upper voltage limits to the SINAMIC DCP, achieved via setting of parameter p0848, as shown in Figure 6.23.

686	r55125	CO/BO: Limitation status	OH
687	r55125.0	Positive current limiting active	No
688	r55125.1	Negative current limiting active	No
689	r55125.2	Voltage in the undervoltage range	No
690	r55125.3	Voltage in the normal voltage range below rated voltage	No
691	r55125.4	Voltage in the normal voltage range above rated voltage	No
692	r55125.5	Voltage in the overvoltage range	No
693	r55125.6	Voltage in illegal range	No
694	r55125.7	PV flying connection active	No
695	r55125.8	Lower voltage limit reached on side 1	No
696	r55125.9	Upper voltage limit reached on side 1	No
697	r55125.10	Upper voltage limit reached on side 2	No
698	r55125.11	Lower voltage limit reached on side 2	No
699	r55125.12	Dynamic voltage limit reached on side 1	No
700	r55125.13	Dynamic voltage limit reached on side 2	No
701	r55125.14	PWM limited reached	No
702	r55125.15	Main current controller has reached its limit	No

(a)



(b)

Figure 6.23: Overvoltage protection control: (a) status monitoring; (b) limitation function against overcharging

6.4 Experimental results

In order to assess the performance of the proposed control methods and demonstrate their applicability to real systems, several cases emulating real traffic conditions were implemented experimentally for one typical operation cycle also referred to as a journey. Voltage profiles for the operational cases discussed in Chapter 5 were injected to the programmable power supply after they were scaled down to 400 V no-load voltage. For the purpose of these experiments, the SINAMICS DCP DC/DC converter received commands from the CompactRIO controller to charge, discharge or to work on standby mode. For charging the supercapacitor, the SINAMICS DCP converter applied 100 V on the ESS side and 5 V for discharging. The standby mode was achieved by feeding a 0 A current demand to the SINAMICS DCP converter, which served as the current limit. The aim of implementing a controller is always to reduce the gap between the desired SOC – which was set to 50% for all experiments – and the measured SOC before the end of the operational cycle.

6.4.1 Ideal traffic scenario

The voltage at Passenger Station A based on the ideal traffic scenario before applying the ESS that is shown in Figure 6.11 (a), was injected into the Zenone Elettronica power supply. The CompactRIO controller was responsible for managing the energy in the system based on the power supply voltage imitating the track voltage. The impact of applying the static control method, SOC controller 1, and SOC controller 2 is shown in Figure 6.24. Applying the static control method depicted in Figure 6.19 to manage the power flow between the power supply and the supercapacitor caused the SOC drift to be -55.1%. The SOC controller 1 depicted in Figure 6.20 (implementing state machine method) reduced the SOC drift to -25.3% and the SOC controller 2 depicted in Figure 6.21 (implementing fuzzy method) was able to reduce the SOC drift toward the end of the experiment to 3.5%, as indicated by a

small deviation from the initial SOC value. The fuzzy control technique produced a smaller SOC drift because it was capable of maintaining the SOC in a narrower range, allowing it to rapidly minimise the error at the end of the experiment.

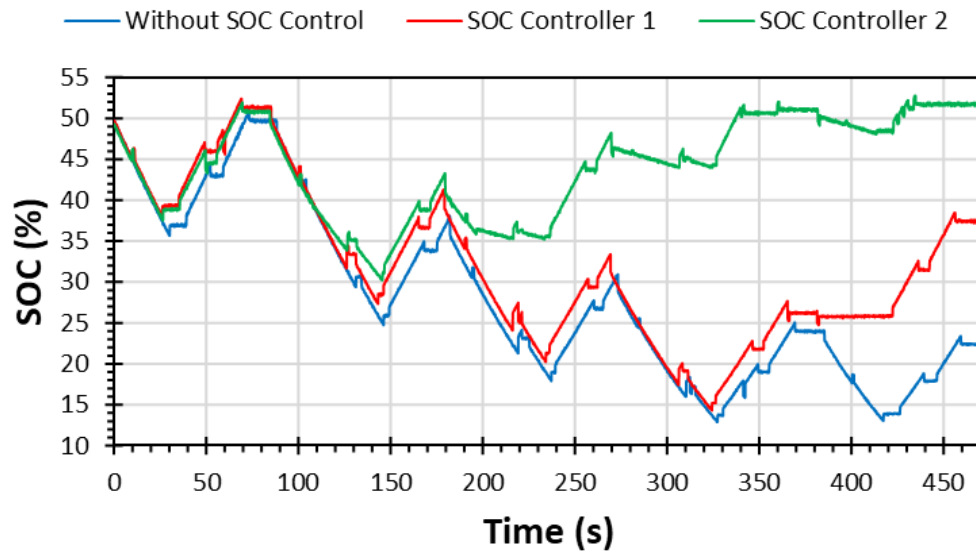


Figure 6.24: Experimentally obtained supercapacitor SOC values based on different control approaches under the ideal traffic scenario

6.4.2 Changing train headway scenario

The significant impact on railway system energy calculations of changing train headway has already been discussed in detail in Chapter 3, Section 3.4.6. Moreover, in Chapter 5, it was demonstrated that, when Train 8 was delayed by 100 s than scheduled (headway was changed from 90 to 190 s), the SOC drift increased significantly. Therefore, it is crucial to experimentally establish whether the proposed control methods are capable of handling this undesirable situation. The track voltage profile before implementing the ESS is shown in Figure 6.11 (b). The graph displayed in Figure 6.25 shows that the SOC controllers 1 and 2 were able to correct the SOC profile toward the end of the experiment, thus resulting in minimal deviation from the desired value. Applying the static controller resulted in a SOC drift of -43.7% while the SOC controller 1 reduced it to -11.2% and the SOC controller 2 reduced it to 2.4%.

It is noticed that the fuzzy technique had a narrower boundary than the state machine technique, which introduced significant reduction of the SOC deviation from the desired SOC at the end of the experiment. On the other hand, the impact of the state machine control method on the SOC drift reduction was less than the fuzzy control method while outperforming the static controller.

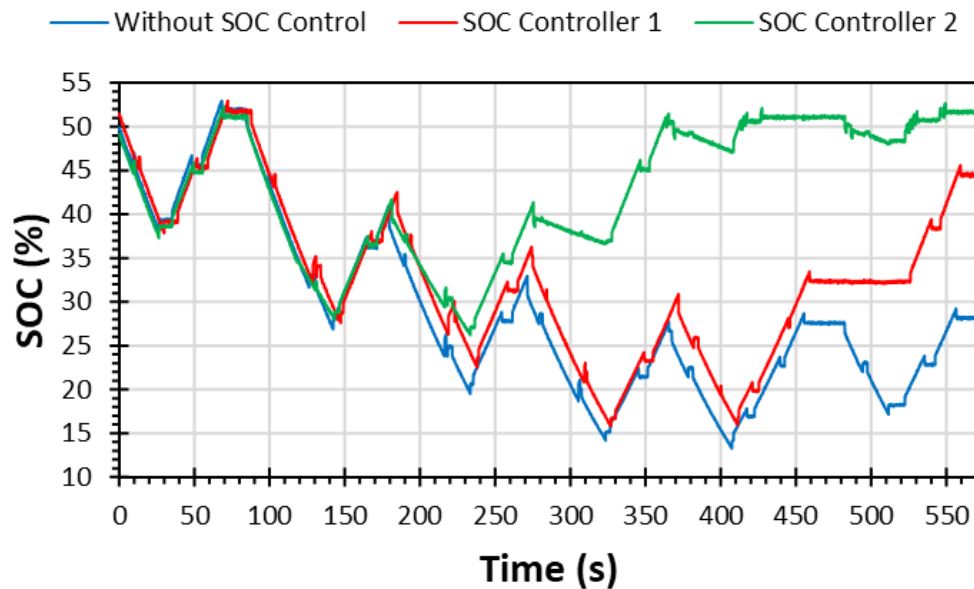


Figure 6.25: Experimentally obtained supercapacitor SOC values based on different control approaches when Train 8 headway was modified

6.4.3 Stochastic traffic scenario

During the work performed as a part of the present study, it emerged that emulating changes to the traffic tended to introduce variability to the substation voltage. The applied changes had significant impact especially for those arising from major changes to the dwell time, headway, and speed profiles. The use of simplified traffic models might lead to an inaccurate assessment of the proposed controllers. Thus, as parameters such as dwell time, train operation interval, and speed profile have a significant impact on energy calculations, they must be allowed to fluctuate randomly. Consequently, it is crucial to experimentally apply the proposed control

methods on the stochastic traffic scenario described in Chapter 5, Section 5.3.2. The track voltage profile before implementing the ESS is shown in Figure 6.11 (c). The impact of the three proposed control methods on the supercapacitor SOC when applying the stochastic traffic scenario is shown in Figure 6.26. Unsurprisingly, the static control method imposed the highest SOC drift among other control methods with a value of 14.1%, while the SOC controllers 1 and 2 reduced the SOC drift to -1.8% and 2.2%, respectively. Indeed, both methods were capable of reducing the error to minimal values toward the end of the experiment, as they succeeded in maintaining the SOC within narrow boundaries. Moreover, the state machine control technique initially allowed for a flexible charge and discharge in the typical operation cycle before abruptly reducing the gap between the measured value and the reference value. However, owing to this smoothness and flexibility, the final SOC error was higher relative to that produced by the fuzzy control technique. It can also be noted that the fuzzy controller boosted the SOC profile gradually before causing more abrupt changes near the end of the experiment.

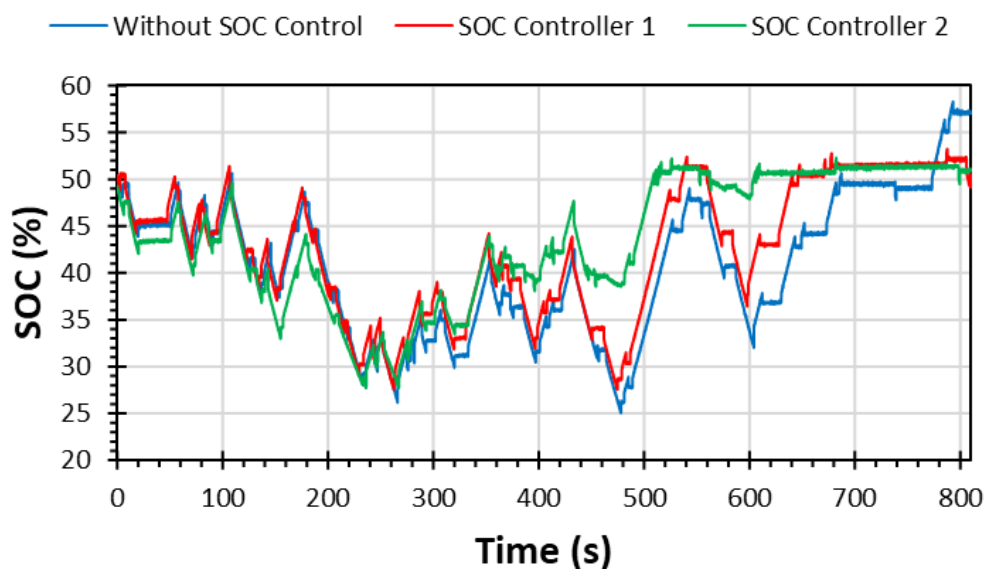


Figure 6.26: Experimentally obtained supercapacitor SOC values based on different control approaches under a realistic traffic scenario

6.5 Comparison of experimental and simulation results

In this section, the experimental results presented in the previous section are compared with the simulation results in order to validate the proposed methods. For this purpose, the test rig shown in Figure 6.1 was built in MATLAB Simulink as shown in Figure 6.27. The solver type in MATLAB was set to ode45 and the time step was set to 0.5 ms. It is worth mentioning that in this particular case the solver type was not restricted to ode45 and the user could select ode23, ode113, ode15s, ode23t, or ode23tb. The time step was reduced from 0.1 s to 0.5 ms to reduce the ripples resulting from the switches involved in the DC/DC converter that was assumed to be ideal in previous chapters. The time step was reduced in steps until observing an approximate response to the experimental one in terms of SOC and current.

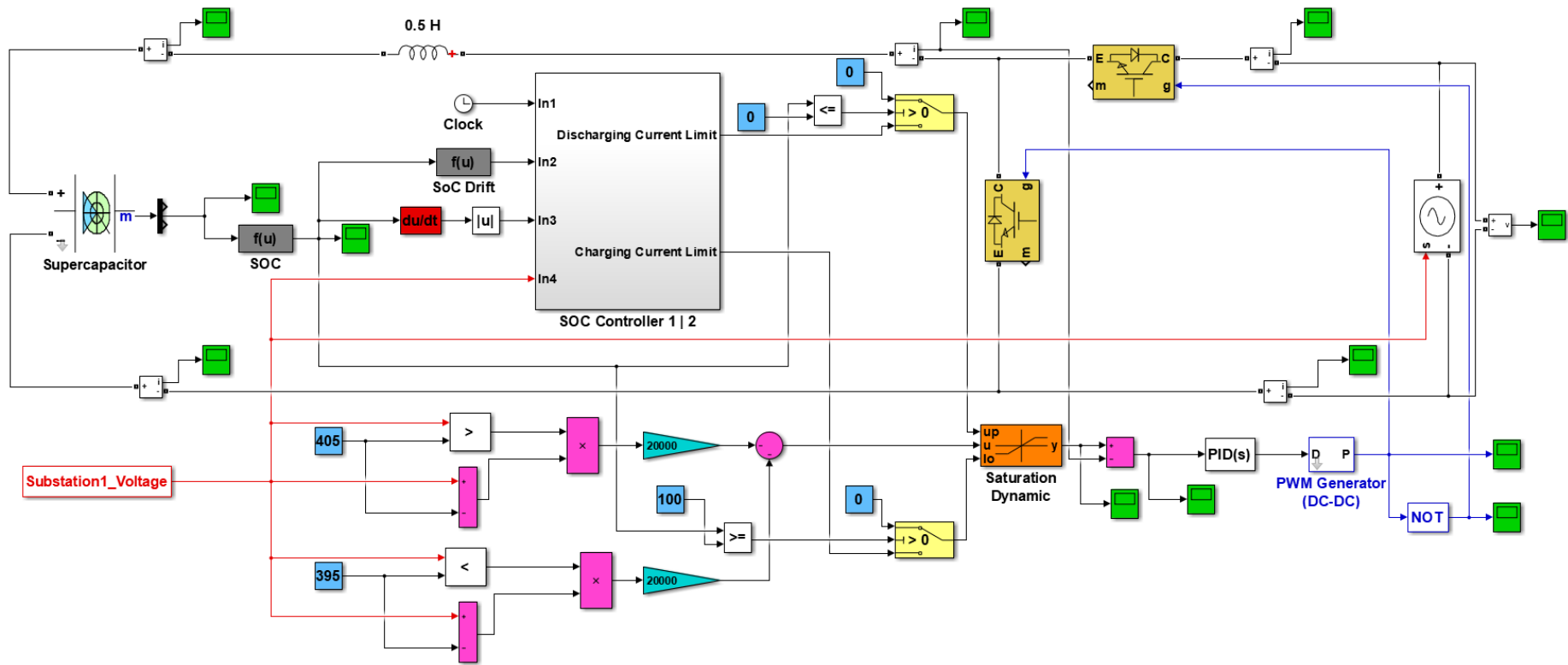


Figure 6.27: Screen capture of the power system model created in MATLAB Simulink

Figure 6.28 shows the supercapacitor SOC comparison when applying the SOC controller 1 under the typical traffic scenario, indicating good alignment between the measured and simulated results with an error of 3.6%. The measured and simulated supercapacitor current are compared in Figure 6.29. The fuzzy controller was applied to the same test scenario and the comparison results are shown in Figure 6.30 and Figure 6.31. The total percentage error of the SOC was only 3%. As can be seen from the graphs, at the beginning of the journey, the error between the measured and simulated SOC was small, after which, toward the middle of the journey, it increased slightly before it decreased again toward the end of the journey.

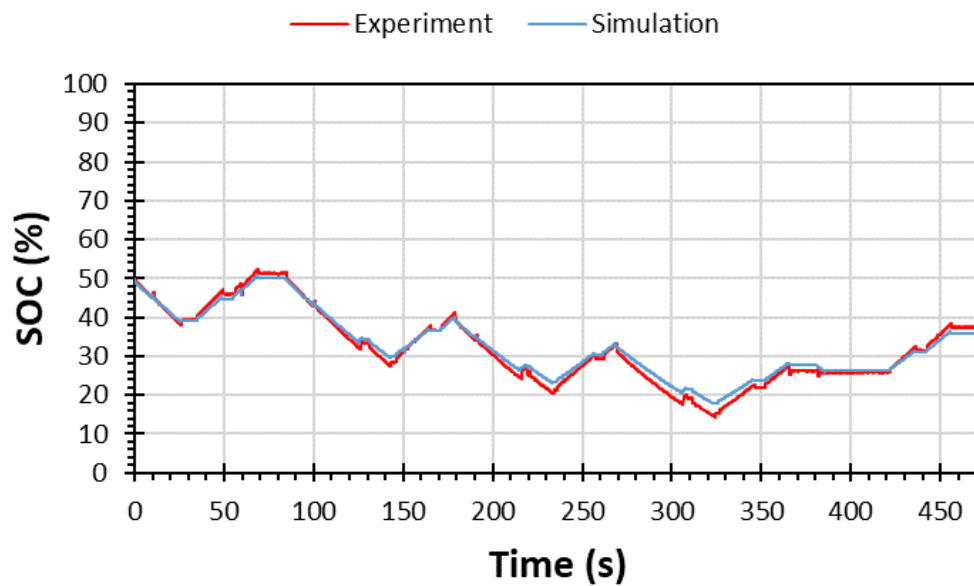


Figure 6.28: Comparison between the experimental and simulation results pertaining to the supercapacitor SOC determined by the state machine control under the ideal traffic scenario

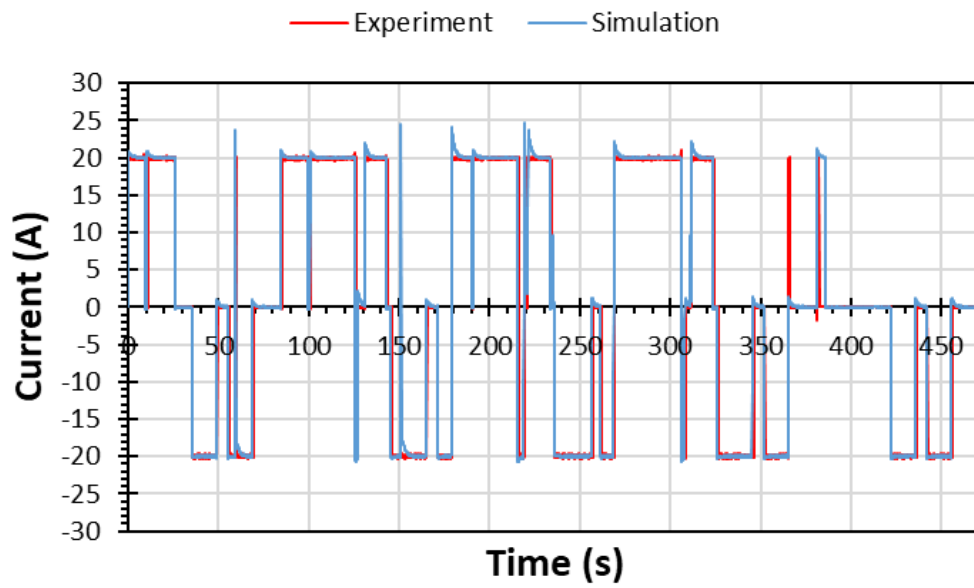


Figure 6.29: Comparison between the experimental and simulation results pertaining to the supercapacitor current determined by the state machine control method under the ideal traffic scenario

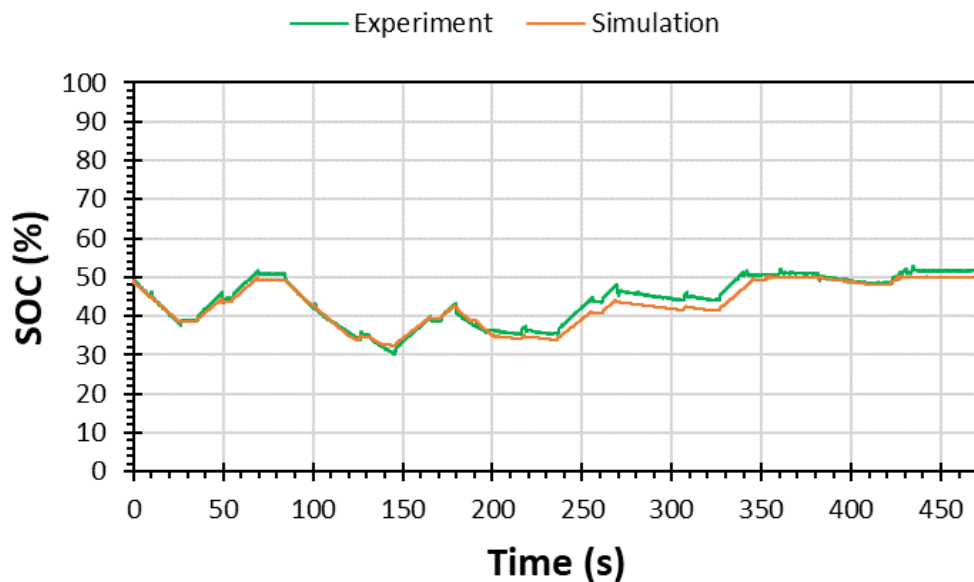


Figure 6.30: Comparison between the experimental and simulation results pertaining to the supercapacitor SOC based on the fuzzy control approach under the ideal traffic scenario

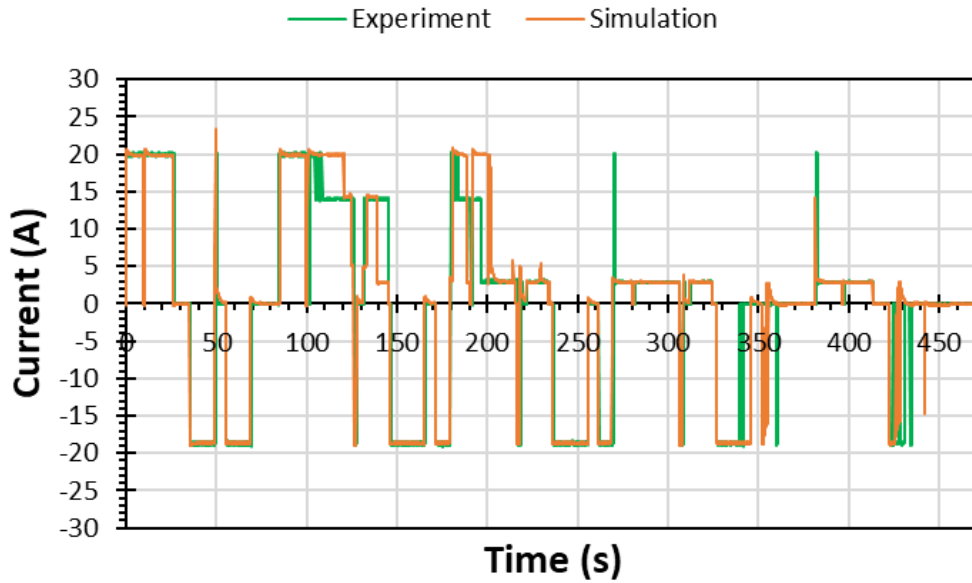


Figure 6.31: Comparison between the experimental and simulation results pertaining to the supercapacitor current based on the fuzzy control method under the ideal traffic scenario

The SOC and current profile of the supercapacitor obtained during the experiments aimed to assess the SOC controller 1 performance with respect to the track voltage when Train 8 headway was modified, are shown in Figure 6.32 and Figure 6.33, respectively. The impact of the SOC controller 2 on the SOC profile is shown in Figure 6.34, and the graph displayed in Figure 6.35 depicts the supercapacitor current profile. It can be noticed that as the current difference increased, so did the SOC. This issue is particularly prominent in the middle part of the operating cycle. The total percentage error of the SOC profile when applying the SOC controller 1 was 3.3% while it was 2% when applying the SOC controller 2.

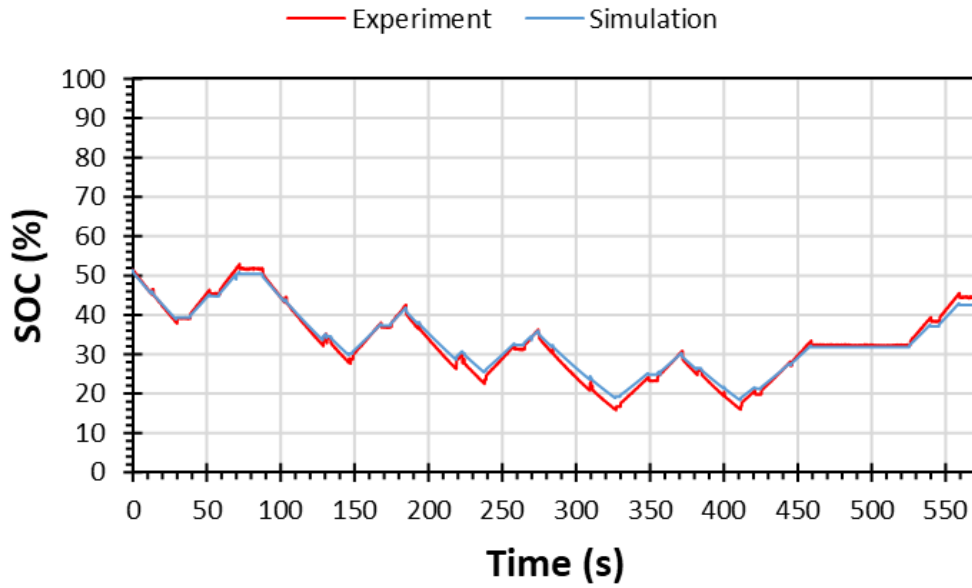


Figure 6.32: Comparison between the experimental and simulation results pertaining to the supercapacitor SOC yielded by the state machine control method when Train 8 headway was modified

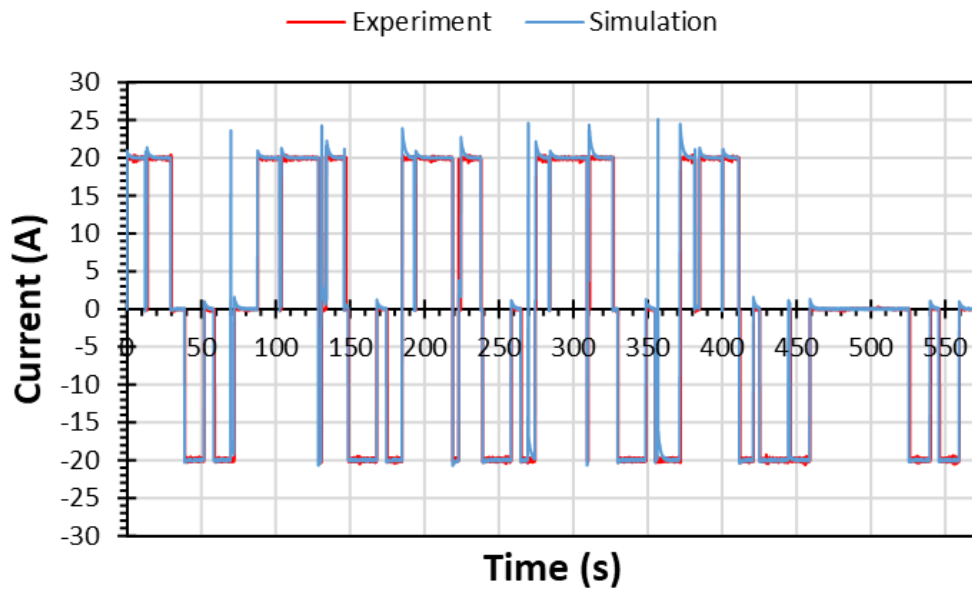


Figure 6.33: Comparison between the experimental and simulation results pertaining to the supercapacitor current yielded by the state machine control method when Train 8 headway was modified

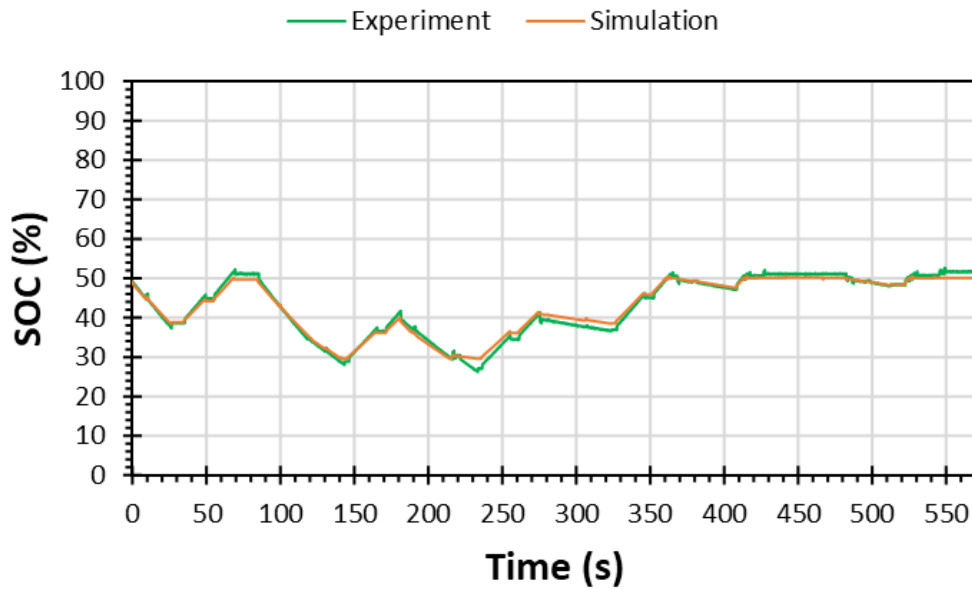


Figure 6.34: Comparison between the experimental and simulation results pertaining to the supercapacitor SOC imposed by the fuzzy control approach when Train 8 headway was modified

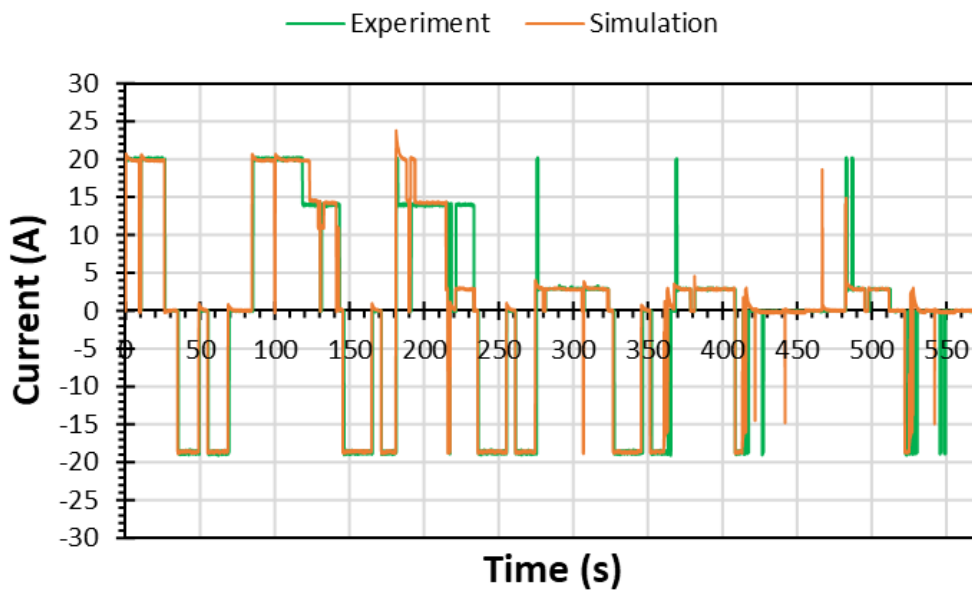


Figure 6.35: Comparison between the experimental and simulation results pertaining to the supercapacitor current imposed by the fuzzy control approach when Train 8 headway was modified

Figure 6.36 shows a good agreement between the supercapacitor SOC experimental and simulation results with only 2.4% error pertaining to the case under the stochastic traffic scenario when the SOC controller 1 was applied. The current profile comparison when applying the SOC controller 1 is shown in Figure 6.37 while

the current profile comparison when applying the SOC controller 2 can be seen in Figure 6.39. The fuzzy controller was more dynamic in changing the current limits as it was attempting to rapidly reduce the SOC drift. The supercapacitor SOC profile yielded by the fuzzy control method when applying the stochastic traffic scenario is shown in Figure 6.38 where the total percentage error was 1.8%.

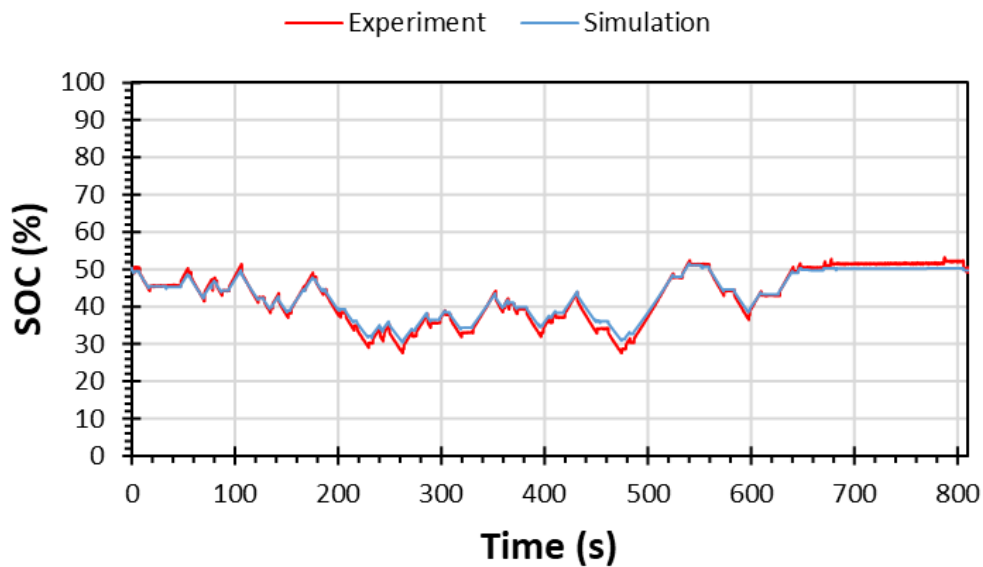


Figure 6.36: Comparison between the experimental and simulation results pertaining to the supercapacitor SOC produced by the state machine control under a realistic traffic scenario

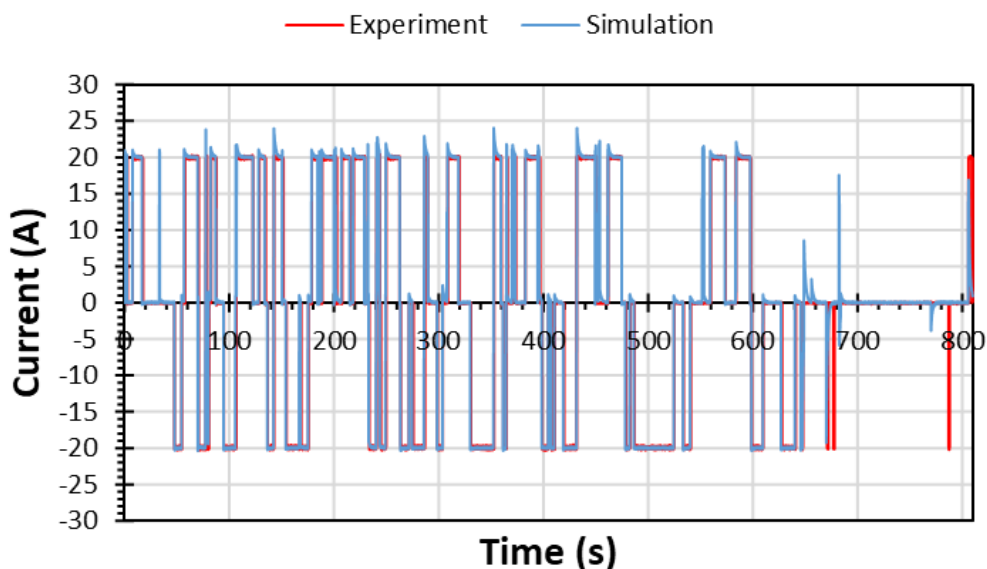


Figure 6.37: Comparison between the experimental and simulation results pertaining to the supercapacitor current determined by the state machine control under a realistic traffic scenario

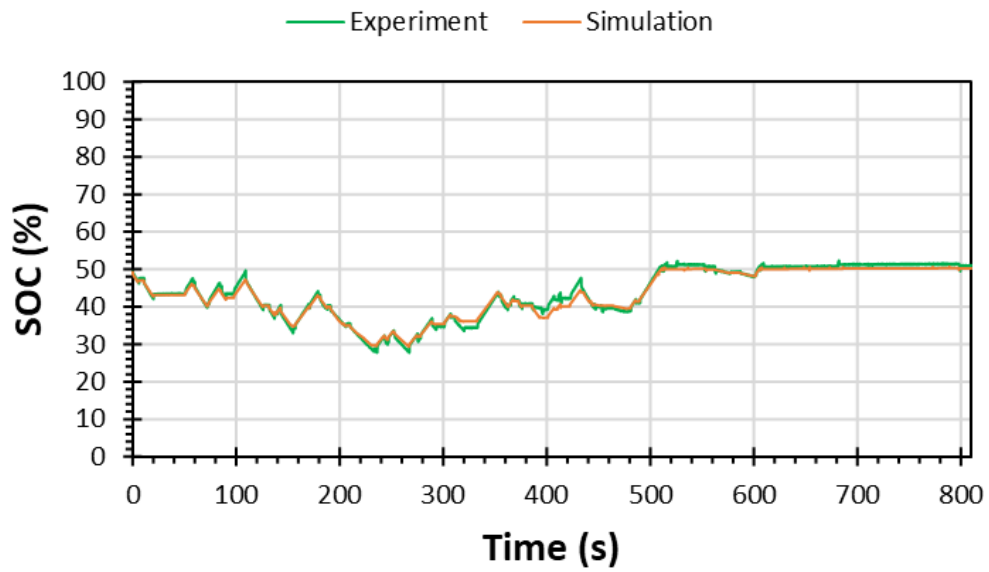


Figure 6.38: Comparison between the experimental and simulation results pertaining to the supercapacitor SOC obtained by applying the fuzzy control approach under a realistic traffic scenario

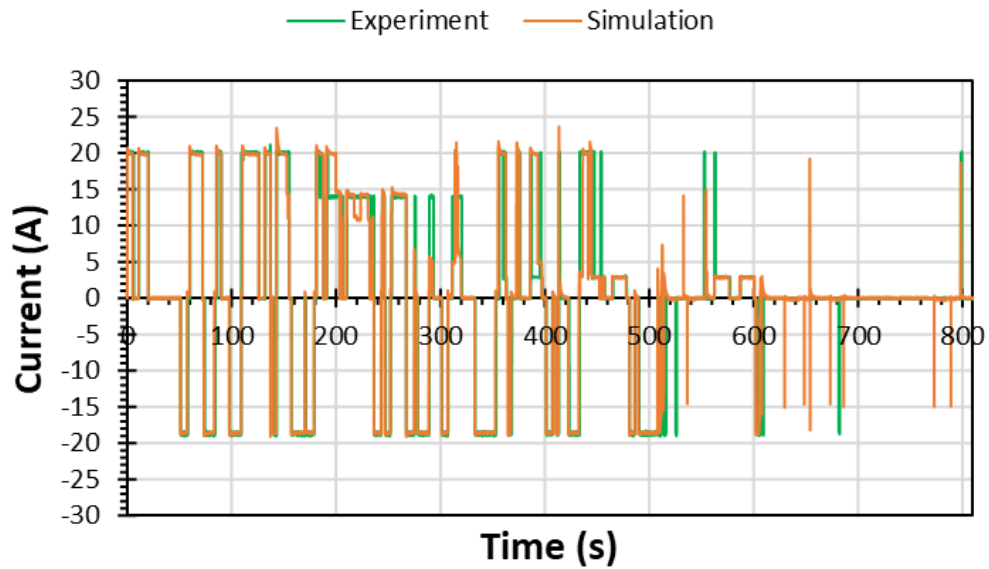


Figure 6.39: Comparison between the experimental and simulation results pertaining to the supercapacitor current obtained by applying the fuzzy control approach under a realistic traffic scenario

The similarity between the experimental and simulation results reported in this section is deemed to be satisfactory with respect to the following challenges. The supercapacitor model available in the MATLAB/Simulink environment was used in the simulations and was merely adapted to match the parameters of the real device used in the experiment without accurate representation of the response of the actual device. It is also noteworthy that a time delay in executing the devices contributed to the observed error. Specifically, during the experiment, three codes were needed to be run simultaneously to control the Zenone power supply, the CompactRIO microcontroller, and the SINAMICS DCP converter. However, as the user could not initiate all three codes simultaneously, the controller downloaded to the CompactRIO was not able to match the accurate timing of the operation cycle to the SOC deviation. This inaccurate timing affected the controller accuracy in dealing with the SOC deviation, because time is a vital aspect of the controller's design. Further, the fuzzy controller included a fuzzy set representing the running time with four membership functions. Therefore, the inaccurate timing might cause the measured time to fall within a different membership from the simulated time. This should only happen in the overlapping regions of the running time membership functions which caused different rules to be fired in the experiment from those in the simulation. This impact can be seen clearly in Figures 6.31, 6.35, and 6.39.

After operating the controller, the SINAMICS DCP power converter was switched on, which caused a delay in sending the readings to the controller. It is crucial for the SINAMICS DCP converter not to be started before the microcontroller because it will discharge the supercapacitor promptly, before involving the controller. This rapid discharge of the supercapacitor could contribute to the deviation from the initial SOC due to the low energy capacity of the device. It has been established that the controller behaviour is primarily driven by the deviation from the initial SOC, which was set to 50% in all experiments performed in this work. Therefore, if the SINAMICS DCP converter discharges the ESS to values that significantly deviate from 50% before operating the controller, the error between the simulation and the experimental results will be high, leading the controller to perform differently from the simulation.

6.6 Conclusion

In this chapter, the experimental results that enabled validation in hardware of the control methods proposed in Chapter 5 were presented and discussed. For this purpose, a test rig comprising a bidirectional power supply, an ESS, a power converter, and a microcontroller was built, and full details of the hardware and software configuration were provided. A number of traffic scenarios were applied to test the controller performance and the obtained results indicate that the control methods developed as a part of this work are capable of operating in real applications with good performance. Thereafter, the test rig was implemented in MATLAB software, thus allowing real measurements to be verified against simulations. The experimental results were shown to be in good agreement with the simulation results as the error percentage was ranging from 1.8 to 3.6% depending on the applied control method and traffic scenario.

Chapter 7

Conclusions and Future Work

7.1 Summary of research objectives

The first goal of this thesis was to develop a DC electric railway model to examine the capabilities of ESSs in improving the energy efficiency of DC electric railways as a means of reducing energy consumption and losses. The second goal of this research was to avoid the ESSs unavailability whilst maximising the electric railway energy efficiency. When an ESS is deployed in an electric railway and interfaced with the track while lacking access to the main grid, it will potentially be unavailable to charge/discharge energy due to being full/empty, which could limit its contribution to energy efficiency maximisation. Therefore, as part of this research, a number of control methods that could be adopted to ensure the ESS availability and, at the same time, maximise electric railway energy efficiency were investigated and assessed.

7.2 Conclusions

The findings yielded by this study provide several original and highly relevant contributions to both research and practice. First, a DC electric railway simulation method was developed. Second, an ESS was integrated into the railway model and a

sensitivity analysis was carried out on the import/export of power. Finally, control methods for SOC management were designed and validated experimentally.

The simulation methodology developed for this work and presented in Chapter 3 differs from other methods reported in pertinent literature as it facilitates modifications to the model by avoiding the common approach of forming iterative methods for solving the power flow. This novel simulation approach can thus be used to expand current knowledge of DC electric railways by observing the power system when modifying certain parameters such as speed profile, headway, dwell time, number of trains, number of substations, and location of substations. Consequently, this simulation method will be of interest to researchers and industry practitioners when testing the performance of innovative methods for energy efficiency improvement in electric railways.

It was concluded in Chapter 4 that introducing a wayside ESS to the railway model was also highly beneficial, as it increased the total energy saving by 42.38% (206.3 kWh) in a single journey when applying the ideal traffic scenario. Therefore, a comprehensive analysis of the system was carried out, involving studying the impact of ESS voltage control on different factors (i.e. energy demand at substations, transmission line losses, braking resistor losses, peak power demand, and SOC drift). This was the first comprehensive assessment of the effects of ESS application on electric railway performance conducted to date, yielding findings on which railway operators can base their systems to maximise the benefits of ESS deployment. Moreover, results reported in this study will allow operators to choose the appropriate voltage control values that meet their specific requirements. For example, some operators may give priority to reduction of substations energy demand, braking and transmission losses. Therefore, they could avoid upgrading infrastructure that is at capacity (asset deferral) and reduce heat dissipation that minimises the energy required for cooling. SOC drift is likely to be of high importance to some operators where it is not possible to connect the ESS to an external source/sink of power.

Three traffic scenarios were discussed in Chapter 5 and applied to the model incorporating a stationary ESS before being simulated for two days to show the

adverse impact of SOC drift in the long term. Compared to the case when the SOC boundaries were not reached, the total energy saving reduced by 0.08%, 4%, and 17.9% when applying the static controller under the first (ideal), second (changing train headway), and third (stochastic) traffic scenario, respectively. The total energy saving measuring the reduction in substations energy consumption, braking losses, and transmission losses was 42.34% (56,482 kWh), 41.02% (46,112 kWh), and 30.18% (10,629 kWh), respectively. The SOC drift was -82.38%, 100%, and 100%, respectively. Therefore, two adaptive controllers named SOC controller 1 and SOC controller 2 that aimed to reduce SOC drift were proposed. The first method was based on a state machine, including a control algorithm specifically designed for this purpose that succeeded in reducing the drift to 0.52% but was less effective in terms of energy saving as it only saved 38.96% (51,971 kWh) when simulating the first traffic scenario for two days. Further, when simulating the second traffic scenario the proposed controller saved 41.55% (46,728 kWh) with 0.5% SOC drift, while saving 38.75% (13,646 kWh) with 0.5% SOC drift when simulating the third traffic scenario. Therefore, another approach incorporating a fuzzy logic controller was developed that further reduced the SOC drift to 0.04% and increased the energy saving to 41.43% (55,278 kWh) when simulating the first traffic scenario. The fuzzy logic controller saved 43.08% (48,416 kWh) with 0.06% SOC drift when simulating the second traffic scenario while it saved 39.21% (13,806 kWh) with 0.2% SOC drift when simulating the third traffic scenario. It is worth mentioning that the adaptive controllers did not require retuning when applying different traffic scenarios.

Both adaptive control methods were tested experimentally to evaluate their performance in real applications as presented in Chapter 6. The adaptive controllers were compared with simulation results for validation where the error between the SOC profiles when applying the SOC controller 1 to the first traffic scenario was 3.6% while it was 3% when applying the SOC controller 2. Applying the SOC controller 1 to the second traffic scenario resulted in an error of 3.3% between the measured and simulated SOC profiles while it was only 2% when applying the SOC controller 2. The percentage error was 2.4 and 1.8% when applying the SOC controllers 1 and 2, respectively, to the third traffic scenario.

Based on extensive literature search, this appears to be the first attempt to examine the SOC drift issue relative to its impact on the energy efficiency of electric railways with unpredictable traffic density. Hence, the findings yielded by this study lay the groundwork for future research into control methods aimed at addressing this issue.

7.3 Study limitations and recommendations for future work

In research studies, certain limitations cannot be avoided, and in this particular case, the main limitation stemmed from the simulation tool utilised in this research, as it could not easily provide analysis over long operational cycles. The simulation model accuracy was demonstrated by applying multiple verification methods, none of which incorporated other simulation tools. To assess the modelling approach accuracy more objectively, it could be compared with the available commercial tools such as TrainOps, Sitras Sidytrac, eTraX, and TOM on like-for-like scenarios. Experimental investigations involving online simulators are required to accurately assess the performance of the proposed control methods in terms of their capability of energy efficiency improvement. Despite these limitations, the work presented in this thesis has certainly enhanced the current understanding of the SOC drift issue and the dynamic performance of the designed control methods in practical applications.

Finally, several questions still remain to be answered. These include the following: What is the impact of the energy efficiency maximisation methods developed in this research on the energy price of various electric railway systems?; and What is the ESS investment recuperation period with respect to its lifetime limitations? These and other issues offer ample opportunities to extend this research further, as it is essential to precisely determine the economic benefits of incorporating ESSs into electric railways along with the technical analysis in this thesis.

References

- [1] J. Chen, Y. Wu, C. Xu, M. Song and X. Liu, "Global non-fossil fuel consumption: driving factors, disparities, and trends," *Management Decision*, vol. 57, no. 4, pp. 791–810, Apr 2019. DOI: 10.1108/MD-04-2018-0409.
- [2] Europe 2020 indicators – climate change and energy, *Eurostat*, Luxembourg, Aug 2019. [Online]. Available: <https://ec.europa.eu/eurostat/statistics-explained/pdfscache/29304.pdf> (Accessed: Dec 09, 2020).
- [3] H. Steele, C. Roberts and S. Hillmansen, "Railway smart grids: Drivers, benefits and challenges," *Proceedings of the Institution of Mechanical Engineers, Part F: Journal of Rail and Rapid Transit*, vol. 233, no. 5, pp. 526–536, Sep 2018. DOI: 10.1177/0954409718800523.
- [4] M. Khodaparastan, O. Dutta, M. Saleh and A. Mohamed, "Modeling and simulation of DC electric rail transit systems with wayside energy storage," *IEEE Transactions on Vehicular Technology*, vol. 68, no. 3, pp. 2218–2228, Mar 2019. DOI: 10.1109/TVT.2019.2895026.
- [5] R. White, "DC electrification supply system design," in *7th IET Professional Development Course on Railway Electrification Infrastructure and Systems (REIS 2015)*, London, UK. DOI: 10.1049/ic.2015.0330.
- [6] G. Abad, *Power Electronics and Electric Drives for Traction Applications*. West Sussex, UK: John Wiley & Sons, 2017. ISBN: 9781118954423.
- [7] B. Mohamed, P. Arboleya and C. Gonzalez-Moran, "Modified current injection method for power flow analysis in heavy-meshed DC railway networks with nonreversible substations," *IEEE Transactions on Vehicular Technology*, vol. 66, no. 9, pp. 7688–7696, Sep 2017. DOI: 10.1109/TVT.2017.2687061.
- [8] H. Douglas, C. Roberts, S. Hillmansen and F. Schmid, "An assessment of available measures to reduce traction energy use in railway networks," *Energy Conversion and Management*, vol. 106, pp. 1149–1165, Dec 2015. DOI: 10.1016/j.enconman.2015.10.053.
- [9] M. Steiner, M. Klohr and S. Pagiela, "Energy storage system with ultracaps on board of railway vehicles," in *2007 European Conference on Power Electronics and Applications*, Aalborg, Denmark. DOI: 10.1109/EPE.2007.4417400.
- [10] E. Shabanova and V. Biryukov, "Analysis of the effectiveness of regenerative braking on subway trains," in *2019 20th International Conference of Young Specialists on*

- Micro/Nanotechnologies and Electron Devices (EDM)*, Altai Republic, Russia. DOI: 10.1109/EDM.2019.8823221.
- [11] S. Su, T. Tang and Y. Wang, "Evaluation of strategies to reducing traction energy consumption of metro systems using an optimal train control simulation model," *Energies*, vol. 9, no. 2, pp. 105–123, Feb 2016. DOI: 10.3390/en9020105.
- [12] Z. Tian, P. Weston, N. Zhao, S. Hillmansen, C. Roberts and L. Chen, "System energy optimisation strategies for metros with regeneration," *Transportation Research Part C: Emerging Technologies*, vol. 75, pp. 120–135, Feb 2017. DOI: 10.1016/j.trc.2016.12.004.
- [13] M. Ceraolo and G. Lutzemberger, "Stationary and on-board storage systems to enhance energy and cost efficiency of tramways," *Journal of Power Sources*, vol. 264, pp. 128–139, Oct 2014. DOI: 10.1016/j.jpowsour.2014.04.070.
- [14] Y. Yoshida, H. Figueroa and R. Dougal, "Comparison of energy storage configurations in railway microgrids," in *2017 IEEE Second International Conference on DC Microgrids (ICDCM)*, Nuremberg, Germany. DOI: 10.1109/ICDCM.2017.8001034.
- [15] S. Smiles, *Lives of Boulton and Watt*. London, UK: William Clowes and Sons, 1865.
[Online]. Available:
<https://books.google.com.sa/books?id=6EUOAAAAYAAJ&printsec=frontcover&vq=1698&hl=ar#v=onepage&q=1698&f=false> (Accessed: Dec 10, 2020).
- [16] L. Hebert, *The Engineer's and Mechanic's Encyclopedia*. London, UK: Thomas Kelly, 1835.
[Online]. Available:
https://books.google.com.sa/books?id=rXQRh2TeCZAC&printsec=frontcover&hl=ar&source=gbg_summary_r&cad=0#v=onepage&q&f=false (Accessed: Dec 10, 2020).
- [17] M. Kirby, *The Origins of Railway Enterprise: The Stockton and Darlington Railway 1821–1863*. Cambridge, UK: Cambridge University Press, 1993. ISBN: 9780521384452.
- [18] S. Clark, "A history of railway signalling (from the bobby to the balise)," in *IET Professional Development Course on Railway Signalling and Control Systems (RSCS 2012)*, London, UK, pp. 6–25. DOI: 10.1049/ic.2012.0040.
- [19] M. Klein, "Replacement technology: The diesel as a case study," *Railway & Locomotive Historical Society (R&LHS)*, no. 162, pp. 109–120, Apr 1990. [Online]. Available:
<http://www.jstor.org/stable/43521391> (Accessed: Dec 10, 2020).
- [20] O. Melsted and I. Pallua, "The historical transition from coal to hydrocarbons: Previous explanations and the need for an integrative perspective," *Canadian Journal of History*, vol. 53, no. 3, pp. 395–422, Dec 2018. DOI: 10.3138/cjh.ach.53.3.03.
- [21] A. Hoffrichter, "Hydrogen as an energy carrier for railway traction," Ph.D. thesis, College of Engineering and Physical Sciences, The University of Birmingham, UK,

2013. [Online]. Available:
<https://theses.bham.ac.uk/id/eprint/4345/9/Hoffrichter13PhD1.pdf> (Accessed: Dec 10, 2020).
- [22] P. Ransome-Wallis, *Illustrated Encyclopedia of World Railway Locomotives*. New York, US: Dover Publications, 1959. ISBN: 0486412474.
- [23] J. Serra, *Electric Vehicles Technology, Policy and Commercial Development*. New York, US: Earthscan, 2012. ISBN: 9781849714150.
- [24] M. Guarnieri, "When cars went electric – part 1," *IEEE Industrial Electronics Magazine*, vol. 5, no. 1, pp. 61–62, Mar 2011. DOI: 10.1109/MIE.2011.940248.
- [25] Siemens, "A detour to success." Siemens.
<https://new.siemens.com/global/en/company/about/history/stories/first-electric-streetcar.html> (Accessed: Dec 11, 2020).
- [26] P. Radu and Z. Drazek, "Analysis of wayside energy storage devices for DC heavy rail transport," in *13th International Conference Modern Electrified Transport – MET'2017*, Warsaw, Poland. DOI: 10.1051/mateconf/201818004001.
- [27] New Zealand Government Railways Department, "Edison storage battery rail car. – successful in canterbury district," *The New Zealand Railways Magazine*, vol. 2, no. 10, Feb 1928. [Online]. Available: http://nzetc.victoria.ac.nz/tm/scholarly/tei-Gov02_10Rail-t1-body-d4.html (Accessed: Dec 11, 2020).
- [28] M. Mulvihill, *Ingenious Ireland: A County-by-county Exploration of Irish Mysteries and Marvels*. Dublin, Ireland: Town House and Country House, 2002. ISBN: 1860591450.
- [29] D. Murray-Smith, "A review of development in electrical battery, fuel cell and energy recovery systems for railway applications," *The Scottish Association for Public Transport*, Glasgow, Scotland, UK, Nov 2019. DOI: 10.13140/RG.2.2.16555.67362.
- [30] J. Pagenkopf and S. Kaimer, "Potentials of alternative propulsion systems for railway vehicles – A techno-economic evaluation," in *2014 Ninth International Conference on Ecological Vehicles and Renewable Energies (EVER)*, Monte-Carlo, Monaco. DOI: 10.1109/EVER.2014.6843995.
- [31] A. Hoffrichter, A. Miller, S. Hillmansen and C. Roberts, "Well-to-wheel analysis for electric, diesel and hydrogen traction for railways," *Transportation Research Part D: Transport and Environment*, vol. 17, no. 1, pp. 28–34, Jan 2012. DOI: 10.1016/j.trd.2011.09.002.
- [32] S. Ricci and C. A. Brebbia, *Transport and the City*. Southampton, UK: WTT Press, 2018. ISBN: 9781784663179.
- [33] S. Frey, *Railway Electrification Systems & Engineering*. Delhi, India: White Word Publications, 2012. ISBN: 9788132343950.

- [34] L. Liudvinavicius and L. Lingaitis, "Electrodynamic braking in high-speed rail transport," *Transport*, vol. 22, no. 3, pp. 178–186, Oct 2010. DOI: 10.1080/16484142.2007.9638122.
- [35] Y. Lino, H. Hayashiya, M. Hino, S. Abe, K. Nakao and K. Kudo, "Evaluation of installation effect of the energy storage system in D.C. traction power supply system," in *2016 IEEE International Power Electronics and Motion Control Conference (PEMC)*, Varna, Bulgaria. DOI: 10.1109/EPEPEMC.2016.7752011.
- [36] N. Ghaviha, M. Bohlin, C. Holmberg and E. Dahlquist, "Speed profile optimization of catenary-free electric trains with lithium-ion batteries," *Journal of Modern Transportation*, vol. 27, no. 3, pp. 153–168, Jan 2019. DOI: 10.1007/s40534-018-0181-y.
- [37] A. Gonzalez-Gil, R. Palacin and P. Batty, "Sustainable urban rail systems: Strategies and technologies for optimal management of regenerative braking energy," *Energy Conversion and Management*, vol. 75, pp. 374–388, Nov 2013. DOI: 10.1016/j.enconman.2013.06.039.
- [38] A. Rufer, "Energy storage for railway systems, energy recovery and vehicle autonomy in Europe," in *The 2010 International Power Electronics Conference – ECCE ASIA*, Sapporo, Japan. DOI: 10.1109/IPEC.2010.5542334.
- [39] C. Carlini and D. Moneta, "Flash recharging tram catenary-free: Impact analysis on Italian distribution networks," in *1st E-Mobility Power System Integration Symposium*, Berlin, Germany, 2017.
- [40] A. Zurkowski, *High-Speed Rail in Poland: Advances and Perspectives*. London, UK: Taylor & Francis Group, 2018. ISBN: 9781351003308.
- [41] S. Kamra, *DMRC Exam for Jr. Engineer (Electrical) Guide + Practice Workbook, 2nd ed.* New Delhi, India: Disha Publications, 2017. ISBN: 9789384089337.
- [42] M. Chymera and C. Goodman, "Overview of electric railway systems and the calculation of train performance," in *IET Professional Development Course on Electric Traction Systems*, London, UK, 2012. DOI: 10.1049/ic.2012.0070.
- [43] A. Zaboli, B. Vahidi, S. Yousefi and M. Hosseini-Biyouki, "Evaluation and control of stray current in dc-electrified railway systems," *IEEE Transactions on Vehicular Technology*, vol. 66, no. 2, pp. 974–980, Apr 2016. DOI: 10.1109/TVT.2016.2555485.
- [44] Wikipedia, "Third rail." Wikipedia. https://en.wikipedia.org/wiki/Third_rail (Accessed: Dec 12, 2020).
- [45] H. Douglass, C. Roberts and S. Hillmansen, "Optimising energy saving in metro systems through characteristic evaluation," in *International Conference on Railway Engineering (ICRE 2016)*, Brussels, Belgium. DOI: 10.1049/cp.2016.0517.

- [46] F. Lin, S. Liu, Z. Yang, Y. Zhao, Z. Yang and H. Sun, "Multi-train energy saving for maximum usage of regenerative energy by dwell time optimization in urban rail transit using genetic algorithm," *Energies*, vol. 9, no. 3, pp. 208–228, Mar 2016. DOI: 10.3390/en9030208.
- [47] M. Khodaparastan, A. Mohamed and W. Brandauer, "Recuperation of regenerative braking energy in electric rail transit systems," *IEEE Transactions on Intelligent Transportation Systems*, vol. 20, no. 8, pp. 2831–2847, Aug 2019. DOI: 10.1109/TITS.2018.2886809.
- [48] Wongm's Rail Gallery, "Resistor grids on the roof of an X'Trapolis train." Wongm's Rail Gallery. https://railgallery.wongm.com/melbourne-suburban-bits/F105_1552.jpg.html (Accessed: Dec 12, 2020).
- [49] T. Kulworawanichpong, "Multi-train modeling and simulation integrated with traction power supply solver using simplified Newton-Raphson method," *Journal of Modern Transportation*, vol. 23, no. 4, pp. 241–251, Dec 2015. DOI: 10.1007/s40534-015-0086-y.
- [50] Z. Gao, J. Fang, Y. Zhang, L. Jiang, D. Sun and W. Guo, "Control of urban rail transit equipped with ground-based supercapacitor for energy saving and reduction of power peak demand," *International Journal of Electrical Power & Energy Systems*, vol. 67, pp. 439–447, May 2015. DOI: 10.1016/j.ijepes.2014.11.019.
- [51] K. Mongkoldee, U. Leeton and T. Kulworawanichpong, "Single train movement modelling and simulation with rail potential consideration," in *2016 IEEE/SICE International Symposium on System Integration (SII)*, Sapporo, Japan. DOI: 10.1109/SII.2016.7843967.
- [52] R. Jabr and I. Dzafic, "Solution of DC railway traction power flow systems including limited network receptivity," *IEEE Transactions on Power Systems*, vol. 33, no. 1, pp. 962–969, Jan 2018. DOI: 10.1109/TPWRS.2017.2688338.
- [53] P. Arboleya, B. Mohamed and I. El-Sayed, "DC railway simulation including controllable power electronic and energy storage devices," *IEEE Transactions on Power Systems*, vol. 33, no. 5, pp. 5319–5329, Sep 2018. DOI: 10.1109/TPWRS.2018.2801023.
- [54] P. Arboleya, G. Diaz and M. Coto, "Unified AC/DC power flow for traction systems: A new concept," *IEEE Transactions on Vehicular Technology*, vol. 61, no. 6, pp. 2421–2430, Jul 2012. DOI: 10.1109/TVT.2012.2196298.
- [55] Z. Tian, S. Hillmansen, C. Roberts, P. Weston, N. Zhao, L. Chen and M. Chen, "Energy evaluation of the power network of a DC railway system with regenerating trains," *IET Electrical Systems in Transportation*, vol. 6, no. 2, pp. 41–49, Jun 2016. DOI: 10.1049/iet-est.2015.0025.

- [56] P. Arboleya, M. Coto, C. Gonzalez-Moran and R. Arregui, "On board accumulator model for power flow studies in DC traction networks," *Electric Power Systems Research*, vol. 116, pp. 266–275, Nov 2014. DOI: 10.1016/j.epsr.2014.06.016.
- [57] M. Chymera, A. Renfrew, M. Barnes and J. Holden, "Modeling electrified transit systems," *IEEE Transactions on Vehicular Technology*, vol. 59, no. 6, pp. 2748–2756, Jul 2010. DOI: 10.1109/TVT.2010.2050220.
- [58] H. Xia, H. Chen, Z. Yang, F. Lin and B. Wang, "Optimal energy management, location and size for stationary energy storage system in a metro line based on genetic algorithm," *Energies*, vol. 8, no. 10, pp. 11618–11640, Oct 2015. DOI: 10.3390/en81011618.
- [59] C. Mayet, P. Delarue, A. Bouscayrol, E. Chattot and J. Verhille, "Comparison of different EMR-based models of traction power substations for energetic studies of subway lines," *IEEE Transactions on Vehicular Technology*, vol. 65, no. 3, pp. 1021–1029, Mar 2016. DOI: 10.1109/TVT.2015.2474148.
- [60] P. Fernandez, C. Roman and R. Franco, "Modelling electric trains energy consumption using neural networks," in *Transportation Research Procedia*, Valencia, Spain, 2016, pp. 59–65. DOI: 10.1016/j.trpro.2016.12.008.
- [61] M. Ceraolo, G. Lutzemberger, E. Meli, L. Pugi, A. Rindi and G. Pancari, "Energy storage systems to exploit regenerative braking in DC railway systems: Different approaches to improve efficiency of modern high-speed trains," *Journal of Energy Storage*, vol. 16, pp. 269–279, Apr 2018. DOI: 10.1016/j.est.2018.01.017.
- [62] M. Khodaparastan and A. Mohamed, "Modeling and simulation of regenerative braking energy in DC electric rail systems," in *2018 IEEE Transportation Electrification Conference and Expo (ITEC)*, Long Beach, CA, USA. DOI: 10.1109/ITEC.2018.8450133.
- [63] A. Fernandez-Rodriguez, A. Fernandez-Cardador, A. Cucala, M. Dominguez and T. Gonsalves, "Design of robust and energy-efficient ATO speed profiles of metropolitan lines considering train load variation and delays," *IEEE Transactions on Intelligent Transportation Systems*, vol. 16, no. 4, pp. 2061–2071, Aug 2015. DOI: 10.1109/TITS.2015.2391831.
- [64] S. Su, T. Tang and C. Roberts, "A cooperative train control model for energy saving," *IEEE Transactions on Intelligent Transportation Systems*, vol. 16, no. 2, pp. 622–631, Apr 2015. DOI: 10.1109/TITS.2014.2334061.
- [65] X. Yang, B. Ning, X. Li and T. Tang, "A two-objective timetable optimization model in subway systems," *IEEE Transactions on Intelligent Transportation Systems*, vol. 15, no. 5, pp. 1913–1921, Oct 2014. DOI: 10.1109/TITS.2014.2303146.

- [66] S. Su, X. Li, T. Tang and Z. Gao, "A subway train timetable optimization approach based on energy-efficient operation strategy," *IEEE Transactions on Intelligent Transportation Systems*, vol. 14, no. 2, pp. 883–893, Jun 2013. DOI: 10.1109/TITS.2013.2244885.
- [67] N. Zhao, C. Roberts, S. Hillmansen, Z. Tian, P. Weston and L. Chen, "An integrated metro operation optimization to minimize energy consumption," *Transportation Research Part C: Emerging Technologies*, vol. 75, pp. 168–182, Feb 2017. DOI: 10.1016/j.trc.2016.12.013.
- [68] V. Gelman, "Energy storage that may be too good to be true: Comparison between wayside storage and reversible thyristor controlled rectifiers for heavy rail," *IEEE Vehicular Technology Magazine*, vol. 8, no. 4, pp. 70–80, Dec 2013. DOI: 10.1109/MVT.2013.2283350.
- [69] M. Popescu and A. Bitoleanu, "A review of the energy efficiency improvement in DC railway systems," *Energies*, vol. 12, no. 6, pp. 1092–11117, Mar 2019. DOI: 10.3390/en12061092.
- [70] J. Ortega, H. Ibaiondo and A. Romo, "Kinetic energy recovery on railway systems with feedback to the grid," in *9th World Congress on Railway Research (WCRR)*, Lille, France, 2011. [Online]. Available: http://www.railway-research.org/IMG/pdf/a5_romo_asier.pdf (Accessed: Dec 14, 2020).
- [71] F. Meishner and D. Sauer, "Wayside energy recovery systems in DC urban railway grids," *eTransportation*, vol. 1, Aug 2019. DOI: 10.1016/j.etrans.2019.04.001.
- [72] S. Gazafzudi, A. Langerudy, E. Fuchs and K. Al-Haddad, "Power quality issues in railway electrification: A comprehensive perspective," *IEEE Transactions on Industrial Electronics*, vol. 62, no. 5, pp. 3081–3090, May 2015. DOI: 10.1109/TIE.2014.2386794.
- [73] A. Gonzalez-Gil, R. Palacin, P. Batty and J. Powell, "A systems approach to reduce urban rail energy consumption," *Energy Conversion and Management*, vol. 80, pp. 509–524, Apr 2014. DOI: 10.1016/j.enconman.2014.01.060.
- [74] S. Koochi-Fayegh and M. Rosen, "A review of energy storage types, applications and recent developments," *Journal of Energy Storage*, vol. 27, Feb 2020. DOI: 10.1016/j.est.2019.101047.
- [75] L. Wong, V. Ramachandaramurthy, P. Taylor, J. Ekanayake, S. Walker and S. Padmanaban, "Review on the optimal placement, sizing and control of an energy storage system in the distribution network," *Journal of Energy Storage*, vol. 21, pp. 489–504, Feb 2019. DOI: 10.1016/j.est.2018.12.015.

- [76] A. Dehghani-Sanij, E. Tharumalingam, M. Dusseault and R. Fraser, "Study of energy storage systems and environmental challenges of batteries," *Renewable and Sustainable Energy Reviews*, vol. 104, pp. 192–208, Apr 2019. DOI: 10.1016/j.rser.2019.01.023.
- [77] P. Nikolaidis and A. Poullikkas, "Cost metrics of electrical energy storage technologies in potential power system operations," *Sustainable Energy Technologies and Assessments*, vol. 25, pp. 43–59, Feb 2018. DOI: 10.1016/j.seta.2017.12.001.
- [78] A. Tomczewski, L. Kasprzyk and Z. Nadolny, "Reduction of power production costs in a wind power plant-flywheel energy storage system arrangement," *Energies*, vol. 12, no. 10, pp. 1942–1965, May 2019. DOI: 10.3390/en12101942.
- [79] M. Khodaparastan and A. Mohamed, "Flywheel vs. supercapacitor as wayside energy storage for electric rail transit systems," *Energies*, vol. 4, no. 4, pp. 62–76, Oct 2019. DOI: 10.3390/inventions4040062.
- [80] X. Liu and K. Li, "Energy storage devices in electrified railway systems: A review," *Transportation Safety and Environment*, vol. 2, no. 3, pp. 183–201, Sep 2020. DOI: 10.1093/tse/tdaa016.
- [81] F. Ciccarelli, A. Pizzo and D. Iannuzzi, "Improvement of energy efficiency in light railway vehicles based on power management control of wayside lithium-ion capacitor storage," *IEEE Transactions on Power Electronics*, vol. 29, no. 1, pp. 275–286, Jan 2014. DOI: 10.1109/TPEL.2013.2253492.
- [82] V. Kleftakis and N. Hatzargyriou, "Optimal control of reversible substations and wayside storage devices for voltage stabilization and energy savings in metro railway networks," *IEEE Transactions on Transportation Electrification*, vol. 5, no. 2, pp. 515–523, Jun 2019. DOI: 10.1109/TTE.2019.2913355.
- [83] I. Buchmann, *Batteries in a Portable World: A Handbook on Rechargeable Batteries for Non-Engineers, 4th ed.* Richmond, Canada: Cadex Electronics Inc, 2016. ISBN: 9780968211847. [Online]. Available: <http://www.batteryuniversity.com> (Accessed: Dec 15, 2020).
- [84] D. Linden and T. Reddy, *Handbook of Batteries, 3rd ed.* New York, US: McGraw-Hill, 2001. ISBN: 0071359788.
- [85] M. Kumar, S. Ghosh and S. Das, "Charge-discharge energy efficiency analysis of ultracapacitor with fractional-order dynamics using hybrid optimization and its experimental validation," *International Journal of Electronics and Communications*, vol. 78, pp. 274–280, Aug 2017. DOI: 10.1016/j.aeue.2017.05.011.
- [86] T. Ratniyomchai, S. Hillmansen and P. Tricoli, "Recent developments and applications of energy storage devices in electrified railways," *IET Electrical Systems in Transportation*, vol. 4, no. 1, pp. 9–20, Mar 2014. DOI: 10.1049/iet-est.2013.0031.

- [87] T. Konishi, H. Morimoto, T. Aihara and M. Tsutakawa, "Fixed energy storage technology applied for DC electrified railway," *IEEJ Transactions on Electrical and Electronic Engineering*, vol. 5, no. 3, pp. 270–277, May 2010. DOI: 10.1002/tee.20529.
- [88] M. Ogasa, "Application of energy storage technologies for electric railway vehicles—examples with hybrid electric railway vehicles," *IEEJ Transactions on Electrical and Electronic Engineering*, vol. 5, no. 3, pp. 304–311, May 2010. DOI: 10.1002/tee.20534.
- [89] P. Radcliffe, J. Wallace and L. Shu, "Stationary applications of energy storage technologies for transit systems," in *2010 IEEE Electrical Power & Energy Conference*, Halifax, Canada. DOI: 10.1109/EPEC.2010.5697222.
- [90] O. Solis, F. Castro, L. Bukhin, K. Pham, D. Turner and G. Thompson, "Saving money every day: La metro subway wayside energy storage substation," in *Proceedings of the 2015 Joint Rail Conference*, San Jose, California, USA. DOI: 10.1115/JRC2015-5691.
- [91] G. Rechard and R. Gouttefangeas, "Recovering energy from train braking for traction and grid use," *Energy Procedia*, vol. 143, pp. 61–66, Dec 2017. DOI: 10.1016/j.egypro.2017.12.648.
- [92] Z. Yang, Z. Yang, X. Li and F. Lin, "The real-time optimization of charge/discharge voltage threshold for energy storage system in urban rail transit," in *IECON 2017 – 43rd Annual Conference of the IEEE Industrial Electronics Society*, Beijing, China. DOI: 10.1109/IECON.2017.8216672.
- [93] M. Meinert, "New mobile energy storage system for rolling stock," in *2009 13th European Conference on Power Electronics and Applications*, Barcelona, Spain. ISBN: 9781424444328.
- [94] P. Arboleya, P. Bidaguren and U. Armendariz, "Energy is on board: Energy storage and other alternatives in modern light railways," *IEEE Electrification Magazine*, vol. 4, no. 3, pp. 30–41, Sep 2016. DOI: 10.1109/MELE.2016.2584938.
- [95] C. Nash, J. Nilsson and H. Link, "Comparing three models for introduction of competition into railways," *Journal of Transport Economics and Policy (JTPEP)*, vol. 47, no. 2, pp. 191–206, May 2013. ISSN: 0022-5258.
- [96] F. Ciccarelli, D. Iannuzzi, K. Kondo and L. Fratelli, "Line-voltage control based on wayside energy storage systems for tramway networks," *IEEE Transactions on Power Electronics*, vol. 31, no. 1, pp. 884–899, Jan 2016. DOI: 10.1109/TPEL.2015.2411996.
- [97] F. Zhu, Z. Yang, H. Xia and F. Lin, "Hierarchical control and full-range dynamic performance optimization of the supercapacitor energy storage system in urban railway," *IEEE Transactions on Industrial Electronics*, vol. 65, no. 8, pp. 6646–6656, Aug 2018. DOI: 10.1109/TIE.2017.2772174.

- [98] Z. Yang, Z. Yang, H. Xia and F. Lin, "Brake voltage following control of supercapacitor-based energy storage systems in metro considering train operation state," *IEEE Transactions on Industrial Electronics*, vol. 65, no. 8, pp. 6751–6761, Aug 2018. DOI: 10.1109/TIE.2018.2793184.
- [99] F. Ciccarelli, D. Iannuzzi, D. Lauria and P. Natale, "Optimal control of stationary Lithium-Ion capacitor-based storage device for light electrical transportation network," *IEEE Transactions on Transportation Electrification*, vol. 3, no. 3, pp. 618–631, Sep 2017. DOI: 10.1109/TTE.2017.2739399.
- [100] D. Iannuzzi, E. Pagano and P. Tricoli, "The use of energy storage systems for supporting the voltage needs of urban and suburban railway contact lines," *Energies*, vol. 6, no. 4, pp. 1802–1820, Mar 2013. DOI: 10.3390/en6041802.
- [101] G. Graber, V. Calderaro, V. Galdi, A. Piccolo, R. Lamedica and A. Ruvio, "Techno-economic sizing of auxiliary-battery-based substations in DC railway systems," *IEEE Transactions on Transportation Electrification*, vol. 4, no. 2, pp. 616–625, Jun 2018. DOI: 10.1109/TTE.2018.2825651.
- [102] A. Gillespie, E. Johanson and D. Montvydas, "Energy storage in Pennsylvania: SEPTA's novel and innovative integration of emerging smart grid technologies," *IEEE Vehicular Technology Magazine*, vol. 9, no. 2, pp. 76–86, Jun 2014. DOI: 10.1109/MVT.2014.2313030.
- [103] J. Aguado, A. Racero and S. Torre, "Optimal operation of electric railways with renewable energy and electric storage systems," *IEEE Transactions on Smart Grid*, vol. 9, no. 2, pp. 993–1001, Mar 2018. DOI: 10.1109/TSG.2016.2574200.
- [104] J. Torreglosa, P. Garcia, L. Fernandez and F. Jurado, "Predictive control for the energy management of a fuel-cell-battery-supercapacitor tramway," *IEEE Transactions on Industrial Informatics*, vol. 10, no. 1, pp. 276–285, Feb 2014. DOI: 10.1109/TII.2013.2245140.
- [105] Q. Li, T. Wang, C. Dai, W. Chen and L. Ma, "Power management strategy based on adaptive droop control for a fuel cell-battery-supercapacitor hybrid tramway," *IEEE Transactions on Vehicular Technology*, vol. 67, no. 7, pp. 5658–5670, Jul 2018. DOI: 10.1109/TVT.2017.2715178.
- [106] Q. Li, B. Su, Y. Pu, Y. Han, T. Wang, L. Yin and W. Chen, "A state machine control based on equivalent consumption minimization for fuel cell/supercapacitor hybrid tramway," *IEEE Transactions on Transportation Electrification*, vol. 5, no. 2, pp. 552–564, Jun 2019. DOI: 10.1109/TTE.2019.2915689.
- [107] R. Takagi and T. Amano, "Optimisation of reference state-of-charge curves for the feed-forward charge/discharge control of energy storage systems on-board DC electric

- railway vehicles," *IET Electrical Systems in Transportation*, vol. 5, no. 1, pp. 33–42, Mar 2015. DOI: 10.1049/iet-est.2012.0014.
- [108] Z. Tian, "System energy optimisation strategies for DC railway traction power networks," Ph.D. thesis, College of Engineering and Physical Sciences, The University of Birmingham, UK, 2017. [Online]. Available: <https://etheses.bham.ac.uk/id/eprint/7779/1/Tian17PhD.pdf> (Accessed: Dec 21, 2020).
- [109] S. Kaewunruen and T. Tang, "Idealisations of dynamic modelling for railway ballast in flood conditions," *Energies*, vol. 9, no. 9, pp. 1785–1812, Apr 2019. DOI: 10.3390/app9091785.
- [110] F. Lin, X. Li, Y. Zhao and Z. Yang, "Control strategies with dynamic threshold adjustment for supercapacitor energy storage system considering the train and substation characteristics in urban rail transit," *Energies*, vol. 9, no. 4, pp. 257–274, Mar 2016. DOI: 10.3390/en9040257.
- [111] L. Yu, J. He, M. Li, Z. Bo, T. Yip, J. Hu and A. Klimek, "Simulation and protection algorithm development of sequential tripping in DC traction system," in *10th IET International Conference on Development in Power System Protection (DPSP 2010)*, Manchester, UK. DOI: 10.1049/cp.2010.0249.
- [112] B. Rai, *Handbook of Research on Emerging Innovations in Rail Transportation Engineering*. Pennsylvania, US: IGI Global, 2016. ISBN: 9781522500858.
- [113] L. Yu, J. He, Z. Bo, M. Li, T. Yip and A. Klimek, "Simulation and protection scheme analysis of articulated neutral section insulator in DC railway system," in *2010 Asia-Pacific Power and Energy Engineering Conference*, Chengdu, China. DOI: 10.1109/APPEEC.2010.5448260.
- [114] X. Yang, X. Li, Z. Gao, H. Wang and T. Tang, "A cooperative scheduling model for timetable optimization in subway systems," *IEEE Transactions on Intelligent Transportation Systems*, vol. 14, no. 1, pp. 438–447, Mar 2013. DOI: 10.1109/TITS.2012.2219620.
- [115] N. Zhao, "Railway traffic flow optimisation with differing control systems," Ph.D. thesis, School of Electronic, Electrical and Computer Engineering, The University of Birmingham, UK, 2013. [Online]. Available: <https://etheses.bham.ac.uk/id/eprint/4725/1/Zhao13PhD.pdf> (Accessed: Dec 22, 2020).
- [116] X. Li and H. Lo, "Energy minimization in dynamic train scheduling and control for metro rail operations," *Transportation Research Part B: Methodological*, vol. 70, pp. 269–284, Dec 2014. DOI: 10.1016/j.trb.2014.09.009.

- [117] M. Leigh, "Brake blending," *Proceedings of the Institution of Mechanical Engineers, Part F: Journal of Rail and Rapid Transit*, vol. 208, no. 1, pp. 43–49, Jan 1994. DOI: 10.1243/PIME_PROC_1994_208_232_02.
- [118] J. Yin, D. Chen, L. Yang, T. Tang and B. Ran, "Efficient real-time train operation algorithms with uncertain passenger demands," *IEEE Transactions on Intelligent Transportation Systems*, vol. 17, no. 9, pp. 2600–2612, Sep 2016. DOI: 10.1109/TITS.2015.2478403.
- [119] R. Hill, "Electric railway traction. I. Electric traction and DC traction motor drives," *Power Engineering Journal*, vol. 8, no. 1, pp. 47–56, Feb 1994. DOI: 10.1049/pe:19940105.
- [120] N. Zhao, L. Chen, Z. Tian, C. Roberts, S. Hillmansen and J. Lv, "Field test of train trajectory optimisation on a metro line," *IET Intelligent Transport Systems*, vol. 11, no. 5, pp. 273–281, Jun 2017. DOI: 10.1049/iet-its.2016.0214.
- [121] S. Su, T. Tang and X. Li, "Driving strategy optimization for trains in subway systems," *Proceedings of the Institution of Mechanical Engineers, Part F: Journal of Rail and Rapid Transit*, vol. 232, no. 2, pp. 369–383, Oct 2016. DOI: 10.1177/0954409716671546.
- [122] F. Richard, *Advances in Communications-Based Train Control Systems*. Florida, US: Taylor & Francis Group, 2016. ISBN: 9781482257458.
- [123] Y. Wu, Z. Wei, J. Weng and R. Deng, "Position manipulation attacks to balise-based train automatic stop control," *IEEE Transactions on Vehicular Technology*, vol. 67, no. 6, pp. 5287–5301, Jun 2018. DOI: 10.1109/TVT.2018.2802444.
- [124] Y. Huang, L. Yang, T. Tang, Z. Gao, F. Cao and K. Li, "Train speed profile optimization with on-board energy storage devices: A dynamic programming based approach," *Computers & Industrial Engineering*, vol. 126, pp. 149–164, Dec 2018. DOI: 10.1016/j.cie.2018.09.024.
- [125] A. Nasri, M. Moghadam and H. Mokhtari, "Timetable optimization for maximum usage of regenerative energy of braking in electrical railway systems," in *International Symposium on Power Electronics, Electrical Drives, Automation and Motion*, Pisa, Italy, 2010, pp. 1218–1221. DOI: 10.1109/SPEEDAM.2010.5542099.
- [126] D. Roch-Dupre, A. Lopez-Lopez, R. Pecharroman, A. Cucala and A. Fernandez-Cardador, "Analysis of the demand charge in DC railway systems and reduction of its economic impact with energy storage systems," *International Journal of Electrical Power & Energy Systems*, vol. 93, pp. 459–467, Dec 2017. DOI: 10.1016/j.ijepes.2017.06.022.
- [127] B. Ning, J. Xun, S. Gao and L. Zhang, "An integrated control model for headway regulation and energy saving in urban rail transit," *IEEE Transactions on Intelligent Transportation Systems*, vol. 16, no. 3, pp. 1469–1478, Jun 2015. DOI: 10.1109/TITS.2014.2366495.

- [128] D. Fletcher, R. Harrison and S. Nallaperuma, "TransEnergy - a tool for energy storage optimization, peak power and energy consumption reduction in DC electric railway systems," *Journal of Energy Storage*, vol. 30, Aug 2020. DOI: 10.1016/j.est.2020.101425.
- [129] V. Gelman, "Comparison between wayside storage and reversible thyristor controlled rectifiers (RTCR) for heavy rail applications," in *The 2013 Joint Rail Conference*, Tennessee, USA. DOI: 10.1115/JRC2013-2460.
- [130] D. Iannuzzi and P. Tricoli, "Speed-based state-of-charge tracking control for metro trains with onboard supercapacitors," *IEEE Transactions on Power Electronics*, vol. 27, no. 4, pp. 2129–2140, Apr 2012. DOI: 10.1109/TPEL.2011.2167633.
- [131] R. Teymourfar, B. Asaei, H. Iman-Eini and R. Nejati, "Stationary super-capacitor energy storage system to save regenerative braking energy in a metro line," *Energy Conversion and Management*, vol. 56, pp. 206–214, Apr 2012. DOI: 10.1016/j.enconman.2011.11.019.
- [132] D. Iannuzzi, P. Pighetti and P. Tricoli, "A study on stationary supercapacitor sets for voltage droops compensation of streetcar feeder lines," in *Electrical Systems for Aircraft, Railway and ship Propulsion*, Bologna, Italy, 2010. DOI: 10.1109/ESARS.2010.5665196.
- [133] B. Wang, Z. Yang, F. Lin and W. Zhao, "An improved genetic algorithm for optimal stationary energy storage system locating and sizing," *Energies*, vol. 7, no. 10, pp. 6434–6458, Oct 2014. DOI: 10.3390/en7106434.
- [134] R. Barrero, X. Tackoen and J. Van Mierlo, "Stationary or onboard energy storage systems for energy consumption reduction in a metro network," *Proceedings of the Institution of Mechanical Engineers, Part F: Journal of Rail and Rapid Transit*, vol. 224, no. 3, pp. 207–225, Apr 2010. DOI: 10.1243/09544097JRRT322.
- [135] G. Graber, V. Galdi, V. Calderaro and A. Piccolo, "Sizing and energy management of on-board hybrid energy storage systems in urban rail transit," in *2016 International Conference on Electrical Systems for Aircraft, Railway, Ship Propulsion and Road Vehicles & International Transportation Electrification Conference (ESARS-ITEC)*, Toulouse, France. DOI: 10.1109/ESARS-ITEC.2016.7841408.
- [136] R. Teymourfar, R. Fard, B. Asaei and H. Iman-Eini, "Energy recovery in a metro network using stationary supercapacitors," in *2011 2nd Power Electronics, Drive Systems and Technologies Conference*, Tehran, Iran. DOI: 10.1109/PEDSTC.2011.5742440.
- [137] V. Calderaro, V. Galdi, G. Graber and A. Piccolo, "Optimal siting and sizing of stationary supercapacitors in a metro network using PSO," in *2015 IEEE International Conference on Industrial Technology (ICIT)*, Seville, Spain. DOI: 10.1109/ICIT.2015.7125493.

- [138] R. Teymourfar, G. Farivar, H. Iman-Eini and B. Asaei, "Optimal stationary super-capacitor energy storage system in a metro line," in *2011 2nd International Conference on Electric Power and Energy Conversion Systems (EPECS)*, Sharjah, United Arab Emirates. DOI: 10.1109/EPECS.2011.6126828.
- [139] R. Barrero, X. Tackoen and J. Van Mierlo, "Quasi-static simulation method for evaluation of energy consumption in hybrid light rail vehicles," in *2008 IEEE Vehicle Power and Propulsion Conference*, Harbin, China. DOI: 10.1109/VPPC.2008.4677763.
- [140] T. Ratniyomchai, "Optimal design and control of stationary electrochemical double-layer capacitors for light railways," Ph.D. thesis, Department of Electronic, Electrical and Systems Engineering, The University of Birmingham, UK, 2016. [Online]. Available: <https://etheses.bham.ac.uk/id/eprint/7133/1/Ratniyomchai16PhD.pdf> (Accessed: Dec 22, 2020).
- [141] F. Zhu, Z. Yang, F. Lin and Y. Xin, "Decentralized cooperative control of multiple energy storage systems in urban railway based on multiagent deep reinforcement learning," *IEEE Transactions on Power Electronics*, vol. 35, no. 9, pp. 9368–9379, Sep 2020. DOI: 10.1109/TPEL.2020.2971637.
- [142] P. Radu, M. Lewandowski and A. Szelag, "On-board and wayside energy storage devices applications in urban transport systems – case study analysis for power applications," *Energies*, vol. 13, no. 8, Apr 2020. DOI: 10.3390/en13082013.
- [143] Z. Yang, F. Zhu and F. Lin, "Deep-reinforcement-learning-based energy management strategy for supercapacitor energy storage systems in urban rail transit," *IEEE Transactions on Intelligent Transportation Systems*, Jan 2020. DOI: 10.1109/TITS.2019.2963785.
- [144] T. Edwards and K. Chelst, *Mathematical Modeling with Algebra: Using Authentic Problem Contexts*. Detroit, US: Wayne State University, 2017. ISBN: 9781979305655.
- [145] M. Rathi and N. Prabha, "Interval type-2 fuzzy logic controller-based multi-level shunt active power line conditioner for harmonic mitigation," *International Journal of Fuzzy Systems*, vol. 21, no. 1, pp. 104–114, Feb 2019. DOI: 10.1007/s40815-018-0547-7.
- [146] L. Reznik, *Fuzzy Controllers*. Oxford, UK: Newnes, 1997. ISBN: 0750634294.
- [147] Zenone Elettronica S.r.l, "DC power supplies AL3000 series user's manual," Avellino, Italy, Feb 2015. [Online]. Available: https://www.zenoneelettronica.it/manuali/um_al3000_r04e.pdf (Accessed: Dec 23, 2020).
- [148] Zenone Elettronica S.r.l, "DC bidirectional power supply with line regenerator," Avellino, Italy, Mar 2014.

- [149] Siemens, "Sinamics drives: Sinamics DCP DC/DC power converter operating instructions," Nuremberg, Germany, May 2016. [Online]. Available: https://cache.industry.siemens.com/dl/files/223/109480223/att_884380/v1/Manual_en.pdf (Accessed: Dec 23, 2020).
- [150] National Instruments, "Specifications NI cRIO-9063 embedded real-time controller with reconfigurable FPGA for C series modules," Texas, US, Oct 2015. [Online]. Available: https://www.ni.com/pdf/manuals/376330a_02.pdf (Accessed: Dec 23, 2020).
- [151] National Instruments, "User manual NI cRIO-9063 embedded real-time controller with reconfigurable FPGA for C series modules," Texas, US, Jun 2016. [Online]. Available: <https://www.ni.com/pdf/manuals/376507b.pdf> (Accessed: Dec 23, 2020).
- [152] National Instruments, "Getting started guide NI 9206," Texas, US, Jun 2017. [Online]. Available: <https://www.ni.com/pdf/manuals/374231e.pdf> (Accessed: Dec 23, 2020).
- [153] National Instruments, "Getting started guide NI 9263," Texas, US, Mar 2016. [Online]. Available: <https://www.ni.com/pdf/manuals/373781h.pdf> (Accessed: Dec 23, 2020).
- [154] Maxwell Technologies, "Datasheet 125V heavy transportation module," California, US, 2013. [Online]. Available: https://www.maxwell.com/images/documents/125V_Module_datasheet.pdf (Accessed: Dec 23, 2020).
- [155] Maxwell Technologies, "User manual notes on using ultracapacitor modules," California, US, 2013. [Online]. Available: <https://www.maxwell.com/images/documents/NotesOnUsingUltracapacitorModules.pdf> (Accessed: Dec 23, 2020).

Appendices

Appendix 1 Fuzzy controller rules

Table A1: Rule table of the fuzzy logic controller consisting five inputs and two outputs

Rule	Input Variables					Output Variables	
	Journey Time	Positive SOC Drift	Negative SOC Drift	ROC	Track Voltage	Charging Current Limit	Discharging Current Limit
1	Beginning	L	N/A	L	Below	N/A	H
2	Beginning	L	N/A	A	Below	N/A	H
3	Beginning	L	N/A	H	Below	N/A	H
4	Beginning	L	N/A	VH	Below	N/A	H
5	Beginning	N/A	L	L	Below	N/A	H
6	Beginning	N/A	L	A	Below	N/A	H
7	Beginning	N/A	L	H	Below	N/A	H
8	Beginning	N/A	L	VH	Below	N/A	H
9	Beginning	A	N/A	L	Below	N/A	H
10	Beginning	A	N/A	A	Below	N/A	H
11	Beginning	A	N/A	H	Below	N/A	H
12	Beginning	A	N/A	VH	Below	N/A	H
13	Beginning	N/A	A	L	Below	N/A	H
14	Beginning	N/A	A	A	Below	N/A	H
15	Beginning	N/A	A	H	Below	N/A	H
16	Beginning	N/A	A	VH	Below	N/A	H
17	Beginning	H	N/A	L	Below	N/A	H
18	Beginning	H	N/A	A	Below	N/A	H
19	Beginning	H	N/A	H	Below	N/A	H
20	Beginning	H	N/A	VH	Below	N/A	H
21	Beginning	N/A	H	L	Below	N/A	H
22	Beginning	N/A	H	A	Below	N/A	H
23	Beginning	N/A	H	H	Below	N/A	H
24	Beginning	N/A	H	VH	Below	N/A	H
25	Beginning	VH	N/A	L	Below	N/A	H
26	Beginning	VH	N/A	A	Below	N/A	H
27	Beginning	VH	N/A	H	Below	N/A	H
28	Beginning	VH	N/A	VH	Below	N/A	H
29	Beginning	N/A	VH	L	Below	N/A	H
30	Beginning	N/A	VH	A	Below	N/A	H
31	Beginning	N/A	VH	H	Below	N/A	A

32	Beginning	N/A	VH	VH	Below	N/A	A
33	First-Mid	L	N/A	L	Below	N/A	H
34	First-Mid	L	N/A	A	Below	N/A	H
35	First-Mid	L	N/A	H	Below	N/A	H
36	First-Mid	L	N/A	VH	Below	N/A	H
37	First-Mid	N/A	L	L	Below	N/A	H
38	First-Mid	N/A	L	A	Below	N/A	H
39	First-Mid	N/A	L	H	Below	N/A	H
40	First-Mid	N/A	L	VH	Below	N/A	H
41	First-Mid	A	N/A	L	Below	N/A	H
42	First-Mid	A	N/A	A	Below	N/A	H
43	First-Mid	A	N/A	H	Below	N/A	H
44	First-Mid	A	N/A	VH	Below	N/A	H
45	First-Mid	N/A	A	L	Below	N/A	H
46	First-Mid	N/A	A	A	Below	N/A	H
47	First-Mid	N/A	A	H	Below	N/A	H
48	First-Mid	N/A	A	VH	Below	N/A	H
49	First-Mid	H	N/A	L	Below	N/A	H
50	First-Mid	H	N/A	A	Below	N/A	H
51	First-Mid	H	N/A	H	Below	N/A	H
52	First-Mid	H	N/A	VH	Below	N/A	H
53	First-Mid	N/A	H	L	Below	N/A	H
54	First-Mid	N/A	H	A	Below	N/A	H
55	First-Mid	N/A	H	H	Below	N/A	A
56	First-Mid	N/A	H	VH	Below	N/A	A
57	First-Mid	VH	N/A	L	Below	N/A	H
58	First-Mid	VH	N/A	A	Below	N/A	H
59	First-Mid	VH	N/A	H	Below	N/A	H
60	First-Mid	VH	N/A	VH	Below	N/A	H
61	First-Mid	N/A	VH	L	Below	N/A	A
62	First-Mid	N/A	VH	A	Below	N/A	L
63	First-Mid	N/A	VH	H	Below	N/A	L
64	First-Mid	N/A	VH	VH	Below	N/A	VL
65	Second-Mid	L	N/A	L	Below	N/A	H
66	Second-Mid	L	N/A	A	Below	N/A	H
67	Second-Mid	L	N/A	H	Below	N/A	H
68	Second-Mid	L	N/A	VH	Below	N/A	H
69	Second-Mid	N/A	L	L	Below	N/A	H
70	Second-Mid	N/A	L	A	Below	N/A	H
71	Second-Mid	N/A	L	H	Below	N/A	H
72	Second-Mid	N/A	L	VH	Below	N/A	H
73	Second-Mid	A	N/A	L	Below	N/A	H
74	Second-Mid	A	N/A	A	Below	N/A	H
75	Second-Mid	A	N/A	H	Below	N/A	H
76	Second-Mid	A	N/A	VH	Below	N/A	H
77	Second-Mid	N/A	A	L	Below	N/A	H
78	Second-Mid	N/A	A	A	Below	N/A	H
79	Second-Mid	N/A	A	H	Below	N/A	H
80	Second-Mid	N/A	A	VH	Below	N/A	H

81	Second-Mid	H	N/A	L	Below	N/A	H
82	Second-Mid	H	N/A	A	Below	N/A	H
83	Second-Mid	H	N/A	H	Below	N/A	H
84	Second-Mid	H	N/A	VH	Below	N/A	H
85	Second-Mid	N/A	H	L	Below	N/A	L
86	Second-Mid	N/A	H	A	Below	N/A	VL
87	Second-Mid	N/A	H	H	Below	N/A	VL
88	Second-Mid	N/A	H	VH	Below	N/A	VL
89	Second-Mid	VH	N/A	L	Below	N/A	H
90	Second-Mid	VH	N/A	A	Below	N/A	H
91	Second-Mid	VH	N/A	H	Below	N/A	H
92	Second-Mid	VH	N/A	VH	Below	N/A	H
93	Second-Mid	N/A	VH	L	Below	N/A	VL
94	Second-Mid	N/A	VH	A	Below	N/A	VL
95	Second-Mid	N/A	VH	H	Below	N/A	VL
96	Second-Mid	N/A	VH	VH	Below	N/A	VL
97	End	L	N/A	L	Below	N/A	H
98	End	L	N/A	A	Below	N/A	H
99	End	L	N/A	H	Below	N/A	H
100	End	L	N/A	VH	Below	N/A	H
101	End	N/A	L	L	Below	N/A	VL
102	End	N/A	L	A	Below	N/A	VL
103	End	N/A	L	H	Below	N/A	VL
104	End	N/A	L	VH	Below	N/A	VL
105	End	A	N/A	L	Below	N/A	H
106	End	A	N/A	A	Below	N/A	H
107	End	A	N/A	H	Below	N/A	H
108	End	A	N/A	VH	Below	N/A	H
109	End	N/A	A	L	Below	N/A	VL
110	End	N/A	A	A	Below	N/A	VL
111	End	N/A	A	H	Below	N/A	VL
112	End	N/A	A	VH	Below	N/A	VL
113	End	H	N/A	L	Below	N/A	H
114	End	H	N/A	A	Below	N/A	H
115	End	H	N/A	H	Below	N/A	H
116	End	H	N/A	VH	Below	N/A	H
117	End	N/A	H	L	Below	N/A	VL
118	End	N/A	H	A	Below	N/A	VL
119	End	N/A	H	H	Below	N/A	VL
120	End	N/A	H	VH	Below	N/A	VL
121	End	VH	N/A	L	Below	N/A	H
122	End	VH	N/A	A	Below	N/A	H
123	End	VH	N/A	H	Below	N/A	H
124	End	VH	N/A	VH	Below	N/A	H
125	End	N/A	VH	L	Below	N/A	VL
126	End	N/A	VH	A	Below	N/A	VL
127	End	N/A	VH	H	Below	N/A	VL
128	End	N/A	VH	VH	Below	N/A	VL
129	Beginning	N/A	L	L	Above	H	N/A

130	Beginning	N/A	L	A	Above	H	N/A
131	Beginning	N/A	L	H	Above	H	N/A
132	Beginning	N/A	L	VH	Above	H	N/A
133	Beginning	L	N/A	L	Above	H	N/A
134	Beginning	L	N/A	A	Above	H	N/A
135	Beginning	L	N/A	H	Above	H	N/A
136	Beginning	L	N/A	VH	Above	H	N/A
137	Beginning	N/A	A	L	Above	H	N/A
138	Beginning	N/A	A	A	Above	H	N/A
139	Beginning	N/A	A	H	Above	H	N/A
140	Beginning	N/A	A	VH	Above	H	N/A
141	Beginning	A	N/A	L	Above	H	N/A
142	Beginning	A	N/A	A	Above	H	N/A
143	Beginning	A	N/A	H	Above	H	N/A
144	Beginning	A	N/A	VH	Above	H	N/A
145	Beginning	N/A	H	L	Above	H	N/A
146	Beginning	N/A	H	A	Above	H	N/A
147	Beginning	N/A	H	H	Above	H	N/A
148	Beginning	N/A	H	VH	Above	H	N/A
149	Beginning	H	N/A	L	Above	H	N/A
150	Beginning	H	N/A	A	Above	H	N/A
151	Beginning	H	N/A	H	Above	H	N/A
152	Beginning	H	N/A	VH	Above	H	N/A
153	Beginning	N/A	VH	L	Above	H	N/A
154	Beginning	N/A	VH	A	Above	H	N/A
155	Beginning	N/A	VH	H	Above	H	N/A
156	Beginning	N/A	VH	VH	Above	H	N/A
157	Beginning	VH	N/A	L	Above	H	N/A
158	Beginning	VH	N/A	A	Above	H	N/A
159	Beginning	VH	N/A	H	Above	A	N/A
160	Beginning	VH	N/A	VH	Above	A	N/A
161	First-Mid	N/A	L	L	Above	H	N/A
162	First-Mid	N/A	L	A	Above	H	N/A
163	First-Mid	N/A	L	H	Above	H	N/A
164	First-Mid	N/A	L	VH	Above	H	N/A
165	First-Mid	L	N/A	L	Above	H	N/A
166	First-Mid	L	N/A	A	Above	H	N/A
167	First-Mid	L	N/A	H	Above	H	N/A
168	First-Mid	L	N/A	VH	Above	H	N/A
169	First-Mid	N/A	A	L	Above	H	N/A
170	First-Mid	N/A	A	A	Above	H	N/A
171	First-Mid	N/A	A	H	Above	H	N/A
172	First-Mid	N/A	A	VH	Above	H	N/A
173	First-Mid	A	N/A	L	Above	H	N/A
174	First-Mid	A	N/A	A	Above	H	N/A
175	First-Mid	A	N/A	H	Above	H	N/A
176	First-Mid	A	N/A	VH	Above	H	N/A
177	First-Mid	N/A	H	L	Above	H	N/A
178	First-Mid	N/A	H	A	Above	H	N/A

179	First-Mid	N/A	H	H	Above	H	N/A
180	First-Mid	N/A	H	VH	Above	H	N/A
181	First-Mid	H	N/A	L	Above	H	N/A
182	First-Mid	H	N/A	A	Above	H	N/A
183	First-Mid	H	N/A	H	Above	A	N/A
184	First-Mid	H	N/A	VH	Above	A	N/A
185	First-Mid	N/A	VH	L	Above	H	N/A
186	First-Mid	N/A	VH	A	Above	H	N/A
187	First-Mid	N/A	VH	H	Above	H	N/A
188	First-Mid	N/A	VH	VH	Above	H	N/A
189	First-Mid	VH	N/A	L	Above	A	N/A
190	First-Mid	VH	N/A	A	Above	L	N/A
191	First-Mid	VH	N/A	H	Above	L	N/A
192	First-Mid	VH	N/A	VH	Above	VL	N/A
193	Second-Mid	N/A	L	L	Above	H	N/A
194	Second-Mid	N/A	L	A	Above	H	N/A
195	Second-Mid	N/A	L	H	Above	H	N/A
196	Second-Mid	N/A	L	VH	Above	H	N/A
197	Second-Mid	L	N/A	L	Above	H	N/A
198	Second-Mid	L	N/A	A	Above	H	N/A
199	Second-Mid	L	N/A	H	Above	H	N/A
200	Second-Mid	L	N/A	VH	Above	H	N/A
201	Second-Mid	N/A	A	L	Above	H	N/A
202	Second-Mid	N/A	A	A	Above	H	N/A
203	Second-Mid	N/A	A	H	Above	H	N/A
204	Second-Mid	N/A	A	VH	Above	H	N/A
205	Second-Mid	A	N/A	L	Above	H	N/A
206	Second-Mid	A	N/A	A	Above	H	N/A
207	Second-Mid	A	N/A	H	Above	H	N/A
208	Second-Mid	A	N/A	VH	Above	H	N/A
209	Second-Mid	N/A	H	L	Above	H	N/A
210	Second-Mid	N/A	H	A	Above	H	N/A
211	Second-Mid	N/A	H	H	Above	H	N/A
212	Second-Mid	N/A	H	VH	Above	H	N/A
213	Second-Mid	H	N/A	L	Above	L	N/A
214	Second-Mid	H	N/A	A	Above	VL	N/A
215	Second-Mid	H	N/A	H	Above	VL	N/A
216	Second-Mid	H	N/A	VH	Above	VL	N/A
217	Second-Mid	N/A	VH	L	Above	H	N/A
218	Second-Mid	N/A	VH	A	Above	H	N/A
219	Second-Mid	N/A	VH	H	Above	H	N/A
220	Second-Mid	N/A	VH	VH	Above	H	N/A
221	Second-Mid	VH	N/A	L	Above	VL	N/A
222	Second-Mid	VH	N/A	A	Above	VL	N/A
223	Second-Mid	VH	N/A	H	Above	VL	N/A
224	Second-Mid	VH	N/A	VH	Above	VL	N/A
225	End	N/A	L	L	Above	H	N/A
226	End	N/A	L	A	Above	H	N/A
227	End	N/A	L	H	Above	H	N/A

228	End	N/A	L	VH	Above	H	N/A
229	End	L	N/A	L	Above	VL	N/A
230	End	L	N/A	A	Above	VL	N/A
231	End	L	N/A	H	Above	VL	N/A
232	End	L	N/A	VH	Above	VL	N/A
233	End	N/A	A	L	Above	H	N/A
234	End	N/A	A	A	Above	H	N/A
235	End	N/A	A	H	Above	H	N/A
236	End	N/A	A	VH	Above	H	N/A
237	End	A	N/A	L	Above	VL	N/A
238	End	A	N/A	A	Above	VL	N/A
239	End	A	N/A	H	Above	VL	N/A
240	End	A	N/A	VH	Above	VL	N/A
241	End	N/A	H	L	Above	H	N/A
242	End	N/A	H	A	Above	H	N/A
243	End	N/A	H	H	Above	H	N/A
244	End	N/A	H	VH	Above	H	N/A
245	End	H	N/A	L	Above	VL	N/A
246	End	H	N/A	A	Above	VL	N/A
247	End	H	N/A	H	Above	VL	N/A
248	End	H	N/A	VH	Above	VL	N/A
249	End	N/A	VH	L	Above	H	N/A
250	End	N/A	VH	A	Above	H	N/A
251	End	N/A	VH	H	Above	H	N/A
252	End	N/A	VH	VH	Above	H	N/A
253	End	VH	N/A	L	Above	VL	N/A
254	End	VH	N/A	A	Above	VL	N/A
255	End	VH	N/A	H	Above	VL	N/A
256	End	VH	N/A	VH	Above	VL	N/A

Appendix 2 SOC control test rig

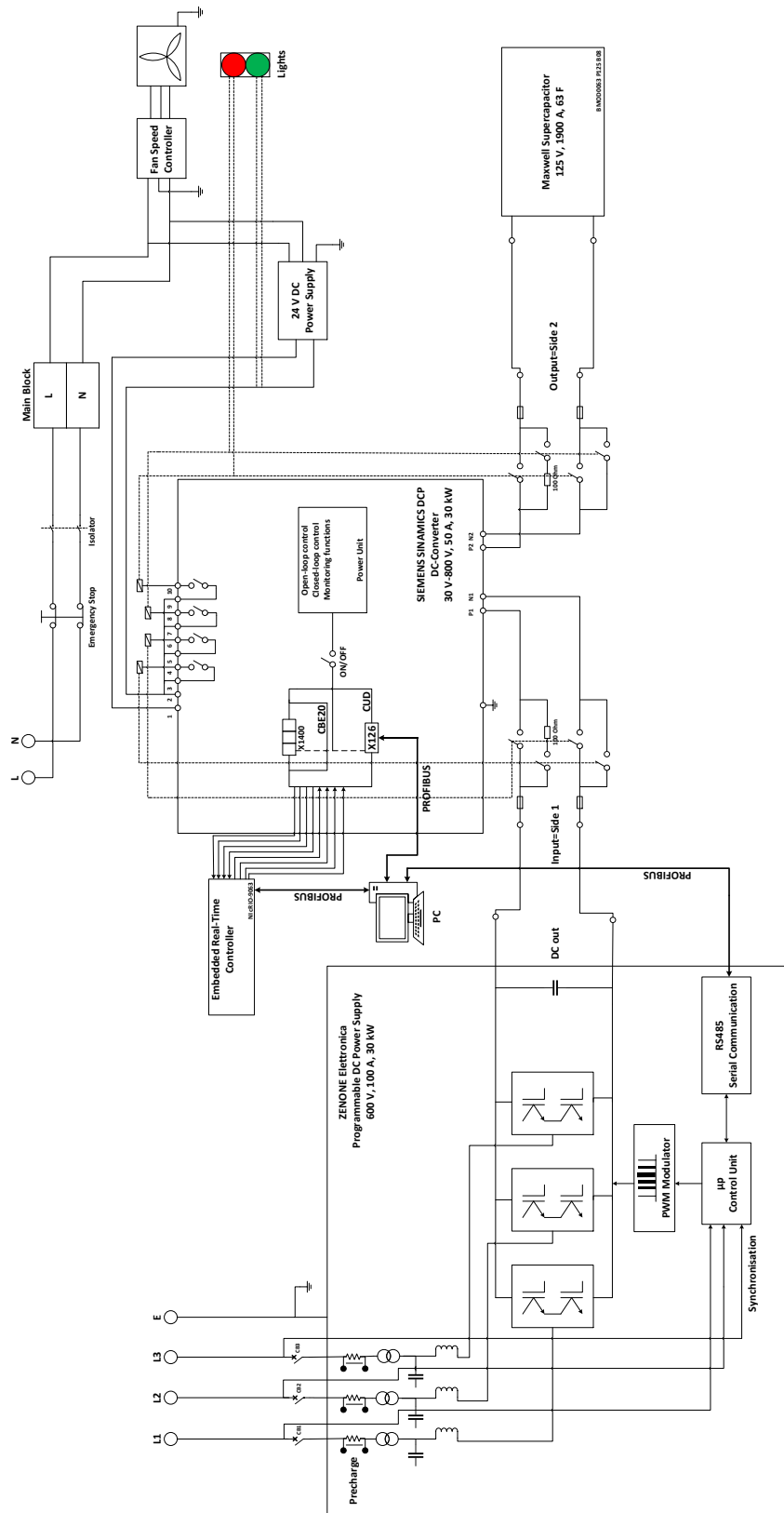
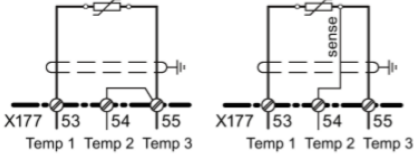


Figure A1: Single-line diagram for the experimental setup

Appendix 3 SINAMICS DCP electrical connection

Table A2: Terminals on the connector board of the SINAMICS DCP power converter [147]

Terminal -X177	Function		Technical specifications	
Analog inputs (assignable inputs)				
1 2	AI 3 + AI 3 -	Analog input 3	Input type (signal type): Differential input ± 10 V; 150 k Ω resolution approx. 5.4 mV (± 11 bits) common-mode controllability: ± 15 V	
3 4	AI 4 + AI 4 -	Analog input 4		
5 6	AI 5 + AI 5 -	Analog input 5		
7 8	AI 6 + AI 6 -	Analog input 6		
Digital inputs (assignable inputs)				
9 10	DC 24 V	24 V supply (output)		24 VDC, short-circuit proof Max. load 200 mA (terminals 9 and 10 combined), internal supply in relation to internal ground
11	DI 0	Digital input 0	H signal: +15 V to +30 V	
12	DI 1	Digital input 1	L signal: -30 V to +5 V or terminal open circuit 8.5 mA at 24 V	
13	DI 2	Digital input 2		
14	DI 3	Digital input 3		
Digital inputs/outputs (assignable inputs/outputs)				
15	DI/DO 4	Digital input /output 4	Type, parameterizable input/output Input characteristics: H signal: +15 V to +30 V L signal: 0 V to +5 V or terminal open 8.5 mA at 24 V	
16	DI/DO 5	Digital input /output 5	Output characteristics: H signal: +20 V to +26 V L signal: 0 to +2 V short-circuit proof; max. current carrying capacity: 100 mA per DO; max. total load of all DO (CUD left -X177:15-22 + CUD right -X177:15-22): 800 mA Internal protection circuit (free-wheeling diode) If overload occurs: Alarm A60018	
17	DI/DO 6	Digital input /output 6		
18	DI/DO 7	Digital input /output 7		
19	DO 0	Digital output 0		
20	DO 1	Digital output 1	H signal: +20 V to +26 V L signal: 0 to +2 V short-circuit proof; max. current carrying capacity: 100 mA per DO; max. total load of all DO (CUD left -X177:15-22 + CUD right -X177:15-22): 800 mA	
21	DO 2	Digital output 2		
22	DO 3	Digital output 3		
23 ... 24	M	Ground, digital	Internal protection circuit (free-wheeling diode) If overload occurs: Alarm A60018	
Analog inputs, setpoint inputs (assignable inputs)				

25 26	AI 0 + AI 0 -	Analog input 0	Parameterizable input type (signal type): Differential input ± 10 V; 150 k Ω
27 28	AI 1 + AI 1 -	Analog input 1	Current input 0 mA - 20 mA; 300 Ω or 4 mA - 20 mA; 300 Ω resolution approx. 0.66 mV (± 14 bit) Common-mode controllability: ± 15 V
29 30	AI 2 + AI 2 -	Analog input 2	Input type (signal type): - Differential input ± 10 V; 150 k Ω Resolution approx. 0.66 mV (± 14 bits) Common mode controllability ± 15 V
Reference voltage			
31 32	P10 N10	Reference voltage ± 10 V (output)	Tolerance $\pm 1\%$ at 25° C Stability 0.1% per 10° K 10 mA short-circuit proof
33, 34	M	Ground, analog	
Terminals not used			
35, 36	M	Ground, digital	
37		Not used	
38		Not used	
39		Not used	
40		Not used	
Terminals not used			
41	Supply		+13.7 V to +15.2 V, 300 mA short-circuit proof (electronically protected) If overload occurs: Alarm A60018
42	Ground		
43	Not used		
44	Not used		
45	Not used		
46	Not used		
47	Not used		
48	Not used		
Analog outputs (assignable outputs)			
49	AO 0	Analog output 0	± 10 V, max. 2 mA short-circuit proof, resolution ± 15 bits
50	M	Ground, analog	
51	AO 1	Analog output 1	
52	M	Ground, analog	
Connections for temperature sensors			
53	Temp1		Sensor according to P50490 (see SINAMICS DCP List Manual). The cable to the temperature sensor must be shielded and connected to
54	Temp2 (sense cable)		
55	Temp3		ground at both ends. The cables from the Temp 1 and Temp 3 connections to the temperature sensor must have approximately the same length. The sense cable (Temp 2) is used for compensating for the cable resistances. If you are not using a sense cable, connect terminals 54 and 55. Connection with / without sense cable: 
56	M	Ground, analog	